UNIVERSIDAD COMPLUTENSE DE MADRID
FACULTAD DE CIENCIAS FÍSICAS
DEPARTAMENTO DE ASTROFÍSICA Y
CIENCIAS DE LA ATMÓSFERA

TESIS DOCTORAL

Lessons from high-energy studies of AGN: X-ray absorption and its variability

Lecciones del estudio de AGN a altas energías: absorción de rayos X y su variabilidad

MEMORIA PARA OPTAR AL GRADO DE DOCTOR

PRESENTADA POR

Mario Sanfrutos Carreras

DIRECTOR

Giovanni Miniutti

Madrid, 2017

UNIVERSIDAD
COMPLUTENSE
MADRID

Lessons from high–energy studies of AGN: X–ray absorption and its variability

Lecciones del estudio de AGN a altas energías: Absorción de rayos X y su variabilidad

Memoria con la que

Mario Sanfrutos Carreras

aspira al grado de
Doctor en Ciencias Físicas

Tesis doctoral dirigida por

Dr. Giovanni Miniutti

Departamento de Astrofísica y Ciencias de la Atmósfera
(Facultad de Ciencias Físicas, UCM)

Centro de Astrobiología
(CSIC / INTA)

30 de mayo de 2016

Resumen

Esta tesis consiste en el estudio tanto observacional como teórico de los núcleos activos de galaxias (AGN, por las siglas en inglés de *active galactic nuclei*), especialmente en la banda de los rayos X. A continuación expongo las líneas de investigación generales que he abordado a lo largo de este trabajo, para después profundizar en cada una de ellas.

Desde un punto de vista puramente teórico, el trabajo de mi tesis doctoral se enmarca dentro del paradigma del AGN consistente en un agujero negro supermasivo central alrededor del cual se forma un disco por efecto de la gravedad. El agujero negro acrece materia desde dicho disco —geométricamente plano y delgado, físicamente denso y opaco—, favoreciendo la disipación de una fracción significativa de energía en sus regiones más internas a causa de las tensiones asociadas a la viscosidad del flujo de acrecimiento. Esta energía es disipada en forma de fotones energéticos, en su mayoría en el rango del ultravioleta, que se emiten desde las regiones más internas del disco de acrecimiento. Los fotones ultravioletas ganan energía en su interacción con electrones libres muy calientes de las capas adyacentes al disco por efecto *Compton* inverso, alcanzando el rango de energías de los rayos X duros, que son emitidos en todas las direcciones. Por analogía con la región del sol que emite en esta banda de energía, el material que actúa como fuente primaria de rayos X suele ser llamado «corona». La irradiación del disco de acrecimiento por estos rayos X da lugar a un característico espectro de reflexión y a las líneas de emisión fluorescente —la más importante de las cueles es la del hierro, dada su abundancia y su relativo aislamiento en el espectro—. Por consiguiente, lo que detectamos desde nuestros observatorios en órbita es una complicada mezcla de al menos dos componentes: rayos X sin procesar —el llamado «continuo», que proviene directamente de la corona—, más rayos X procesados que son producto de la reflexión de dicho continuo desde el material irradiado por el mismo —esencialmente, el disco de acrecimiento y las paredes interiores del toro—. Ambas componentes espectrales están, además, deformadas debido a los efectos relativistas que la proximidad del agujero negro imprime en el espacio tiempo, en el que están localizadas las diversas fuentes de emisión de la radiación observada: efecto *Doppler*, aberración, curvatura de la luz y corrimiento al rojo.

Desde el punto de vista observacional, por todo lo mencionado en el párrafo anterior, las características espectrales de cada observación —y en especial la forma de la línea relativista del hierro— acarrean una valiosa información acerca de las regiones más internas de los AGN. Complementariamente, del análisis de las curvas de luz se obtiene información sobre la variabilidad intrínseca del AGN, y de ésta se puede inferir información adicional acerca de los mecanismos que producen los rayos X, sobre las propiedades de las distintas componentes espectrales y sobre la geometría de las regiones emisoras. A este respecto, los objetos de interés para mi disertación son los AGN no oscurecidos, es decir, aquellos AGN que ofrecen una visión directa de sus regiones más internas, sin que las estructuras del llamado «toro» de polvo y gas propuesto en los modelos de unificación se interpongan en nuestra línea de visión al núcleo. Los datos empleados a lo largo de esta tesis provienen tanto de observaciones propuestas *ad hoc* por nuestro grupo, como de los archivos de *XMM–Newton* y *Chandra*.

La variabilidad espectral y de flujo en rayos X es una propiedad muy común entre los AGN. Esta variabilidad que se observa es tanto intrínseca a cualquier escala de tiempo —debido a la propia variabilidad de la fuente— como producto de la absorción por parte de diversas estructuras. La variabilidad asociada con fenómenos de absorción fue originalmente identificada en tiempos de escala relativamente largos —de meses a años—. No obstante, en los años previos al comienzo de mi trabajo de doctorado, ya se habían publicado varios ejemplos de fuentes de rayos X que también presentan variabilidad por absorción en tiempos de escala cortos —de horas a días—, la cual es probablemente debida a la presencia de estructuras absorbentes que cruzan nuestra línea de visión a la fuente primaria de rayos X: conjuntos de nubes compactas y frías con densidades de columna típicamente comprendidas en el rango equivalente a 10^{22} – 10^{24} átomos de hidrógeno por cada centímetro cuadrado, densidades físicas de entre 10^{9} y 10^{11} átomos por cada centímetro cúbico, velocidades del orden de unos pocos miles de kilómetros por segundo y situadas a una distancia de entre cien y diez mil radios gravitacionales del agujero negro central. Estas propiedades son llamativamente parecidas a las de las nubes responsables de la emisión de las líneas anchas presentes en las bandas óptica y ultravioleta de los espectros de los AGN. La primera parte de mi tesis, que detallo extensamente en el capítulo 2, consiste en el estudio de la variabilidad en rayos X en la galaxia de *Seyfert* de tipo 1 de líneas estrechas «SWIFT J2127.4+5654». Encontramos que esta variabilidad es debida a fenómenos de absorción, e identificamos las estructuras físicas responsables de la misma a tiempos de escala cortos con las nubes compactas de la llamada «región de las líneas anchas». La variabilidad en tiempos de escala más largos, en cambio, está asociada más probablemente a estructuras más extensas, seguramente del toro de gas y polvo.

Una extensión de este primer bloque derivó en el estudio teórico de los efectos relativistas que afectan a la física del disco de acrecimiento. En el capítulo 3 desarrollamos un método para sondear la cantidad de flujo que es emitida desde cada región del disco y de la corona por medio de un eclipse causado por el tránsito de una nube de la región de las líneas anchas por nuestra línea de visión a las regiones emisoras de rayos X. El punto de partida es el resultado del estudio de los tamaños de la nube y la corona de SWIFT J2127.4+5654, que resultan ser comparables, por lo que un modelado detallado de estos eventos de ocultamiento en AGN tiene el potencial de permitir inferir con gran precisión la geometría del sistema. Con este fin hicimos uso de un modelo espectral relativista para elaborar predicciones teóricas de los diferentes parámetros observables que pueden ser medidos estudiando simulaciones de eclipses en rayos X. Entre dichos parámetros se incluyen el espín del agujero negro, la inclinación del sistema y los tamaños de la fuente y de la nube, así como la densidad y el estado de ionización de esta última. En este estudio concluimos que la absorción varía en función del rango de energías y que es máxima al cubrirse la parte del disco de acrecimiento que se aproxima al observador, es decir, las anisotropías detectadas en el flujo computado desde espectros tomados a lo largo de un mismo eclipse son atribuibles al efecto *Doppler* relativista, resultando de este modo útiles para determinar la geometría de las regiones más próximas al agujero negro. Esta es la motivación para estudiar las ratios de diferentes curvas de luz en las bandas de rayos X duros y blandos producidas durante varios momentos de un mismo eclipse y usarlas para caracterizar las propiedades de las regiones más internas del disco de acrecimiento de una manera novedosa e independiente de modelos espectrales.

El tercer y último bloque de mi disertación tiene que ver con el llamado «*warm absorber*», gas fotoionizado por las fuentes centrales de rayos X, que habitualmente se halla en forma de vientos de hasta varios miles de kilómetros por segundo. La absorción que aún se encuentra presente en los AGN no oscurecidos es debida a este *warm absorber*. Esta parte de mi tesis se desarrolla en el capítulo 4, y consiste en el estudio detallado de las propiedades de los *warm absorbers* —su localización, velocidad, tamaño, estado de ionización, densidad, temperatura y origen, entre otras—,

con precisiones hasta ahora inéditas gracias a la espectroscopía de rayos X de alta resolución que ofrecen los observatorios espaciales como *XMM–Newton* y muy especialmente *Chandra*. En ella estudio la variabilidad espectral de la galaxia de *Seyfert* de tipo 1.2 «ESO 323-G77» a tiempos de escala cortos y largos. Para ello utilicé observaciones de entre 2006 y 2013 tomadas por *XMM–Newton*, *Chandra*, *Swift* y *Suzaku*. Las cuatro observaciones de alta resolución tomadas por *Chandra* en 2010 supusieron una oportunidad única de estudiar las propiedades de las estructuras absorbentes en detalle, así como la variabilidad espectral del sistema en tiempos de escala tan cortos como unos pocos días. A partir del profuso conjunto de líneas de absorción reveladas en estos datos, se identifican dos *warm absorbers* con densidades de columna e ionizaciones constantes a cualquier tiempo de escala, lo cual sugiere que dichas líneas son debidas a un flujo de material homogéneo y extenso escapando del sistema. Una tercera nube absorbente, ionizada en menor grado que las otras, también está presente en sustitución del material absorbente estrictamente neutro que se infiere habitualmente del análisis en rayos X de las llamadas fuentes oscurecidas por nubes de densidades «*Compton–thin*». Este material absorbente, más frío, varía de manera significativa en densidad de columna a largos tiempos de escala, lo cual demuestra su naturaleza heterogénea. Además, su ionización responde a las variaciones intrínsecas de luminosidad de la fuente primaria de rayos X en tiempos de escala de unos pocos días, lo que indica que la nube absorbente está en equilibrio de fotoionización con la fuente a dichas escalas de tiempo. Esto nos permite calcular unos límites para la densidad del gas. Los datos analizados son compatibles con que todas las nubes absorbentes —o fases— cohabiten entre los extremos interior y exterior del toro. Si esta configuración física es la verdadera, las tres fases comparten la misma presión, lo que sugiere que las estructuras más calientes confinan a las más frías.

Abstract

This is a doctoral dissertation about the X–ray observational and theoretical study of active galactic nuclei (AGN). In the following paragraphs, the research lines addressed during my Ph. D. work are exposed.

From a theoretical approach, my work belongs to the supermassive black hole (SMBH) + accretion disc paradigm for AGN. Material within the geometrically thin, optically thick disc, accretes onto the black hole, dissipating a significant amount of energy in its innermost regions due to viscous tensions. This energy is dissipated as energetic photons, most in the ultraviolet (UV) range, which gain energy in their interaction with very hot, free electrons near the disc, up to reaching the X–ray wavelength. This process is referred to as inverse Compton upscattering. The primary X–ray source is called "corona", by analogy with the X–ray–emitting region in the Sun. Irradiation of the accretion disc by those X–rays, yields a characteristic reflection spectrum, and the fluorescent emission lines (being the Fe Kα the most important of them). Hence, an intrincate blend of at least two spectral components is detected by our observatories in orbit: unprocessed X–rays (the so–called "continuum", emitted by the corona), and reprocessed X–rays (result of the reflection of the continuum in the irradiated material, namely the accretion disc and the torus inner boundaries). Both components are relativistically blurred due to the proximity of the X–ray sources to the black hole. The relativistid effects involved in this process are: Doppler boosting, aberration, light bending and gravitational redshift.

From an observational point of view, given the facts stated in the upper paragraph, the spectral features of each observation (especially, the relativistic iron line profile), carry valuable information of the innermost regions of AGN. Also, light curves analyses shed light on AGN intrinsic variability, providing additional information about the mechanisms producing the X–rays, about the properties of the different spectral components, and about the geometry of the emitting regions. In this regard, the interesting objects for this dissertation are unobscured AGN, i.e., those AGN that allow a direct view of their innermost regions, with the so–called "torus" of the Unification models not blocking our line of sight (LOS) to the nucleus. The data used in this thesis are both proprietary and from the *XMM–Newton* and *Chandra* archives.

X–ray spectral and flux variability is very common in AGN, and it can be due to intrinsic variability of the source, as well as to absorption by different structures. Intrinsic variability occurs at all timescales. Variability associated to absorption phenomena was first found at relatively long time scales (months to years, associated with the torus). However, several examples of X–ray sources with absorption variability on short time scales (hours to days) were published in the last few years prior to the start of my Ph. D. thesis. It was pointed that this kind of absorption was probaly due to absorbers crossing our LOS to the primary X–ray source. Such absorbers were proposed to be cold and compact clouds with column densities in the range from $10^{22} - 10^{24}\,\mathrm{cm}^{-2}$, number densities of $10^{9} - 10^{11}\,\mathrm{cm}^{-3}$, velocities of a few thousands kilometers per second, and located at distances of $10^{2} - 10^{5}$ gravitational radii (r_{g}) from the central black hole. These properties are remarkably similar to those of the broad optical and UV line–emitting clouds. The first part of my thesis, extensively detailed in Chapter 2, consists on the X–ray variability study of the narrow line Seyfert 1 (NLS1) galaxy SWIFT J2127.4+5654. We found its variability to be due to absorption events, and we identified the physical structures responsible for it on short time scales as compact clouds within the broad line region (BLR). However, variability on longer time scales is most likely related to larger structures, probably within the dusty torus.

The extension of this first project became a theoretical study of the relativistic effects influencing the accretion disc emission. In Chapter 3 we develop a method to probe the flux emitted from every region within the disc and the corona, taking advantage of the outstanding conditions provided by a BLR cloud eclipse of the X–ray–emitting regions. The starting point is the result of the cloud / corona sizes estimation in SWIFT J2127.4+5654, which turn out to be comparable. Hence, a detailed modelling of such occultation events in AGN has the potential to precisely infer the system's geometry. With this goal in mind, we made use of a relativistic spectral model to predict different observables in X–rays eclipses: the black hole's spin, the system's inclination, the source's and cloud's sizes, as well as the cloud's column density and ionization state. We conclude that absorption varies as a function of energy range, and that its maximum takes place when the approaching side of the accretion disc is covered. Therefore, flux anisotropies detected along one single eclipse, can be attributed to relativistic Doppler effects, turning out to be useful for determining the geometry of the closest regions to the black hole. This inspires us to analyze the hard–to–soft (H / S) light curves ratios produced along an eclipse, and use them to characterize the innermost accretion disc properties in a new, model–independent way.

The third and last block of my dissertation is about the so–called warm absorber, gas photoionized by the central X–ray source, that is usually found as a wind with outflowing velocity of up to several thousands of kilometers per second. Absorption that is still present in unobscured AGN is due to this warm absorber. This part of my dissertation, addressed in Chapter 4, consists on the detailed study of the warm absorber's properties (location, velocity, size, ionization state, density, temperature, and origin) with unprecedented precision thanks to space observatories such as *XMM–Newton*, and most remarkably *Chandra*. We study the spectral variability of the Seyfert 1.2 galaxy ESO 323–G77 on all timescales, by using *XMM–Newton*, *Chandra*, *Swift*, and *Suzaku* observations. The four high–resolution *Chandra* observations allowed us a thorough study of the absorbers' properties, as well as the days–scale X–ray spectral variability. We identify two warm absorbers with constant column density and ionization, pointing to a homogeneous and extended outflow escaping from the system. One more cloud, ionized tyo a lesser degree, takes the place of the strictly neutral material usually inferred from the X–ray analysis of obscured sources by Compton–thin clouds. The column density of this colder cloud, varies significantly on long time scales, which demonstrates its clumpiness. Moreover, intrinsic luminosity changes of the primary X–ray source on days time scales are followed by the cloud's ionization. This indicates that the cloud is in photoionization equilibrium with the source on such short time scales, which allows us to set a constraint on the gas density. Finally, our data are consistent with a physical configuration in which all the absorbers are co–spatial within the inner and outer limits of the torus. Assuming the verity of this configuration, the three clouds are in pressure–equilibrium, hinting that the hotter structures pressure–confine the colder ones.

Contents

Acronyms

ΛCDM Λ cold dark matter. 40, 95

ACIS Advanced CCD Imaging Spectrometer. 32

ADAF advection dominated accretion flow. 6

AGN active galactic nuclei. v, vi, 1, 3, 4, 6–9, 11–24, 26, 27, 30, 32, 33, 36, 52, 55, 56, 60, 62, 65, 67, 81, 88, 90, 91, 93, 96, 114, 123–126, 130, 131, 133, 134

BBB big blue bump. 13, 22

BHB black hole binary. 9

BLR broad line region. vi, 6, 8, 9, 11, 12, 14–16, 20, 21, 33, 35, 36, 39, 42, 52, 55, 56, 61, 62, 64, 65, 67, 77, 79, 81, 88, 89, 91, 93, 94, 96, 118, 123, 125–127, 129–131

BLRG broad line radio galaxy. 7

CCD charge–coupled device. 30–32

CF covering fraction. 49, 50, 52, 57, 62, 64, 81, 129, 130

dof degrees of freedom. 42, 44, 47, 87, 96, 97, 99, 100, 105, 108, 109, 111, 114, 116, 120, 121

EPIC European Photon Imaging Camera. 24, 30, 31, 40, 42, 44, 47, 95, 113, 117, 120

ESA European Space Agency. 30

EUV extreme ultraviolet. 20, 21

EW equivalent width. 14, 42, 44, 96, 114, 121

FoV field of view. 31, 93

FR Fanaroff and Riley. 7, 8, 17

FWHM full width at half maximum. 6, 12, 22, 31, 40, 42, 52, 96, 129

GC Galactic Centre. 2, 3

GR general relativity. 27, 56, 64, 83, 87, 88, 130

H/S hard–to–soft. vi, 44, 47, 55, 70, 75, 77, 79, 141

HBL high–frequency BL Lac. 7

HEASARC High Energy Astrophysics Science Archive Research Center. 61

HEG High Energy Gratings. 92

HETGS High–Energy Transmission Grating Spectrometer. 32, 95, 113, 126

HRC High Resolution Camera. 32

HXD Hard X–ray Detector. 93

IR infrared. 2, 15, 16, 18

ISCO innermost stable circular orbit. 11, 13, 58, 60, 61, 64, 65, 79

ISM interstellar medium. 17

LBL low–frequency BL Lac. 7

LETGS Low–Energy Transmission Grating Spectrometer. 32

LINER low ionization nuclear emission–line region. 6, 8

LOS line of sight. v, 7, 15, 16, 19, 20, 32, 36, 56–58, 61, 64, 65, 90, 91, 93, 94, 97, 113, 114, 124, 129, 136, 138, 140

maser microwave / molecular amplification by stimulated emission of radiation. 2, 3

MHD magnetohydrodynamic. 11, 13

MOS metal–oxide–semiconductor. 30, 31

NASA National Aeronautics and Space Administration. 31, 61

NLR narrow line region. 6, 9, 14, 16

NLRG narrow line radio galaxy. 7

NLS1 narrow line Seyfert 1. vi, 6, 8, 19, 35, 36, 39, 40, 44, 51, 56, 129

NLXG narrow line X–ray galaxy. 6

OVV Optically Violent Variable. 7

PSF point spread function. 31

QSO quasi–stellar object. 4, 7, 8, 12, 13

RGS Reflection Grating Spectrometer. 30, 31, 40, 95

RMS root mean square. 12

SDSS Sloan Digital Sky Survey. 6

SED spectral energy distribution. 7, 11, 97, 99, 100, 105–109, 111, 112, 118, 123

SMBH supermassive black hole. v, 1, 2, 6, 8, 9, 11–17, 19, 21, 22, 32, 33, 56–58, 60, 61, 65, 67, 79, 83, 87, 88, 130, 133

UV ultraviolet. v–vii, 2, 8, 13–15, 17–21, 36, 91, 93, 125, 133

VLBA Very Long Baseline Array. 3

XIS X–ray Imaging Spectrometer. 93

XRB X–ray binary. 20, 27

List of Tables

List of Figures

1

Introduction

AGN is the appellation commonly used to designate the central regions of active galaxies, which are galaxies whose centre emits, at least, as much energy at visual wavelengths as the sum of all of its stars. This is commonly explained by the existence of a central SMBH, defined as a black hole with mass greater than $10^5\ M_\odot$. From a more quantitative point of view, an active galaxy is that containing an accreting SMBH, and whose bolometric luminosity exceeds $10^{-5}\times L_{\rm Edd}$, where $L_{\rm Edd}$ is the Eddington luminosity, i.e. the maximum luminosity that can be extracted from the system by means of accretion–driven processes:

$$L_{\rm Edd} = \frac{4\pi G M m_{\rm p} c}{\sigma_{\rm T}} \simeq 1.26 \times 10^{38} M/M_\odot\ \ {\rm erg\ s^{-1}}\ , \tag{1.1}$$

where M is the black hole mass, $m_{\rm p}$ is the proton mass, and $\sigma_{\rm T}$ is the Thomson cross–section. According to this criterion, our own galaxy would not be an AGN. However, other criteria consider every accreting SMBH as an AGN. Within this paradigm, low bolometric luminosity accreting SMBHs are "radiatively inefficient" AGN.

Efficienf AGN have luminosities of at least $0.01 \times L_{\rm Edd}$, usually ranging from $L \sim 10^{43}$ erg s^{-1} for near galaxies hosting a $10^7 M_\odot$ SMBH, up to more than $L \sim 10^{46}$ erg s^{-1} for typical quasars. The emission of that overwhelming amount of energy from such reduced regions cannot be explained by usual stellar processes. This is why the standard model of AGN is proposed. In the following sections, I will first review the observational evidence for SMBHs, then I will outline the current classification of AGN, and explain in what the standard model consists. Later, I will talk about the variability of AGN, with a focus on X–ray variability, as well as about their X–ray spectral features. Also, I will introduce very briefly the instruments of which I made use during my work. Finally, I will detail the aims of this Thesis.

1.1 Observational evidence of SMBH

The innermost parsecs around the Galactic Centre (GC) have been broadly mapped in the last years. It is located at only 8 kpc from us, therefore it is an exceptional laboratory for the study of a galactic nucleus. Regardless of our closeness to the Milky Way nucleus, extinction due to interstellar dust and gas is so extreme that optical and UV photons are almost completely absorbed. Therefore, radio, infrared (IR), and X–ray radiation are the most useful bands of the electromagnetic spectrum for the observational study of the GC. Balick & Brown (1974) discovered that the GC hosts the compact radio source Sgr A*, that turned out to be a massive ($3.61 \pm 0.32 \times 10^6 M_\odot$, Eisenhauer et al., 2005), compact (~ 1 AU, Shen et al., 2005), and dark object, located at the dynamical centre of the Milky Way (proper motion less than $20\,\mathrm{km\,s^{-1}}$, Reid et al., 1999). Two major groups have studied in detail the potential of the central mass in Sgr A*, by means of extensive IR observations of the stars within the central cluster: one of these groups is based at the Max–Planck–Institut für extraterrestrische Physik (Germany), and the other one at the University of California (USA). The study of stellar kinematics, radial velocities (Genzel et al., 1997), stellar proper motions (Eckart & Genzel, 1996; Ghez et al., 1998), stellar accelerations (Ghez et al., 2000; Eckart et al., 2002), and high–precision IR astrometry and spectroscopy, allowed the European and the American groups to determine, independently, the position of the centre of acceleration of the stars, and to identify it with the radio source Sgr A*, whose size corresponds to only 10–20 Schwarzschild radii for a $3.61 \times 10^6 M_\odot$ mass black hole. None of the known astronomical objects could contain that mass in such a small volume, except a black hole. Nowadays, Sgr A* and its close environment are therefore the most robust observational proof for the existence of SMBHs.

The nuclei of galaxies other than Ours are extensively studied in order to look for SMBHs signatures. Dynamical mass measurements are based on the simplified idea that galaxies are collisionless stellar systems in which every star moves in the gravitational potential of all the others. Then, the system can be described analytically by the Collisionless Boltzmann Equation, that links the distribution function of the stars, the gravitational potential (Φ), and the velocity field. Then, the potential, Φ, is related to the mass density through the standard Poisson's equation. Since the mass density includes contributions of any mass distribution, observable or not, the difference between the observed mass distribution and the total one implies the existence of an extra, dark mass in the center of the galaxy: most likely a SMBH (see e.g. the review by Ferrarese & Ford, 2005). Up to date, 87 galaxies have been found to host SMBHs, by dynamical modeling of spatially resolved kinematics (namely almost any galaxy that has been observed in detail with *HST* requires a central SMBH with a mass of $10^7 - 10^9 M_\odot$). By using high spatial resolution *HST* data, a tight correlation between the velocity dispersion σ of the stars of the galactic bulge and the central SMBH mass was found (see e.g. the review by Kormendy & Ho, 2013). In most cases, the rotation and velocity dispersion curves require a central mass not contributing to the galactic emission, which points to the existence of a SMBH. We show an example in Fig. 1.1, where the peak in the velocity dispersion curve at the center of the galaxy and the rotation curve hint a central black hole with a mass of $\sim 3 \times 10^7\,M_\odot$ in the Andromeda galaxy.

Finally, the third greatest observational evidence for SMBHs arises from the study of the 22 GHz microwave / molecular amplification by stimulated emission of radiation (maser) emission from water molecules in the closeby galaxy NGC 4258. A maser is a mechanism by which coherent, monochromatic electromagnetic waves are produced. Maser emission from molecular discs around accreting SMBHs is stimulated by the accretion processes close to the black hole, which provides a powerful tool to study the motion of the mentioned disc. When its motion is (quasi–)

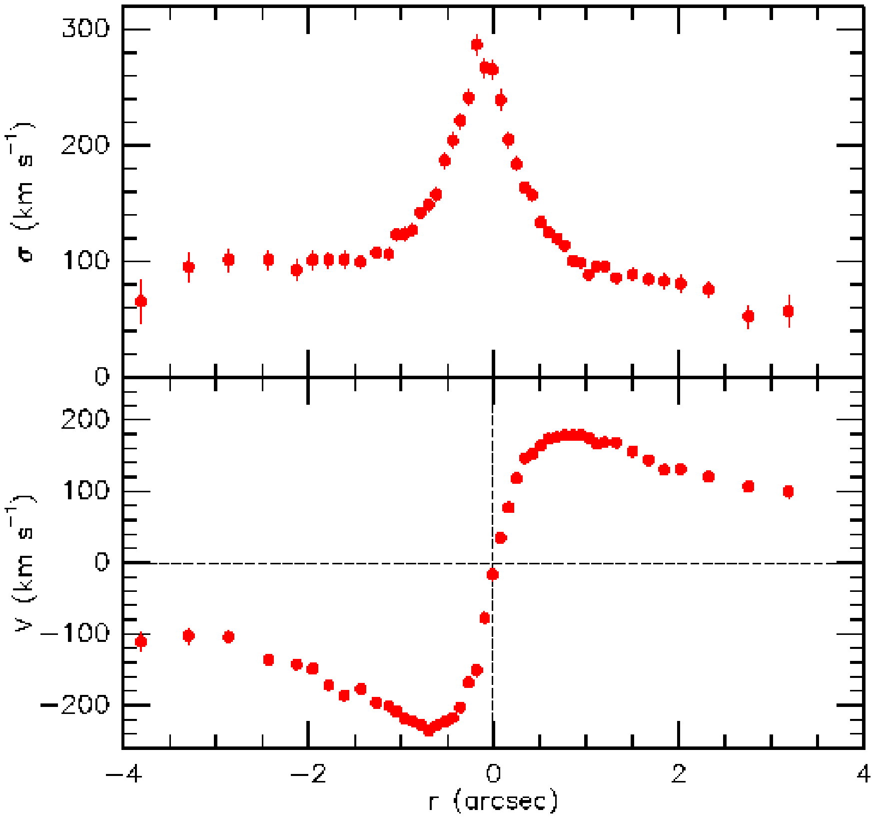

Figure 1.1: The velocity dispersion (top) and rotation curve (bottom) profiles from *HST* observations of M 31 (Andromeda galaxy). The symmetry point of the rotation curve coindides with the sharp peak in the dispersion, as expected when a SMBH sits at the center of the star motions.

Keplerian, the central mass can be precisely computed. The most remarkable results are those from observations of the AGN within the spiral galaxy NGC 4258 (Miyoshi et al., 1995). By means of the Very Long Baseline Array (VLBA) interferometer, a resolution of 0.017 pc can be achieved (two orders of magnitude better than with *HST* and only one order of magnitude worse than that obtained in the GC). Water maser clouds are found to be part of a warped Keplerian disc, and their high radial velocities indicate the presence of a compact mass of $3.6 \times 10^7 \, M_\odot$.

1.2 Classification of AGN

The first Seyfert galaxy of which an optical spectrum was acquired by Fath (1909), in the context of his dissertation on spiral nebulae and globular star clusters. One of the objetcs of his sample, NGC 1068, which was supposed to be a nebula, turned out to show unexpected strong emission lines. Slipher (1915) got a higher–quality spectrum of the same object, finding that the resolved emission lines had widths of $\sim 1100\,\mathrm{km\,s^{-1}}$. In the following three decades, some other spiral nebulae were found to present nuclear emission lines (see e.g. Hubble, 1926, in NGC 1068, NGC 4051 and NGC 4151). The first author who noted that these galaxies formed a class apart was Seyfert (1943), who selected the twelve high–excitation nuclear emission extragalactic nebulae known at the date (actually, bright galaxies with stellar–like nuclei), finding out that the spectra of six of them were dominated by broad nuclear emission lines of up to 8500 km s^{-1}: NGC 1068, NGC 1275, NGC 3516, NGC 4051, NGC 4151 and NGC 7469.

The late 1950s radio surveys led to the discovery of quasi–stellar objects (QSOs), which initially were not identified as galaxies because the luminosity of the nuclear source overwhelms the rest of the galaxy. By the same time, Minkowski (1958) detected the first two Seyfert galaxies in the radio wavelength (NGC 1068 and NGC 1275). A few years later, Schmidt (1963) and Oke (1963) reported the discovery of the first QSO in the Optical: 3C 273, an extremely luminous star–like object with large redshift (z = 0.158), showing a spectrum that did not look like any tipycal stellar object. Due to the huge gap in luminosity between QSOs and Seyfert galaxies, at the beginning these were not identified as the same kind of object. This is why even today the taxonomical classification of AGN is still somehow over–complicated. In the following paragraphs I present a classification of active galaxies up to date.

Conventionally, AGN are classified according to their radio emission as radio–quiet and radio–loud. It was noted by Kellermann et al. (1989) that the ratio of total radio flux density (6 cm, measured with a resolution of 18") to optical flux density (4400 Å), $R = F_{6\,\mathrm{cm}}/F_{4400\,\mathrm{\AA}}$, show a bimodal distribution, with $R \sim 10^2 - 10^5$ for radio–loud AGN and $R \sim 0.1 - 10$ for radio–quiet AGN (but see also White et al., 2007, who states that this dichotomy is not clear in different parts of the space of parameters).

Radio sources in AGN consist of two extended regions characterized by the presence of magnetic fields and synchrotron–emitting relativistic electrons (Begelman et al., 1984). In these extended radio–emitting regions is where the jets and the intergalactic medium interact, giving place to the radio emission due to the violent shock waves produced as a result of their contact. Radio–quiet AGN are thought to be due to a reduced version of the radio–loud AGN, in which lower power jets vanish close to the region where they are launched (Miller et al., 1993; Falcke et al., 1996), or are not ejected at all.

Seyfert galaxies

Originally, Seyfert galaxies were defined in a morphological basis by Seyfert (1943), as galaxies (mostly spirals) with high surface brightness cores. Following studies exposed their specific spectroscopic properties, namely prominent high–ionization emission lines. The distinction between Seyfert 1 and Seyfert 2 galaxies is due to the work of Khachikian & Weedman (1974), who found that class 1 Seyferts show a set of narrow emission lines (hundreds of km s^{-1}), representative of ionized gas of electron densities as low as $n_e \sim 10^3 - 10^6\,\mathrm{cm}^{-3}$, as well as a set of broad emission lines (up to $10^4\,\mathrm{km\,s}^{-1}$). These broad lines are only detected in the permitted lines, but not in the forbidden lines, pointing that a high density gas $n_e \geq 10^9\,\mathrm{cm}^{-3}$ is responsible of such broad lines. Spectra of class 2 Seyferts do not show the broad lines seen in those of class 1. Osterbrock & Pogge (1985) define Seyfert 1 galaxies as those whose [H I] Balmer lines are broader than the forbidden lines, and Seyfert 2s as those in which both sets of lines have the same width. Spectra of Seyfert 1 and Seyfert 2 galaxies are shown in Fig. 1.2, together with a spectrum of the non–active galaxy Andromeda, for comparison purposes. An extended decimal notation has been proposed by Osterbrock (1977): Seyfert 1.5 galaxies would be in the middle of typical Seyfert 1s and Seyfert 2s, based on the profile of the Hβ line, as in the cases of NGC 4151, NGC 5548 and Mrk 6, for example. Additional subdivisions are given as Seyfert 1.2 and Seyfert 1.8 for objects

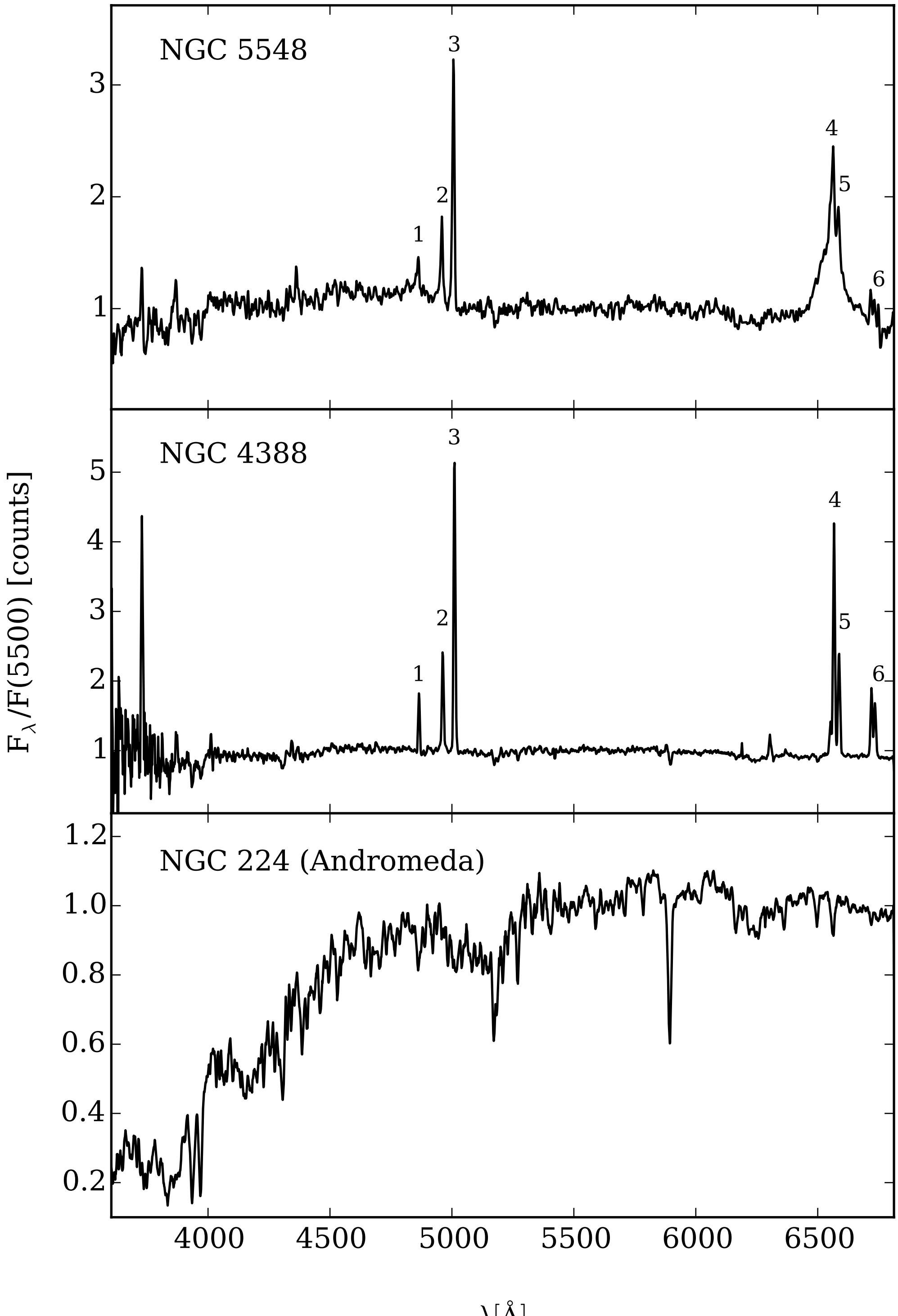

Figure 1.2: The optical spectrum of the Seyfert 1 galaxy NGC 5548 (top panel), to be compared with that of the Seyfert 2 galaxy NGC 4388 (middle panel). Prominent emission lines are labelled as follows: 1 = Hβ λ4861; 2 = [O III] λ4959; 3 = [O III] λ5007; 4 = Hα λ6563; 5 = [N II] λ6583; 6 = [S II] $\lambda\lambda$6716, 6731. In the bottom panel we show the spectrum of a non–active galaxy, Andromeda, for comparison reasons. All spectra are shown in their local restframes. Data from Kennicutt (1992), Gavazzi et al. (2004), and Lira et al. (2007), respectively.

with weaker or stronger Hβ profiles respectively. Osterbrock (1981) introduces an extra subclass between types 1.8 and 2, Seyfert 1.9, in which the Hα line is the only broad component. It is important to highlight that this nomenclature must be used carefully, since the high variability observed sometimes in the broad emission–line could lead to inconsistent classifications of the same object (e.g. the type of NGC 1097 has changed over time).

Maiolino & Rieke (1995) found that Seyfert galaxies are more common that what was thought in the past. They find them to be more than 5%, although according to apparent magnitude distribution chriteria this percentage could increase up to 16% ± 5% of all galaxies. Grouping types 1.8, 1.9 and 2 as Seyfert 2s, and types 1, 1.2 and 1.5 as Seyfert 1s, they get that Seyfert 2s are four times more common than Seyfert 1s (i.e. a 4:1 ratio). Osterbrock & Shaw (1988) find this ratio to be 3:1, while McLeod & Rieke (1995) derive a 1:1 ratio. Maiolino & Rieke (1995) claim that the 1:1 ratio is not correct due to selection effects. In addition, Maiolino & Rieke (1995) study the properties of the nuclei with respect to the inclination of the host galaxy, finding that types 1, 1.2 and 1.5 take place in face–on galaxies, whilst type 1.8 and 1.9 occur in edge–on systems, in good agreement with the BLR obscuration by the torus postulated by the unified model (see Section 1.2.1).

Narrow–Line X–ray galaxies

Out of the first X–ray surveys (2A and 4U, Cooke et al., 1978; Forman et al., 1978, respectively), a new class of Seyfert 1 galaxies was defined, the narrow line X–ray galaxies (NLXGs), characterized by emission lines much more narrow than those of Seyfert 1s but broader than lines in Seyfert 2 spectra (see Ward et al., 1978). NLXGs, also called NLS1 galaxies, show heavy reddening in their optical spectra as well as heavy extinction due to dust in the host galaxy, which makes them less luminous than usual Seyfert galaxies. They show very steep soft X–rays spectra, narrow optical emission lines (full width at half maximum (FWHM) $\sim 2000\,\mathrm{km\,s^{-1}}$), and conspicuous optical Fe II emission (Osterbrock & Pogge, 1985; Boller et al., 1996).

LINERs

Heckman (1980) was the first to define a class of active galaxies characterized by low ionization nuclear emission–line regions (LINERs), whose optical spectra are dominated by low ionization species through narrow emission–lines whose widths are similar to those from the narrow line region (NLR) in Seyferts, but with a much lower luminosity. There exists some controversy about their origin. On the one hand, some authors sustain that they are related to starbursts (see e.g. Alonso-Herrero et al., 2000). On the other hand, (Ho et al., 1997; González-Martín et al., 2009) point that these galaxies are true AGN (i.e. powered accretion onto a central SMBH) with lower luminosity. Also, the emission lines of LINERs have been explained by advection dominated accretion flow (ADAF) accretion models (see e.g. Narayan & Yi, 1995; Abramowicz et al., 1995; Filho et al., 2004). Kewley et al. (2006) analysed 85224 emission–line galaxies from the Sloan Digital Sky Survey (SDSS), finding that Seyfert galaxies and LINERs lie on separated regions of the diagnostic diagrams. The also distinguish Seyferts and LINERs by their [O III] luminosities. LINERs dominate at low luminosities while Seyferts do it at high luminosities.

Quasars or QSOs

QSOs are the most luminous class of AGN, reaching luminosities of up to 10^{48} erg s^{-1} (Gu et al., 2001; Woo & Urry, 2002). The main difference between QSOs and Seyfert galaxies is that due to the huge luminosity of their nuclei, the host galaxy is not resolved. QSOs can be radio–loud and radio–quiet, and following the same scheme as for Seyfert galaxies, they can be classified in types 1 and 2 according to their optical spectral properties (and obscuration state). Radio–loud QSOs were the first ones to be discovered, so that these kind of quasars are the ones that originally defined the class (Schmidt, 1968). Nowadays we know that only around $\sim 5\% - 10\%$ of all QSOs emit in the radio wavelength (Peterson, 1997). Radio emission is usually related to jets (via synchrotron emission, see e.g. Miley, 1980), however quasars without jets have been found (Kellermann et al., 2004).

Blazars

Blazar is the ordinary term used to refer to Optically Violent Variables (OVVs) and BL Lac objects, both of which are radio sources characterized by having a strong relativistically beamed component in our LOS.

OVVs show large flux variability (greater or around 0.1 mag in the optical) at short time–scales (down to one day). Most AGN have polarizations lower than $\sim 1\%$, however, OVVs show much higher polarizations, of up to few percent. As well as their flux, their polarization state is variable.

There exist two different subclasses of BL Lacs according to the ratio between the X–ray flux (0.3-3.5 keV) and the radio flux (5 GHz): low–frequency BL Lacs (LBLs) and high–frequency BL Lacs (HBLs), with their X–ray to radio ratio lower or greater than $10^{-11.5}$, respectively (Padovani & Giommi, 1996).

There are differences among the spectral energy distributions (SEDs) of the three subclasses of blazars, however unifying schemes have been proposed. In this direction, it has been found that their distribution is continuous in the broadband colour–colour diagram: HBLs lie in a completely separate region from that of OVVs, being the LBLs the connection between both sets (Sambruna et al., 1996; Ghisellini et al., 1998). On multiwavelength blazar unification theory, see Xie et al. (2001). Supporting unification of the blazar phenomenon, see also Fossati et al. (1998), who expose that there is continuity in the properties among different classes of BL Lac objects as a function of luminosity, and conclude that blazars lie within a continuous spectral sequence, rather than in separate spectral classes.

Radio galaxies

Out of all radio–emitting galaxies, two types have typical AGN optical spectra: the radio–loud counterparts of type 1 and 2 Seyfert galaxies, called broad line radio galaxies (BLRGs) and narrow line radio galaxies (NLRGs) respectively. The main difference between Seyferts and radio galaxies, appart of the absence or presence of radio emission, occurs in terms of morphology of the host galaxy. Radio galaxies are usually elliptical, whilst Seyferts tend to be spiral galaxies.

Depending on if radio emission is extended or nuclear, radio galaxies are also classified in Fanaroff and Riley (FR) classes, after the work by Fanaroff & Riley (1974). FR I radio galaxies commonly show bright jets near the central engine, therefore they are brightest in the centre. On the other hand, energy is efficiently transported outwards in FR II objects, so that their jets are faint while their lobes are bright. Urry et al. (1991) hypothesize that FR I radio galaxies are misaligned BL Lacs. For a comprehensive explanation of the Fanaroff and Riley radio galaxy classification see Saripalli (2012).

1.2.1 The unified model

AGN are far from being spherical celestial bodies. The components considered in the standard model imply that symmetry in AGN is, at best, axial (see Section 1.3). Therefore, the same AGN would appear different when observed from diferenf points of view, or what is the same, intrinsically identical AGN seem different to us due to their orientation in the space. This is the basis for the unification schemes (Barthel, 1989; Antonucci, 1993; Antonucci & Miller, 1985; Urry, 2003). A standard illustration of such schemes is shown in Fig. 1.4.

When many authors write about AGN unification models, they ordinarily allude to IR, optical, UV and X–ray unification on the one hand (the so–called radio–quiet unification), and radio–loud unification on the other. The first scheme, proposed by Antonucci & Miller (1985), involves a dusty molecular torus to address the differences between type–I and type–II AGN. The radio unification scheme adds the relativistic jet, which is observed in around one tenth of AGN. In the workframe of this model, the jet is launched nearby the SMBH in the same direction of the axis of the system. Radio unification schemes are discussed by Urry (2003) and Tadhunter (2008). For an extensive review on a third unified theory of AGN, founded on the physics of accretion onto SMBHs, see Begelman (1986).

Radio–quiet unified model states that both Seyfert 1 and Seyfert 2 galaxies (or type 1 and 2 QSOs) have a BLR. Both types differ only in their inclination angles, that cause that in the case of Seyfert 2s (or type 2 QSOs) the BLR cannot be detected due to obscuration by the dusty torus. On one side, radio–loud unified schemes identify radio–loud QSOs with FR II galaxies (see e.g. Urry & Padovani, 1995). This would be the case of an edge–on radio–loud QSO: the jets would become conspicuous, so that this object would appear as a FR II radio galaxy. On the other side, a FR I radio galaxy would be classified as a BL Lac if one of the jets were beamed towards us (see e.g. Urry et al., 1991).

Spectropolarimetry data provided observational support for the unified model. A number of objects originally classified as type 2 turned out to have polarized broadened lines (see Fig. 1.3). Miller & Goodrich (1990) found that four out of eight high–polarization Seyfert 2 galaxies had a hidden BLR, detectable only in the polarized flux spectra. Also, broad polarized Hα and Hβ lines were found in the spectra of other four Seyfert 2s by Tran et al. (1992).

However, there exist some problems with the Unification models. Some type 2 objects lack a BLR when observed in polarized light. Moreover, some other objects do not fit well in the unified scheme, such as LINERs and NLS1 galaxies. In this context, the Unification model requires significant modifications (see the review by Netzer, 2015, for details on this issue).

1.3 The standard model of AGN

The current AGN paradigm requires a huge amount of matter confined within the central parsec in order to allow the large energy release that we observe in active galaxies. The general landscape

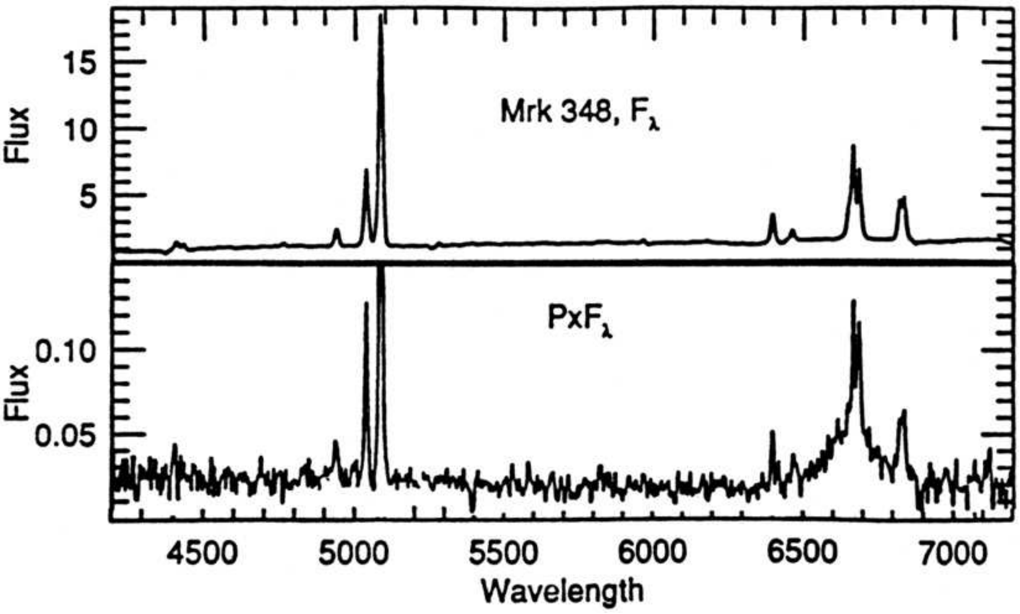

Figure 1.3: Top panel: optical spectrum of the Seyfert 2 galaxy Mkn 348. Bottom panel: polarized flux spectrum of the same galaxy. The broad emission lines, typical of Seyfert 1 galaxies, reveal a hidden BLR in polarized light (note especially the Hα broad wings). See Miller & Goodrich (1990).

dates back to half a century ago (Salpeter, 1964), and it consists of a SMBH surrounded by a hot accretion disc from which high energetic radiation is emitted as a result of viscous energy dissipation of infalling gas in the disc.

Apart from a black hole and an accretion disc, structures that are also present in black hole binaries (BHBs), AGN usually incorporate most of the structures shown in white labels in Fig. 1.4: a BLR, an obscuring molecular torus, a NLR, and relativistic radio jets. In this section we proceed to introduce all of the components of AGN in the standard model.

1.3.1 The supermassive black hole

A black hole is defined as a region of space–time in which resides an object of a certain mass, M_{BH}, that is completely engulfed within its own event horizon (which equals 1 $r_{\rm g}$ for maximally rotating Kerr black holes, and 2 $r_{\rm g}$ for Schwarzschild ones, where the gravitational radius is defined as $r_{\rm g} = GM_{BH}/c^2$, being G the gravitational constant, M_{BH} the black hole mass, and c the speed of light). The central black holes in AGN have masses ranging from 10^5 to 10^9 $M_\odot$, that is why we call them supermassive.

The broad acceptance of the SMBH paradigm is due to the many pieces of evidence supporting it, in terms of compactness and persistency in time (i), line widths (ii), variability (iii), velocity dispersion of stars in the galactic center (iv), colimation of the jets (v), and the broadened Fe Kα line emission (vi).

i) AGN are characterized by being compact and extremely luminous persistent sources. SMBHs are compact objects too, and can give place to high Eddington luminosities by converting potential energy in the accretion disc into radiation, so that they are ideal candidates to explain the high, persistent luminosity (Lynden-Bell, 1969; Fabian, 1999).

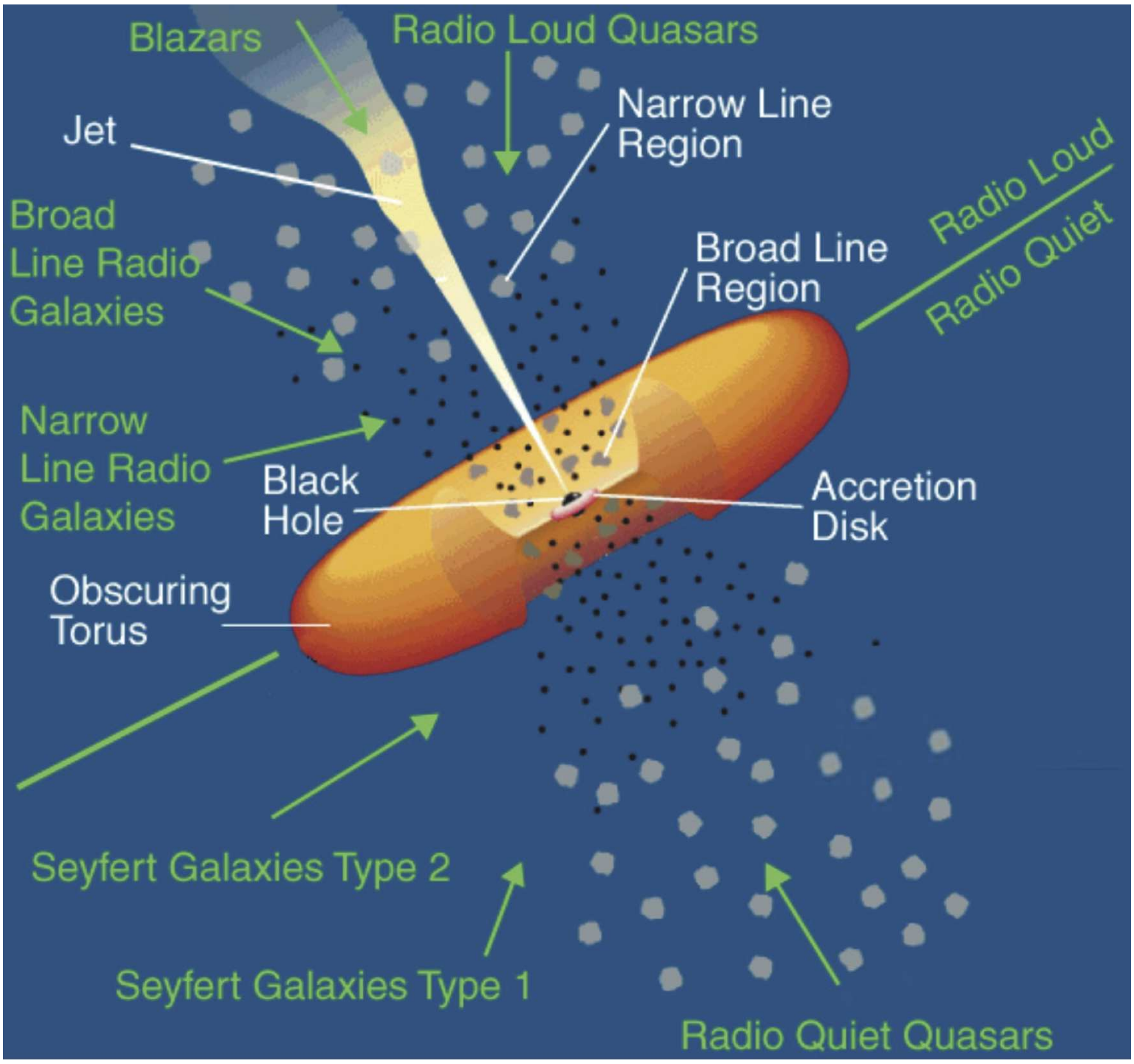

Figure 1.4: In white labels, the various components usually found in AGN. In green labels, the Unification model for AGN, explained in Sections 1.2 and 1.2.1. AGN whose jets are close to our LOS are blazars. If the inclination angle is $\sim 30°$, the narrow and broad line regions are visible, hence the object is a "normal" quasar or a Seyfert 1 galaxy. At larger angles, the the BLR is hidden by the torus, then the object is a Seyfert 2 galaxy. When viewed close to the perpendicular to the axis, the jets are seen at low frequencies, therefore the object is a radio galaxy. Credit: M. Polletta, from an original figure by Urry & Padovani (1995).

ii) Emission lines in AGN spectra have velocity widths of $1000 - 30000\,\mathrm{km\,s^{-1}}$, associated with the BLR clouds (Peterson & Wandel, 1999; Kaspi et al., 2000; Wills et al., 2000; Wang et al., 2011). These velocities are much higher than common stellar velocities, which are one or two orders of magnitude lower ($\sim 200\,\mathrm{km\,s^{-1}}$).

iii) AGN emission is characterized by its high variability, both in SED shape and flux, especially in the X–ray band, related with the compact active regions. Hence, studying this variability, information about the size and geometry of the X–ray–emitting regions can be derived (see Section 2 and also Risaliti et al., 2007, 2009b; Sanfrutos et al., 2013; Agís-González et al., 2014).

iv) Evidence supporting the existence of massive, non–stellar objects in the centre of most active and non–active large galaxies, including our own, is provided by the high velocity dispersion of stars when crossing the galactic nucleus (see e.g. the reviews by Kormendy & Richstone, 1995; Ferrarese & Ford, 2005; Kormendy & Ho, 2013, and Section 1.1). Young et al. (1978) and Sargent et al. (1978) present photometric and spectroscopic observations of the elliptical active galaxy M87, pointing to a supermassive object in its centre ($M = 5 \times 10^9 M_\odot$, $r < 110\,\mathrm{pc}$). Dressler & Richstone (1988) confirm rapid rotation and high velocity dispersions in the central parsecs of the non–active galaxies M31 and M32, and conclude that they contain SMBHs of $\sim 3-7\times10^7 M_\odot$ and $8\times10^6 M_\odot$ respectively within their central regions ($r < 2\,\mathrm{pc}$).

v) The collimated, straight jets, sustained in timescales of even 10^7 years, are explained in a natural way invoking a large disc with a high accretion rate onto a black hole (Abramowicz & Piran, 1980). Blandford & Payne (1982) solve the equations of magnetohydrodynamic (MHD) for axially–simmetric, non–relativistic outflow from a Keplerian accretion disc, showing that the toroidal component of the magnetic field collimates the outflow into two jets perpendicular to the accretion disc. Lovelace et al. (1987) find that the jets are self–collimated by the magnetic fields induced within the accretion disc.

vi) AGN X–ray spectra often present broadened Fe Kα line emission (see Section 1.5.2), due to gravitational redshift from the inner accretion disc, where this feature arises. When the Fe Kα line is resolved, the innermost stable circular orbit (ISCO) can be determined, and consequently the spin of the SMBH can be constrained (see e.g. Reynolds & Nowak, 2003; Nandra et al., 2007a; Reynolds & Fabian, 2008; Brenneman & Reynolds, 2009). The dependence of the ISCO with the spin of the black hole is shown in Fig. 1.5. The ISCO is located at 6, 1.24 and 9 r_g for the case of a Schwarzschild ($a/M_{BH} = 0$), and a prograde / retrograde maximally rotating Kerr ($a/M_{BH} = \pm\, 0.998$) black hole, respectively.

The mass of a SMBH at AGN is estimated by using a number of techniques: dynamical mass measurements (i), reverberation mapping (ii), the mass / velocity dispersion relation (iii) and the BLR size / luminosity relationship (iv).

i) As already mentioned a few lines above, the velocity dispersion of stars in the galactic nuclei can be used to derive the central mass in active and non–active galaxies (Young et al., 1978; Sargent et al., 1978).

ii) Reverberation mapping consists on measuring the time delay between the continuum variation and the emission lines response. The SMBH mass is proportional to this time delay (Blandford & McKee, 1982; Peterson, 1993, 1997).

iii) There is a correlation between the masses of SMBHs and the velocity dispersions of their host bulges, based on measurements of stellar kinematics: $M_{BH} \propto \sigma^\alpha$, where α ranges from

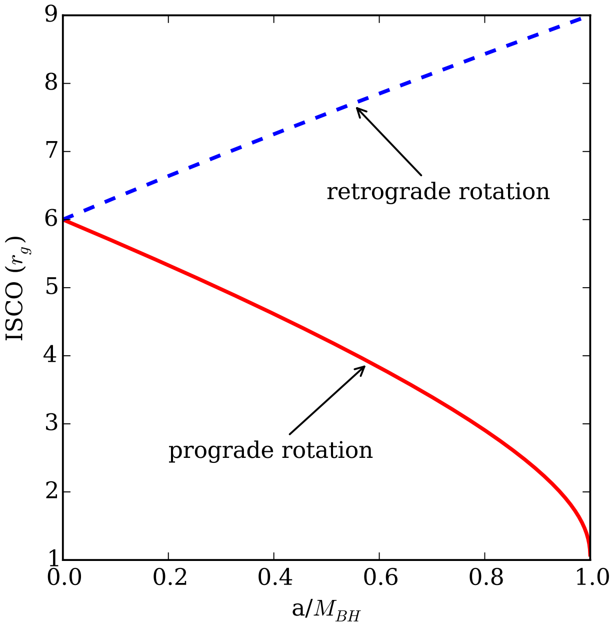

Figure 1.5: The ISCO as a function of the spin parameter (a/M_{BH}). The cases of prograde and retrograde (with respect to the accretion disc) Kerr black holes are shown in solid red and dashed blue lines, respectively.

3.75 ± 0.30 (Gebhardt et al., 2000) to 4.8 ± 0.5 (Ferrarese & Merritt, 2000). Gültekin et al. (2009) finds an intermediate relationship, $M_{BH} \propto \sigma^{4.24\pm0.41}$, as well as a correlation between the central mass and the bulge luminosity: $M_{BH} \propto L^{1.11\pm0.18}$.

iv) Wandel et al. (1999) derived a scaling correlation between the size of the BLR and the AGN luminosity from the reverberation–mapping study of 17 Seyfert 1 galaxies, and Kaspi et al. (2000) measured the size of the BLR (also using reverberation–mapping) of other 17 QSOs from the Palomar–Green sample. Kaspi et al. (2000) combined both studies and concluded that the size of the BLR scales with optical luminosity at 5100 Å as $R_{BLR} \propto L^{0.70\pm0.03}$. Their mass estimates based on the computation of the FWHM from the mean spectra and from the root mean square (RMS) spectra are given in Eqs. 1.2 and 1.3 respectively.

$$M_{BH}^{\mathrm{(mean)}} = \left(5.71^{+0.46}_{-0.37}\right) \times 10^{7} \times \left(\frac{\lambda L_{\lambda}(5100\text{Å})}{10^{44}\mathrm{erg\ s^{-}1}}\right)^{0.545\pm0.036} M_{\odot} \tag{1.2}$$

$$M_{BH}^{\mathrm{(RMS)}} = \left(5.75^{+0.39}_{-0.36}\right) \times 10^{7} \times \left(\frac{\lambda L_{\lambda}(5100\text{Å})}{10^{44}\mathrm{erg\ s^{-}1}}\right)^{0.402\pm0.034} M_{\odot} \tag{1.3}$$

1.3.2 The accretion disc

The radiatively efficient infall of matter towards the central SMBH is thought to be the only process efficient enough to fuel the AGN power (Rees, 1984). The average efficiency of converting a certain amount of mass accreted by a black hole into bolometric luminosity is $\eta = L/\dot{M}c^2$, where

$\dot{M}$ is the mass accretion rate. A simple mathematical relation for the accretion efficiency is cited by Fanidakis et al. (2011) from a conference by Novikov & Thorne (1973). We reproduce it in Eq. 1.4:

$$\eta = 1 - \sqrt{1 - \frac{2}{3}\frac{1}{R_{\mathrm{ISCO}}}} \tag{1.4}$$

Then, according to Eq. 1.4, efficiencies are expected to be found between $\eta = 0.06$ for a non rotating black hole, and $\eta = 0.32$ for a maximally rotating black hole ($a^* = 0.998$). However, efficiencies are estimated within a wider range, e.g. by Shankar et al. (2009), who propose that all black holes grow by gas accretion with efficiencies $\eta \sim 0.06 - 0.1$; or by Davis & Laor (2011), who find a strong correlation of the efficiency with the black hole mass in a sample of 80 QSOs: $\eta = 0.089 \times M_8^{0.52}$, where M_8 is the mass of the SMBH in units of $10^8\,M_\odot$. For the majority of the sources in their sample, they find efficiencies from $\eta \sim 0.03$ for masses of $10^7\,M_\odot$ up to $\eta \sim 0.40$ for masses of $10^9\,M_\odot$, which is consistent with the values predicted by Novikov & Thorne (1973). However, at the high mass regime, they compute $\eta > 0.32$ for few sources. It is interesting to compare these accretion efficiency values with that computed for the nuclear conversion of rest–mass to energy. The efficiency of nuclear fusion of H into He is only $\eta = 0.007$, which is at least one order of magnitude lower than accretion efficiency. Hence, there is wide consensus on the fact that accretion onto black holes yields the greatest efficiency when converting rest–mass into luminosity within the most luminous sources in the Universe.

In its journey towards the singularity, matter does not follow straight paths. Angular momentum must be conserved, so that a disc–shaped structure is formed as a consequence of angular momentum extraction that follows the inwards transportation of matter being accreted onto the SMBH (Shakura & Sunyaev, 1973). In this framework, most of the matter jumps to inner orbits, while a minor part of it moves outward, carrying angular momentum with it. This process implies some viscous energy dissipation (Pringle, 1981), which is being progressively better understood within the context of MHD simulations (see e.g. Balbus & Hawley, 2003).

This accretion flow extends from the ISCO (Fabian et al., 1989) up to several hundreds or thousands of gravitational radii (i.e. at sub–parsec scales). If the disc is optically thick, every disc element at an orbit of radius r radiates as a blackbody with a temperature $T(r)$ given by Eq. 1.5 (see e.g. Section 3.3 in Peterson, 1997):

$$T(r) = \left\{ \frac{3GM\dot{M}}{8\pi\sigma r^3} \left[1 - \left(\frac{R_{\mathrm{in}}}{r} \right)^{1/2} \right] \right\}^{1/4} , \tag{1.5}$$

where R_{in} is the inner edge of the disc. Thus, the total spectrum emitted by the accretion disc is the superposition of blackbodies with temperature $T(r)$ emitted from the annuli defined within the orbits of radius r, integrated over the surface of the disc. Eq. 1.5 clearly states that the maximum temperature within the surface of the accretion disc is reached at its inner limit, commonly postulated to correspond to the ISCO. The emission from the accretion disc has its peak in the far / extreme UV depending on the SMBH mass (in the band where QSOs and AGN are more bright, Zhou et al., 1997); this is the so–called big blue bump (BBB).

1.3.3 The broad line region

AGN emission–line spectra consist of narrow components, whose widths are usually less than $\sim 500\,\mathrm{km\,s^{-1}}$, and broad components, with widths between ~ 1000 and $\sim 25000\,\mathrm{km\,s^{-1}}$. Both components originate in a system of discrete clouds, different in their physical properties, sizes and locations. In this section we will introduce the properties of the region from which the broad spectral components emanate, leaving the explanation of the NLR for Section 1.3.5. The large widths of the broad lines point to the existence of a strong gravitational potential in the region from which these lines arise. This makes the broad spectral component an extremely valuable tool to probe the central regions of AGN. As an example, some of the broad lines in the Seyfert 1 galaxy NGC 5548 are shown in the top panel of Fig 1.2 (especifically, Hβ λ4861 and Hα λ6563, marked as "1" and "4", respectively).

The BLR is defined as the region inhabited by the high density, dust–free gas clouds responsible for the optical broad emission lines of AGN. They orbit at Keplerian velocities the SMBH at a distance between 0.01 and 1 pc, also depending on the central mass. Osterbrock (1989) argues that the physical density of the clouds in the BLR is $n \sim 10^9\,\mathrm{cm}^{-3}$, based on the appearance of the C III] λ1909 recombination line, whose critical density is $\sim 3 \times 10^9\,\mathrm{cm}^{-3}$. In his textbook, he combines that density and the luminosity of the Hβ emission line, $L_{\mathrm{H}\beta} \sim 2 \times 10^{44}\,\mathrm{erg\,s}^{-1}$, to estimate the mass of the BLR as $M_{\mathrm{BLR}} = 2 \times 10^3\,M_\odot$.

On the other hand, modelling the C IV and Lyα zones, Ferland et al. (1992) show that the BLR clouds are more likely to have particle densities of $n \sim 10^{11}\,\mathrm{cm}^{-3}$. Reverberation observations of the BLR confirm this higher density to be more characteristic of the clouds from which these permitted emission lines arise, although still some quantity of low density gas must exist in a different part of the BLR to account for the C III] lines (see Peterson, 1993). In the Eq. 5.9 of his classic textbook, Peterson (1997) uses the higher density and the C IV λ1549 luminosity to give an estimation of the mass of the line–emitting material in the BLR, $M_{\mathrm{BLR}} < 10\,M_\odot$ (even for the most massive AGN).

Krolik (1999) derives a value depending on the covering factor, the column density of the ionized gas, the luminosity of the ionizing continuum and an ionization parameter of the gas (defined as the ratio of radiation pressure to gas pressure), obtaining a range of masses in between those derived by Osterbrock (1989) and Peterson (1997).

Baldwin et al. (2003) criticise the heterogeneity in the election of luminosity and density among these different textbooks, and recalculate the estimates given above adopting a particle density of $n \sim 10^{11}\,\mathrm{cm}^{-3}$ and a monochromatic continuum luminosity at rest wavelength 1450 Å of $L_{1450} \sim 10^{44}\,\mathrm{erg\,s}^{-1}\,\mathrm{Å}^{-1}$, typical of bright quasars (Hewett et al., 1995; Boyle et al., 2000; Dietrich et al., 2002). They also take into account the Baldwin effect, responsible for the variation of the emission–line equivalent widths (EWs) with luminosity. This way their estimates turn out to be $M_{\mathrm{BLR}} = 290\,M_\odot$, $3\,M_\odot$ and $100\,M_\odot$ from the Osterbrock (1989), Peterson (1997) and Krolik (1999) works respectively. Morover, Baldwin et al. (2003) implement some further improvements in their mass calculation of the BLR: considering reverberation results, they find that there must be $10^3 - 10^4\,M_\odot$ of inefficiently radiating gas only. To this it should be added the partially ionized and / or neutral gas within every single cloud, as well as the hot phase gas not emitting any optical or UV lines hipothesised by Krolik et al. (1981)They thus conclude that their estimate of the M_{BLR} is just a lower limit for luminous quasars.

The size of the BLR, i.e. the distance between the continuum source and the BLR clouds, has been measured by Bentz et al. (2007) in NGC 5548 by reverberation mapping of the Hβ time lags respect to the continuum flux. Also, it has been studied in other twelve nearby Seyfert 1 galaxies with central masses of $\sim 10^6 - 10^7 M_\odot$ (Bentz et al., 2009), finding lags of the order of a few days. Once known these Hβ time lags, which are connected with the mean sizes of the Hβ–emitting BLRs, sizes in the range $R_{\mathrm{BLR}} \sim 0.001 - 0.007$ pc are derived.

In order to address the issue of ionization of the clouds in the BLR, it is necessary to define an ionization parameter. The ionization degree of photoionized gas is proportional to the ratio between the ionizing photon density and the physical density of the gas itself (Netzer, 2008). This way, two ionization parameters are usually defined from the conditions of photoionization equilibrium: ξ (Eq. 1.6), given by the energy flux, and U (Eq. 1.7), based on the photon flux instead. This way, the ionization parameter ξ is defined in terms of luminosity (L_E) as

$$\xi = \frac{1}{nR^2} \int_{E_1}^{E_2} L_E dE, \tag{1.6}$$

where $E_1 = 13.6\,\mathrm{eV}$ and $E_2 = 13.6\,\mathrm{keV}$. Another extensively used ionization parameter is that defined by the photon flux in stead of the energy flux, which is given in terms of luminosity (L_E) and energy (E) as

$$U = \frac{Q}{4\pi R^2 cn} = \frac{1}{4\pi R^2 cn} \int_{E_1}^{E_2} \frac{L_E}{E} dE, \tag{1.7}$$

where n is the density of the cloud, R is its distance to the continuum source, c is introduced to make U dimensionless, and Q is the photon flux computed between two energies, E_1 and E_2, chosen in such a way that E_1 is about the lowest energy required to ionise the main ions and E_2 is large enough to include most of the radiation. For instance, in the case of a soft–UV ionized gas, $E_1 = 13.6\,\mathrm{eV}$ (the energy of the hydrogen Lyman limit) and $E_2 = \infty$. A X–ray dominated gas could be transparent to UV radiation, so that these limits would not be suitable to produce an ionization parameter representative of the true ionization state of the gas. In this case, $E_1 = 0.1\,\mathrm{keV}$ and $E_2 = 10\,\mathrm{keV}$ would be good choices. It is usually found that ionizations of the clouds in the BLR in the range $U \sim 10^{-1} - 10^{-2}$ reproduce well the emission lines observed in the energy ranges of interest.

1.3.4 The torus

The existence of an obscuring dusty structure (the torus) around the central SMBH was first pointed by the detection of broad emission lines in spectropolarimetry observations. The photons from the hidden BLR are scattered into our LOS by material (free electrons) above the torus in several type 2 AGN (see e.g. Miller & Goodrich, 1990; Tran et al., 1992; Heisler et al., 1997). Beyond these indirect detections, direct proofs of the dusty torus are yielded from IR observations. The circumnuclear dust absorbs the photons emitted by the central source, and emits the absorbed energy in the IR band. A near–IR excess emission above the $\sim 2-10\,\mu$m continuum (the so–called IR "bump") is detedted in several type 1 AGN (Barvainis, 1987; Rodríguez-Ardila & Mazzalay, 2006). This bump is commonly attributed to cold material heated by the source up to the sublimation temperature of silicates ($\sim 1200 - 1500$ K). Imaging at the near– and mid–IR band has been performed, providing constraints on the location of the torus, as well as on its size and its structure (see e.g. Elitzur & Shlosman, 2006). The torus is described as an axisymmetric dusty molecular structure located around the equatorial plane of the system between 0.1 and 10 pc, depending of the SMBH mass. This component is the main responsible for obscuration in obscured AGN, and in this context it becomes the fundamental basis for AGN unification models, as explained in Section 1.2.1.

Two phenomenological torus models have been proposed in order to better understand how the radiative transfer from the inner regions of the central engine outwards takes place: the homogeneous torus and the clumpy torus. The homogeneous models are treated by Pier & Krolik (1992); Efstathiou & Rowan-Robinson (1995); Granato et al. (1997); Dullemond & van Bemmel (2005); Fritz et al. (2006). The clumpy models are addressed by Dullemond & van Bemmel (2005); Nenkova et al. (2008a,b); Hönig et al. (2010).

Both models share some basic propeties. They are geometrically characterized by being axisymmetric, and are assumed to extend from the dust sublimation radius up to an outer radius, within the space limited by the torus opening angle. The homogeneous models, in which the torus is a continuos gas distribution whose temperature decreases with the square of the distance from the SMBH, is completely determined by these parameters plus the density profile. The clumpy models, however, need extra parameters appart of those ones: the column densities of the clumps, their radial and density distribution, and the filling factor.

Differences between the clumpy and homogeneous models are addressed by Feltre et al. (2012); Lira et al. (2013), including: in clumpy models, every clump has and illuminated and a non–illuminated (or back) side, which allows the existence of a large temperature range at every point of the torus; also, the empty space among clumps allows un–attenuated LOSs to distant inner regions of high temperaure within the torus.

A third model is explored by Stalevski et al. (2012) as a combination of the other two, in which the clumps are embedded in a homogeneous dusty gas, responsible of some additional absorption.

Some other models have been proposed, like the tilted disc model by Lawrence & Elvis (2010), that deals with the true type 2 AGN nature; and the torus plus dusty polar wind model by Hönig et al. (2013), where most of the mid–IR emission in Seyfert galaxies originates from a dusty wind in their polar regions.

1.3.5 The narrow line region

The opening of the torus defines two conical–shaped regions with their apexes coincidental with the SMBH and their axes coincidental with the symmetry axis of the system. The ionizing radiation from the innermost regions of the AGN reaches the gas and dust within these ionization cones, being reprocessed into optical narrow emission lines from low (O I), intermediate (O III, O IV), and high ionization isotopes (Si VI), as well as into X–ray emission lines (O VII).

This region extends from the torus surface itself up to thousands of parsecs (in Mrk 573 X–ray emission reaches 7 kpc, as shown by Paggi et al., 2012). The location of the clouds in the NLR, at distances of up to several kpc from the central engine, is discussed in e.g. Schmitt et al. (2003); Augusto et al. (2001). The narrow lines observed in AGN have been proposed to be due to photoionization by the central source (Dopita & Sutherland, 1995), and also due to shock excitation by the relativistic jets (Koski, 1978; Stasińska, 1984). The clouds within the NLR have lower densities ($\sim 10^3 - 10^4\,\mathrm{cm}^{-3}$) than those in the BLR. Typical velocities are also much lower, of the order of $10^2\,\mathrm{km\,s}^{-1}$ (De Robertis & Osterbrock, 1985; Stirpe, 1990; Zamanov et al., 2002).

1.3.6 The relativistic radio jets

Sometimes a central radio jet, associated with γ–ray emission, is observed in AGN. At least 10 per cent of AGN show this component. The jets are two collimated outflows rising from the innermost regions of the central engine at relativistic velocities in opposite directions along the symmetry axis of the system (Wilson & Tsvetanov, 1994; Fabian et al., 2002; Wiita, 2001). The jets radiate energy in the entire elctromagnetic spectrum, by means of inverse–Compton emission and synchrotron processes, being the most prominent emission in the radio wavelengths (Fabian et al., 2002).

Jets are divided in two classes, FR I and FR II, depending on their radio luminosities, being those of FR II type more luminous than those of FR I type. FR I jets reach scales of kpc, slowing down from relativistic to sub–relativistic velocities due to the interaction of the flow with the interstellar medium (ISM), being thus efficient radiators. On the other hand, FR II jets transport energy up to much greater distances, of hundreds of kpc (Worrall, 2009). These jets are low–efficiency radiators in contrast.

Nor the jet production mechanisms nor the composition of the flow itself are known yet. There exist several theories, among which the most accepted are the Blandford–Znajek process (Blandford & Znajek, 1977) and the Blandford–Payne process (Blandford & Payne, 1982). Both theories involve energy extraction from within the central regions to fuel the jets. In the Blandford–Znajek process, energy is obtained by angular momentum extraction from the rotating SMBH, and transported outwards by the open magnetic field lines. However, in the Blandford–Payne process, the jet is powered by the magnetic fields created in the accretion disc, which extract energy from the disc itself.

1.4 Spectral variability of AGN

AGN observations have revealed them as highly variable objects at all wavelengths. Their variations, of erratic amplitude, do not appear to follow any periodic pattern. Variability of AGN (both of the continuum and the emission–line) is a powerful tool to map microarcsecond–sized structures in their central regions, via reverberation mapping. Also, the most robust and efficient technique for measuring the central SMBH mass is the analysis of the broad emission line variability.

Significant flux variability in AGN ($\gtrsim 0.1$ mag) was first found in quasars on time scales as long as years and as short as few days (Matthews & Sandage, 1963; Smith & Hoffleit, 1963). Studies on AGN variability are crucial to understand the physics of their innermost regions, which cannot be resolved even with the highest resolution interferometers. The delays between variations in different continuum or emission line components, the spectral variations, and the time scales involved provide essential information on the constitution and location of those components. For instance, when variability at days timescales is found, strong implications on the size of the coherently continuum–emitting region arise: those sizes must be then of the order of light days ($1\,\mathrm{ld} \sim 2.6 \times 10^{15}$ cm).

1.4.1 Optical and UV variability

Continuum flux variations at optical and UV wavelengths are sometimes observed to be simultaneous, although this is not always the case. It was reported by Recondo-Gonzalez et al. (1997) that

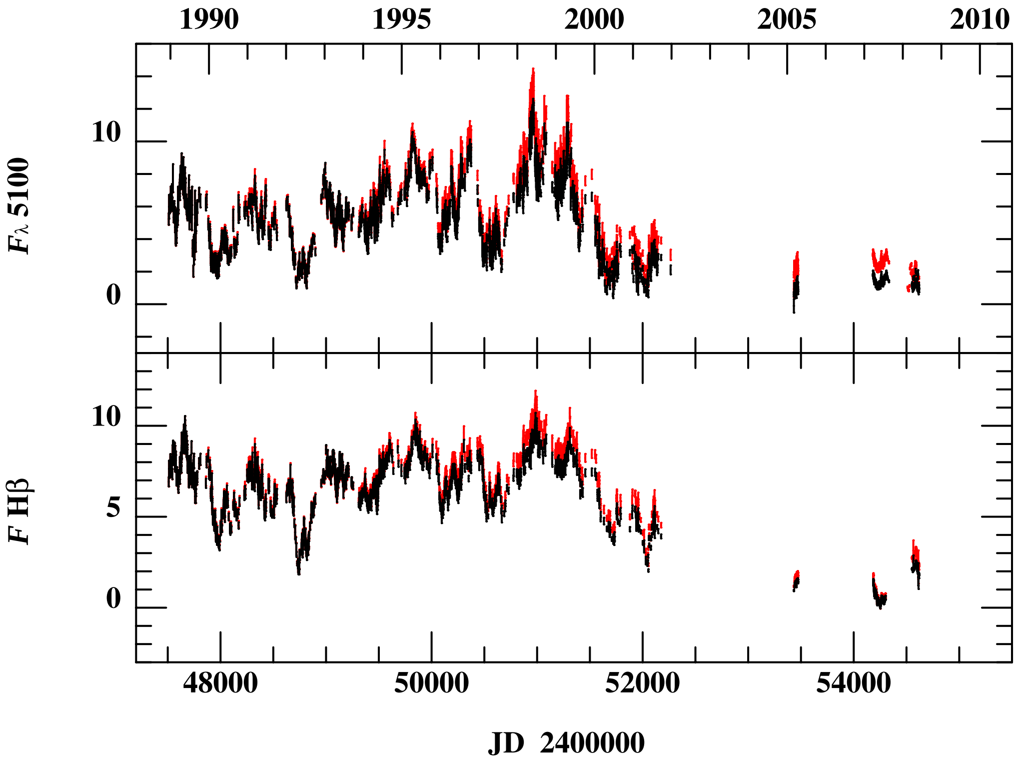

Figure 1.6: Observed–frame 20–years–long optical continuum (5100 Å, upper panel) and Hβ (lower panel) light curves of NGC 5548. The continuum fluxes are in units of 10^{-15} erg s^{-1} cm^{-2} Å^{-1} and the broad line fluxes are in units of 10^{-13} erg cm^{-2} s^{-1}. The continuum is corrected for the contribution of the stars in the host galaxy, and a narrow Hβ contribution has been subtracted from the broad Hβ light curve. The original / recalibrated light curves are plotted in red / black. Figure from Peterson et al. (2013).

UV continuum of Fairall 9 varied by a factor of over 30 in 180 days. Also, that of NGC 4151 varied similarly along two years (Ulrich et al., 1997). The best explanation for the variable continuum emission is reprocessing in a dense medium illuminated by variable X–rays.

IR variations, if detected, show smaller amplitude and longer timescales than in the optical (Neugebauer et al., 1989; Hunt et al., 1994). These results point to the delayed response of dust in the surroundings of the central source to variations of the flux in the UV wavelengths.

Variability studies of the broad line–emitting gas have contributed significantly to understand the innermost regions of AGN, by allowing estimations of the emitting region size, which depends on the line velocity. Also, the central black hole mass can be calculated from the motion of the gas in its gravity field.

Continuum (5100 Å) and Hβ light curves of the archetypical Seyfert 1 galaxy NGC 5548 are shown in Fig. 1.6. This AGN is one of the most extensively studied objects of its type. Its behaviour is aperiodic, and shows smalls variations on time scales shorter than few days, but very large on long time scales (from several weeks to months).

1.4.2 X–ray variability

AGN are highly and rapidly variable at X–ray energies (see e.g. the review by Mushotzky et al., 1993). Moreover, X–ray emission presents the shortest timescale variability when compared with any other wavelength range (Grandi et al., 1992). Variability in the emission from the X–ray source has been found to be stochastic in nature (Lehto et al., 1993). Also, the soft excess is more variable than the power law component, and it is usually correlated with the medium energy X–rays. The intensity of the power law component generally varies keeping the spectral index constant, or almost constant. It was already known in the eighties that an important number of Seyfert galaxies presented fast, large X–ray variability (amplitude $\delta I/I > 1$) on days timescales (Marshall et al., 1981; Pounds & McHardy, 1988). However, it is important to note that Seyfert 1s usually vary faster than Seyfert 2s (Wandel & Mushotzky, 1986), which is explained by Mulchaey et al. (1992), who claims that the luminosity of Seyfert 2 galaxies in the optical–UV range is underestimated. This is one more argument in favour of the unified model, which was addressed in Section 1.2.1. Up to date, the procedure by which X–ray variability happens is yet not kwown.

This kind of variability can be used to derive the size of the X–ray source. Variability can only be observed on timescales larger than the light crossing time of the source, Δt, this constraining the maximum size of the X–ray source to $D_{\rm c} < v_{\rm c}\Delta$t.

The light curves of different AGN show distinct behaviours. Some show singular variability events with no or little variability between them, such as in the case of NGC 3783 (Grandi et al., 1992). However, other AGN have light curves whose variability is continuous, like in NGC 5506, for which McHardy & Czerny (1987) find X–ray time variability showing a fractal–like pattern, pointing to the possibility that X–ray variability may be driven by a number of physical variables, in stead of being really stochastic.

Finally, the soft X–rays are expected to be dominated by a scattered radiation component, and therefore to vary more slowly than the hard X–rays. This is exactly what happens for e.g. NGC 1068 (Monier & Halpern, 1987), and for NGC 4549 (Iwasawa et al., 1993). The most extreme soft X–ray variability takes place in NLS1 galaxies. The steep soft X–ray spectrum of NLS1s may point either to a low SMBH mass or to a high accretion rate. Among some of the most prominent examples of variability, are the following objects: RE J1237+264, with a factor of 70 in one year (Brandt et al., 1996); PHL 1092, with strong variations in the Fe II line (Forster & Halpern, 1996); IRAS 13224-3809, with soft X–ray flux variability of about a factor of 60 (explained by relativistic Doppler boosting, see Boller et al., 1997); E1615+061, with X–ray variability of a factor of about 50 (Piro et al., 1997); and WPVS007, with a factor of 400 in three years (Grupe, 1996).

X–ray absorption variability

Spectral variability at X–ray wavelengths on relatively long time–scales (months to years) is often associated with absorption events (see e.g. Warwick et al., 1988; Risaliti et al., 2002; Marinucci et al., 2013; Miniutti et al., 2014). In many cases, such long–term absorption variability can be associated with the transit of dusty clouds in our LOS, which reveals the presence of a clumpy, dusty torus at relatively large spatial scales, see e.g. Markowitz et al. (2014); Agís-González et al. (2014). In recent years, several examples of short time–scale (hours to days) absorption variability have been reported too, e.g. in NGC 4388 (Elvis et al., 2004), NGC 4151 (Puccetti et al., 2007), NGC 1365 (Risaliti et al., 2005, 2007, 2009b; Maiolino et al., 2010), NGC 7582 (Bianchi et al., 2009), Mrk 766 (Risaliti et al., 2011a) or SWIFT J2127.4+5654 (Sanfrutos et al., 2013).

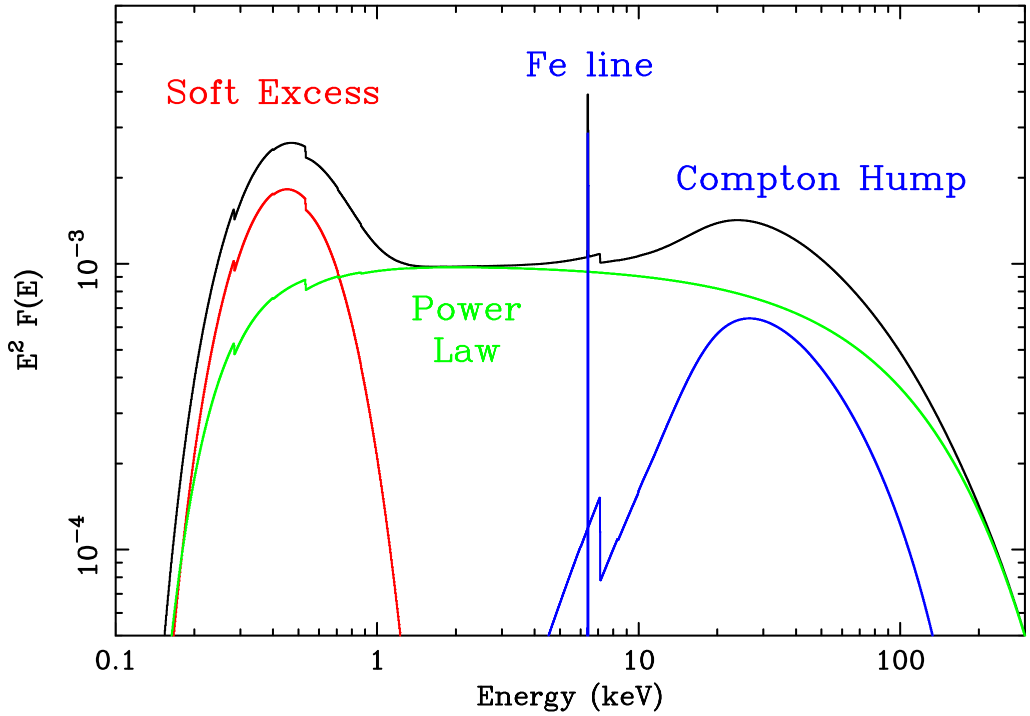

Figure 1.7: Components of AGN X–ray spectra (Fabian & Miniutti, 2005). In red we show the thermal emission from the disc; in green the power law resulting of Compton up–scattering of the optical, UV, and soft X–ray photons by the corona; and in blue the component due to hard X–rays reflection by dense gas in the system.

The detailed analysis of the short time–scale absorption variability in these sources strongly suggests the presence of absorbing structures, or clouds, crossing the LOS to a rather compact X–ray source. As an example, the in–depth study of the short time–scale absorption variability in SWIFT J2127.4+5654 reveals unambiguously the transit of a single cloud, as it will be extenseively explained in Chapter 2.

The data are generally consistent with the presence of an ensemble of compact, cold clouds with typical column density of $10^{22} - 10^{24}$ cm^{-2}, density of $10^9 - 10^{11}$ cm^{-3}, velocity of few times 10^3 km s^{-1}, and located at distances of $10^2 - 10^4\, r_g$ from the central engine. These properties are remarkably similar to those of the clouds responsible for the emission of the broad optical and UV emission lines in AGN (the clouds in the BLR, see Section 1.3.3). Hence, X–ray absorption variability studies suggest to identify the X–ray compact absorbers responsible for the shortest time–scale absorption variability events with BLR clouds, while variability on longer time–scales (months to years) is likely associated with more extended structures, possibly associated with a clumpy torus (see Section 1.3.4). A long– and short–term X–ray spectral analysis of variability of the polar–scattered Seyfert 1.2 galaxy ESO 323–G77 is reported in Chapter 4.

1.5 X–ray spectral features of AGN

While in accreting stellar–mass black holes, in X–ray binaries (XRBs) the accretion disc thermal emission peaks in the X–rays, AGN discs are much colder, with thermal emission peaking in the UV / extreme ultraviolet (EUV) regime. However, X–ray emission is always present in AGN

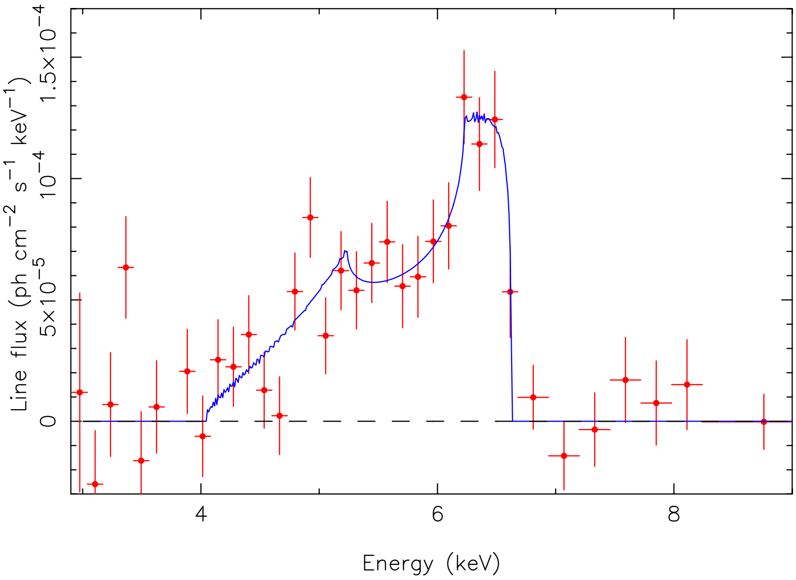

Figure 1.8: Fe line profile from an *ASCA* observation of MCG–6-30-15 (figure credit: Tanaka et al., 1995, image generated by Dr. Nandra).

spectra. Hence AGN are routinely observed in the X–rays up to hundreds of keV, at least. This thermal radiation emitted is thought to be due to inverse Compton upscattering of the UV / EUV seed photons from the accretion disc in a corona of hot electrons (see e.g. Reynolds & Nowak, 2003). This region is probably heated by magnetic reconnection processes, and located somewhere along the rotation axis of the SMBH and / or off–axis, in the proximity of the inner parts of the accretion disc. Comptonization gives rise to a high energy tail which can be well approximated by a power law with a photon index of $\Gamma \sim 1.8-2$, and high energy cutoff at around few hundreds keV, depending on the optical depth and temperature of the hot electronic plasma responsible for this emission (green component in Fig. 1.7). This cutoff is marked by the energy at which the photons reach the electrons energy and thus cannot be upscattered anymore. Then, the power law emission irradiates the accretion disc and other material in the surroundings and is reprocessed, giving rise to a characteristic reflection spectrum whose main properties are an iron emission line at 6.4 keV and a Compton hump at 20–30 keV. Therefore, the underlying disc reflection signatures are easily exposed when subtracting the power–law continuum.

Part of the primary X–ray radiation is reprocessed by the disc, the BLR and the torus, causing the reflection features typically seen in AGN sectra (blue components in Fig. 1.7). This reprocessed emission consists of a Compton hump and an Fe Kα line. The Fe Kα emission line is located at 6.4 keV, and is always present. This feature might be composed of a broad component (from the accretion disc) and a narrow one (arising from material in the BLR and / or the molecular torus).

When the continuum X–ray emission from the close environments of a black hole illuminates relatively cold matter, a spectrum of fluorescent emission lines is yielded. The most prominent one is the Fe K line, which is emitted at 6.4–6.97 keV, depending on its ionization state. This line is intrinsically narrow, but its double–peaked spectral shape due to Newtonian effects is distorted and broadened by relativistic Doppler beaming and gravitational redshift (see e.g. Fabian et al., 2000, and Section 1.5.2). A typical resulting shape is that of the iron line in the Seyfert 1 galaxy MCG–6-30-15 (Fig. 1.8), the first AGN whose X–ray reflection from neutral material was detected. Studying these spectral features we can investigate the physics taking place in the close environments of astrophysical black holes.

The Compton emission, with its peak at 20–40 keV, is more prominent the thicker the reprocessing material is (nominally, this component is present only when the column density is greater than $10^{24}\,\mathrm{cm}^{-2}$). Incident X–rays are either absorbed or scattered by the matter within the accretion disc, essentially, depending on their energy. While most of the soft X–rays suffer photoelectric absorption, hard X–rays are mostly Compton scattered out of the accretion disc. Nevertheless, above ~ 10 keV, Compton recoil favours the appearance of a broad excess, due to Compton reflection of the power law continuum by low ionization, optically thick matter, the so–called Compton hump. This hump–like structure typically peaks around 20–40 keV (Perola et al., 2002; De Rosa et al., 2012).

A great number of AGN exhibit an excess of flux over the continuum in the soft band, below ~ 2 keV (red component in Fig. 1.7). This is the so–called soft excess, whose origin is different for absorbed and unabsorbed AGN. Various interpretations have been proposed for the case of unabsorbed AGN: blurred reflection from the ionized disc, absorption by an ionized wind, and the existence of another cooler corona. In the case of absorbed AGN, the X–ray spectra are imprinted by photoelectric absorption and Compton scattering. The first is noticeable even at column densities as low as $10^{21}\,\mathrm{cm}^{-2}$, although it is not important above 10 keV for Compton–thin column densities ($N_{\mathrm{H}} < 10^{24}\,\mathrm{cm}^{-2}$). The second is relevant only with Compton–thick column densities ($N_{\mathrm{H}} > 10^{24}\,\mathrm{cm}^{-2}$). Sulentic et al. (2000) identify two sets of radio–quiet AGN: those with FWHM(Hβ) $\leq 4000\,\mathrm{km\,s}^{-1}$, usually strong Fe II emission, and a soft X–ray excess; and those with radio–loud–like optical properties, FWHM(Hβ) $\geq 4000\,\mathrm{km\,s}^{-1}$, generally weak Fe II emission, and no soft X–ray excess. Also some BL Lacs show a soft X–ray excess similar to that observed in radio–quiet sources (see e.g. White et al., 1984; Padovani & Giommi, 1996).

This soft X–ray excess, the dominant spectral feature below 2 keV, is widely interpreted as thermal emission rising from the accretion disc. Nevertheless, this point is still heatedly debated. In the case of the spectral study of NGC 4051 (Ponti et al., 2006), the origin of the soft excess is not thermal, but due to a relativistically blurred ionized reflection component, i.e. the soft end of the ionized reflection from the accretion disc (for a theoretical treatment of this problem see Ross & Fabian, 2005). In this scenario, the light–bending model explains the spectral variability observed in NGC 4051: in this object, the continuum is emitted from a compact region close to the accretion disc, i.e. in the SMBH vicinity. Hence, relativistic effects do indeed affect this kind of radiation.

The soft excess has also been identified with the comptonization of thermal photons from the disc atmosphere or from the jet base (see Haardt & Maraschi, 1991; Mannheim et al., 1995, respectively). Other authors suggest the soft X–ray excess to be due to the continuation of the BBB (Walter & Fink, 1993; Grupe et al., 1998), or even invoke a less substantial secondary warm absorber (Done et al., 1995). Pounds et al. (1995) suggested to replace the traditional thin disc approximation (Shakura & Sunyaev, 1973) by a slim disc one (Abramowicz et al., 1988), capable to reproduce steep soft X–ray spectra (Szuszkiewicz et al., 1996; Wang et al., 1999).

1.5.1 The role of absorption

Typical models of X–ray spectra of AGN are shown in Fig. 1.9, as affected by different intervening absorptions ranging from the unabsorbed case (type 1) to the Compton–thick case (type 2). It is clear that absorption only affects components that are not associated to extended emission larger than the absorber scale. Hence, neither extended emission due to scattering on kpc scales nor

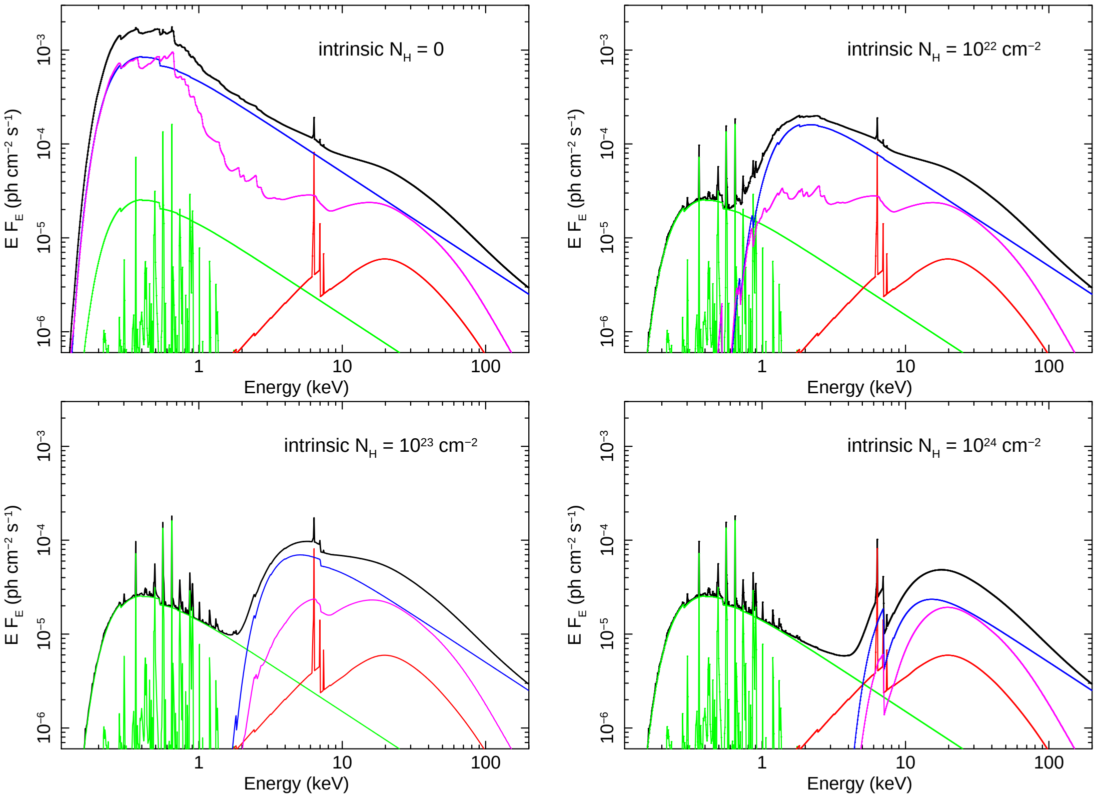

Figure 1.9: Typical X–ray spectra of AGN. Top left–hand panel: unabsorbed case (type 1); top right–hand panel: intrinsic absorption of 10^{22} cm^{-2}; bottom left–hand panel: intrinsic absorption of 10^{23} cm^{-2}; bottom right–hand panel: Compton–thick case (intrinsic absorption of 10^{24} cm^{-2}). Black: total resulting X–ray spectrum. Blue: power law X–ray continuum. Green: extended emission (on kpc scales) due to scattering (green power law) and emission lines (gas photoionized by the AGN and / or star–forming regions). Red: reflection of the power law continuum off neutral distant gas (e.g. the torus). Lines are narrow because distant gas moves only very slowly. Magenta: reflection of the power law continuum off the partially ionized accretion disc. The spectrum is distorted by the high velocities and strong gravity effects close to the black hole.

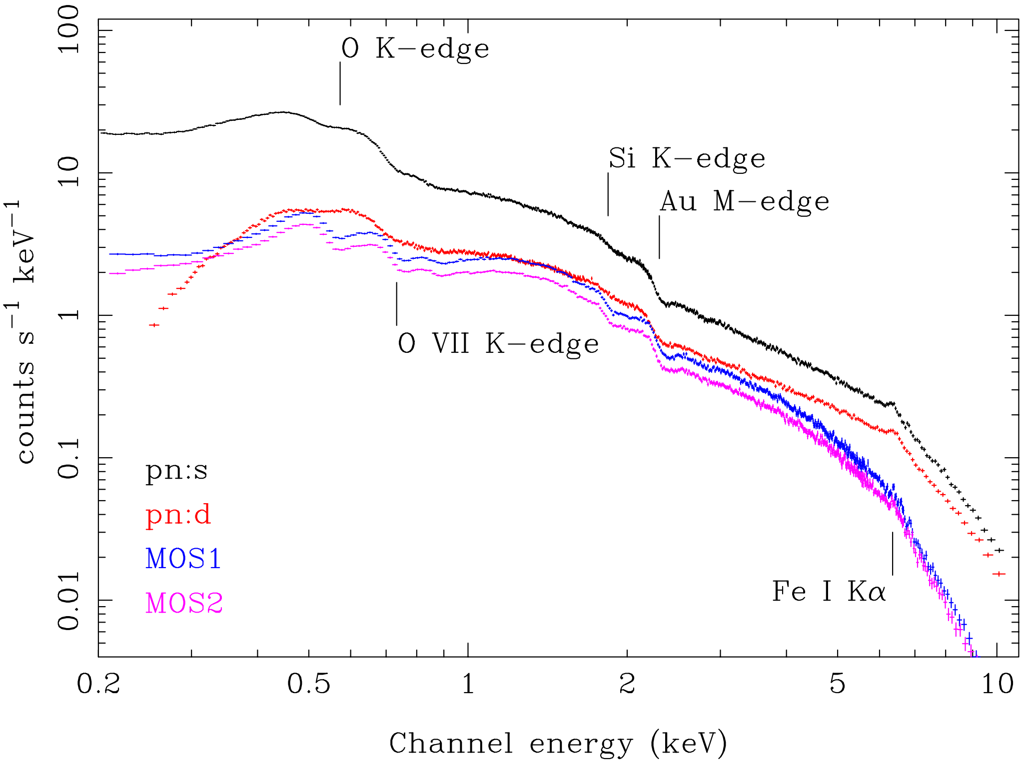

Figure 1.10: The broad–band EPIC spectra of the Seyfert 1 galaxy MCG 6-30-15. The four data sets are the pn spectra for single (black) and double (red) events, and the MOS1 (blue) and MOS2 (magenta) spectra. The MOS2 spectrum is shifted downwards by 20 per cent, for the sake of clarity. The positions of the most significant instrumental features are marked: the edges due to neutral O, Si and Au. Also, the [O VII] edge and the Fe Kα emission line are shown on the positions in which they appear in the source spectrum. The spectrum is continuum–dominated, showing no emission lines (specifically in the soft band, below 2 keV). Credit: Vaughan & Fabian (2004).

emission lines due to star–forming regions and to gas photoionized by the AGN are affected (green component in Fig. 1.9). Reflection of the power law continuum off neutral distant gas (e.g. from the torus) is also unaffected (red in Fig. 1.9). This means that a very absorbed AGN will have strong Fe line equivalent width due to distant reflection (red) and a series of emission lines in the soft X–ray band (photoionized gas and / or star–forming regions) which would otherwise be unobservable, since these components would be buried much below the continuum level in unabsorbed sources.

An example of 0.2–10 keV European Photon Imaging Camera (EPIC) spectra of the Seyfert 1 active galaxy MCG 6-30-15 is shown in Fig. 1.10. It is clear that, when absorption is unimportant, X–ray spectra are continuum–dominated, being any emission line overwhelmed by the source's continuum (specifically, in the soft X–rays band). On the other hand, examples of the soft X–ray spectra of the Seyfert 2 active galaxy NGC 1068 are depicted in Fig. 1.11, showing that type 2 AGN spectra are dominated by narrow emission lines as a result of reflection of the continuum in distant material.

In many AGN, even in those of type 1, it is observed extra absorption due to outflowing ionized gas, namely the so–called 'warm absorber' (Reynolds & Fabian, 1995). Its effect is shown in Fig. 1.12. The effect of two outflowing warm absorbers is modelled by means of two ZXIPCF components, one with low and one with high ionization. The emergent absorption lines can be used to infer the column densities, ionization states and outflowing velocities of the warm absorbers, which are

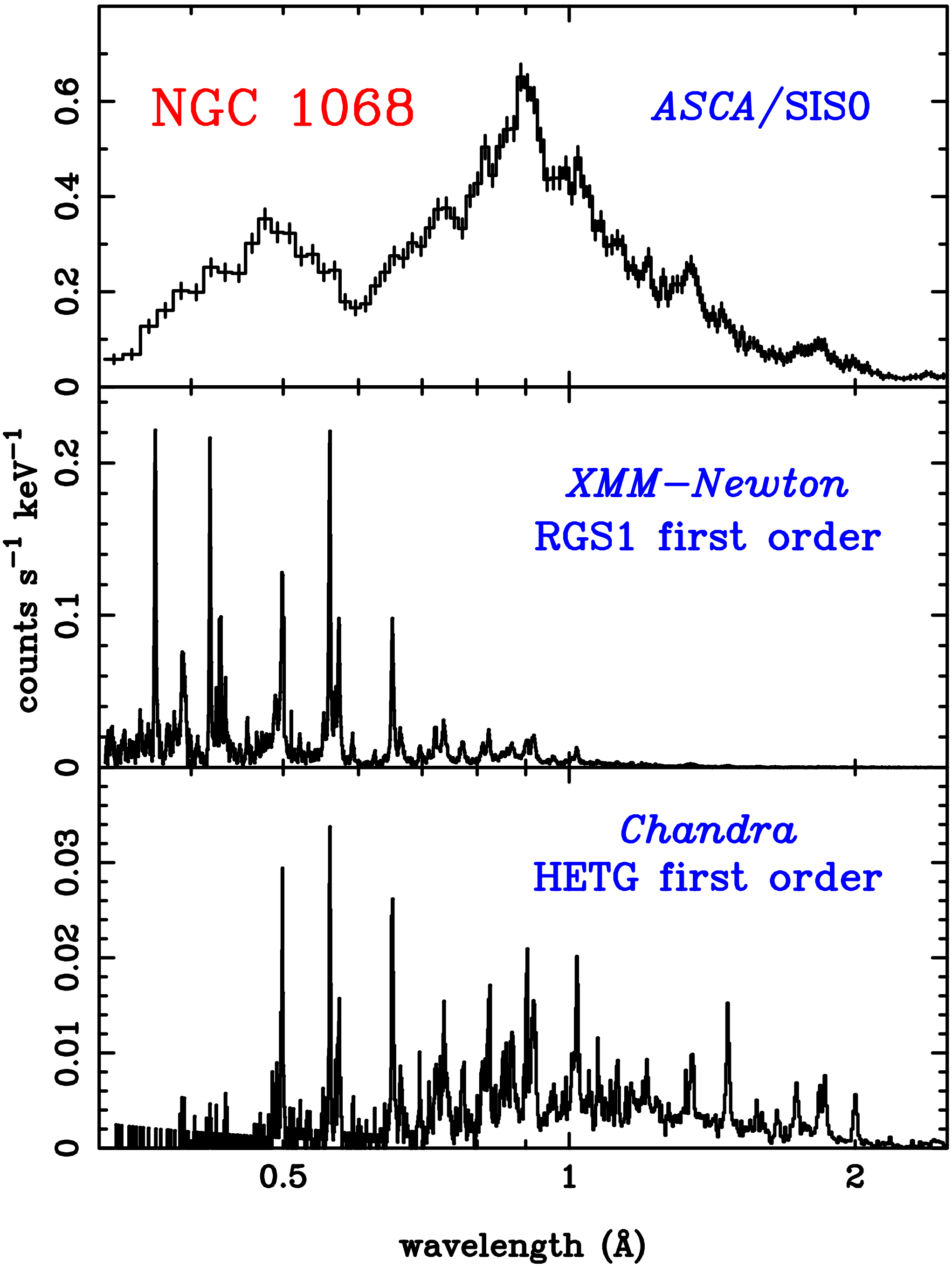

Figure 1.11: The soft X–ray spectrum of the Seyfert 2 galaxy NGC 1068 obtained with *ASCA* (top panel), *XMM–Newton* (middle panel), and *Chandra* (bottom panel). The spectrum is reflection–dominated, showing a forest of narrow emission lines (resolved with *XMM–Newton* and *Chandra*, but not with *ASCA*). Credit: Sako et al. (2002).

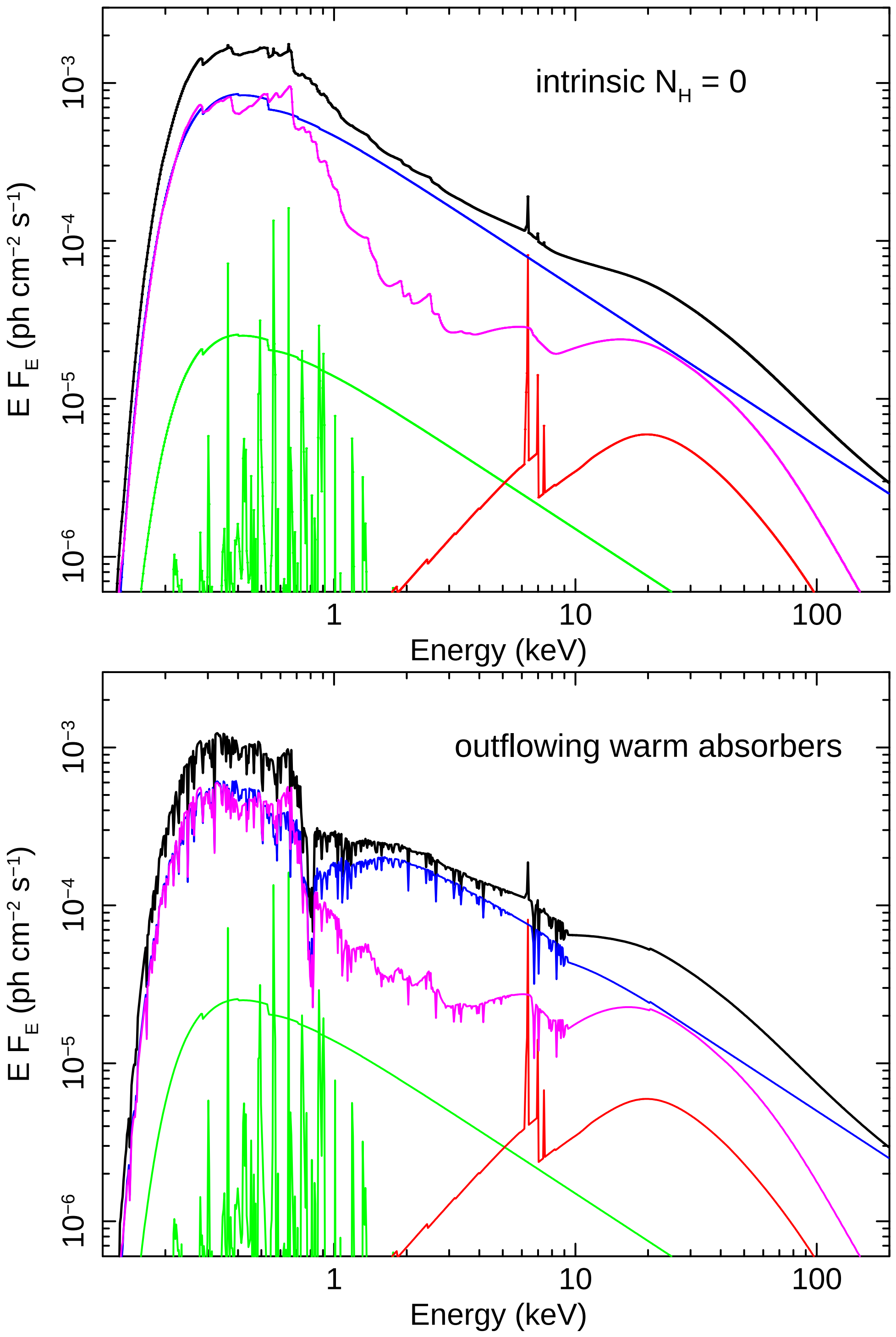

Figure 1.12: Typical X–ray spectra of AGN. Top panel: unabsorbed spectrum; bottom panel: the same spectrum, but affected by the presence of two outflowing warm absorbers, one with low and one with high ionization. Colour code as in Fig. 1.9

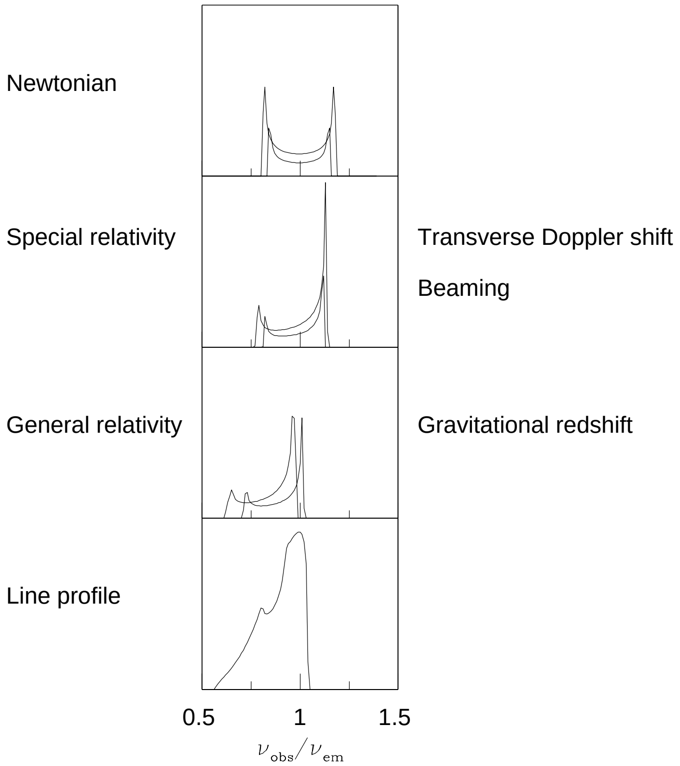

Figure 1.13: The profile of an intrinsically narrow emission line is modified by the interplay of Doppler / gravitational energy shifts, relativistic beaming, and gravitational light bending occurring in the accretion disc. Upper panel: symmetric double–peaked profile from two annuli on a Newtonian disc; second panel: effects of transverse Doppler shifts (reddening of the profiles) and of relativistic beaming (enhancing the blue peak with respect to the red); third panel: gravitational redshift is shifts the overall profile to the red side and reduces the blue peak strength. Bottom panel: the broad, skewed line profile as a result of combinating all these effects, and integrating over the contributions from all the annuli. Figure from Fabian et al. (2000).

usually found to be rather compact and located at distances of the inner torus or closer. Therefore, they do not affect the extended emission (green and red components in Fig. 1.12), but they do affect the inner, compact emission sites (the power law and disc reflection, blue and magenta components in the same figure).

1.5.2 The role of relativistic effects

Relativistic broad iron lines are seen in the spectrum of several AGN (MCG–6-30-15 and IRAS 18325–5926) and Galactic XRBs (XTE J1650–500 and GX 339-4) (see e.g. the reviews by Fabian et al., 2000; Reynolds & Nowak, 2003; Fabian & Miniutti, 2005). The puzzling spectral variability of many sources can be well understood within the framework of the strong gravity regime (Miniutti et al., 2003; Fabian et al., 2004). Also, the short–timescale variability of the broad iron line reveals general relativity (GR) as the most relevant physical constraint (see e.g. Iwasawa et al., 2004).

The Fe I Kα emission line actually comprises two lines at 6.404 keV and 6.391 keV, but it is usually assumed to be a single line at 6.4 keV at the current X–ray detectors resolution. This line is

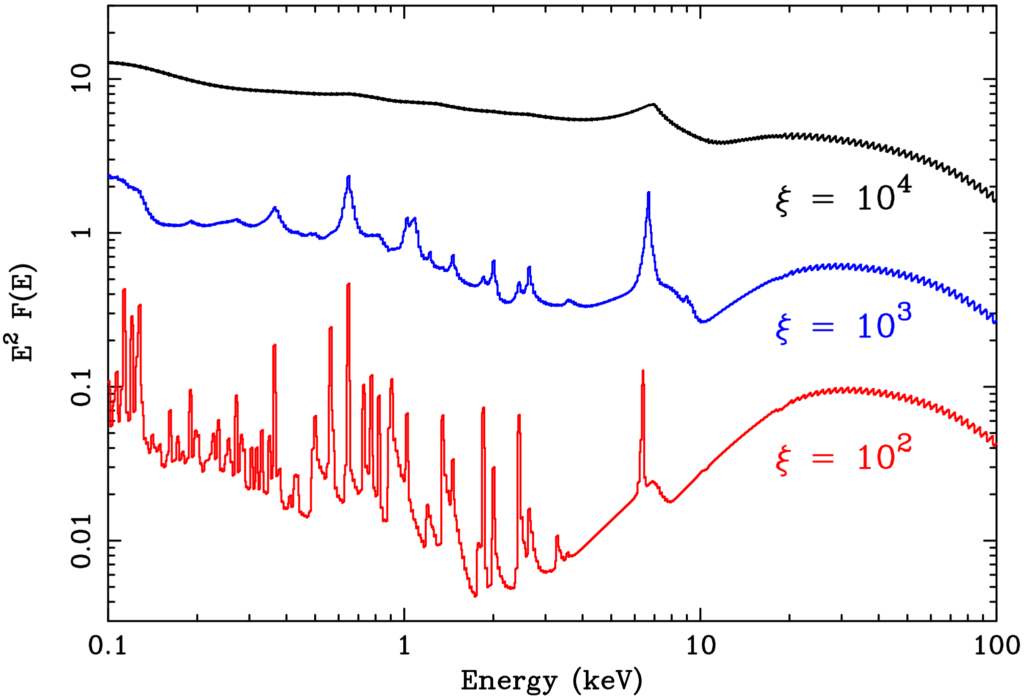

Figure 1.14: Computed X–ray reflection spectra for different ionization parameters (code by Ross & Fabian, 2005). The continuum photon index is $\Gamma = 2$ and the reflector has solar abundances.

symmetric and intrinsically narrow, hence, the analysis of its detailed shape and broadening is a powerful too to study the dynamics of the emitting region. If the reflection spectrum arises from the accretion disc, distortion by Newtonian, special and general relativistic effects takes place (see Fabian et al., 2000, and Fig. 1.13). In the Newtonian case (top panel in Fig. 1.13), a symmetric, double–peaked line profile emerges from each radius on the disc. The two peaks correspond to emission from the approaching (blue) and receding (red) sides of the disc. In the vicinity of the black hole, orbital velocities become relativistic. Therefore, the blue peak is enhanced by relativistic beaming (second panel). Also, the transverse Doppler effect shifts the profile to longer wavelengths (lower energies). Even closer to the central black hole, gravity becomes so strong that gravitational redshift becomes important. It causes the overall line profile to be shifted to lower energies (third panel). The disc inclination determines the maximum energy at which the line can still be seen. This is due to the angular dependence of relativistic beaming and of gravitational light bending effects. Integrating over all radii, a broad, skewed line profile is produced (bottom panel of Fig. 1.13). The potential of this detailed broad relativistic line profile from the accretion disc is twofold: it can be used to reveal the dynamics of the innermost accretion flow in accreting black holes, and it is a unique laboratory to test Einstein's theory of General Relativity in a way that is unaccessible from other regions of the electromagnetic spectrum.

1.5.3 The role of ionization

The radiation illuminating the disc is modelled as a power law with photon index (Γ) between 1 and 3 and with a cut–off at 300 keV. The ionization parameter (ξ) is the ratio between the isotropic total illuminating flux and the comoving hydrogen number density of the gas. The fractional ionization and local temperature of the gas are computed self–consistently by solving the equa-

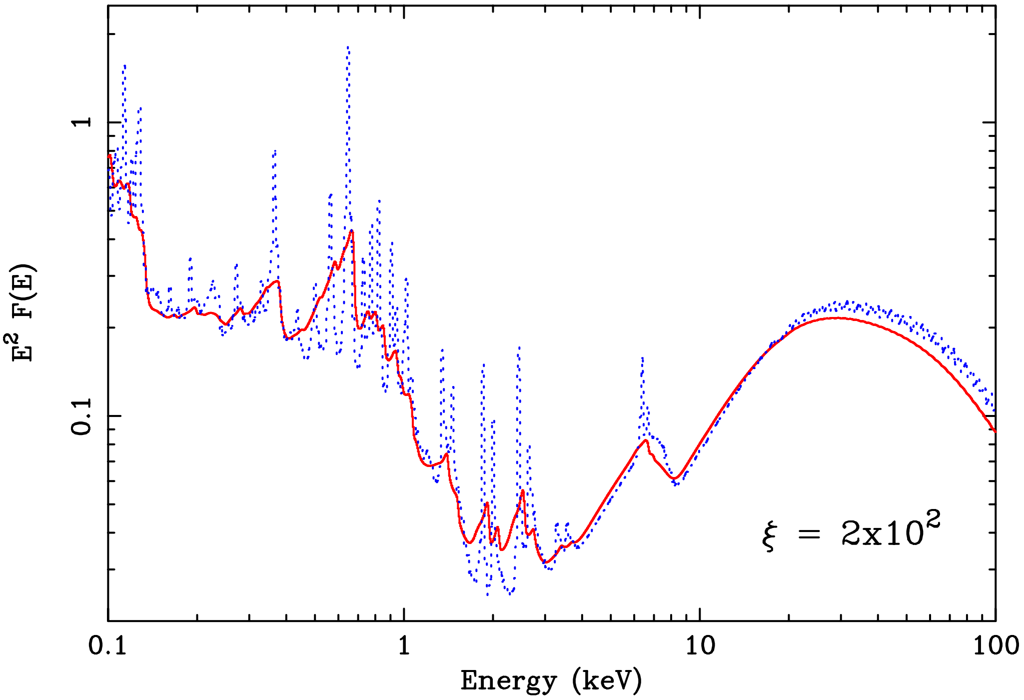

Figure 1.15: Relativistic effects on the X–ray reflection spectrum. Dotted blue line: intrinsic rest–frame spectrum, emitted from the accretion disc. Solid red line: relativistically–blurred reflection spectrum.

tions of ionization and thermal equilibrium for C, N, O, Ne, Mg, Si, S, and Fe ions. Fig. 1.14 shows X–ray reflection spectra produced by the code developed by Ross & Fabian (2005) for three different values of the ionization parameter: $\xi = 10^4\,\mathrm{erg\,cm\,s^{-1}}$, $\xi = 10^3\,\mathrm{erg\,cm\,s^{-1}}$, and $\xi = 10^2\,\mathrm{erg\,cm\,s^{-1}}$. All the other parameters are fixed. The effect of the ionization parameter is remarkable, especially on the emission lines. For $\xi = 10^4\,\mathrm{erg\,cm\,s^{-1}}$ (black) the surface layer of the disc is extremely ionized and the only the highly Compton–broadened Fe Kα line is seen, at 7 keV. For $\xi = 10^3\,\mathrm{erg\,cm\,s^{-1}}$ (blue) the strong Fe Kα line is dominated by Fe XXV. The Kα lines from other elements, lighter than iron, dominate the band between 0.3 and 3 keV. For the lowest value of the ionization parameter, $\xi = 10^2\,\mathrm{erg\,cm\,s^{-1}}$, a spectrum dominated by emission features below 3 keV arises over the largely absorbed continuum. The most important line corresponds to Fe Kα at 6.4 keV, basically free from any Compton broadening. Fig. 1.15 shows two versions of the same model with $\xi = 2\times10^2\,\mathrm{erg\,cm\,s^{-1}}$. The dotted blue line is the rest–frame X–ray reflection spectrum not affected by any relativistic effect. The solid red line shows the same model relativistically blurred, due to reflection emerging from the accretion disc. Every sharp spectral feature of the non–relativistic spectrum (blue) appear relativistically broadened by the effects detailed above (red). The importance of the iron line resides in its isolation, its strength, and its location in the relatively absorption–free region of the X–ray spectrum, making this feature clearly visible, and an exceptional tool to study the innermost regions of the accretion disc by means of the analysis of relativistic effects.

1.5.4 The role of variability

Finally, on X–ray variability, we must distinguish between flux variability and spectral variability. As we mentioned in Section 1.4.2, flux variability is driven by the variability of the intrinsic X–

ray continuum, and occurs in a range of timescales from seconds to years timescales. However, spectral variability implies a change in the spectral shape. On the one hand, the latter can occur due to spectral changes associated with intrinsic phenomena, such as the steepening of the continuum when the continuum source is brighter, or the changes in the temperature and / or optical depth of the corona. On the other hand, it can be due to external phenomena, like absorption. In this case, there can be spectral variability even if the intrinsic flux (and hence the properties of the AGN) are exactly the same. Spectral variability due to absorption variability is the major argument of the work contained within these pages, so that we will further discuss on this topic. The reader can find an extended discussion of this phenomenon in Section 2.1.

1.6 Instruments

Luckily for all of us, cosmic X–rays are screened by Earth's atmosphere. In return, the only way to study X–ray sources in the sky is placing the detectors above it. This mission can be accomplished by means of high–altitude balloons, during rockets sub–orbital flights, and by using space observatories on satellites into orbit. Instruments on satellites are the best option because their location well beyond Earth's atmosphere make accesible the complete X–ray spectrum, and because they are able to collect data for much longer time lapses than rockets. The first X–ray observatory ever put into orbit was *UHURU* in 1970 (Giacconi et al., 1971). Many X–rays dedicated space observatories came later, four of which are still operational: *Chandra* (June 1999), *XMM–Newton* (December 1999), *Swift* (November 2004), and the Nuclear Spectroscopic Telescope Array (*NuSTAR*, June 2012). Moreover, the Japanese / American satellite *Suzaku*, lauched in July 2005, has been fully operational until its recent shutdown, in September 2015.

Along this thesis I have used data from *Chandra*, *XMM–Newton*, *Swift* and *Suzaku*. In the following I very briefly elaborate on *XMM–Newton* and *Chandra* only, because I have reduced data from instruments on board those two satellites.

1.6.1 XMM–Newton

XMM–Newton ("XMM" standing for "X–ray Multi–Mirror Mission") is an European Space Agency (ESA) space observatory (Jansen et al., 2001). It was launched in December 1999 on board an Ariane 504. The observatory is equipped with three X–ray telescopes with high effective area, and an optical monitor. The main advantages of the X–ray telescopes on board *XMM–Newton* are their large collecting area and their capability to perform long and continuous exposures.

Each one of the three X–ray telescopes on board *XMM–Newton* consists of 58 Wolter I grazing–incidence mirrors, nested in a coaxial, cofocal configuration, designed in order to obtain the highest possible effective area over a wide range of energies, especifically around 7 keV.

At the focal plane of each one of the telescopes is located a X–ray charge–coupled device (CCD) camera, comprising the EPIC (Strüder et al., 2001). One of the cameras uses pn CCDs, that collect the photons of an unobstructed beam. The other two cameras are metal–oxide–semiconductor (MOS) CCD arrays (Turner et al., 2001), installed behind two of the telescopes, equipped with the gratings of the Reflection Grating Spectrometer (RGS). These gratings divert arond half of the telescope incident flux towards the RGS detectors. The third X-ray telescope has an unobstructed beam; the EPIC instrument at the focus of this telescope uses pn CCDs and is referred to as the pn camera.

EPIC detectors

Extremely sensitive imaging observations over the a field of view (FoV) of $30'$ are provided by the EPIC cameras in the $0.15 - 15$ keV energy range, with moderate spectral and angular resolutions of $E/\Delta E \sim 20 - 50$, and point spread function (PSF) of $6''$ FWHM, respectively. All EPIC CCDs operate in photon counting mode, listing event attributes such as the position at which they were registered, their arrival time, their energies, etc.

Several modes of data acquisition are allowed by the EPIC cameras. In the case of MOS the outer ring of 6 CCDs remain in standard full–frame imaging mode while the central CCD can be operated separately. The pn camera CCDs can be operated in full frame, extended full frame and large window modes, or just with one single CCD for small window, timing and burst modes.

i) Full frame and extended full frame (pn only): The full FoV is covered as all pixels of all CCCDs are read out.

ii) Partial window

  MOS: The central CCD can be operated in a different mode of science data acquisition, reading out only part of the CCD (100 × 100 pixels in small window, 300 × 300 pixels in large window).

  pn: In large window mode half the area of all 12 CCDs is read out; in small window mode only the part of CCD0 in quadrant 1 at the focal point is used.

iii) Timing mode

  MOS and pn: imaging is made only in one dimension in order to be read out at high speed.

  pn only: burst mode allows very high time resolution, but with a low duty cycle of 3%.

Reflection Grating Spectrometers

The RGS instruments (Den Herder et al., 2001) offer high resolving power (150 to 800) over a range from 5 to 35 Å (0.33 to 2.5 keV) in the first spectral order. The effective area peaks around 15 Å (0.83 keV) at around 150 cm^2.

The grating arrays consist of 181 and 182 identical gratings, respectively, mounted in a toroidal surface at grazing incidence to the beam. The diffracted X–rays are detected with a bench of CCDs operated in the frame transfer mode: the image is first accumulated in one half of the CCD, and 20 ms later transferred to the other half, doubling the read out speed.

1.6.2 Chandra

The *Chandra* X–ray Observatory, launched on July 23, 1999, is the principal mission of the National Aeronautics and Space Administration (NASA) for X–ray astronomy.

The incoming photons from the X–ray astronomical sources are focused by the mirrors into the focal plane, where two science instruments, Advanced CCD Imaging Spectrometer (ACIS) and High Resolution Camera (HRC), capture and list the information carried by every X–ray photon (position, energy, time of arrival, etc.). Two more science instruments, consisting on grating arrays which can be inserted into the path of the X–rays behind the mirrors, diffract the X–ray photons. These instruments are the Low–Energy Transmission Grating Spectrometer (LETGS) and High–Energy Transmission Grating Spectrometer (HETGS).

The Advanced CCD Imaging Spectrometer

This is one of the two instruments mounted on the focal plane, and consists on an array of ten CCDs disposed in two arrays, providing imaging with spatial resolution of up to around $1''$ and spectroscopy within the $0.2 - 10$ keV band (Garmire et al., 2003). Appart of its overwhelming resolition, its major strength resides on its ability to make X–ray imaging and spectroscopy at the same time.

The High– and Low– Energy Transmission Grating Spectrometers

These are the instruments dedicated to high resolution spectroscopy. These gratings diffract the incoming X–rays, and the spectrometers measure their energy to an accuracy of up to one part in a thousand, allowing us to distinguish individual X–ray absorption or emission lines.

The LETGS gratings have a regular spacing of $1\,\mu$m, covering an energy range of 0.08 to 2 keV (Drake, 2002). On the other hand, the HETGS gratings have a much finer period: $0.2\,\mu$m or 2000 Å for the high energy gratings, and $0.4\,\mu$m or 4000 Å for the medium energy ones (Dewey, 2003). The HETGS gratings cover an energy range of 0.4 to 10 keV.

In order to distinguish between them, the two types of gratings are oriented at slightly different angles, so that the X–ray are diffracted in an "X" pattern at the focal plane.

1.7 Aim of this Thesis

Along this section I have pivoted around the idea that unobscured AGN allow a direct view of the central engine. This very special feature is what justifies and boosts the work carried out during my thesis, which is depicted in the following pages. The study of the central engine is the most powerful to understand the physics ruling the accretion onto the SMBH, the mechanics of X–ray variability, the winds and outflows, and the relativistic effects imprinted from the innermost regions of AGN.

Large spectral variability is intended to be used with the purpose of better understand the nature and dynamics of the central regions in AGN, including those from which the X–ray emission arise. Regarding this point, relativistically distorted spectral components (such as the broad relativistic Fe K emission line) are extremely useful to accurately measure parameters like the black hole spin or the inclination angle between the axis of the system and our LOS.

Also, unobscured AGN are perfect laboratories to learn about absorption phenomena. The detailed study and characterization of the properties of the warm absorber, outflowing gas photoionized by the central source, is the other main goal of this dissertation. It is possible, through high resolution X–ray spectroscopy, to dig deeply into the nature, origin and location of this absorbing warm absorber, as well as in its relationship with the inner (the BLR) and outer (the torus) regions of AGN, all of them not well known up to this date. These outflows enclose crucial information about how the AGN and the host galaxy interact, therefore its study provide valuable knowledge on SMBH/ galaxy co–evolution.

2

The X–ray source size in SWIFT J2127.4+5654

This chapter is adapted from what was published as an article entitled "The size of the X–ray emitting region in SWIFT J2127.4+5654 via a broad line region cloud X–ray eclipse" (Sanfrutos et al., 2013, MNRAS, 436, 1588).

We present results obtained from the time–resolved X–ray spectral analysis of the NLS1 galaxy SWIFT J2127.4+5654 during a ~ 130 ks *XMM–Newton* observation. We reveal large spectral variations, especially during the first ~ 90 ks of the *XMM–Newton* exposure. The spectral variability can be attributed to a partial eclipse of the X–ray source by an intervening low–ionization / cold absorbing structure (cloud) with column density $N_{\rm H} = 2.0^{+0.2}_{-0.3} \times 10^{22}$ cm^{-2} which gradually covers and then uncovers the X–ray emitting region with covering fraction ranging from zero to ~ 43 per cent. Our analysis enables us to constrain the size, number density, and location of the absorbing cloud with good accuracy. We infer a cloud size (diameter) of $D_{\rm c} \leq 1.5 \times 10^{13}$ cm, corresponding to a density of $n_{\rm c} \geq 1.5 \times 10^{9}$ cm^{-3} at a distance of $R_{\rm c} \geq 4.3 \times 10^{16}$ cm from the central black hole. All of the inferred quantities concur to identify the absorbing structure with one single cloud associated with the BLR of SWIFT J2127.4+5654. We are also able to constrain the X–ray emitting region size (diameter) to be $D_{\rm s} \leq 2.3 \times 10^{13}$ cm which, assuming the black hole mass estimated from single–epoch optical spectroscopy ($1.5 \times 10^{7}\, M_{\odot}$), translates into $D_{\rm s} \leq 10.5\, r_{\rm g}$ with larger sizes (in $r_{\rm g}$) being associated with smaller black hole masses, and viceversa. We also confirm the presence of a relativistically distorted reflection component off the inner accretion disc giving rise to a broad relativistic Fe K emission line and small soft excess (small because of the high Galactic column density), supporting the measurement of an intermediate black hole spin in SWIFT J2127.4+5654 that was obtained from a previous *Suzaku* observation.

2.1 Introduction

X–ray flux and spectral variability is a rather common property of AGN. Spectral variability on relatively long time–scales (months to years) is often associated with absorption variability (e.g. Warwick et al., 1988; Risaliti et al., 2002; Marinucci et al., 2013). In recent years, several examples of short time–scale (hours to days) absorption variability have been reported, e.g. NGC 4388 (Elvis et al., 2004), NGC 4151 (Puccetti et al., 2007), NGC 1365 (Risaliti et al., 2005, 2007, 2009b; Maiolino et al., 2010), NGC 7582 (Bianchi et al., 2009), Mrk 766 (Risaliti et al., 2011a). The detailed analysis of the short time–scale absorption variability in these sources strongly suggests the presence of absorbing structures (clouds) crossing the LOS to a rather compact X–ray source. The data are generally consistent with the presence of an ensemble of compact, cold clouds with typical column density of $10^{22} - 10^{24}\,\mathrm{cm}^{-2}$, density of $10^{9} - 10^{11}\,\mathrm{cm}^{-3}$, velocity of few times $10^{3}\,\mathrm{km\,s}^{-1}$, and distance of $10^{2} - 10^{4}\,r_{\mathrm{g}}$ from the centre. These properties are remarkably similar to those of the clouds responsible for the emission of the broad optical and UV emission lines in AGN. Hence, X–ray absorption variability studies suggest to identify the X–ray compact absorbers responsible for the shortest time–scale absorption variability events with BLR clouds, while variability on longer time–scales (months to years) is likely associated with more extended structures, possibly associated with a clumpy torus (Nenkova et al., 2008b).

Previous results on occultation events have been presented previously, e.g. by Risaliti et al. (2007), who first presented an occultation event of the central X–ray source in the Seyfert 1.8 galaxy NGC 1365, with extreme spectral variability from a Compton–thin state to one reflection–dominated, and back to Compton–thin again in a timescale as short as only four days (see Fig. 2.1). They interpret this event as a Compton–thick cloud crossing our LOS to the source, and estimate an upper limit to the X–ray source size of 10^{14} cm and a cloud–source distance smaller than 10^{16} cm. Their results dealt with two key points about the geometry of this kind of systems: on the one hand, they showed that the distance between the X–ray source and the region where the Compton–thick circumnuclear gas is located is consistent with the scale of the BLR. On the other hand, they proved the theoretical predictions on the extremely compact size of the central X–ray source.

Maiolino et al. (2010) use a 300 ks *Suzaku* observation of NGC 1365 to discern the structure of the clouds of the BLR. From their analysis of the variations of the column density and covering factor during the occultation of the X–ray source, they infer that these clouds are comet–like, comprising a dense head (n$\sim 10^{11}\,\mathrm{cm}^{-3}$) and an expanding tail, longer than a few times 10^{13} cm. The peculiar shape of the BLR clouds in the model proposed by Maiolino et al. (2010) may be due to shocks and hydrodynamical instabilities as a result of the high velocity reached by the clouds through the intracloud medium.

Risaliti et al. (2011a) analyzed a 9 day *XMM–Newton* monitoring of the NLS1 galaxy Mrk 766. They observed that strong spectral shape changes could be due to BLR clouds moving across our LOS to the X–ray source. They estimated tight constraints to the geometrical structure, location and physical properties of the absorbing clouds, from the temporal and spectral analisys of the three occultation events found in this monitoring. Specifically, they deduce that these clouds have column densities greater than a few $10^{23}\,\mathrm{cm}^{-2}$ and transversal velocities of several thousands $\mathrm{km\,s}^{-1}$. Also, they detected two iron absorption lines associated with each one of the eclipses, which suggests the existence of highly ionized gas surrounding the clouds, at an outflow velocity from 3000 to 15000 $\mathrm{km\,s}^{-1}$. All the phases of one of the eclises detected in the *XMM–Newton* monitoring of Mrk 766 by Risaliti et al. (2011a) is shown in Fig. 2.2.

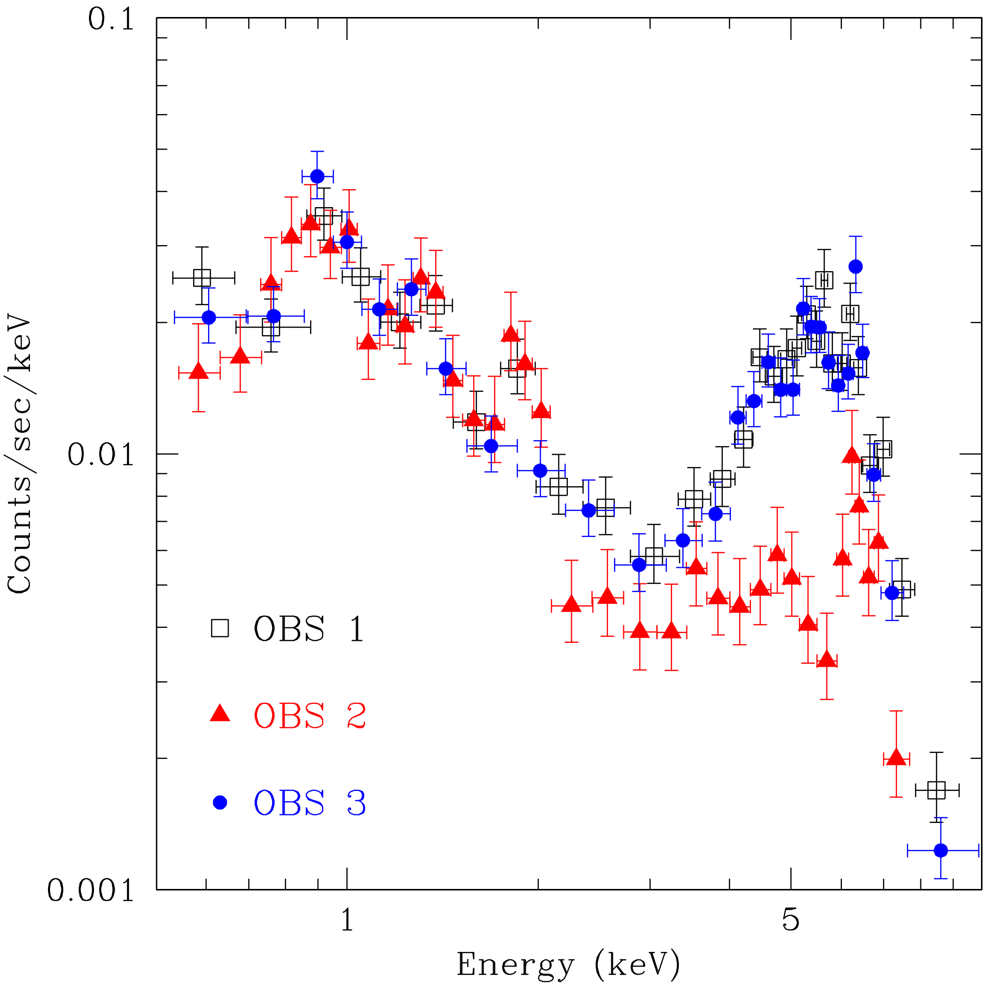

Figure 2.1: Spectra from three *Chandra* observations of NGC 1365. The time lapse between one observation and the next is two days. Observations 1 and 3 are typical of transmission–dominated states. Observation 2, ~ 10 times fainter, shows the flat continuum and prominent iron emission line proper of a reflection–dominated state. Credit: Risaliti et al. (2007).

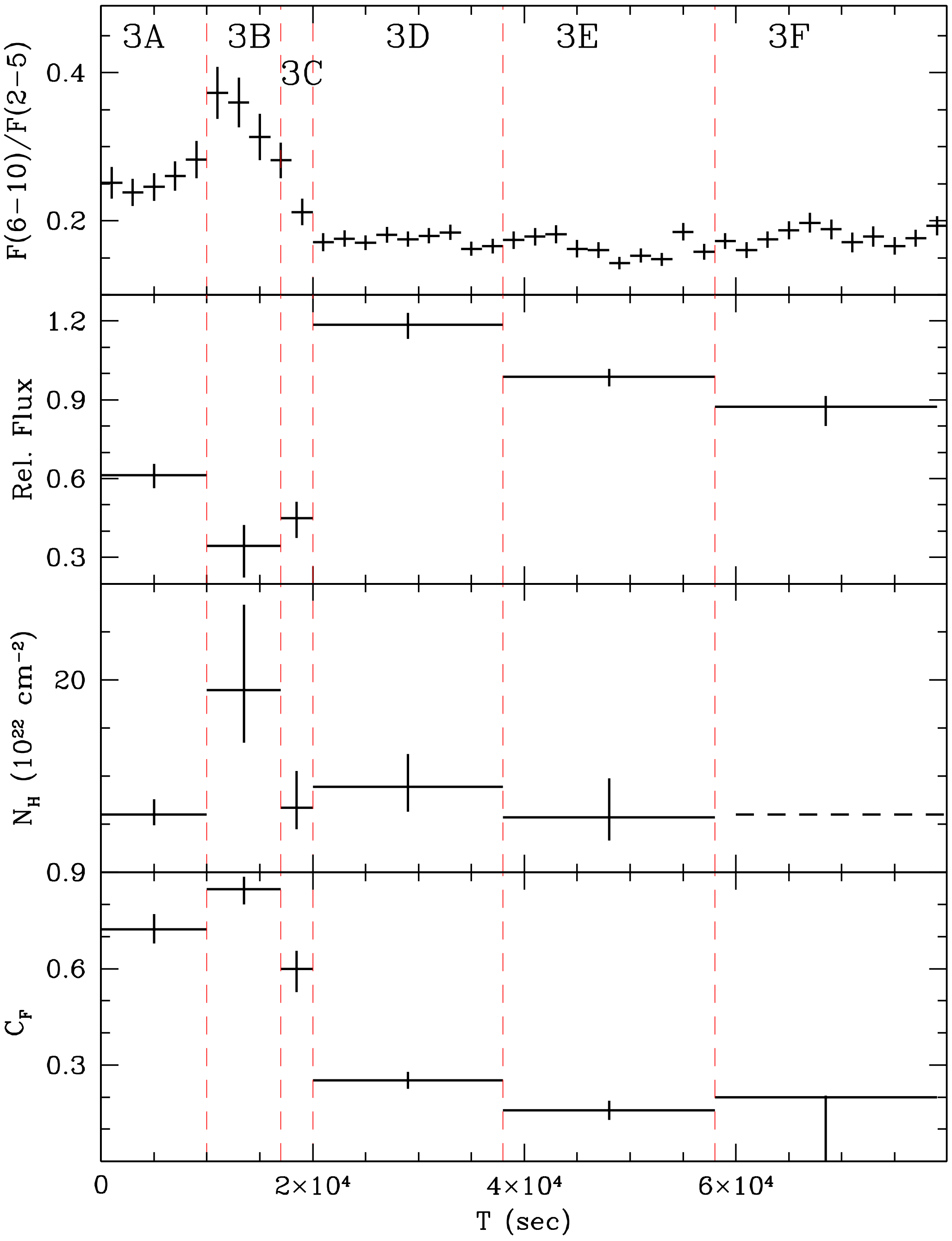

Figure 2.2: Upper panel: hardness ratio lightcurve for the second orbit of the *XMM–Newton* observation of Mrk 766. Second panel: intrinsic flux lightcurve in the 2 – 10 keV band, normalized to the unabsorbed flux. Third panel: column density lightcurve. Bottom panel: CF lightcurve. Credit: Risaliti et al. (2011a).

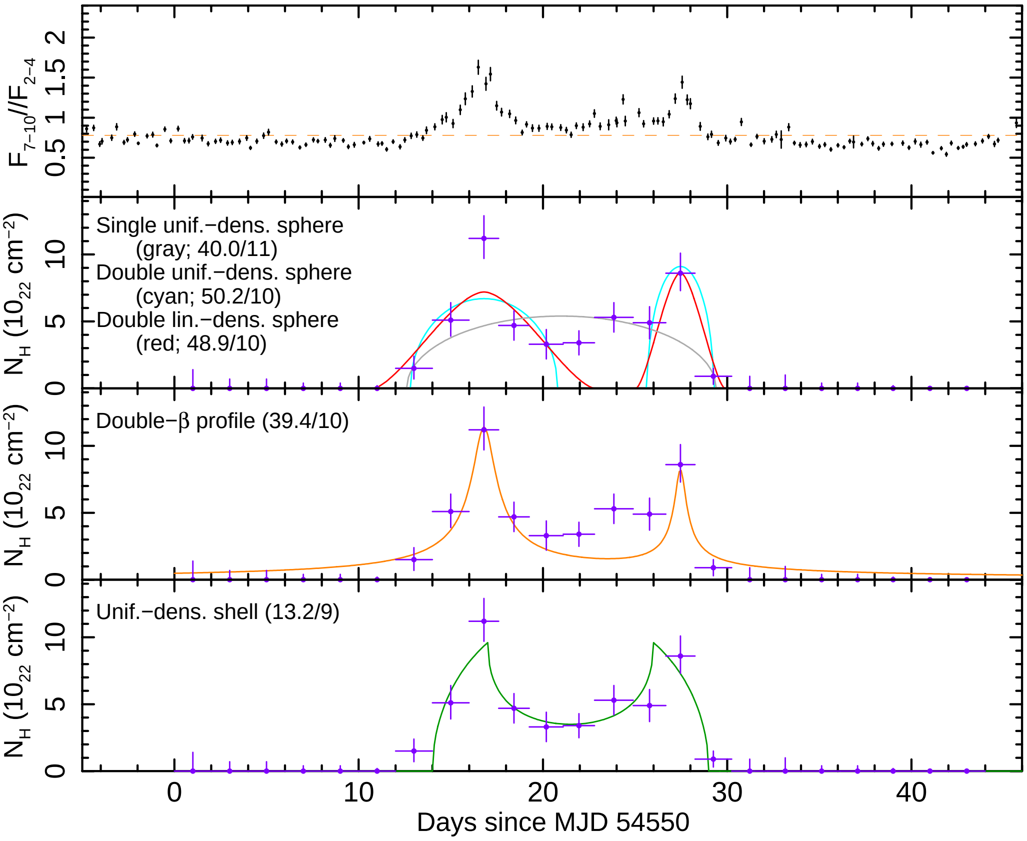

Figure 2.3: From top to bottom: the first panel depicts the hardness ratio (F_{7-10}/F_{2-4}) lightcurve of NGC 3783, and the others the $N_H(t)$ lightcurves, with their best–fitting models (solid lines). Second panel: a uniform–density sphere (gray), two uniform–density spheres (cyan), two linear–density spheres (red). Third panel: a double β–profile (orange). Fourth panel: a uniform–density shell (green). Values of χ^2/dof are in parentheses. Figure credit: Markowitz et al. (2014).

Markowitz et al. (2014) analysed multi–timescale X–ray absorption variability, looking for absorption events in a large sample of Seyfert galaxies in the *RXTE* archive. They detected 12 eclipses in eight objects, with durations of hours to months, caused by clouds that are consistent with being located at the outer BLR or the inner regions of the torus in seven of the objects. One of these eclipses, in the Seyfert 1 galaxy NGC 3783, shows a hardness ratio lightcurve with a doubly spiked profile, suggesting two eclipses separated by only 11 days, as shown in the upper panel of Fig. 2.3. Markowitz et al. (2014) model the time–dependent column density profile of the absorber in NGC 3783 in a number of unsuccessful ways: one sphere of uniform density (gray line in the second panel of Fig. 2.3, underestimating the spikes), two spheres of uniform density / linearly variable density (cyan / red lines, not correctly fitting the $N_H(t)$ profile), and a phenomenological β–profile of each one of the spikes (orange in the third panel, underestimates the middle region of the profile). Also, they modelled a uniform–density shell (green in the lower panel, successfully fitting the spikes and the region between them), but recognize that this model is merely phenomenological, and they speculate that the profile could actually be produced by two connected clumps, namely a cloud that is being tidally sheared.

Here we report results from a ~ 130 ks observation of the NLS1 galaxy SWIFT J2127.4+5654 with *XMM–Newton*. This object, also kwon as IGR J21277+5656, is a low Galactic latitude hard X–ray source which has been first detected at hard X–rays with *Swift* / BAT (Tueller et al., 2005). Later, the source was identified as a NLS1 galaxy at redshift 0.0147 based on the observed Hα FWHM of ~ 1180 km s^{-1} (Halpern, 2006). Subsequent work by Malizia et al. (2008) supported the NLS1 classification by obtaining, despite a slightly larger FWHM of ~ 2000 km s^{-1}, a relatively low O III/Hβ ratio of 0.72 ± 0.05 and significantly enhanced Fe II emission (Fe II/Hβ = 1.3 ± 0.2). SWIFT J2127.4+5654 was then observed with *Suzaku* for a total net exposure of 92 ks and results have been presented and discussed by Miniutti et al. (2009). The major result of the *Suzaku* observation is the detection of a relativistically broadened Fe Kα emission line which strongly suggests that SWIFT J2127.4+5654 is powered by accretion onto a rotating Kerr black hole, with an intermediate spin value of $a = 0.6 \pm 0.2$. This result has been confirmed (using the same data set) also by Patrick et al. (2011) who report $a = 0.70^{+0.10}_{-0.14}$, although a different interpretation of the Fe Kα shape, based on reprocessing and scattering in a Compton–thick disc–wind rather than the disc itself, has also been proposed (Tatum et al., 2012).

2.2 X–ray Observations

XMM–Newton observed SWIFT J2127.4+5654 on 2010 November 29 for a full revolution (during ~ 130 ks). The observation (0655450101) was performed using the ‘SMALL WINDOW’ mode for all EPIC cameras, with the optical ‘THIN’ filter applied. The data were reduced as standard using the dedicated SAS v11.0 software. Observation–dependent EPIC and RGS response files were generated using the RMFGEN and ARFGEN tasks. EPIC source products were extracted from circular regions of 40″ centred on the source, and the corresponding background was estimated by using source–free nearby regions. In the time–resolved analysis we present in this work, each time–interval is associated with its own background spectrum contributing less than 2 per cent in any of the considered time–intervals. After filtering for high background periods which occur at the beginning and end of the exposure, the net exposure is ~ 84 ks in the EPIC–pn spectrum and ~ 109 ks and ~ 110 ks in the MOS 1 and MOS 2 spectra respectively. All the EPIC spectra are extracted with common good–time–intervals and they are all grouped in order to guarantee that each background–subtracted bin has at least 25 counts.

The MOS and pn spectra are consistent with each other above ~ 1.6 keV. However, as shown in the upper panel of Fig. 2.4, the spectra are not consistent with each other at softer energies. The largest discrepancies are between the pn and the two MOS detectors below 1.6 keV and between the two MOS cameras below 0.9 keV. In the lower panel, we plot the RGS 2 data–to–model ratio instead of the EPIC–pn. The RGS spectrum confirms the reliability of the MOS data above 0.9 keV and suggests to ignore the pn softest data. Moreover, the spectral shape in the previous *Suzaku* observation (Miniutti et al., 2009) agrees much better with the MOS / RGS spectra than with the pn one. This comparative analysis suggests to make a conservative choice of the energy ranges to be used for spectral analysis. In our work we consider the MOS data in the 0.9 − 10 kev band, and the pn data in the 1.6 − 10 keV band. Our choice of reliable energy bands to be used for the spectral analysis is in fact very conservative, and we have checked a–posteriori that almost exactly the same results on the most relevant best–fitting parameters are obtained considering all data in the 0.5 − 10 keV band, although with worse statistical results due to the discrepancies between the pn and the MOS spectra. In any case, it should also be mentioned that, since the low Galactic latitude of SWIFT J2127.4+5654 corresponds to a relatively high Galactic column density (7.65×10^{21} cm^{-2}, Kalberla et al., 2005), soft X–ray data below 1 keV only provide ~ 7 per cent of the total collected counts, with very little impact on the overall analysis. When needed to convert fluxes into luminosities, we adopt a Λ cold dark matter (ΛCDM) cosmology with H_0 =

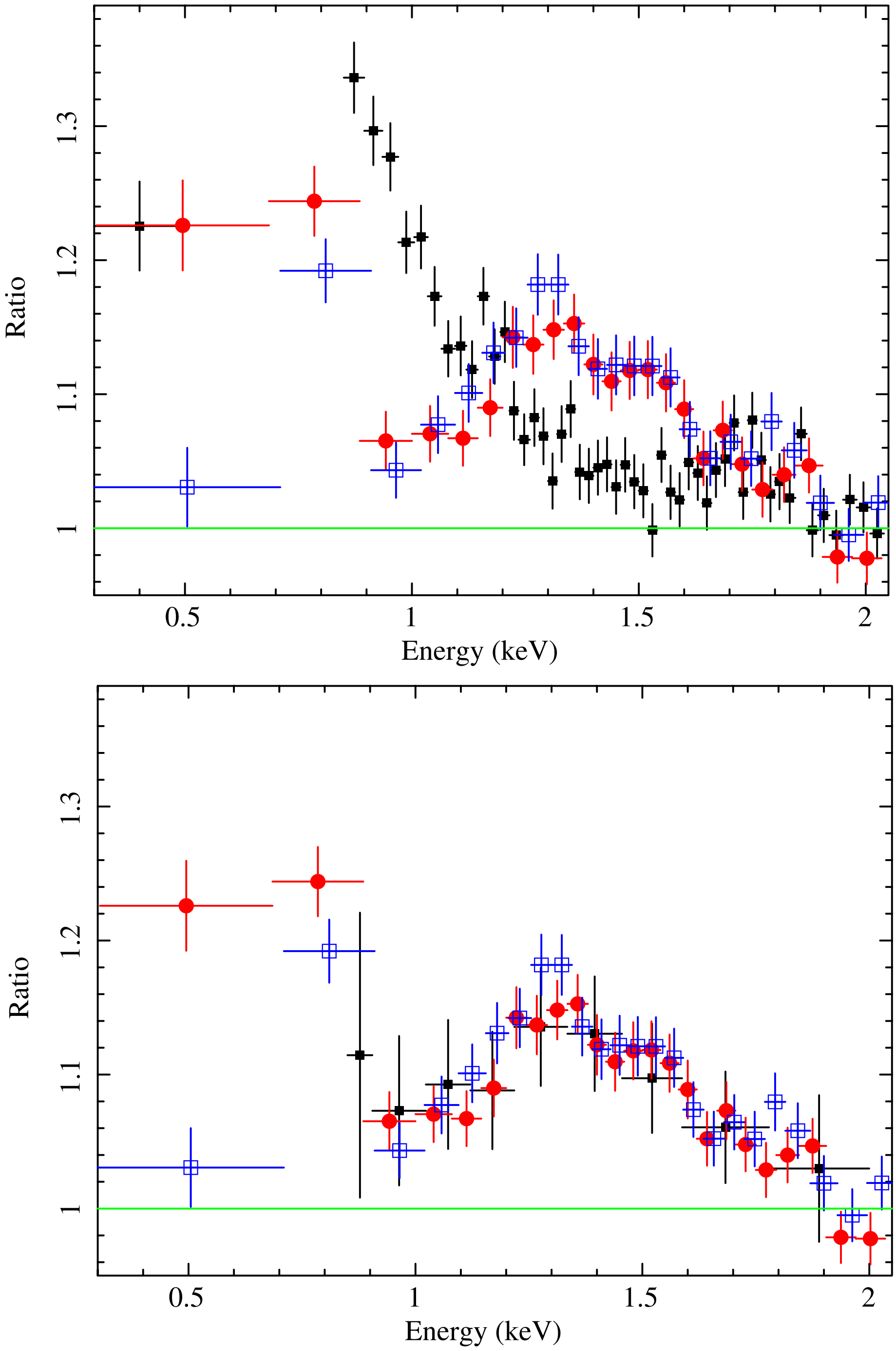

Figure 2.4: In the upper panel, we show a comparison between the EPIC–pn (filled black squares), MOS 1 (filled red circles), and MOS 2 (empty blue squares) spectra in the soft X–ray band. All spectra are fitted in the 2 – 4 keV and 7.5 – 10 keV band (i.e. ignoring the Fe K band) with a common spectral model comprising Galactic absorption and a power law. See the upper panel of Fig. 2.5 for a comparison between the pn and MOS data at higher energies using the same spectral model used here. In the lower panel, we show the same MOS data as above, but we plot the (heavily rebinned) RGS 2 data–to–model ratio instead of the EPIC–pn (we omit the RGS 1 data here because of the gap around the crucial 0.9 – 1.1 keV band affecting the RGS 1 detector). The RGS data below 0.8 – 0.9 keV are too noisy to be used for this comparison. See text in Section 2.2 for details.

$70\,\mathrm{km\,s^{-1}\,Mpc^{-1}}$, $\Omega_\Lambda = 0.73$, and $\Omega_\mathrm{M} = 0.27$.

2.3 The time–averaged spectrum

We start our analysis by considering the time–averaged X–ray spectrum of SWIFT J2127.4+5654 in the 0.9 – 10 keV band using all EPIC detectors. In the upper two panels of Fig. 2.5 we show the data–to–model ratio resulting from a simple absorbed power law model fitted in the 2 – 4 keV and 7.5 – 10 keV, i.e. ignoring the Fe K band (as mentioned, we use the MOS data in the 0.9 – 10 keV band, and the pn data in the 1.6 – 10 keV band). Absorption is here modelled with only the Galactic column density of $7.65 \times 10^{21}\,\mathrm{cm^{-2}}$ (Kalberla et al., 2005). The continuum is modelled with a power law of 1.81 ± 0.02. The model leaves significant residuals around the Fe K band, where a broad feature reminiscent of a relativistic broad Fe line is seen, and below ~ 2 keV where a soft X–ray excess is detected.

We then add a relativistic Fe line using the KERRCONV relativistic convolution model from Brenneman & Reynolds (2006) applied to a 6.4 keV Gaussian emission line with zero intrinsic width. The statistical description of the data is relatively good with $\chi^2 = 4080$ for 3838 degrees of freedom (dof). Adding an intrinsic neutral absorber at the redshift of the source improves the statistic to $\chi^2 = 4030$ for 3837 dof. The nature and properties of the absorber will be discussed in detail in subsequent Sections. Here we only mention that we obtain a column density of $\sim 2 \times 10^{21}\,\mathrm{cm^{-2}}$ in addition to the Galactic one. The resulting data–to–model ratio is shown in the third panel of Fig. 2.5. Some residuals are still present in the soft and hard bands.

As the detected broad line should be associated with a disc reflection continuum, we replace the relativistic line model with a full disc reflection model from partially ionized gas (Ross & Fabian, 2005) to which we apply the same relativistic convolution model as before. The model describes the data better with 3976 for 3836 dof, and accounts for both the soft and hard residuals seen in the middle panel of Fig. 2.5.

Further residuals are however left around the Fe K band, suggesting the presence of a series of narrow emission lines. We find that four narrow lines are indeed required by the data. Their energy is consistent with 6.4 keV (Fe Kα), 6.7 keV (Fe XXV Lyα), 6.97 keV (Fe XXVI Lyα), and 8.25 keV (Fe XXVI Lyβ) so that we fix their energy at the theoretical values. The statistical improvement for the inclusion of these additional narrow lines is $\Delta\chi^2_{6.4} = -22$, $\Delta\chi^2_{6.7} = -11$, $\Delta\chi^2_{6.97} = -10$, and $\Delta\chi^2_{8.25} = -7$, where each line contributes with one additional degree of freedom only (its normalization). Only the narrow Fe Kα emission line was detected during the previous *Suzaku* observation. However, the 2 – 10 keV flux was a factor of ~ 2 higher than during the *XMM–Newton* observation, which can easily explain the non–detection of the ionized Fe lines as, for constant–intensity lines, their EW drops by a similar factor and becomes consistent with zero within the uncertainties. This likely signals that the ionized lines are associated with emission from extended photo–ionized gas, so that their flux remains constant and the lines can only be detected when the X–ray continuum flux is relatively low, as during the *XMM–Newton* observation. The same applies to the narrow Fe Kα line at 6.4 keV, as its EW during the *Suzaku* observation (13 ± 9 eV) is broadly consistent with being half of that measured here (~ 50 ± 17 eV), which is what is expected for a line with a constant intensity and a continuum variation by a factor of ~ 2. We point out that if the width of the Fe Kα line is allowed to vary during the fit, we have $\sigma \leq 0.1$ keV, corresponding to a FWHM $\leq 1.1 \times 10^4\,\mathrm{km\,s^{-1}}$ (consistent with any production site, from the innermost BLR outwards). With the addition of these narrow emission lines, the

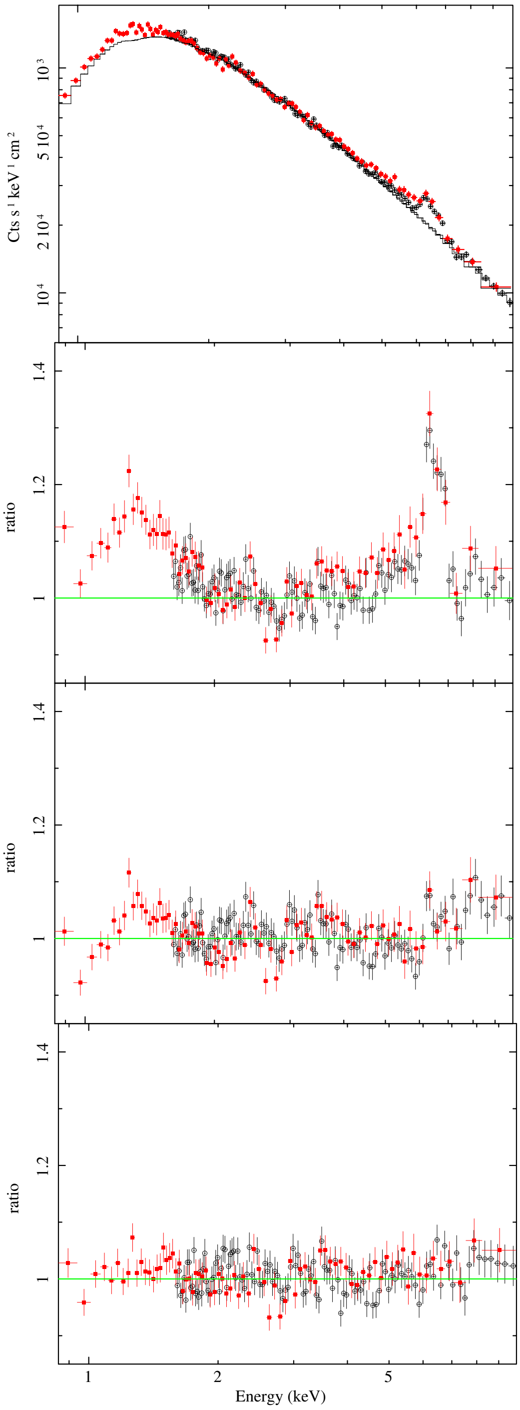

Figure 2.5: In the upper panel, we show the EPIC–pn (empty circles) and MOS 1 data (filled red squares) divided by the detector effective area to show the real spectral shape, together with the best–fitting power law model fitted in the 2 − 4 keV and 7.5 − 10 keV data. Although the MOS 2 data were also used in the spectral analysis in the 0.9 − 10 keV band, they are omitted here for visual clairty. In the second panel, we show the resulting data–to–model ratio. In the third panel, we show the data–to–model ratio resulting from including a relativistacally blurred Fe emission line. In the lower panel we show the final best–fitting model comprising a relativistically blurred reflection model plus a series of narrow emission lines as detailed in the text in Section 2.3.

Table 2.1: Best–fitting parameters from the time–averaged 0.9 – 10 keV spectral analysis of SWIFT J2127.4+5654. The column density of the intrinsic absorber at the redshift of the source is in units of 10^{22} cm^{-2}. The reflector ionization state is given in units of erg cm s^{-1}. The 2 – 10 keV flux is in units of 10^{-11} erg cm^{-2} s^{-1} and is as observed, while the 2 – 10 keV luminosity is unabsorbed and expressed in 10^{42} erg s^{-1}. The EWs are expressed in units of eV and they refer to the narrow emission lines at 6.4 keV (Fe Kα), 6.7 keV (Fe xxv Lyα), 6.97 keV (Fe xxvi Lyα), and 8.25 keV (Fe xxvi Lyβ). See text in Section 2.3 for details.

Γ	2.00 ± 0.04
$N_{\rm H}$	0.2 ± 0.1
q	4.9 ± 0.9
a	0.5 ± 0.3
i	44° ± 8°
$\xi_{\rm ref}$	10 ± 6
$EW_{6.4}$	50 ± 17
$EW_{6.7}$	23 ± 11
$EW_{6.97}$	25 ± 10
$EW_{8.25}$	18 ± 14
F_{2-10}	1.90 ± 0.04
L_{2-10}	9.6 ± 0.2
χ^2/dof	3926/3832

final best–fitting model for the 0.9 – 10 keV spectrum produces a statistical result of 3926 for 3832 dof. The best–fitting data–to–model ratio is shown in the lower panel of Fig. 2.5. The most important best–fitting parameters are reported in Table 2.1. All relativistic parameters (emissivity index, black hole spin, disc inclination) are consistent with the results of Miniutti et al. (2009) who measured $q \sim 5.3$, $a \sim 0.6$ and $i \sim 46°$ from the previous *Suzaku* observation. The good agreement between the *XMM–Newton* and *Suzaku* data provides independent support to the interpretation of the spectral shape in terms of relativistically distorted disc reflection, as originally proposed by Miniutti et al. (2009).

2.4 Spectral variability

As already shown in previous work (e.g. Miniutti et al., 2009), SWIFT J2127.4+5654 is highly variable in X–rays, an almost ubiquitous property of NLS1 galaxies. X–ray flux variability is also present in the *XMM–Newton* observation. In Fig. 2.6, we show the EPIC–pn light curve in a soft (S: 1 – 2 keV) and a hard (H: 2 – 10 keV) band. We extend the EPIC–pn energy range down to 1 keV although we only use the pn data above 1.6 keV in our spectral analysis, as light curves and, even more so, hardness ratios are reasonably calibration–independent. The shape of the pn light curves shown in Fig. 2.6 and Fig. 2.7 has been checked against the MOS data which confirm that the EPIC–pn light curves are reliable. The source is variable on all probed time–scales and exhibits variability up to a factor of ~ 4 during the *XMM–Newton* exposure. Significant bin–to–bin variability is present down to the chosen bin–size of 500 s, with more than one third of any two consecutive bins being inconsistent with each other. We then consider the H / S ratio light curve, to investigate whether spectral variability is also present during the observation. The H / S light curve is shown in Fig. 2.7 with the same bin–size as in Fig. 2.6. Clear spectral variability is present in the

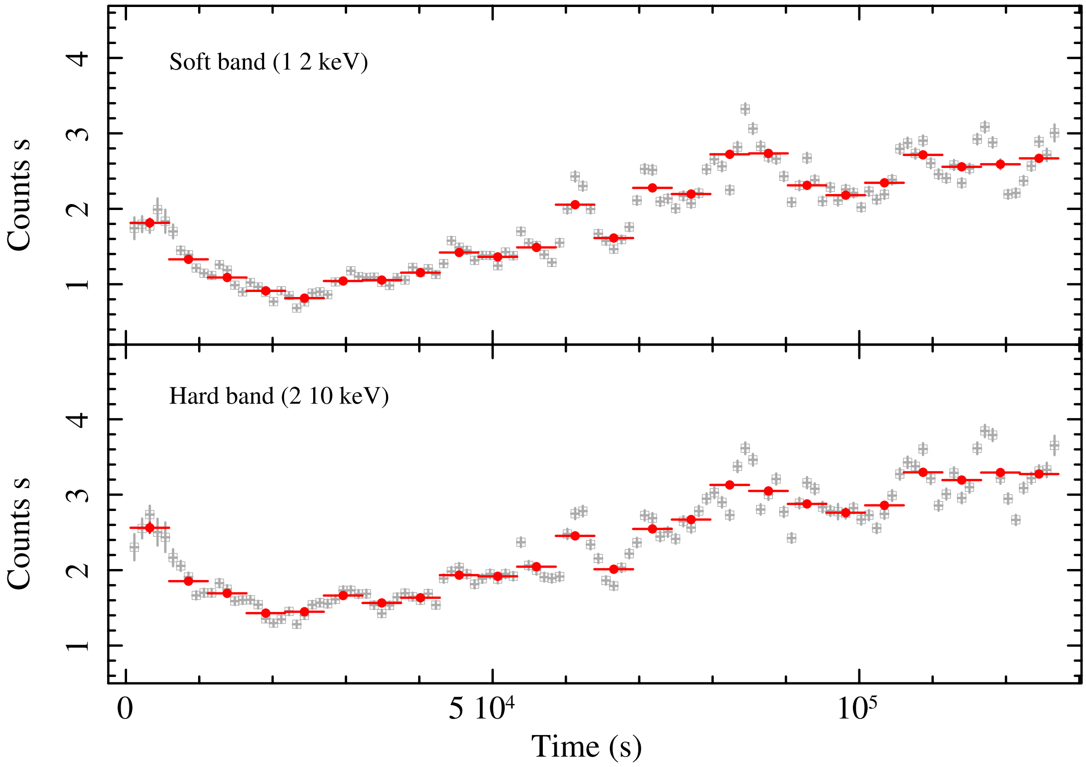

Figure 2.6: The soft (S: 1 – 2 keV, upper) and hard (H: 2 – 10 keV, lower) X–ray light curves of SWIFT J2127.4+5654 from the pn detector are shown in bins of 500 s (empty grey squares) and 5271.8 s (filled red circles). The latter bin–size is chosen to divide the total exposure in 24 uniform time–intervals which will be used to perform a time–resolved spectral analysis of the data. See Section 2.4.

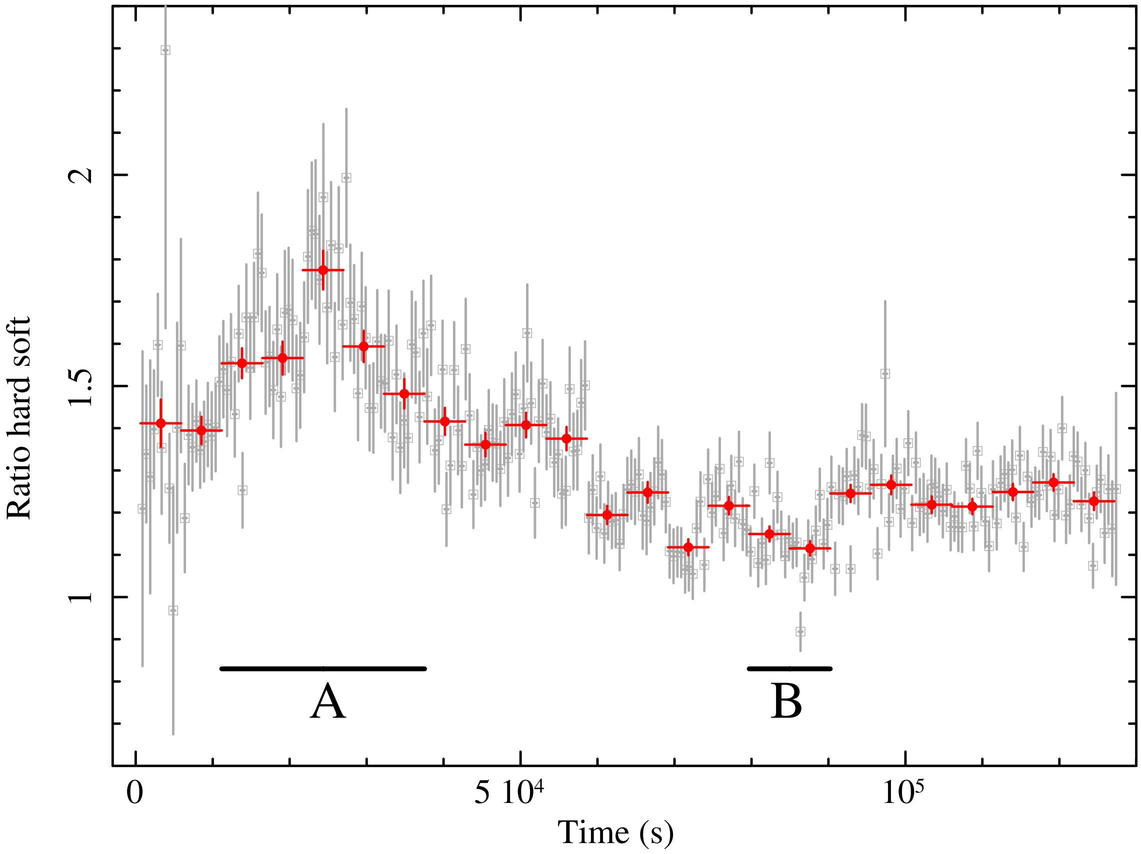

Figure 2.7: The H / S ratio light curve of SWIFT J2127.4+5654 from the pn detector is shown with the same bin–size as in Fig. 2.6. SWIFT J2127.4+5654 exhibits highly significant spectral variability during the first ~ 90 ks, while H / S remains approximately constant during the subsequent ~ 35 ks. We also highlight the two intervals of highest (A) and lowest (B) H / S that are used in the spectral variability analysis (see Section 2.4 for details).

first ~ 90 ks of the exposure, while H / S remains approximately stable in the subsequent ~ 35 ks.

2.4.1 Time–resolved analysis and spectral variability

In order to understand the origin of the spectral variability, we first extract X–ray spectra from the two time–intervals, denoted as A and B in Fig. 2.7, which correspond to the highest and lowest H / S ($1.59^{+0.24}_{-0.15}$ and 1.13 ± 0.04 respectively). The different duration of intervals A and B is justified by the different flux levels, and by the requirement that the two spectra share a similar spectral quality (i.e that the spectra have similar number of counts). Interval A is ~ 26 ks long and corresponds to a 0.9–10 keV flux of ~ 1.46×10^{-11} erg cm^{-2} s^{-1}, while interval B is ~ 11 ks long with a flux of ~ 2.83×10^{-11} erg cm^{-2} s^{-1} in the same band. Visual inspection of spectra A and B shows that the two spectra only differ spectrally below ~ $3 - 4$ keV where spectrum A has a deficit of soft photons, possibly the signature of extra–absorption with respect to the lower H / S spectrum B.

The spectra from intervals A and B are fitted jointly with the best–fitting model inferred from the time–avergaed spectral analysis. We fix the relativistic parameters to their time–averaged best–fitting values, as the lower quality of the time–resolved spectra does not allow us to better constrain them. We also fix the normalization of all the narrow emission lines to their time–averaged best–fitting values as these components are not expected to vary on short time–scales. We start our analysis by considering only the data above 3.5 keV. We initially allow for possible variation in the continuum photon index Γ. However, as Γ turns out to be consistent with being constant, we force it to be the same in the A and B spectra. We reach an excellent description of the hard X–ray spectra of intervals A and B at energies above 3.5 keV with $\chi^2 = 1190$ for 1196 dof. However, the extrapolation to soft energies reveals a large spectral difference between the two intervals, as shown in the upper panel of Fig. 2.8. The spectrum from interval A appear to be significantly more absorbed than that from interval B, as already suggested by the H / S difference between the two time–intervals in Fig. 2.7.

We then add a layer of absorbing gas to our model. We use a partial covering model for neutral gas (the ZPCFABS model). In principle, both the column density and the covering fraction may be variable. However, due to the relatively low quality of the data, the two parameters cannot be constrained independently. In order to explain physically the short time–scale spectral variability, we assume that the absorber column density is the same in both spectrum A and B, while its covering fraction is allowed to vary independently. The model provides an excellent description of the data ($\chi^2 = 3179$ for 3135 dof). In the lower panel of Fig. 2.8 we show the resulting best–fitting data–to–model ratio for the spectra A and B. The observed variability between intervals A and B can be entirely explained by a layer of neutral absorbing gas with column density $N_{\rm H} = 2.0^{+0.6}_{-0.5} \times 10^{22}$ cm^{-2} covering ~ 35 per cent of the X–ray source during interval A and ≤ 4 per cent during interval B. If the photon indices of spectra A and B are now allowed to vary independently, no further statistical improvement is obtained, and the two spectral slopes are consistent with each other.

2.4.2 A partial eclipse

We then consider the spectral variability of SWIFT J2127.4+5654 on shorter time–scales within the framework of the partial covering model. We extract 24 spectra (for each of the EPIC cameras) from intervals of equal duration (i.e. from the 5271.8 s long intervals shown in Fig. 2.7), and we

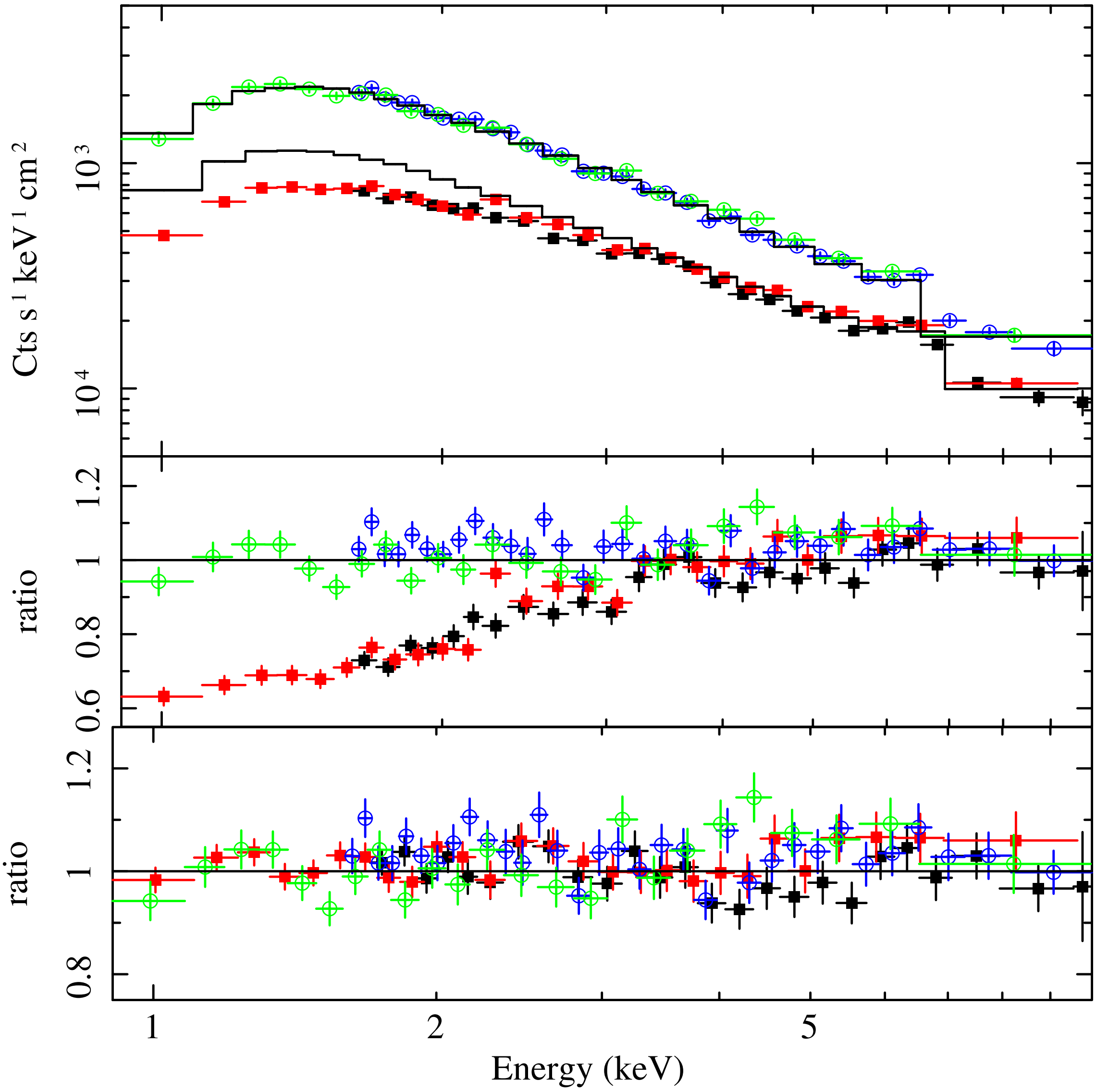

Figure 2.8: In the upper panel we show the data divided by the appropriate detector effective area, best–fitting models, and data–to–model ratio for spectra A (lower two spectra, filled squares, black and red for the pn and MOS 1 cameras respectively) and B (upper two spectra, empty circles, blue and green for the pn and MOS 1 cameras respectively). The MOS 2 data are also used in the analysis in the 0.9 – 10 keV band (as for the MOS 1 data) but are not shown here for visual clarity. The spectral model is fitted only above 3.5 keV and then extrapolated to soft energies to show the significant spectral difference between the two time–intervals. In the lower panel, we show the final best–fitting data–to–model ratio where the spectra A residuals are accounted for by an additional neutral absorber only partially covering the X–ray continuum (see text in Section 2.4.1 for details).

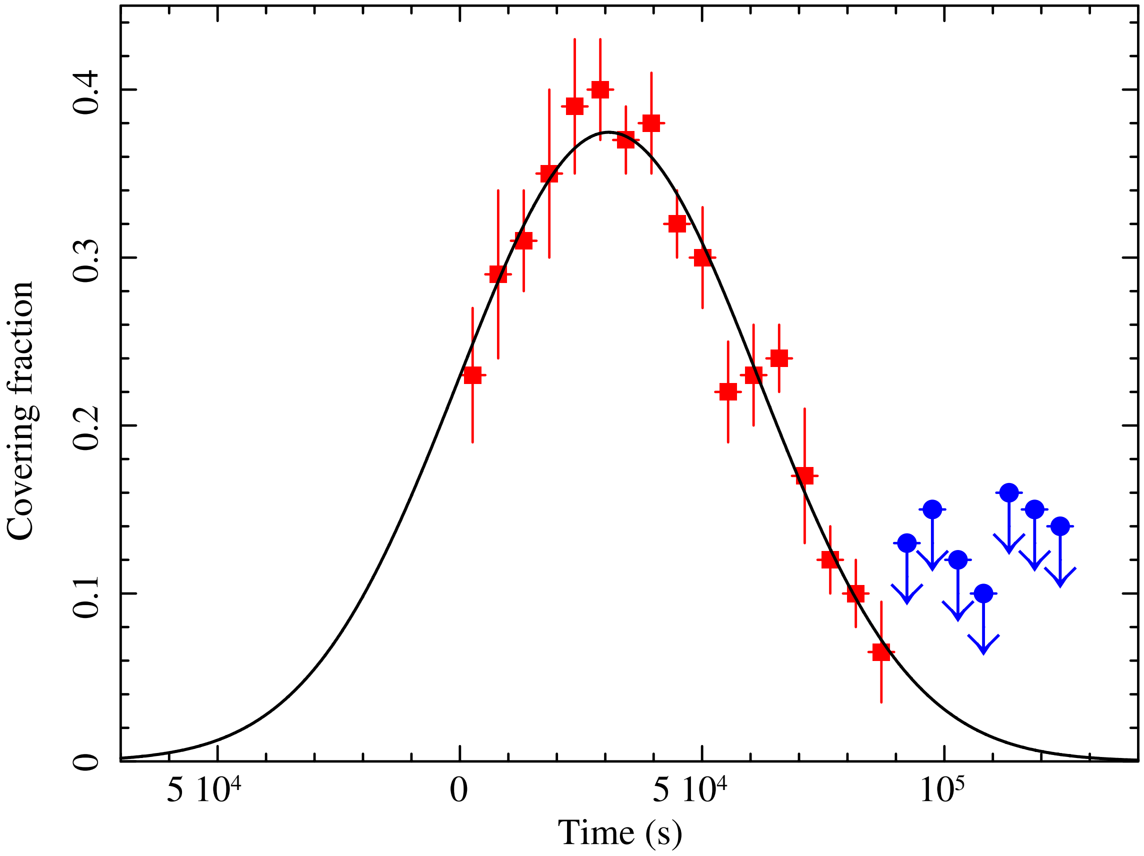

Figure 2.9: The CF evolution during the *XMM–Newton* observation. Significant CF variability is present in the first ~ 90 ks. Our results indicate that the X–ray continuum is partially absorbed during the first 90 ks of the exposure by a column density of ~ 2×10^{22} cm^{-2} with variable CF, while the data are consistent with the X–ray continuum being unabsorbed thereafter. The solid curve represents a simple Gaussian model for the CF evolution during the first ~ 90 ks (see Section 2.4.2).

apply the same model discussed above to all spectra. We force all parameters to be the same, except the power law normalization, the reflector ionization, and the absorber covering fraction. In addition, we impose the same reflection normalization in all spectra. This is because, by definition, two reflection models with the same normalization and illuminating power law slope but with different ionization parameters satisfy a linear relation between ionization and total reflection flux, (see e.g. Miniutti et al., 2012). Imposing that this is the case by forcing all reflection normalization to be the same increases the overall self–consistency of the model, as the two quantities are both linearly correlated with the flux irradiating the disc. It also helps lowering the number of free parameters in the model, reducing the risk of overmodelling data of relatively poor quality. The overall fit is excellent (reduced χ^2 = 0.98), and we obtain a common absorber column density of $N_{\rm H} = 2.0^{+0.2}_{-0.3} \times 10^{22}$ cm^{-2}, consistent with that derived above from the analysis of intervals A and B.

The covering fraction (CF) during the different intervals is clearly variable, and its evolution is shown in Fig. 2.9. The evolution during the first 90 ks of the exposure is smooth and can be roughly described by a Gaussian–like shape, while SWIFT J2127.4+5654 is consistent with being unabsorbed thereafter. The Gaussian–like shape of the covering fraction variability suggests that one single absorbing structure (cloud) with size similar to that of the X–ray source has crossed the line–of–sight during the first 90 ks of the observation. Below, we discuss the implications of the main event that characterizes the first 90 ks of the observation, and we derive the properties of the absorber as well as the size of the X–ray emitting region. Here we simply point out that the intrinsic absorber detected in the time–averaged spectrum (see Section 2.3) is just the flux–weighted average of the absorption column density and CF during the whole exposure, so that little physical meaning should be attached to the derived column density in the time–averaged spectral analysis.

2.5 Cloud properties and the X–ray emitting region size

The behaviour of the covering fraction data in Fig. 2.9, identifies three phases during the eclipse: a fast rise of CF from zero to maximal CF ($\sim 35 - 45$ per cent), a flat plateau with maximal CF, and finally a decaying phase from maximal CF to zero. The existence of a plateau with maximal CF smaller than 1, as well as the steepness of the rising and decaying phases, point towards a physical situation characterized by a cloud, smaller than the source, crossing our line–of–sight. The other possible scenario, specifically a larger cloud misaligned with the source would imply a much smoother and slower growth and decrease of the CF, which is not taking place here.

We then assume here the simplest possible geometry that can explain our data, namely the presence of an X–ray source of size (diameter) D_s and of an obscuring cloud of size $D_\mathrm{c} \leq D_\mathrm{s}$, see Fig. 2.10. The CF evolution identifies three different time–scales: (i) the crossing time $t^{(\mathrm{cr})} = 160 \pm 30$ ks, i.e. the total time during which CF $\neq 0$; (ii) the transit time $t^{(\mathrm{tr})} \leq 26.5$ ks during which the source is maximally covered (i.e. up to 5 intervals are consistent with being maximally covered); (iii) the partially covered rising / decaying time $t^{(\mathrm{pc})} = (t^{(\mathrm{cr})} - t^{(\mathrm{tr})})/2 = 73.5 \pm 21.5$ ks needed to reach the maximal covering fraction starting from zero (and viceversa). On the other hand all these time–scales can be related to the cloud velocity v_c and cloud / source sizes by $v_\mathrm{c} = D_\mathrm{c}/t^{(\mathrm{pc})} = (D_\mathrm{s} - D_\mathrm{c})/t^{(\mathrm{tr})} = (D_\mathrm{s} + D_\mathrm{c})/t^{(\mathrm{cr})}$.

2.5.1 Cloud / source relative sizes

Since the maximum covering fraction $\mathrm{CF}_\mathrm{max} \leq 1$, the cloud never completely covers the X–ray source (or it may, but only for a time shorter than our bin size of ~ 5.3 ks). The simplest interpretation is that $D_\mathrm{c} = \alpha D_\mathrm{s}$ with $\alpha \leq 1$. There are two different ways to derive α. Firstly, as $\mathrm{CF}_\mathrm{max} \geq 0.35$, one has $\alpha = \mathrm{CF}_\mathrm{max}^{1/2} \geq 0.59$. Secondly, as $(D_\mathrm{s} - D_\mathrm{c})/t^{(\mathrm{tr})} = (D_\mathrm{s} + D_\mathrm{c})/t^{(\mathrm{cr})}$, one has $\alpha = (t^{(\mathrm{cr})} - t^{(\mathrm{tr})})/(t^{(\mathrm{cr})} + t^{(\mathrm{tr})}) = [0.66 - 1]$. As the two α must be consistent with each other, we then have that $\alpha = [0.66 - 1]$.

2.5.2 Cloud density / distance

The combination $n_\mathrm{c} R_\mathrm{c}^2$ between cloud density and distance can be estimated from the cloud ionization state $\xi_\mathrm{c} = L_\mathrm{ion}/(n_\mathrm{c} R_\mathrm{c}^2)$ if the overall ionizing luminosity L_ion between 1 and 1000 Ry is known. In the case of SWIFT J2127.4+5654 we have $L_\mathrm{ion} \simeq 2 \times 10^{44}\ \mathrm{erg\,s^{-1}}$. We have then repeated our spectral analysis using an ionized absorber (the ZXIPCF model), and we infer that $\xi_\mathrm{c} \leq 20\ \mathrm{erg\,cm\,s^{-1}}$ with similar column density as inferred for the neutral model, and with consistent covering fraction evolution (no ionization variability is detected). Hence, we have $n_\mathrm{c} R_\mathrm{c}^2 \geq 10^{43}\ \mathrm{cm^{-1}}$.

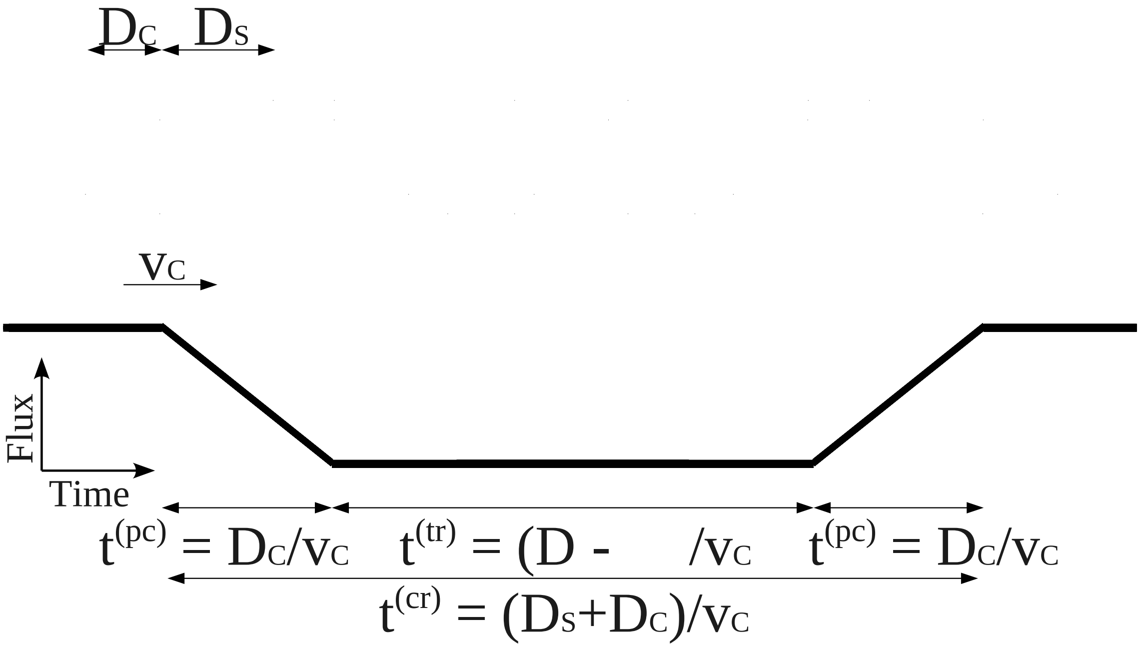

Figure 2.10: The envisaged system geometry. The absorbing cloud (grey) moves with velocity $v_{\rm c}$ and partially covers the X–ray source (red). The relevant quantities used in our discussion ($D_{\rm c}$, $D_{\rm s}$, $t^{\rm (pc)}$, $t^{\rm (tr)}$, and $t^{\rm (cr)}$) are also defined. See text in Section 2.5 for details.

We can now use the only relation that has not yet been used, namely $v_{\rm c} = D_{\rm c}/t^{\rm (pc)}$. Assuming that the cloud transverse velocity is dominated by gravity, and using the relationship between column density, size, and number density, we then have $(GM_{\rm BH}/R_{\rm c})^{1/2} = D_{\rm c}/t^{\rm (pc)} = N_{\rm H}/(n_{\rm c}t^{\rm (pc)})$. For a black hole mass of $M_{\rm BH} = 1.5\times10^{7}\ M_{\odot}$ (as derived from single–epoch optical spectra, see Malizia et al., 2008), $R_{\rm c}n_{\rm c}^{-2} = [1.9 - 3.7] \times 10^{-2}\,{\rm cm}^{7}$. By combining this result with $n_{\rm c}R_{\rm c}^{2} \geq 10^{43}\,{\rm cm}^{-1}$ derived above, one has $n_{\rm c}^{5} \geq 7.3 \times 10^{45}\,{\rm cm}^{-15}$, which then gives $n_{\rm c} \geq 1.5 \times 10^{9}\,{\rm cm}^{-3}$ and $R_{\rm c} \geq 4.3 \times 10^{16}\,{\rm cm}$.

2.5.3 Cloud and X–ray source sizes

The system is now closed, and limits on the cloud and X–ray source sizes can be derived. As $D_{\rm c} = N_{\rm H}/n_{\rm c}$ one has $D_{\rm c} \leq 1.5 \times 10^{13}$ cm = 7 r_g, where we have used a black hole mass of $1.5 \times 10^{7}\ M_{\odot}$ to define 1 $r_g = 1\ GM_{\rm BH}/c^2 = 2.2 \times 10^{12}$ cm. The upper limit on the cloud size translates into an upper limit on the X–ray emitting region size $D_{\rm s} = D_{\rm c}/\alpha \leq 2.3 \times 10^{13}$ cm = 10.5 r_g.

2.6 Summary and conclusions of Chapter 2

We report results from a ∼ 130 ks observation of the NLS1 galaxy SWIFT J2127.4+5654 with *XMM–Newton*. We confirm the detection of a relativistically broadened Fe Kα line, originally detected in a previous *Suzaku* observation (Miniutti et al., 2009). All relativistic parameters are consistent with those inferred from the *Suzaku* data. In particular, we confirm an intermediate black hole spin of $a \sim 0.5$ and a relatively high observer inclination of $i \sim 44°$.

The source exhibits significant flux variability throughout the observation and, most importantly, spectral variability is also present during the first 90 ks of the *XMM–Newton* exposure. We perform a time–resolved spectral analysis of the *XMM–Newton* data with the goal of investigating the origin of the observed spectral variability. Our results are consistent with the same baseline spectral model as in the previous *Suzaku* observation (e.g. Miniutti et al., 2009) affected by additional neutral absorption only partially–covering the X–ray source during the first 90 ks of the *XMM–Newton* exposure. Assuming that the spectral variability is driven by changes of the absorber CF, we show that the CF evolution is consistent with one single absorbing structure (cloud) crossing our line–of–sight during the first 90 ks of the exposure.

By considering the first 90 ks of the observation within the framework of a simple source–cloud geometry, we obtain the following constraints on the absorbing cloud: the cloud has a column density of $N_{\rm H} = 2.0^{+0.2}_{-0.3} \times 10^{22}\,{\rm cm^{-2}}$ which, once combined with the estimated cloud density $n_{\rm c} \geq 1.5 \times 10^{9}\,{\rm cm^{-3}}$ implies a cloud size (diameter) $D_{\rm c} \leq 1.5 \times 10^{13}$ cm at a distance from the center of $R_{\rm c} \geq 4.3 \times 10^{16}$ cm. Assuming that the cloud motion is dominated by gravity the cloud (Keplerian) velocity is then $v_{\rm c} \leq 2100\,{\rm km\,s^{-1}}$. All these properties are consistent with those of a BLR cloud partially covering a compact X–ray source during the *XMM–Newton* observation. The identification of the absorber with a BLR cloud is also supported by the observed optical broad line FWHM $\sim 2000\,{\rm km\,s^{-1}}$ (Malizia et al., 2008). By assuming a flattened BLR geometry and the inclination derived from our disc reflection model ($i = 44°$), the FWHM translates into a Keplerian velocity of $1.4 \times 10^{3}\,{\rm km\,s^{-1}}$, which is fully consistent with the cloud velocity upper limit $v_{\rm c} \leq 2.1 \times 10^{3}\,{\rm km\,s^{-1}}$ we derive from our analysis. The excellent agreement between the derived cloud properties and the BLR physical conditions provides further support to our proposed interpretation of the observed X–ray spectral variability.

The partial eclipse can be used to constrain the size of the X–ray emitting region. The CF evolution time–scales, as well as the maximal observed covering fraction $\rm CF_{max}$ imply that the cloud and X–ray emitting region sizes are related through $D_{\rm c} = [0.66 - 1] \times D_{\rm s}$. The upper limit on the cloud size $D_{\rm c} \leq 1.5 \times 10^{13}$ cm then translates into an upper limit on the X–ray source size of $D_{\rm s} \leq 2.3 \times 10^{13}\,{\rm cm} = 10.5\, r_g/M_{\rm best}$ where $M_{\rm best}$ is the black hole mass in units of $1.5 \times 10^{7}\, M_{\odot}$, i.e. the best available estimate of the black hole mass in SWIFT J2127.4+5654 (Malizia et al., 2008). Such a small X–ray emitting region is consistent with previous results based on similar occultation events in the X–rays (Risaliti et al., 2007, 2009b) as well as with microlensing results (Dai et al., 2010; Mosquera et al., 2013). A very compact X–ray corona is also consistent with the relatively steep emissivity profile we (and Miniutti et al., 2009) measure for the disc reflection component ($q \sim 5$) which strongly suggests a highly compact X–ray emitting region (e.g. Miniutti & Fabian, 2004).

We conclude that we have observed the partial eclipse by a BLR cloud of the X–ray continuum source in SWIFT J2127.4+5654. Our result is in line with the mounting observational evidence that part of the observed X–ray absorption in AGN is due to a clumpy absorber whose properties and location can be identified with either the BLR or with a clumpy torus (in those cases where absorption variability occurs on months to years time–scales) which probably are just different parts of the same obscuring region. Our analysis strongly suggests that the X–ray continuum is produced in a compact region only a few $r_{\rm g}$ in size, which is consistent with the detection of a reflection component off the inner accretion disc. Notice that the relatively high observer inclination we measure from the broad Fe line ($i \sim 44°$) likely enhances the probability of X–ray eclipses (see e.g. Elitzur, 2012).

The advent of the next generation of large–collecting area X–ray observatories (e.g. the proposed *Athena* mission, see Dovčiak et al., 2013; Nandra et al., 2013) will allow us to map with even greater accuracy the innermost regions of the accretion flow around accreting black holes via X–ray spectroscopy and X–ray flux and spectral variability studies, including absorption events as the one discussed here (see e.g. Risaliti et al., 2011a).

3

Eclipsing the innermost X–ray emitting regions in AGN

This chapter is in part adapted from a proceedings article entitled “Eclipsing the innermost accretion disc regions in AGN” (Sanfrutos et al., 2016a, Astron. Nachr., 337, 546) and in part on–going work to be published elsewhere.

Variable X–ray absorption has been observed in AGN on several time scales. Observations allow us to identify the absorber with clouds associated either with the dusty, clumpy torus (parsec scales, long timescales, see e.g. Risaliti et al., 2002; Marinucci et al., 2013, although these authors reject the simplicity of the standard model) or with the BLR (short timescales, see e.g. Elvis et al., 2004; Bianchi et al., 2009). In the latter case, the cloud size has been estimated to be of the order of few gravitational radii from the observed absorption variability. Such small cloud sizes are comparable to the X–ray emitting regions so that a detailed modeling of occultation events in AGN has the potential of enabling us to infer accurately the geometry of the system. We first introduce a Newtonian model and then a relativistic X–ray spectral one for occultation events. We present theoretical predictions on the different observables that can be inferred by studying X–ray eclipses in *XMM–Newton* simulations and actual data. These include the size of the X–ray emitting regions as well as more fundamental parameters such as the black hole spin and the system inclination. We find that absorption varies as a function of the energy range and that its maximum takes place when the approaching part of the accretion disc is covered. Therefore we study the H / S ratio light curves produced during an eclipse and use them to characterize the properties of the inner accretion disc and the corona in a new model–independent way.

3.1 Introduction

Several spectral features such as Doppler boosting, gravitational redshift and light bending are imprinted in the X–ray emission reprocessed by the innermost regions of the accretion disc, which are in the strong gravity regime due to its proximity to the SMBH. In this context, both the black hole spin and the disc properties shape the Kα emission line profile (see e.g. Reynolds & Nowak, 2003). However, there is some controversy on this interpretation: the partial covering scenario proposed e.g. by Turner et al. (2007) claims that such spectral features can be explained by a variable wind composed by several ionized clouds that partially cover the X–ray continuum source. Within this Chapter, we argue that the ultimate test to prove the detectability of general relativistic effects under extreme gravity conditions could be furnished by X–ray time–resolved spectroscopy of AGN, which would definitely rule out the partial covering scenario.

On the side of special relativistic effects, Doppler boosting has a clear and distinct effect on the reflected component: the emission from the parts of the disc approaching us are enhanced, while we detect diminished flux from the receding parts. Due to the fact that the central engine is unresolved, and will remain like this in the future due to the scales and distances involved, one of the most promising ways to distinguish the reflection from the various parts of the disc is by means of the obscuration of the different emitting regions by structures in our LOS. Occultation of the X–ray source by optically thick matter was first proposed by McKernan & Yaqoob (1998). A method to investigate relativistic effects during X–ray eclipses in AGN spectra was developed by Risaliti et al. (2011b), consisting on measuring the emission from half of the disc while the other half is covered, and viceversa. Relativistic effects are revealed when the emission of each half is different, hinting an asymmetric emission from the disc due mostly to Doppler boosting.

Occultation events are rather common in AGN, as we mentioned in the short review of Section 2.1. These objects show X–ray spectral variability on a variety of time–scales, independently of their luminosity or morphology (see e.g. Marshall et al., 1981; Turner et al., 1999). Also, variability can occur at time–scales as short as a few hours in all types of AGN, as shown by Elvis et al. (2004) in NGC 4388 (type 2), Bianchi et al. (2009) in NGC 7582 (type 2), Risaliti et al. (2009b) and Maiolino et al. (2010) in NGC 1365 (Seyfert 1.8), Puccetti et al. (2007) in NGC 4151 (Seyfert 1.5), Risaliti et al. (2011a) in Mrk 766 (NLS1) and Sanfrutos et al. (2013) (as well as in Chapter 2 of this Thesis) in SWIFT J2127.4+5654 (NLS1). The high variability characterized in the references above can be explained in the context of rapid column density changes, which are the result of the interception of material located in the BLR of the system to our LOS (see e.g. Miniutti et al., 2014, and Chapter 4 of this Thesis). Hence, AGN are perfect laboratories to check GR effects by using eclipses to probe the innermost regions of the accretion disc.

3.2 The Newtonian approximation

Spherical source

We start exploring a Newtonian approximation for the problem of occultation events by circular absorbing structures. The geometrical set–up is, basically, the same as described in Fig. 2.10: we assume a geometry consisting of a spherical source with radius $R_{\rm s}$, emitting radiation isotropically. Therefore in our LOS we observe the same emission per unit area from every region of the source,

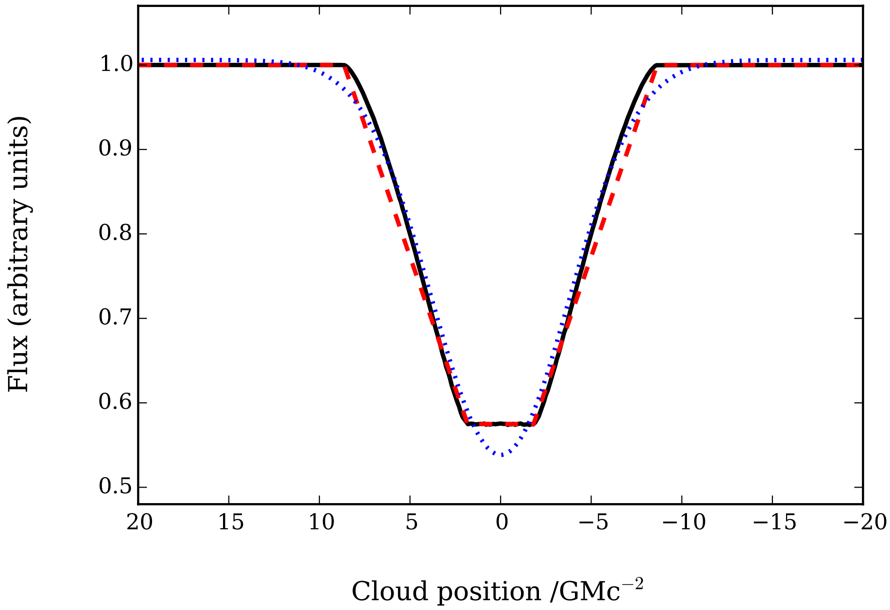

Figure 3.1: Lightcurve of an eclipse of a circular isotropically–emitting source by a circular cloud. The cloud and source radii are $R_c = 3.4\,r_g$ and $R_s = 5.2\,r_g$. The solid black line is the Monte Carlo simulated flux during an eclipse, and the dashed red and dotted blue lines represent the fits to five segments and a Gaussian, respectively.

defined in a circle of radius R_s. The eclipse is due to a spherical Compton–thick (opaque in the X–ray regime below $\sim 10\,$keV) cloud with radius R_c, absorbing all the radiation from the area of the source covered by it in our LOS. The distance between the source and the SMBH is negligible compared to the distance between the source and the cloud, and the cloud is assumed to follow a Keplerian orbit around the source anti–clockwise. Due to geometrical effects, we observe both the source and the cloud as circles of radii R_s and R_c respectively. We add a further constraint forcing the centre of the cloud to pass through the centre of the source at some time during the eclipse. We choose this event as the origin of coordinates of the transit, and define positive the distance towards the left and negative to the right.

With the aim of investigating the parameters of the occultation event, we designed a simple Monte Carlo simulation code to build eclipse lightcurves. In order to compute the flux that reaches us at every moment of the eclipse, we assume that this is proportional to the uncovered area of the source, being $F = 1$ when it is uncovered and $F = 0$ when it is completely covered by the cloud (in arbitrary units). With these conditions, and for every position of the cloud along the eclipse, we randomly generate 10^6 points from a uniform distribution within a rectangular region in which the source is inscribed, compute how many of them are within the source ($\mathrm{n_{emit}}$), and how many of these last ones are within the area blocked by the cloud ($\mathrm{n_{abs}}$). The number of points within the circle defined by the source is proportional to its area, and hence to the emitted flux, while the number of points within the region occulted by the cloud is proportional to the obscured area, and so proportional to the flux absorbed by the cloud. The total flux observed by us at any moment is then $F = 1 - \mathrm{n_{abs}}/\mathrm{n_{emit}}$, i.e. $F = 1{-}\mathrm{CF}$. In Fig. 3.1 we show the lightcurve of an eclipse like the one described here. The cloud and source radii ($R_c = 3.4\,r_g$ and $R_s = 5.2\,r_g$ respectively) have been chosen to be coincidental with the parameters of the system studied in Chapter 2 for comparison. When the centre of the cloud is located at the position $R_c + R_s$, its projected area touches the projected area of the spherical source, and the flux drops. It reaches its minimum ($F_{\rm min} = 1 - R_{\rm c}^2/R_{\rm s}^2$) when the left limits of the projected area of the cloud and the source coincide, when the cloud's centre is at $R_{\rm s} - R_{\rm c}$, and this minimum flux situation remains in the plateau defined between $R_{\rm s} - R_{\rm c}$ and $-R_{\rm s} + R_{\rm c}$, during the whole lapse in which the projected area of the absorbing structure is completely contained in the projected area of the source. When the projected area of the cloud starts getting out of the projected area of the source, the flux starts increasing again, up to its maximum of $F_{\rm max} = 1$ when the left end of the projected area of the cloud leaves the right end of the projected area of the source, i.e. when the centre of the cloud is at $-R_{\rm s} - R_{\rm c}$. This results in a lightcurve of the eclipse that is symmetrical with respect to the centre of the source, as expected in a Newtonian approximation.

Plane–parallel disc source

We now explore the case of a disc–like source, which is more representative of the real geometry of the accretion flow. When the system is observed face–on, there is no difference with respect to the previous case. However, this would not be a physically plausible situation: since the plane of the disc source is perpendicular to the rotation axis of the system, it would be extremely unlikely to find a cloud passing by our LOS to the source, i.e. a cloud whose orbit crosses the rotation axis of the system, as a natural assumption is that clouds orbit close to the equatorial plane. Hence, we allow for some inclination θ of the disc source. The resulting projected area of the disc source is an elipse whose major axis equals the radius of the disc, $R_{\rm s}$, and whose minor axis is $R_{\rm s} \sin\theta$. In this case, the plateau in which the observed flux is minimum drops down to $F_{\rm min} = 1 - R_{\rm c}^2/R_{\rm s}^2 \sin\theta$, given that the projected area of the source is $\pi R_{\rm s}^2 \sin\theta$. The lightcurve with the same parameters as for the spherical case assuming an inclination angle of 45° is shown in Fig. 3.2, where the Newtonian case symmetry is recovered.

Plane–parallel annulus source

We have axplored the cases of spherical sources, like the coronae in the compact spherical model by Fabian et al. (2015); and disc–like also, like the patchy coronae configurations proposed by Stern et al. (1995) or Wilkins & Gallo (2015a). We will now study the case of annulus–like sources, like the inner regions of accretion discs, or the coronae with a slab geometry, in which the primary X–ray emission arises from annular regions that are parallel to the inner accretion disc and very close to it (see e.g. Rozanska et al., 2015). Such sources are disc–like with a hole in their centres, corresponding to the regions at distances from the SMBH smaller than the ISCO. Thus, eclipses are now characterized by inner and outer source radii ($R_{\rm s}^{\rm in}$, $R_{\rm s}^{\rm out}$), inclination angle (θ), and radius of the absorbing spherical cloud ($R_{\rm c}$). An example of eclipse lightcurve is shown in Fig. 3.3, for the case of an annular source of inner radius $R_{\rm s}^{\rm in} = 4\, r_{\rm g}$ and outer radius $R_{\rm s}^{\rm out} = 6\, r_{\rm g}$, inclined $\theta = 45°$ and obscured by a spherical cloud of radius $R_{\rm c} = 3\, r_{\rm g}$. As in the previous configurations, the flux drops when the projected area of the cloud touches the projected area of the source. However, after the flux reaches its first minimum it grows up to a local maximum corresponding to the configuration of the projected area of the cloud crossing the projected area of the hole in the disc. Then the flux drops again, corresponding to the crossing of the other half of the annulus, and increases again as the cloud leaves the projected area of the source. Once more, the lightcurve reveals the symmetric nature of eclipses in a Newtonian approach, when Doppler shifts (as well as all relativistic effects) are ignored.

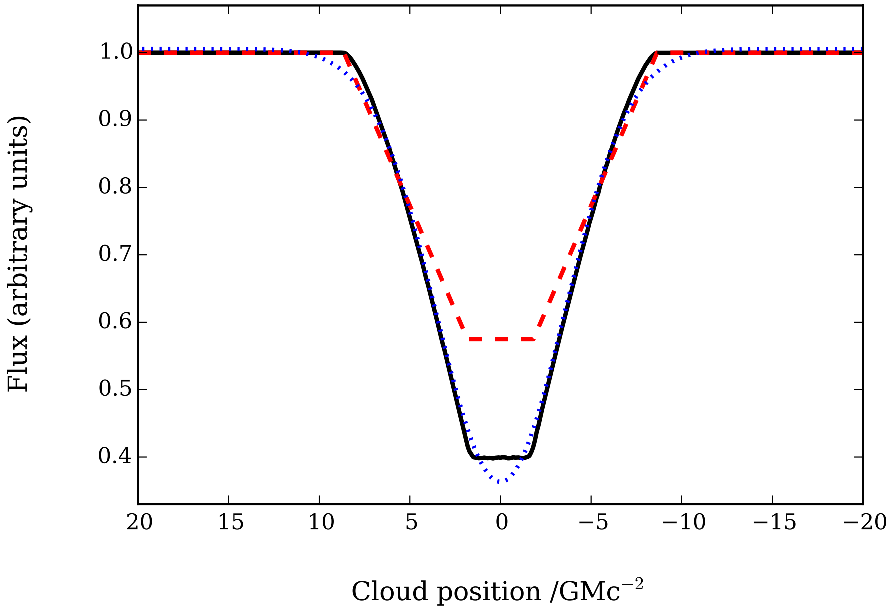

Figure 3.2: Lightcurve of a circular cloud eclipsing a plane–parallel isotropically–emitting disc source inclined 45°. The cloud and source radii are $R_\mathrm{c} = 3.4\, r_\mathrm{g}$ and $R_\mathrm{s} = 5.2\, r_\mathrm{g}$. The solid black line is the Monte Carlo simulated flux during an eclipse, and the dotted blue line represent the fit to a gaussian. Also we plot the same dashed red line as in Fig. 3.1 for comparison reasons.

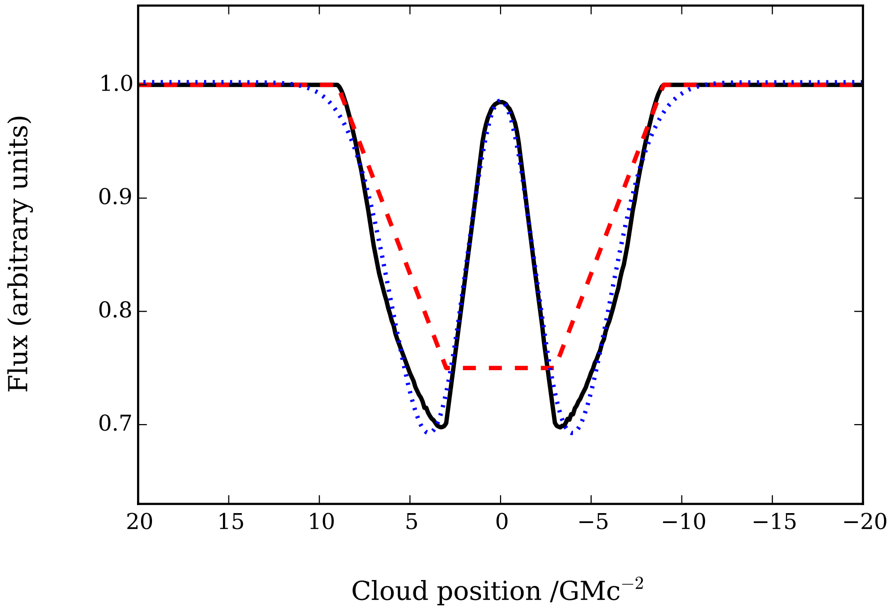

Figure 3.3: Lightcurve of a circular cloud eclipsing a plane–parallel isotropically–emitting annular source inclined 45°. The cloud radius is $R_\mathrm{c} = 3\, r_\mathrm{g}$ and the annular source has inner and outer radii of $R_\mathrm{s}^\mathrm{in} = 4\, r_\mathrm{g}$ and $R_\mathrm{s}^\mathrm{out} = 6\, r_\mathrm{g}$ respectively. The solid black line is the Monte Carlo simulated flux during an eclipse, and the dotted blue line represent the fit to two gaussians. Also we plot the same dashed red line as in Fig. 3.1 for comparison reasons.

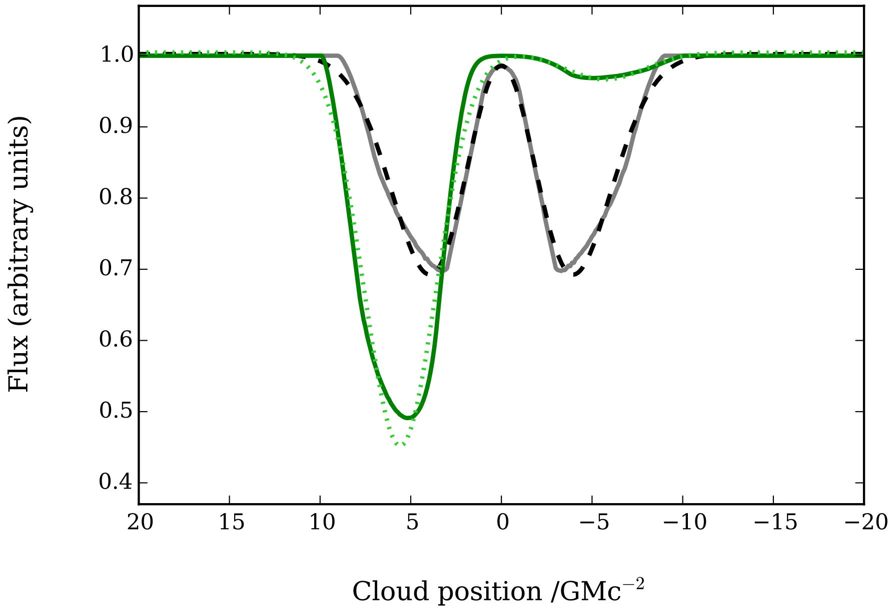

Figure 3.4: Lightcurves created by a circular cloud eclipsing a plane–parallel annular source inclined 45°. The cloud radius is $R_{\rm c} = 3\,r_{\rm g}$ and the annular source has inner and outer radii of $R_{\rm s}^{\rm in} = 4\,r_{\rm g}$ and $R_{\rm s}^{\rm out} = 6\,r_{\rm g}$ respectively. The solid grey line is the Monte Carlo simulated flux during an eclipse involving a Newtonian isotropically–emitting disc, and the dashed black line represents the fit to two gaussians. The solid green line is the flux simulated from the KYNCONV relativistic model, emitted from a disc around a rotating black hole with spin $a = 0.56$ (ISCO = $4\,r_{\rm g}$). The dotted green line is the fit to two gaussians. Notice that the flux from the approaching side of the disc (left wing) is several times greater than that from the receding side (right wing).

3.3 The relativistic model

It is extensively discussed in the literature that there are at least two components in AGN spectra: the continuum power law emission, from the corona, and the reflection–dominated component, from the accretion disc (see e.g. Vaughan & Fabian, 2004; Fabian et al., 2004, 2005; Ponti et al., 2006). The location of the regions where these components arise from, is always the innermost accretion flow. For instance, according to Ponti et al. (2006) these regions are both within $15\,r_{\rm g}$ from the SMBH in the case of the Seyfert 1 galaxy NGC 4051. As for the case of the archetypical Seyfert 1 galaxy MCG–6-30-15, Iwasawa et al. (1996) calculate that the line–emitting region must be relatively small (less than $20\,r_{\rm g}$ in radius) , and locate the continuum source just over the disc, orbiting the central SMBH with it. When the size and / or the location of the continuum and reprocessing regions are different, the same occultation event would lead to distinct signatures on each one of the components, enabling us to disentangle them.

The geometry that we assume for the system consists of a SMBH, characterized by its mass ($M_{\rm BH}$) and spin parameter (a*), around which an optically thick but physically thin ionized accretion disc extends from the ISCO out to $400\,r_{\rm g}$. With respect to the geometry of the system formed by the disc and the X–ray source (or the so–called corona), several configurations have been proposed in the literature: the hot and radiatively compact spherical corona with radius between 3 and $10\,r_{\rm g}$ proposed by Fabian et al. (2015); the slab (Rozanska et al., 2015) or the patchy (Stern et al., 1995; Wilkins & Gallo, 2015a) geometries; and the jet base interpretation (Wilkins & Gallo, 2015b), just to mention some of them. In order to investigate the potential of X–ray eclipses for deriving the general geometry, we choose a slab geometry for the corona, which is therefore a parallel plane above the disc. Since the continuum X–ray source has to be located in the vicinity of the SMBH in order to properly illuminate the innermost regions of the accretion disc, we assume the corona to be placed at a negligible distance from the disc. The inner radius of the corona is forced to be coincidental with the ISCO, while its outer radius is only a few $r_{\rm g}$. As for the reprocessed component, we assume it to arise from the innermost regions of the accretion disc, between the ISCO and an outer limit determined by the steepness of the disc's emissivity index, but always satisfying that at least 99% of the reprocessed emission comes from the innermost $\sim 12\,r_{\rm g}$, i.e. $q \geq 3$. The emissivity index, q, is defined in such a way that the total flux emitted from a ring with inner and outer radii $R_{\rm in}$ and $R_{\rm out}$, respectively, is proportional to $\int_{R_{\rm in}}^{R_{\rm out}} r^{-q}{\rm d}r$. Hence, if $x \in [0, 1]$ is the fraction of flux emitted by an annulus between the orbits of radii $R_{\rm in}$ and $R_{\rm out}$, the emissivity index can be expressed as $q = 1 - \frac{\log(1-x)}{\log R_{\rm out}/R_{\rm in}}$. The eclipsing cloud is assumed to be co–rotating with the disc at a velocity of $3000\,{\rm km\,s^{-1}}$, typical of the BLR of the system. Since these kind of obscuration events are more likely to be detected in unobscured sources, we disregard the torus of the Unification models within the framework of this Chapter.

We build our model within XSPEC (Arnaud, 1996), an X–ray spectral fitting package developed in the NASA's High Energy Astrophysics Science Archive Research Center (HEASARC). This model consists of a power law, accounting for the X–ray continuum emission from the corona, plus the X–ray reflection code XILLVER in XSPEC (García et al., 2013), accounting for the reflection component arising from the accretion disc. These two components are multiplied by the KYNCONV relativistic convolution model from Dovčiak et al. (2004), which adds all relativistic effects due to strong gravity and fast motions close to the SMBH, allowing to obscure part of the emission with a circular cloud whose size and position can be determined. We model the accretion disc to cover at least one half of the sky as seen from the central engine, with a typical ionization of $\xi^{\rm (disc)} \sim 30\,{\rm erg\,cm\,s^{-1}}$ and solar abundances. The energy cutoff is frozen to 300 keV. The main parameters that can be tuned in the KYNCONV relativistic convolution model are: (i) the inclination θ of the system with respect to our LOS (0°: face–on, 89°: edge–on); (ii) the black hole spin a^* (0: not rotating, 0.998: maximally rotating); (iii) the emissivity index q, which specifies the reflection radial emissivity profile, i.e. how the disc is illuminated (low: uniform, high: centrally concentrated); (iv) the cloud position set by the impact parameters α and β in units of $r_{\rm g}$ with horizontal position being positive towards the approaching side of the accretion disc and negative towards the receding part, and with zero vertical position of the cloud (i.e. $\beta = 0$); and (v) the cloud size in terms of its radius r, also in $r_{\rm g}$ units. The intrinsical physical properties of the obscuring cloud such as its column density $N_{\rm H}^{\rm (cl.)}$ and ionization $\log \xi^{\rm (cl.)}$ are set by muliplying the components defined above by the ionized absorption code ZXIPCF (Reeves et al., 2008). We take into consideration the Galactic absorption too, by means of a neutral absorption component. The parameters involved in this modelling are shown in Table 3.1. In the following we are explaining the role of every parameter involved in the model.

Galactic absorption

The absorption due to material in the Milky Way in our LOS to the source is modelled by means of the photoelectric absorption component PHABS in XSPEC. We choose an intermediate arbitrary intermediate value of $N_{\rm H}^{\rm (Gal.)} = 3 \times 10^{20}\,{\rm cm^{-2}}$.

Table 3.1: GR absorption model parameters

Galactic absorber	Local absorber			
$N_{\mathrm{H}}^{(\mathrm{Gal.})} = 0.03$	$N_{\mathrm{H}}^{(\mathrm{cl.})}$	$\log \xi^{(\mathrm{cl.})}$	r	α, β
Continuum			Reflected	
$\Gamma^{(\mathrm{cont.})} = 2$	nor.$^{(\mathrm{cont.})}$		$\Gamma^{(\mathrm{refl.})} = 2$	nor.$^{(\mathrm{refl.})}$
Relativistic convolution parameters				
$\theta = 45°$	a*	r_{in} = ISCO	$r_{\mathrm{out}}^{(\mathrm{cor.})}$	q$^{(\mathrm{disc})}$

Units: column densities (N_{H}) are given in $10^{22}\,\mathrm{cm}^{-2}$, ionizations ($\xi$) in $\mathrm{erg\,cm\,s}^{-1}$, and the inclination (θ) in degrees. The position (α,β) and radius (r) of the cloud, as well as the inner and outer radii of the disc and the corona are given in r_{g}.

Local absorption

We model the absorption due to material in the host galaxy with absorption by partially ionized material (the ZXIPCF model in XSPEC). The equivalent column density parameter, $N_{\mathrm{H}}^{(\mathrm{cl.})}$, ranges from $10^{23}\,\mathrm{cm}^{-2}$ (Compton–thin) to $5 \times 10^{24}\,\mathrm{cm}^{-2}$ (Compton–thick), which is typical for clouds in the BLR. Its ionization, $\log \xi^{(\mathrm{cl.})}$, can take values as low as -3 (neutral) up to 2 (highly ionized material). The radius (r) and position (α, β) of the absorbing structure are determined by a set of parameters within the relativistic code KYNCONV, all in terms of gravitational radii.

The contiuum emission

The primary emission from the corona is modelled with a simple photon power law component proportional to $E^{-\Gamma}$, where E is the energy and Γ is the dimensionless photon index, set to a typical value of $\Gamma = 2$. The proportionality constant is the continuum normalization, chosen in such a way that the unabsorbed $2 - 10\,\mathrm{keV}$ X–ray flux is around $10^{-11}\,\mathrm{erg\,cm}^{-2}\,\mathrm{s}^{-1}$, a fairly typical flux for bright, local AGN. An exponential high–energy cutoff of $E_c = 300\,\mathrm{keV}$ is chosen for the power law.

The reprocessed emission

The reflection from the disc is modelled by means of the X–ray reflection code XILLVER, developed by García et al. (2013). The photon index is chosen to be the same as for the continuum emission component. The iron abundance is frozen to the solar one ($\mathrm{A}_{\mathrm{Fe}} = 1$) and the disc ionization is fixed to a typical value of $\log \xi^{(\mathrm{disc})} = 1.5$ in order to allow the existence of enough reflection features. We set the same cutoff as for the power law ($E_c = 300\,\mathrm{keV}$). Finally, the reflection normalization is fixed in order to get a reflection fraction between 1 and 2, i.e. the disc to cover at least one half of the sky as seen from the central engine, in agreement with observations.

3.3.1 Black hole spin and viewing angle dependency

Both low column densities and large ionizations are associated with more transparent clouds, and therefore with fainter CFs. Our goal in this section is to look for asymmetries in the CF–profiles

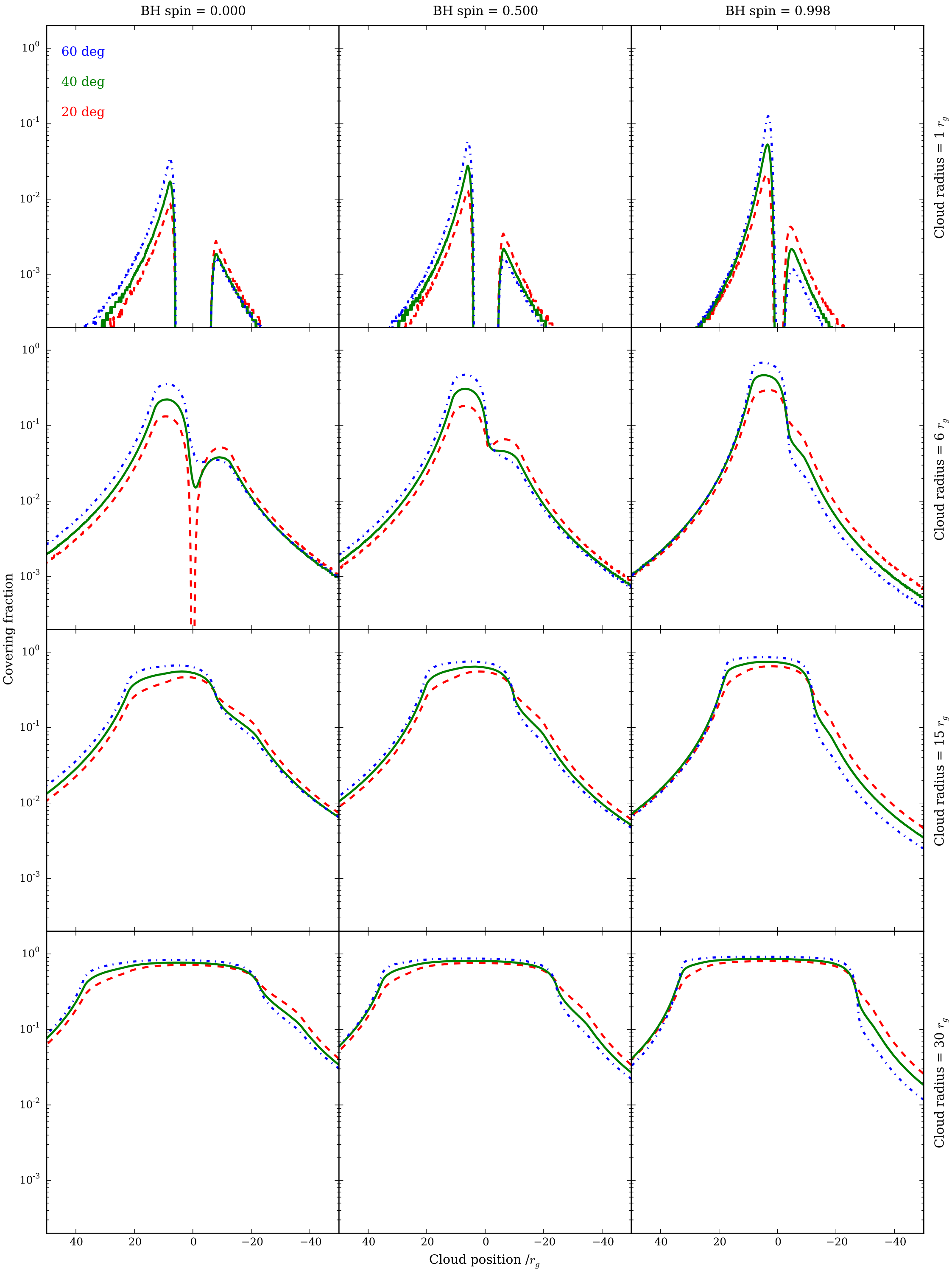

Figure 3.5: A bunch of 36 CF–profiles produced by a neutral cloud of column density $N_{\mathrm{H}} = 10^{24}\,\mathrm{cm}^{-2}$ obscuring a disc illuminated with an emissivity index of q = 3. The black hole spin is 0 (Schwarzschild case) on the left column, 0.5 (intermediate Kerr) on the middle column, and 0.998 on the right (maximally Kerr). The cloud radius is 1 r_{g} on the top row, 6 r_{g} on the second, 15 r_{g} on the third, and 30 r_{g} on the bottom row. In every panel, we show the CF–profiles as observed at a system inclination of 20° (dashed red line), 40° (solid green line) and 60° (dash–dotted blue line) with respect to the disc's normal.

produced in systems characterized by different values of the black hole spin and the inclination angle, pointing to relativistic effects. Therefore, we choose the absorber parameters to be able to produce noticeable coverings of the flux emitted. Hence, we consider a neutral cloud, opaque in the 0.7–10 keV band, i.e. $N_{\mathrm{H}}^{(\mathrm{cl.})} = 10^{24}\,\mathrm{cm}^{-2}$ and $\log \xi^{(\mathrm{cl.})} = -3$. The study of other clouds, with column densities ranging from 10^{23} to $5 \times 10^{24}\,\mathrm{cm}^{-2}$, and ionisations of up to $\xi = 10\,\mathrm{erg\,cm\,s}^{-1}$, is addressed in Section 3.5.

Below we present results from some CF–profiles, obtained from simulations if occultation events produced by a cloud as described above towards a disc–like structure with inner and outer radius equal to the ISCO and $400\,r_{\mathrm{g}}$, respectively, with an intermediate emissivity index of q = 3. The procedure we perform is the following: for every position of the cloud we compute the flux in the $0.7 - 10$ keV energy band, then we compute the intrinsic flux in the same band by removing the cloud, and finally we derive the CF at every position of the cloud all along the eclipse. Any asymmetry in these CF–light curves would be indicative of asymmetries in the emission from the disc, and therefore it would evidence relativistic effects. The CF–profiles are compiled in Fig. 3.5.

The first parameter about which we can establish some conclusions is the inclination of the system, in terms of the angle between the normal to the disc and our LOS. When we observe the system face–on (i.e. 0°), Doppler boosting is undetectable from our point of view: there are no approaching nor receding regions in the disc, since its orbital plane is perpendicular to our LOS. Therefore the CF–profile observed would be symmetric with respect to the position of the black hole. The larger the inclination is, the greater is the Doppler boosting effect, so that the more noticeable is the asymmetry of the CF–profiles, as can be seen in every panel of Fig. 3.5, independently of every other parameter. The CF–profiles during an eclipse in a system at an inclination of 20° (near to pole–on) are shown in dashed red lines; at a greater inclination of 40° in solid green lines, showing a greater asymmetry; and finally at an inclination of 60° in dash–dotted blue lines, when the asymmetry is the largest. We do not show inclinations lower than 20° because one would not expect to find BLR clouds at such high latitudes. We do not show inclinations larger than 60° either because the torus would block the light from the central region.

Three characteristic values of the spin are studied: on the left column of Fig. 3.5 we show the CF–profiles of a Schwarzschild black hole (ISCO = $6\,r_{\mathrm{g}}$). On the column in the middle we show the same for an intermediate Kerr black hole (ISCO = $4.23\,r_{\mathrm{g}}$). On the right column we show the CFs with a maximally rotating Kerr black hole (ISCO = $1.24\,r_{\mathrm{g}}$). In the cases where the cloud size is comparable to the ISCO (upper row in Fig. 3.5, with a cloud radius of $1\,r_{\mathrm{g}}$, and also in the left and even the middle panels in the second row, with a radius of $6\,r_{\mathrm{g}}$), we could measure the ISCO with great precision in a completely new way when the size of the cloud is known, by simply measuring the distance between the two maxima in any of those panels. When larger clouds are involved in the eclipse, GR effects are still detectable, as highlights the asymmetry of the characteristic top hat–shaped CF–profiles shown on any of the panels in the third ($r = 15\,r_{\mathrm{g}}$) and fourth ($r = 30\,r_{\mathrm{g}}$) rows in Fig. 3.5.

It is important to mention that some of the maxima in the CF–profiles shown in Fig. 3.5 are beyond the limits of detectability of available instruments (mainly the upper row cases, when the cloud radius is too small). However, most of them still represent interesting cases that we could discern by using current technology.

3.4 Physical properties of the systems under study

As already stated in the previous Sections, our purpose is to take advantage of the relatively common X–ray eclipses in AGN that are due to clouds of the BLR crossing our LOS to the central source. Before addressing the many physical situations that can occur, we need to clarify some key issues on the nature of the BLR and its relationship with the central engine. The current paradigm for the BLR comprises a large amount of clouds, namely N_c, that are assumed to be spherical and have an average radius of R_c. Peterson (2006) find that for a typical Seyfert galaxy like NGC 5548, the number of clouds in the BLR is $N_c \sim 10^7$ and their radii are $R_c \sim 10^{13}$ cm. Considering a particle density of $n \sim 10^9 - 10^{11}\,\mathrm{cm}^{-3}$ (see Section 1.3), the column density of the clouds in the BLR turns out to be $N_H \sim 10^{22} - 10^{24}\,\mathrm{cm}^{-2}$, though we should consider the high–density end as more representative of the BLR clouds, as extensively argued in Section 1.3.

In order for our instruments to be sensitive enough to detect the effects caused by an obscuring structure passing by the X–ray source, the cloud and source sizes must be comparable. As it was previously explained, when the X–ray source was identified with the corona, its size is of the order of few gravitational radii. Therefore, we impose a lower limit for the cloud size as the size of the ISCO. Adopting the conservative limits of $N_H > 10^{22}\,\mathrm{cm}^{-2}$ and $n \sim 10^9 - 10^{11}\,\mathrm{cm}^{-3}$, the size of one of these clouds must be greater than 10^{11} cm. The smallest central SMBH found up to date is the one in the bulgeless galaxy NGC 4561 (Araya Salvo et al., 2012), with a mass of $M_{BH} > 2 \times 10^4\,M_\odot$. However, we need to impose a further condition on the central mass. As we mentioned before, the cloud size must be greater than 10^{11} cm, i.e. the cloud radius must be $r > 5 \times 10^{10}$ cm, implying that $M_{BH} > 3.4 \times 10^5\,M_\odot$. Hence, we limit our study of the space of parameters to masses greater than $3.4 \times 10^5\,M_\odot$.

Assuming Keplerian orbits for the clouds in the BLR, the distance between the SMBH and the BLR is defined as $R_{BLR} = GM_{BH}/v_c^2$, where G is the Gravitational constant, M_{BH} is the mass of the SMBH, and v_c is the Keplerian velocity of the clouds in the BLR. Then, the distance to the BLR can be given in terms of gravitational radii as $R_{BLR} = r_g \times c^2/v_c^2 = 10^2 - 10^5\,r_g$ (since, typically, $v_c = 1000 - 30000\,\mathrm{km\,s^{-1}}$). Taking into account the velocity ($1000 - 30000\,\mathrm{km\,s^{-1}}$) and mass ranges ($\sim 10^5 - 10^9\,M_\odot$), the BLR distance translates into $R_{BLR} \simeq 10^{12} - 10^{19}$ cm (i.e. from $\sim 10^{-7}$ pc for masses as low as $\sim 10^5\,M_\odot$ up to ~ 4 pc for masses of $10^9\,M_\odot$).

In order to catch at least one complete occultation event during one single observation, the cloud needs to cross the region of the X–ray source in a time inverval shorter than the observation length. A typical long *XMM–Newton* observation lasts $\sim 10^5$ s, although very long observations can be much longer (see e.g. Risaliti et al., 2011a, who observed Mrk 766 during six consecutive orbits for a net exposure time of ~ 800 ks). In consequence, we impose the cloud to travel $50\,r_g$ in less than 500 ks, i.e. $v_c > 10^{-4}\,r_g\,\mathrm{s}^{-1}$. This transforms into an upper limit to the mass of the central SMBH of $M_{BH} < 7 \times 10^6\,M_\odot$ for the slowest clouds and $M_{BH} < 2 \times 10^8\,M_\odot$ in the case of the fastest ones. In Fig. 3.6 we show the parameters space of velocities and masses allowed. The clouds that move fast enough to cross the region of interest ($\sim 50\,r_g$) in less than 500 ks (so that with velocities $v > 10^{-4}\,r_g\,\mathrm{s}^{-1}$), and that are large enough to be part of the BLR, are those within the shaded region in Fig. 3.6.

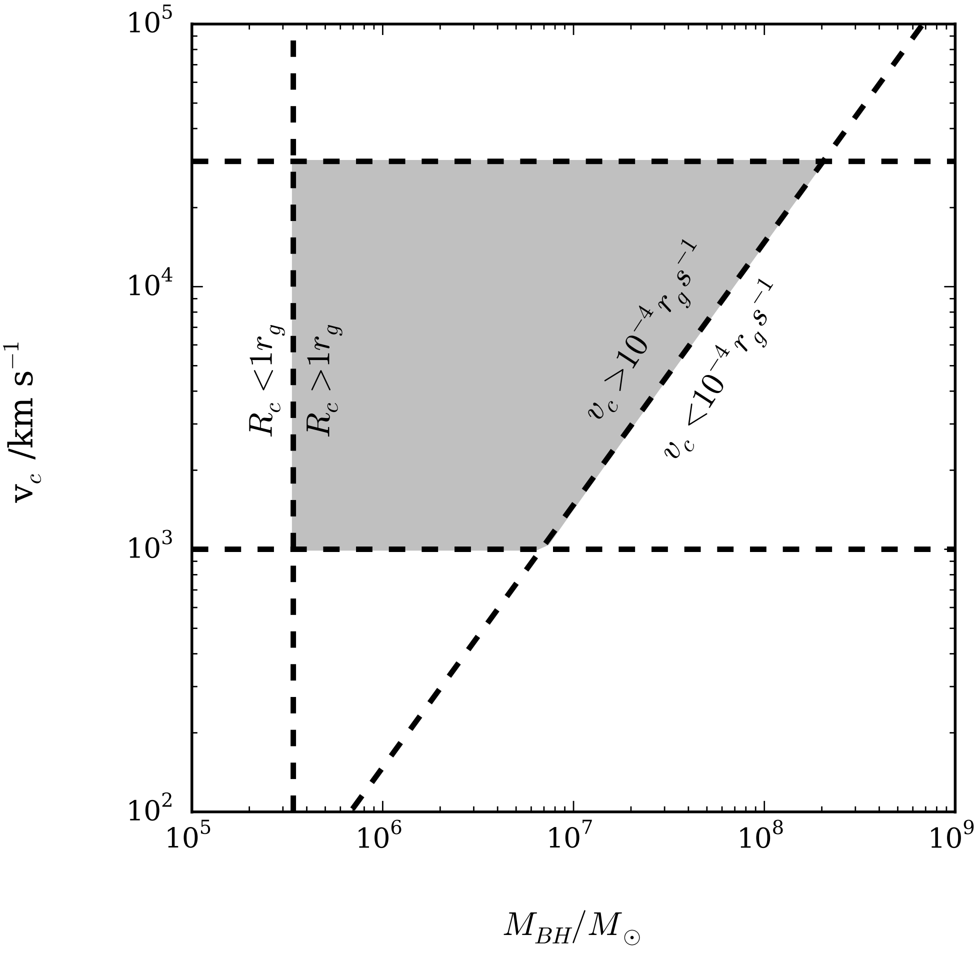

Figure 3.6: Parameters space of allowed BLR clouds velocities and SMBH masses. The range of velocities of the BLR clouds are contained between the two horizontal lines ($v_c = 1000 - 30000\,\mathrm{km\,s^{-1}}$). The vertical line is the set of points where $1\,r_g$ equals the lower limit of the radius of a BLR cloud, i.e. 5×10^{11} cm. To the left of this line, the clouds are too small to be part of the BLR. The oblique line represents the velocity of the BLR clouds crossing the region of interest ($50\,r_g$) in 500 ks, i.e. at $v_c = 10^{-4}\,r_g\,\mathrm{s}^{-1}$. To the right of this line, the clouds are too slow to produce one complete eclipse within the observation time. Within this framework, we focus on systems inside the shaded region.

3.5 Exploring the parameters space

First we set the viewing angle with respect to the normal to the disc to 45°, as we expect occultation events to be more common in AGN viewed at intermediate inclinations. The procedure we perform in order to explore the space of parameters of our absorption model is the following: first of all we build model predicted spectra so that these are physically plausible, i.e. we force the X–ray flux to be $F_{2-10} \sim 10^{-11}\,\mathrm{erg\,cm^{-2}\,s^{-1}}$ and the reflection fraction to be between 1 and 2. Then, for every position of the cloud we compute the flux in three energy bands, namely a soft band ($0.3 - 0.7\,\mathrm{keV}$), an intermediate band ($1 - 4\,\mathrm{keV}$), and a hard band ($7 - 10\,\mathrm{keV}$). We do this separately for the continuum and the reflected emission in order to disentangle the effect of the obscuring cloud over the two components of the spectrum. The power of this technique is two–fold: on one side, any asymmetry in these light curves would be indicative of asymmetries in the emission from the disc and / or its surroundings, and therefore it would indicate relativistic effects. On the other side, by studying the properties of the eclipsing cloud itself, we would be able to probe the nature of the regions responsible for the primary and the reprocessed emissions.

After the characterization of the test clouds and their effects in every band of each one of the spectral components, we proceed to analyse the H / S ratio lightcurves with the goal of checking if any of those effects could be eventually detected in a model–independent way. In a real observation, this will be the previous step to the model fitting to real data, since any asymmetry in the H / S lightcurve like the ones described previously indicates that relativistic effects may be playing a role.

For a comprehensive view of all the simulations carried out in the following sections, see Appendix B.

3.5.1 The Compton–thick neutral obscuring cloud

It is thought that the SMBH spin measurements are biased towards high values in AGN surveys, since the central engine environment determines the accretion rate (see e.g. Brenneman et al., 2011; Reynolds et al., 2012). If that is so, high spin sources are expected to be more luminous; therefore, they are over–represented in all flux–limited surveys. Therefore, in the next paragraphs we are presenting results in a system characterized by a maximally spinning Kerr black hole ($a^* = 0.998$).

We are interested on eclipsing events by clouds of the BLR, so that we set the cloud column density to produce Compton–thick absorption ($N_\mathrm{H} = 10^{24}\,\mathrm{cm^{-2}}$). We will study the effect of ionized clouds in Section 3.5.3, but for now we stick to the neutral case ($\xi = 10^{-3}\,\mathrm{erg\,cm\,s^{-1}}$).

Absorption by a Compton–thick, neutral cloud on a system characterized by maximally Kerr rotation will be studied under three extreme physical situations associated with the compactness of the regions from which both continuum and reprocessed spectral components arise.

Continuum and reprocessed emission from extended regions

Let us first consider the case of a large X–ray source, with typical size of several tens r_g, namely we explore here the case of an extended corona of radius $r^{(\mathrm{cor.})} = 10\,r_\mathrm{g}$. In order to make the region from which the reprocessed emission arises comparable in size to that from which continuum does,

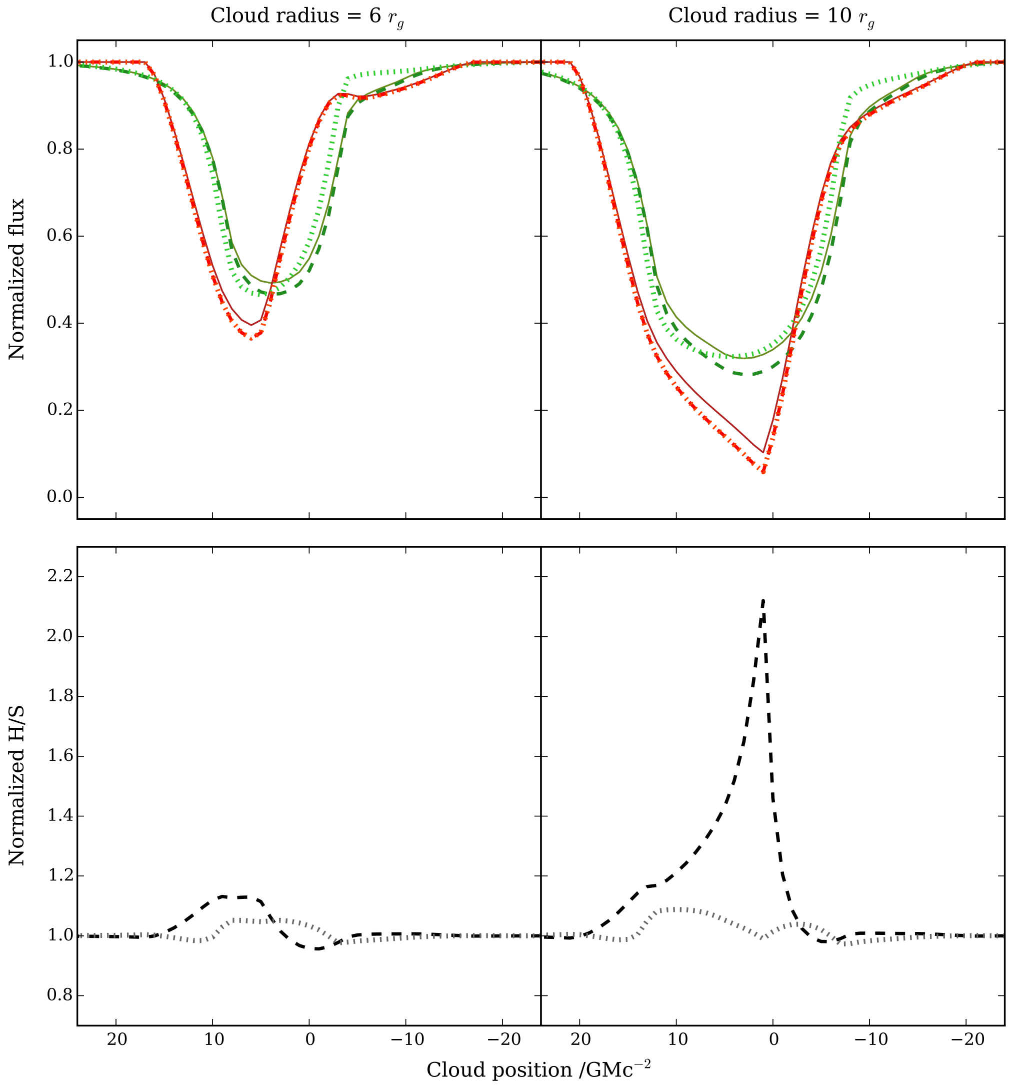

Figure 3.7: Upper row: Lightcurves of a neutral Compton–thick eclipse by a cloud with $N_{\mathrm{H}} = 10^{24}\,\mathrm{cm}^{-2}$ and $\log\xi = -3$. Continuum and reprocessed emission arise from extended regions: the outer radius of the corona is $10\,r_{\mathrm{g}}$ and the emissivity index of the disc is $q = 3$. Reddish lines are for the continuum, while greenish lines represent the reprocessed component. Dotted lines are for the soft X–ray band (0.3–0.7 keV), dashed lines are for the intermediate band (1–4 keV), and solid lines for the hard one (7–10 keV). Notice that the continuum soft and intermediate curves are overlapped.
Lower row: Two hardness ratio lightcurves. The hard band is 7–10 keV in both cases. We used the other two as soft bands: 0.3–0.7 keV (dotted grey lines) and 1–4 keV (dashed black lines), respectively.
In the left panels the cloud radius is $r = 6\,r_{\mathrm{g}}$, while in the right panels it is $r = 10\,r_{\mathrm{g}}$.

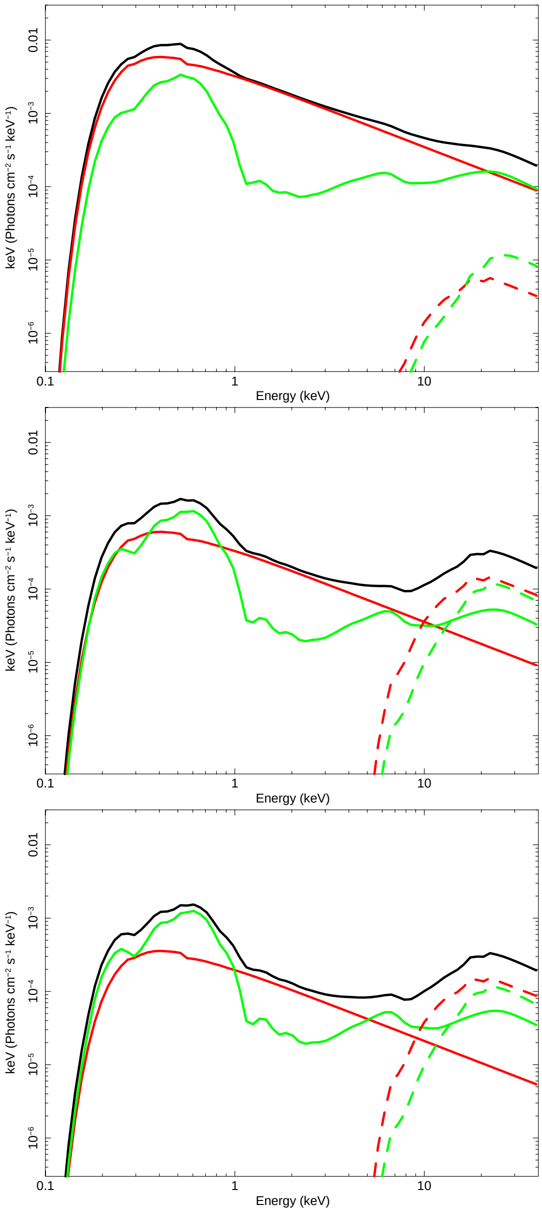

Figure 3.8: Continuum and reprocessed spectral components during an eclipse by a neutral Compton–thick cloud of radius $10\,r_{\mathrm{g}}$. The system is characterized by a maximally Kerr black hole, a $10\,r_{\mathrm{g}}$ radius corona, relatively low emissivity index ($q = 3$) implying reflection from extended regions within the disc, and an inclination of 45° with respect to our LOS. In red we show the continuum component and in green the reprocessed emission one. The solid lines indicate flux that is not affected by the cloud, while dashed lines are the for the flux corresponding to photons that have gone through it. In the top panel we show the almost–unabsorbed spectra, corresponding to when the cloud is at $20\,r_{\mathrm{g}}$. In the middle panel we show the spectra as seen when occultation of the reprocessed component is maximum (cloud at $3\,r_{\mathrm{g}}$), while the continuum component still dominates all over the spectrum above 1 keV. In the bottom panel we show the spectra when covering of the continuum component is the largest (cloud at $1\,r_{\mathrm{g}}$), when the continuum dominates in the $1-4$ keV band but reprocessed emission does in the hard band.

we choose a relatively low emissivity index of $q = 3$, meaning that at least 99% of the reprocessed emission comes from orbits with radii closer than $12\,r_\mathrm{g}$ to the black hole, and more than 95% from the innermost $6\,r_\mathrm{g}$. We performed several simulations of Compton–thick neutral clouds eclipsing both regions, and the results are shown in Fig. 3.7 (an extended set of simulations is included in Figs. B.1–B.8 in Appendix B).

We explain first the flux lightcurves, in the upper row. In the left panel we show an eclipse produced by an obscuring cloud of radius $6\,r_\mathrm{g}$. Its size, smaller than the continuum and reprocessed–radiation emitting regions, makes it possible to probe their emission patterns and the differences between them. The continuum absorption (red) peaks first in any of the X–ray bands, when the cloud is at $7\,r_\mathrm{g}$. The maximum absorption of the reflected component (green) occurs later, with the cloud at $4\,r_\mathrm{g}$, so that we can conclude that most of the reprocessed spectral component arises from further in on the approaching side of the accretion disc than that of the continuum.

In the right panel we show this eclipse as caused by a cloud of radius $10\,r_\mathrm{g}$, i.e. the same size as the corona. Only when the centre of the cloud is located at $1\,r_\mathrm{g}$ from the centre of the geometrical system, the continuum emission is maximally absorbed. Unlike for the continuum, the region from which the reprocessed component arises lacks a sharp boundary, so that the function of observed fluxes behaves in a much smoother way, with its minimum at $3\,r_\mathrm{g}$.

It is by construction that the two emitting regions are very similar in size, therefore the spectral contributions of each one of the components are entangled. In order to disentangle them, we look for their signatures within the H / S ratio lightcurves. These hardness ratios, shown in the lower row of Fig. 3.7, are constructed by dividing the hard band by the intermediate one (dashed black lines) and by the soft one (dotted grey lines), respectively. The signature of a neutral, Compton–thick cloud eclipsing an extended X–ray–emitting region depends on the bands chosen to produce the the H / S ratio lightcurves:

i) The (7-10)/(0.3-0.7) dotted grey lightcurves in the bottom panel of Fig. 3.7 are characterized by a small bump between two drops, with a third drop when the continuum emission is maximally absorbed when the cloud size is comparable to the continuum–emitting region size.

ii) The (7-10)/(1-4) dashed black lightcurves show first a bump, followed by a drop. The position of this drop depends on the cloud size: the larger the cloud is, the later the bump occurs (see middle column in Fig. B.6 in Appendix B for the whole series). These bumps are produced because the maximum absorption of the continuum and the reflected components take place at different moments of the eclipse. We find the bumps described here to be typical of extended emitting regions configurations.

In Fig. 3.8 we show the two spectral components during the $10\,r_\mathrm{g}$–cloud eclipse. It is shown that outside of the eclipse (upper panel), the continuum component dominates the broad band spectrum. However, when the covering of the reflection component is maximum (i.e. when the cloud is at $3\,r_\mathrm{g}$ from the centre of the system, see central panel), the dominant spectral component in the $0.3 - 0.7$ keV band is the reprocessed one. When the covering of the continuum component is maximum (at $1\,r_\mathrm{g}$, see bottom panel), the dominant spectral components in the soft and hard bands is the reprocessed one, while in the intermediate band the continuum keeps dominating the spectrum.

We can conclude that, when the kind of bumps preceeded and followed by drops as those described above are observed in the H / S ratio lightcurves, it is a potential signature of emission from extended regions, both of the continuum and the reflection components.

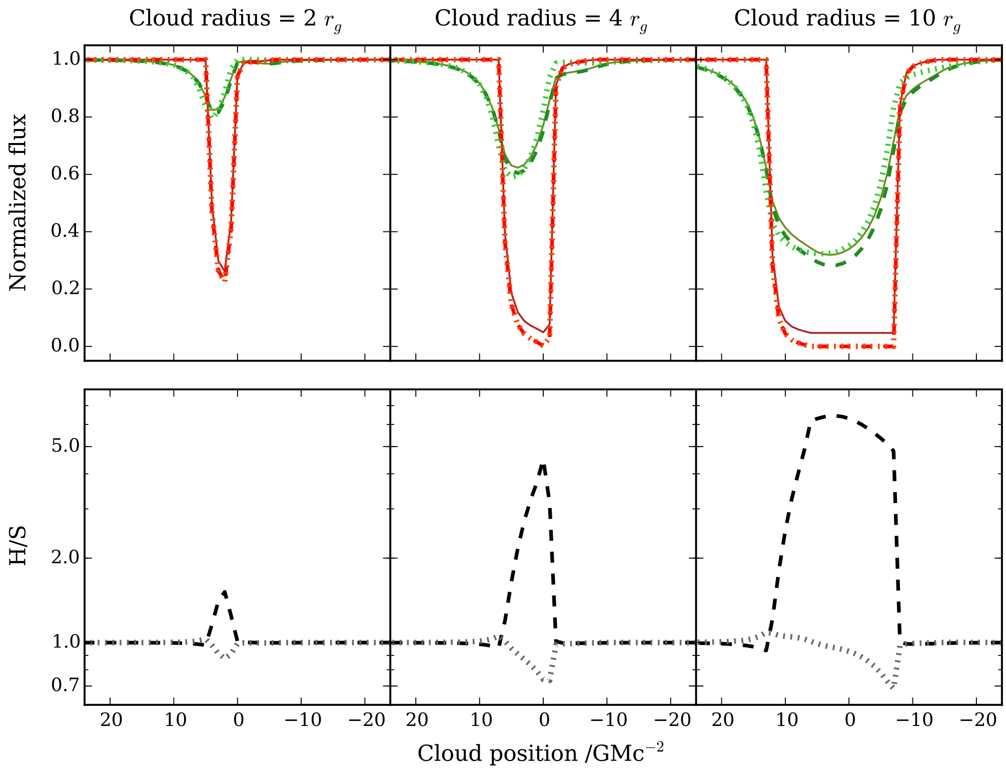

Figure 3.9: Upper row: Lightcurves of a neutral Compton–thick eclipse by a cloud with $N_H = 10^{24}\,\mathrm{cm}^{-2}$ and $\log\xi = -3$. Continuum emission arises from a compact corona with outer radius of $2\,r_g$. The reprocessed component arises from a extended region, given that the emissivity index of the disc is $q = 3$. Reddish lines are for the continuum, while greenish lines represent the reprocessed component. Dotted lines are for the soft X–ray band (0.3–0.7 keV), dashed lines are for the intermediate band (1–4 keV), and solid lines for the hard one (7–10 keV). Notice that the continuum soft and intermediate curves are overlapped. Lower row: Two hardness ratio lightcurves. The hard band is 7–10 keV in both cases. We used the other two as soft bands: 0.3–0.7 keV (dotted grey lines) and 1–4 keV (dashed black lines), respectively. In the left panels the cloud radius is $r = 2\,r_g$, in the middle panels it is $r = 4\,r_g$, and in the right panels it is $r = 10\,r_g$.

Continuum emission from compact corona, reflection from extended regions

A compact X–ray corona is typically $2 - 4\,r_g$ in size. Here we explore the case of a corona of radius $r^{(\mathrm{cor.})} = 2\,r_g$. We keep the same intermediate emissivity index as before, $q = 3$, meaning this that the continuum component comes from a much smaller region ($2\,r_g$) than the reprocessed component ($\sim 12\,r_g$). By construction, the two emitting regions sizes are very dissimilar, therefore we expect important differences between both components during an eclipse. Such differences can be seen in Figs. 3.9 and 3.10 (more simulations are shown in Figs. B.9–B.12 in Appendix B).

As in the previous case, we first focus on the normalized flux lightcurves, depicted in the upper row of Fig. 3.9. In the left and middle panels we show an eclipse produced by an obscuring cloud of radius 2 and 4 r_g, respectively. Its size is comparable to that of the continuum source region, but smaller than the reprocessed emission region, giving rise to important differences between them. The continuum absorption gets its maximum later (at $2\,r_g$) than in the reprocessed component ($4\,r_g$), as expected given the compactness of the continuum–emitting region.

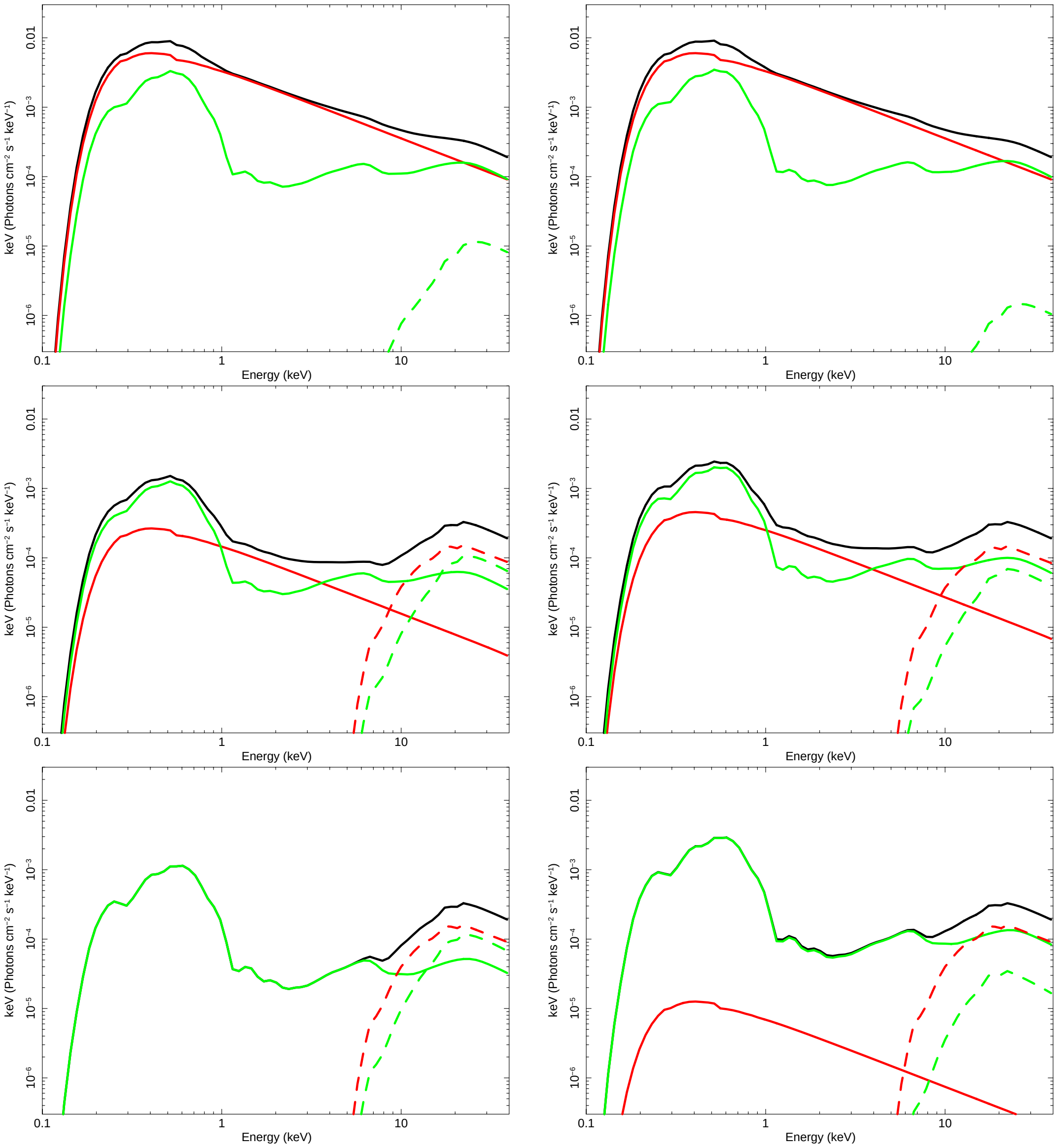

Figure 3.10: Continuum and reprocessed spectral components during an eclipse by neutral Compton–thick clouds of radius $10\,r_g$ (left panels) and $4\,r_g$ (right panels). The system is characterized by a maximally Kerr black hole, a $2\,r_g$ radius corona, relatively low emissivity index ($q = 3$) implying reflection from a much larger area in the disc (99% of the flux from within $12\,r_g$). The inclination angle of the system with respect to our LOS is 45°. In red we show the continuum component and in green the reprocessed emission one. The solid lines indicate flux that is not affected by the cloud, while dashed lines are the for the flux corresponding to photons that have gone through it. In the top panels we show the almost–unabsorbed spectra, corresponding to when the cloud is at $20\,r_g$. In the middle–left–hand panel we show the spectra as seen when the $10\,r_g$–radius cloud is at $10\,r_g$, when the continuum component dominates in the $1 - 4$ keV band and the reprocessed component does between 7 and 10 keV. In the middle–right–hand panel we show the spectra corresponding to the $4\,r_g$–radius cloud at $4\,r_g$, when absorption of the reflection component is maximum, producing the same situation as in the left–hand panel. In the bottom panels we show the spectra when covering of the continuum component is the largest (cloud at $3\,r_g$ on the left–hand–panel, and at $0\,r_g$ on the right). As a consequence of this, the reflection component dominates in the whole X–ray band up to around 10 keV.

In the right panel of the same figure, we show the eclipse by a cloud of radius $10\,r_{\rm g}$, which is much larger than the corona and about the same size as the reprocessing region. Absorption of the continuum is maximum for a wide range of positions of the cloud: from 8 to $-8\,r_{\rm g}$; however, it is zero when the cloud is further away than $12\,r_{\rm g}$ from the centre. The flux lightcurve of the reprocessed component, with its minimum at $3\,r_{\rm g}$, shows a much smoother profile, given that the reprocessing region is extended and a does not have a sharp end.

The signature of a compact corona with respect to the size of the reprocessing region within the hardness ratio lightcurves is shown in the lower row of Fig. 3.9. By dividing the hard band by the soft one (i) and by the intermediate one (ii), respectively, we get two sets of lightcurves:

i) The (7-10)/(0.3-0.7) lightcurves are characterized by a slow drop during the time while the source is gradually covered, followed by a steep increase when the eclipse ends (dotted grey lines in Fig. 3.9).

ii) The (7-10)/(1-4) lightcurves increase during the first part of the eclipse, and then sharply decrease when the cloud moves away. When the cloud is larger than the X–ray–reprocessing region, there is a smooth transition between the two halves of the eclipse (see right panel of Fig. 3.9). The duration of this transition is proportional to the cloud radius, independently of its column density and ionization state (see Figs. B.10 and B.12 in Appendix B).

In Fig. 3.10 we show the two spectral components during the $10\,r_{\rm g}$ (left) and the $4\,r_{\rm g}$ (right) cloud eclipse. Outside the eclipse (upper row), the continuum component dominates the broad band spectrum, while during the eclipse of the innermost regions, the dominant spectral component up to 10 keV is the reprocessed component (lower row). In the intermediate stages of the eclipse (central row), the reflection dominates in the soft and hard bands, while the intermediate band is still dominated by the continuum emission from the corona, hich explains the increase of the (7-10)/(1-4) ratio lightcurves during the eclipse of the innermost regions.

Then, we conclude that when a smooth decrease in the (7-10)/(0.3-0.7) lightcurve followed by a steep increase, simultaneously accompanied by a bump in the (7-10)/(1-4) lightcurve, it is the signature of a geometry characterized by a compact corona and an extended reflection region.

Continuum and reprocessed emission from compact regions

Now we explore the case of a corona of radius $r^{\rm (cor.)} = 4\,r_{\rm g}$, which can be still considered compact, but we introduce the steep emissivity index case, with $q = 7$. This means that more than 95% of the reprocessed component radiation comes from the first $2\,r_{\rm g}$, and more than 99.9% from the first $4\,r_{\rm g}$, i.e. the reflection arises from a region comparable in size to the compact corona. Therefore we would expect similar flux diminishment in both components during an eclipse. Differences between the shape of the lightcurves and also in the moment when absorption gets higher could be used to constrain the system's geometry. We performed several eclipse simulations, and the results are shown in Fig. 3.11. An extended set of simulations is included in Figs. B.13–B.16 in Appendix B.

As in the two cases studied previously, we first analyze the flux lightcurves (upper row of Fig. 3.11). In the left / right panel we show an eclipse produced by an obscuring cloud of radius $4\,/\,6\,r_{\rm g}$. Its size, comparable to / slightly larger than the continuum–emitting and reprocessing regions, make it the ideal probe to study the innermost regions of the central engine. The continuum absorption peaks first when the $4\,r_{\rm g}$–cloud is at $2\,r_{\rm g}$, followed immediately by the reflection, at $1\,r_{\rm g}$ (left

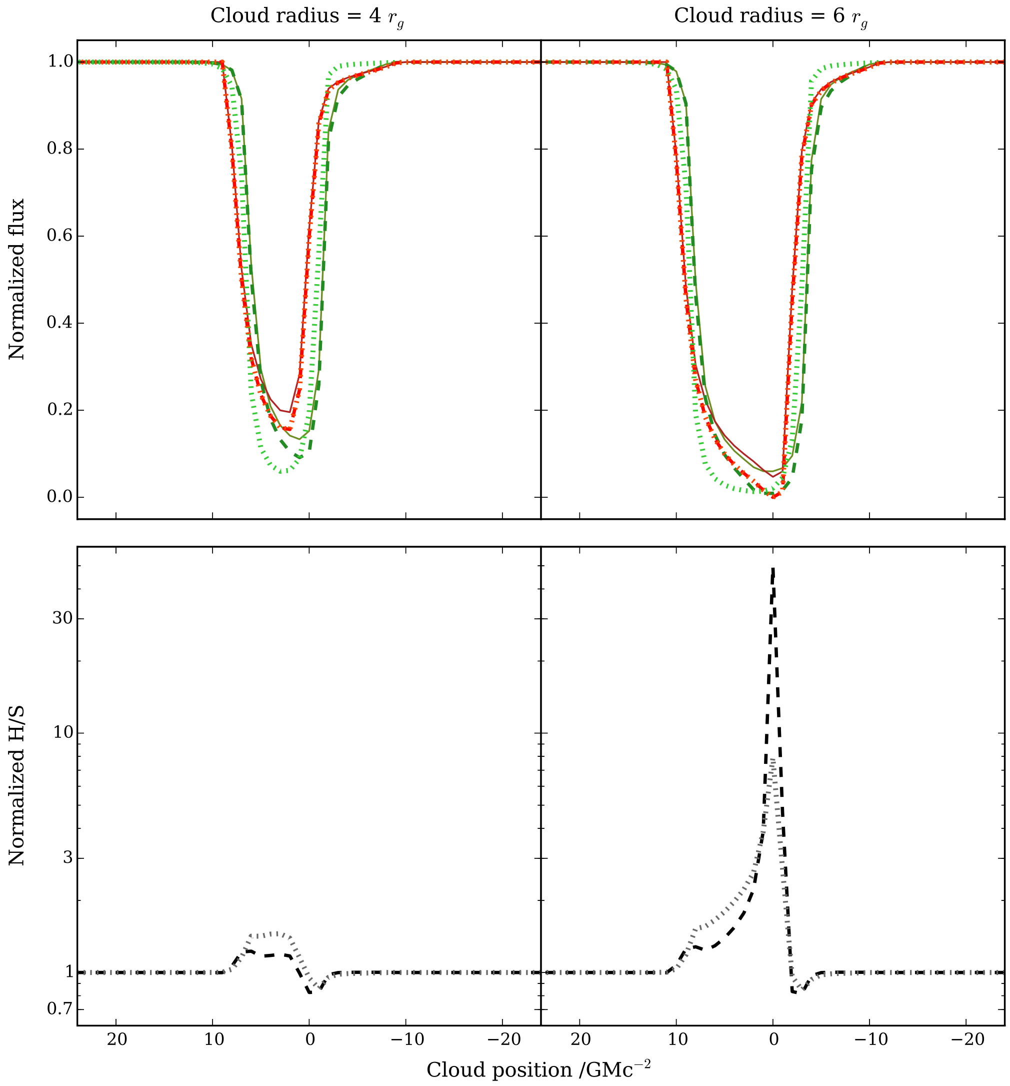

Figure 3.11: Upper row: Lightcurves of a neutral Compton–thick eclipse by a cloud with $N_{\rm H} = 10^{24}\,\rm cm^{-2}$ and $\log\xi = -3$. Continuum and reprocessed emission arise from compact regions: the outer radius of the corona is $4\,r_{\rm g}$ and the emissivity index of the disc is $q = 7$. Reddish lines are for the continuum, while greenish lines represent the reprocessed component. Dotted lines are for the soft X–ray band (0.3–0.7 keV), dashed lines are for the intermediate band (1–4 keV), and solid lines for the hard one (7–10 keV). Notice that the continuum soft and intermediate curves are overlapped.
Lower row: Two hardness ratio lightcurves. The hard band is 7–10 keV in both cases. We used the other two as soft bands: 0.3–0.7 keV (dotted grey lines) and 1–4 keV (dashed black lines), respectively.
In the left panels the cloud radius is $r = 4\,r_{\rm g}$, while in the right panels it is $r = 6\,r_{\rm g}$.

panel of Fig. 3.11). For the case of a cloud slightly larger, the absorption of both components gets its maximum at the same time, when the cloud is over the centre of the system (right panel). In all cases, the occultation of the continuum component starts and ends before than the reflection eclipse. Also, the shape of the reflected component is smoother than that of the continuum. However, these lightcurves are in practice indistinguishable.

As in the first case (extended regions), the sizes of the two emitting regions are similar. The signatures in the H / S ratio lightcurves are shown in the lower row of Fig. 3.11. When the cloud and the source sizes are comparable (left panel), the signature is the same as in the extended sources case. However, when the cloud is larger (right panel), both the (7-10)/(1-4) and the (7-10)/(0.3-0.7) lightcurves have the same shape as in the case of extended sources eclipsed by a cloud comparable in size: first the hardness ratio increases gradually, and then it drops sharply down to a minimum located in a position determined by the size of the source (see also the middle column in Fig. B.14 in Appendix B).

We conclude that we can systematically distinguish among the three cases in a model–independent way, by looking for the different specific signatures in the H / S lightcurves: if we observe first a smooth decrease followed by a steep increase in the (7-10)/(0.3-0.7) lightcurve, and simultaneously there is a bump in the (7-10)/(1-4) lightcurve, then the geometry of the system is described by a compact corona and an extended reflection region. Otherwise, the corona and the reflection region will be comparable in size. In order to discern whether those regions are compact or extended, one must pay attention to the shape of the (7-10)/(1-4) lightcurve, since the intermediate 1–4 keV band is where the reflection component is expected to be lower. If the eclipse is produced by a cloud comparable in size to the emitting regions, the (7-10)/(1-4) lightcurve profile will gradually rise up to a sharp maximum, and then quicky get down when emission is extended. On the other hand, if the emitting regions are compact, the signature expected is a smooth bump followed by a similar drop. Finally, in the unlucky case of an eclipse produced by a cloud much larger or much smaller than the emitting regions, the extended and compact configurations will be virtually undistinguishable in practice from the H / S lightcurves.

3.5.2 Compton–thin vs. –thick cloud

In order to study the influence of the cloud's column density on the absorption during an eclipse, we adopt a geometry with extended emission, both for the continuum and the reprocessed components ($r^{(cor.)} = 10\, r_g$, $q = 3$), in a maximally rotating system ($a = 0.998$). In the upper row of Fig. 3.12, we show the lightcurves depicting two eclipses by a neutral, slightly smaller (8–r_g) cloud. In the left–hand panel, the cloud is Compton–thin ($N_H = 10^{23}\,\mathrm{cm}^{-2}$). When absorption is maximum, its density is enough to absorb 72 and 76 % of the flux in the soft and intermediate bands, respectively. However, only 25 % of the flux in the hard band is absorbed. This gives cause for a smooth bump in the two H / S lightcurves shown in the lower left–hand panel in Fig. 3.12. In the right–hand panels, the cloud is Compton–thick ($N_H = 5 \times 10^{24}\,\mathrm{cm}^{-2}$). It absorbs the same amount of flux in the soft band (72 %, i.e. all of the flux from the regions behind the cloud, the remaining 28 % arising from radii larger than 8 r_g). The flux absorbed in the intermediate band is slightly larger than in the Compton–thin case (77 %). In the hard band, though, the absorption grows up to 75 % of the flux out of the eclipse (to be compared with the 25 % of flux absorbed in the Compton–thin case). The absorption by a Compton–thick cloud is, hence, about the same in all bands, so that the H / S lightcurves do not show any special feature other than the bump followed by a drop at a position depending on the cloud size, as previously described in the extended

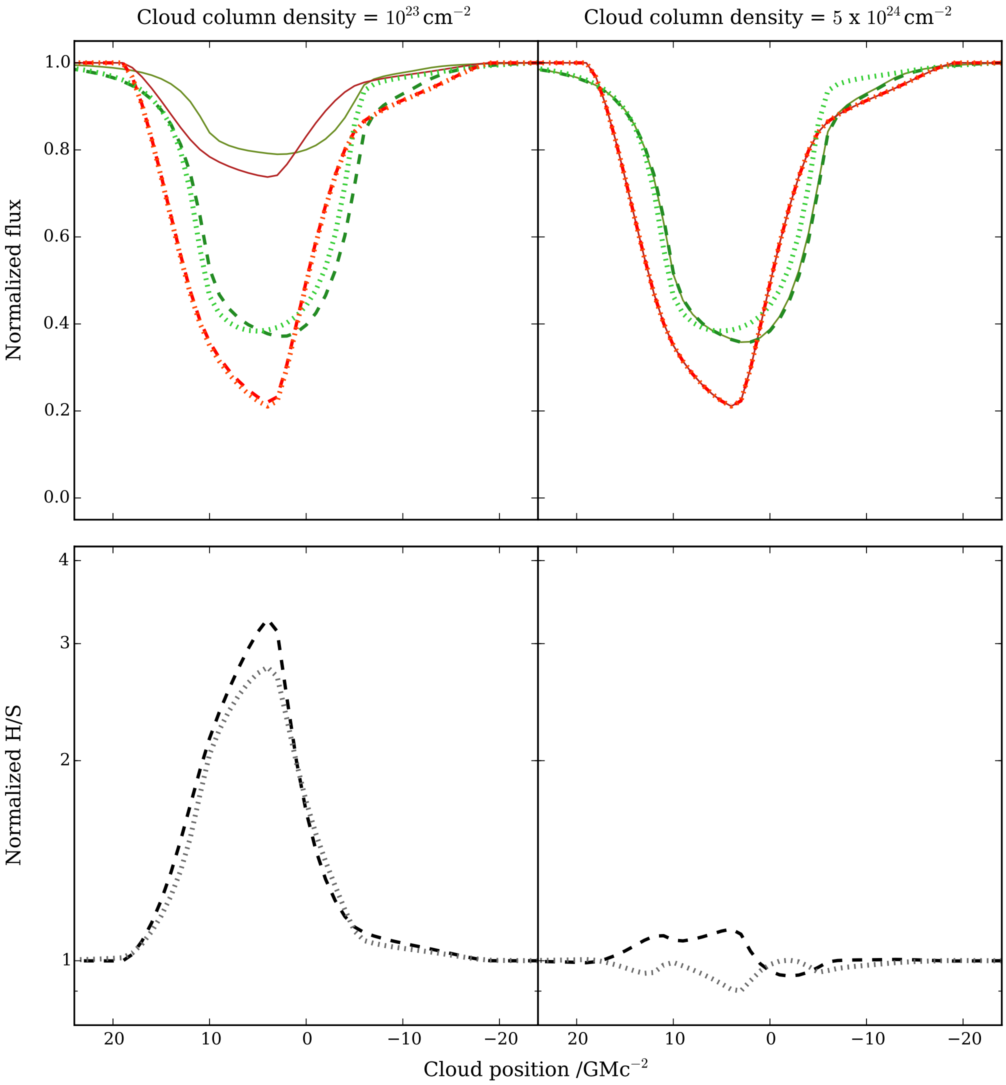

Figure 3.12: Upper row: Lightcurves of an eclipse by a neutral cloud with $\log \xi = -3$ and radius $r = 8\,r_g$. Extended emission geometry (corona outer radius: $10\,r_g$; emissivity index $q = 3$). Reddish lines are for the continuum, while greenish lines represent the reprocessed component. Dotted lines are for the soft X–ray band (0.3–0.7 keV), dashed lines are for the intermediate band (1–4 keV), and solid lines for the hard one (7–10 keV). Notice that the continuum soft and intermediate curves are overlapped.
Lower row: Two hardness ratio lightcurves. The hard band is 7–10 keV in both cases. We used the other two as soft bands: 0.3–0.7 keV (dotted grey lines) and 1–4 keV (dashed black lines), respectively.
In the left panels the cloud column density is $N_H = 10^{23}$ cm^{-2} (Compton–thin), while in the right panels it is $N_H = 5 \times 10^{24}$ cm^{-2} (Compton–thick).

regions case (see lower right–hand panel of Fig. 3.12, as well as Figs. B.6 and B.8 in Appendix B).

On the one hand, we conclude that a Compton–thin cloud is enough to block all the radiation in the 0.3 − 0.7 keV band, and most of it between 1 and 4 keV. However, a cloud 50 times thicker is needed in order to absorb photons in the 7 − 10 keV band with the same efficiency as in the soft and intermediate bands. On the other hand, we can distinguish between Compton–thin and –thick clouds in a model independent way, by looking for long, smooth bumps in the H / S lightcurves, like the ones shown in the lower left–hand panel of Fig. 3.12.

3.5.3 Ionized vs. neutral cloud

Unlike the column density of the cloud, its ionization does not imply a dichotomy between the bands in terms of absorption. Its effect is much more uniform, in the sense that it applies to the broad band of both spectral components, independently of the system geometry. Fig. 3.13 shows the normalized flux (upper half) and H / S (lower half) lightcurves of different eclipses by a Compton–thin 6–$r_{\rm g}$–cloud. In the first and third rows, the eclipsing structure is ionized to a negligible level: $\xi = 10^{-3}\,{\rm erg\,cm\,s^{-1}}$, namely neutral. In the second and fourth rows, its ionization is $\xi = 10\,{\rm erg\,cm\,s^{-1}}$. We choose this value because we already get noticeable effects with it, although it implies a relatively low ionization as compared with those which are typical for BLR clouds ($\log\xi \sim 1 - 4$). However, we tried higher ionizations, getting similar results. The three cases of Section 3.5.1 are revisited: (i) in the left column the X–ray–emitting regions are extense ($r^{\rm (cor.)} = 10\,r_{\rm g}$, $q = 3$); (ii) in the middle column the continuum source is compact ($r^{\rm (cor.)} = 2\,r_{\rm g}$) but the reflection still arises from an extended region ($q = 3$); (iii) and in the right column the continuum and reprocessing X–ray regions are compact ($r^{\rm (cor.)} = 4\,r_{\rm g}$, $q = 7$). In the following paragraphs, we discuss first the normalized flux lightcurves in the first half of the figure, and then the H / S in the second half:

i) For the case of extense X–ray–emitting regions ($r^{\rm (cor.)} = 10\,r_{\rm g}$, $q = 3$, left column in Fig. 3.13), the flux absorbed in the soft band is 60%, independently of the cloud ionization state. In the intermediate band, 62% of the flux is absorbed by a neutral cloud, while it is 55% of it by an ionized cloud. For the hard band, 20% of the flux is absorbed by a neutral cloud, while an ionized cloud absorbs only 12% of it. The flux in the soft band of any spectral component when absorption is the largest, is the same when a neutral or an ionized cloud is involved in the eclipse. In the intermediate band, the difference between the flux absorbed by a neutral cloud and by one that is ionized is only about 11%. The largest difference occurs in the hard band, with a difference of up to 40%. Finally, there are no detectable differences between these two kinds of eclipses in the H / S lightcurves (left column, lower half of Fig. 3.13).

ii) When the continuum X–ray–emitting region is compact ($r^{\rm (cor.)} = 2\,r_{\rm g}$) but the reflection still arises from an extended region ($q = 3$, middle column in Fig. 3.13), most absorption occurs on the continuum spectral component. The total absorbed flux in the soft band during the maximum covering of an eclipse due to a neutral or ionized cloud is 83% (98% of the continuum emission and 53% of the reflection). In the intermediate band, 96% of the total flux is absorbed by a neutral cloud, but an ionized cloud absorbs 86% of the flux, i.e., absorption by an ionized cloud is 12% lower than that by a neutral one. Absorption in the hard band is much lower: a neutral cloud absorbs 30% of the flux between 7 and 10 keV, while the flux absorbed by an ionized cloud is only 17%, this is, 43% lower. As in the previous case, this behaviour does not cause any important difference between eclipses due to neutral or ionized clouds in the H / S lightcurves (see central column of Fig. 3.13).

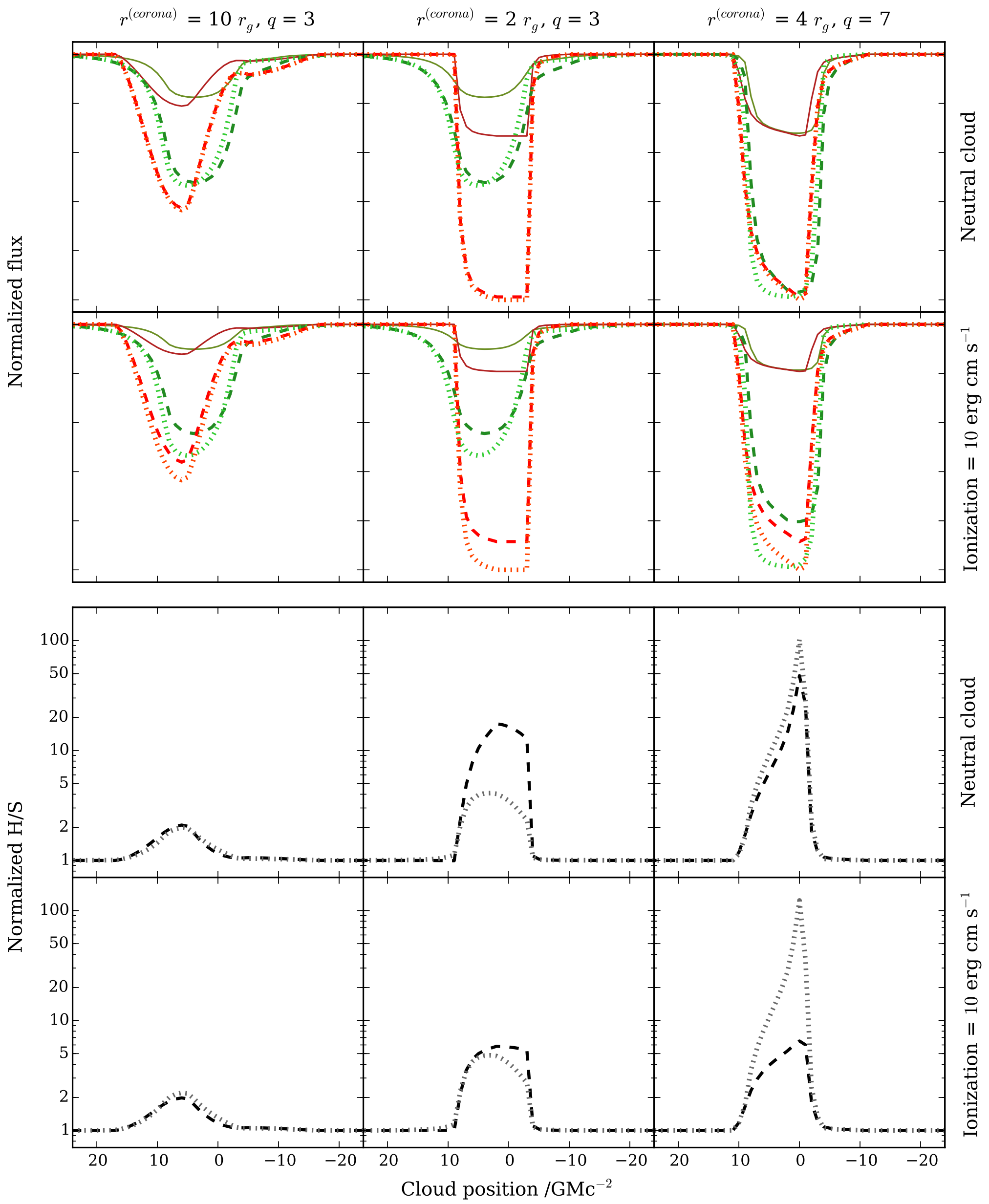

Figure 3.13: Upper half: Normalized flux lightcurves during eclipses by a Compton–thin 6–r_g–cloud. Reddish lines are for the continuum, while greenish lines represent the reprocessed component. Dotted lines are for the soft X–ray band (0.3–0.7 keV), dashed lines are for the intermediate band (1–4 keV), and solid lines for the hard one (7–10 keV). First row: neutral cloud (ξ = 10^{-3} erg cm s^{-1}). The continuum soft and intermediate curves are overlapped. Second row: ionized cloud (ξ = 10 erg cm s^{-1}). The continuum soft and intermediate curves do not overlap anymore.
Lower half: Two hardness ratio lightcurves. The hard band is 7–10 keV in both cases. We used the other two as soft bands: 0.3–0.7 keV (dotted grey lines) and 1–4 keV (dashed black lines), respectively. Third row: neutral cloud. Fourth row: ionized cloud.
Left column: extense X–ray–emitting regions. Middle column: compact corona, extended reprocessing region in the disc. Right column: compact X–ray–emitting regions.

iii) In the case of compact reprocessing regions ($r^{(\mathrm{cor.})} = 4\,r_\mathrm{g}$, $q = 7$, right column in Fig. 3.13), the reflected flux is reduced in a similar amount as the continuum flux, the same way as in the extended regions case. The largest absorption in the soft band during the eclipse is 99.3% of the flux, not depending on the ionization state of the 6–r_g cloud. In the intermediate band, a neutral / ionized cloud absorbs 98.6% / 87.6% of the flux, while in the hard band absorption reaches only 33% / 19% of the total flux. Therefore, the ionization state of the cloud does not make any difference in the absorption level of the flux on the 0.3–0.7 keV band. However, absorption in the intermediate band (1–4 keV) by a neutral cloud ($\xi = 10^{-3}\,\mathrm{erg\,cm\,s^{-1}}$) is 11% larger than with one ionized ($\xi = 10\,\mathrm{erg\,cm\,s^{-1}}$). In the hard X–rays band (7–10 keV), this difference is even larger, reaching 42%.

In general terms, we observe that the ionization state of the cloud is insignificant for the absorption in the soft band. Also, absorption in the intermediate band by a neutral cloud is about ~ 10% larger than by an ionized cloud ($\xi = 10\,\mathrm{erg\,cm\,s^{-1}}$), independently of the system geometry. In the hard band, this number reaches ~ 40%. Other ionizations, larger in several orders of magnitude (as those expected for BLR clouds or clumpy winds), produce similar effects as the ones described within this section due to a $10\,\mathrm{erg\,cm\,s^{-1}}$–ionized cloud. We must conclude that no signatures are left on the H / S lightcurves that could be used to discern the ionization state of the obscuring cloud.

3.5.4 The remarkable Schwarzschild case

As mentioned in Section 3.5.1, there is a bias on SMBH spin measurements towards high values, given that high spin sources are over–represented in flux–limited surveys. However, low spin rotation has been reported in several sources, justifying us to study the Schwarzschild case ($a = 0$).

As shown in Fig. 1.5, the ISCO is a function of the spin, being larger as the spin decreases. Specifically, the inner radii of the accretion disc and the corona, as we have defined them (coincidental with the ISCO), equal $6\,r_\mathrm{g}$ for the case of a Schwarzschild black hole. Taking the system's inclination into account, with a cloud of an appropriate size (smaller than the gap defined by the ISCO), we could in principle map the ISCO itself.

In this section we study the case of extended X–ray–emitting regions. We are compelled to do so because the inner limit of the active regions is already $6\,r_\mathrm{g}$ away from the central black hole. This way, we focus in the first case studied in Section 3.5.1: $r^{(\mathrm{cor.})} = 10\,r_\mathrm{g}$ and $q = 3$; i.e., the corona is sharply confined between 6 and $10\,r_\mathrm{g}$, while the reprocessing region emits at least 99% of the radiation from orbits closer than $60\,r_\mathrm{g}$ to the black hole, and more than 95% from the innermost $27\,r_\mathrm{g}$, down to the mentioned inner sharp boundary at $6\,r_\mathrm{g}$ (note that these numbers have changed respect to the ones in Section 3.5.1 due to the redefinition of the inner radius of the disc). Hence, the reprocessed component arises from a much more extensive region than the continuum does.

The cloud we use to simulate the lightcurves that would be observed during such an eclipse is chosen to be neutral ($\log \xi = -3$) to get as much broad band absorption as possible, and Compton–thin ($N_\mathrm{H} = 10^{23}\,\mathrm{cm^{-2}}$) in order to allow for different absorption degrees in the two energy bands. Its radius is fixed to $4\,r_\mathrm{g}$, because this way the existence of a certain interval during which the cloud is over the black hole shadow is favoured.

The eclipse lightcurves of the continuum and reprocessed spectral components are shown in the upper and middle panels of Fig. 3.14. The unabsorbed flux of the continuum component is one

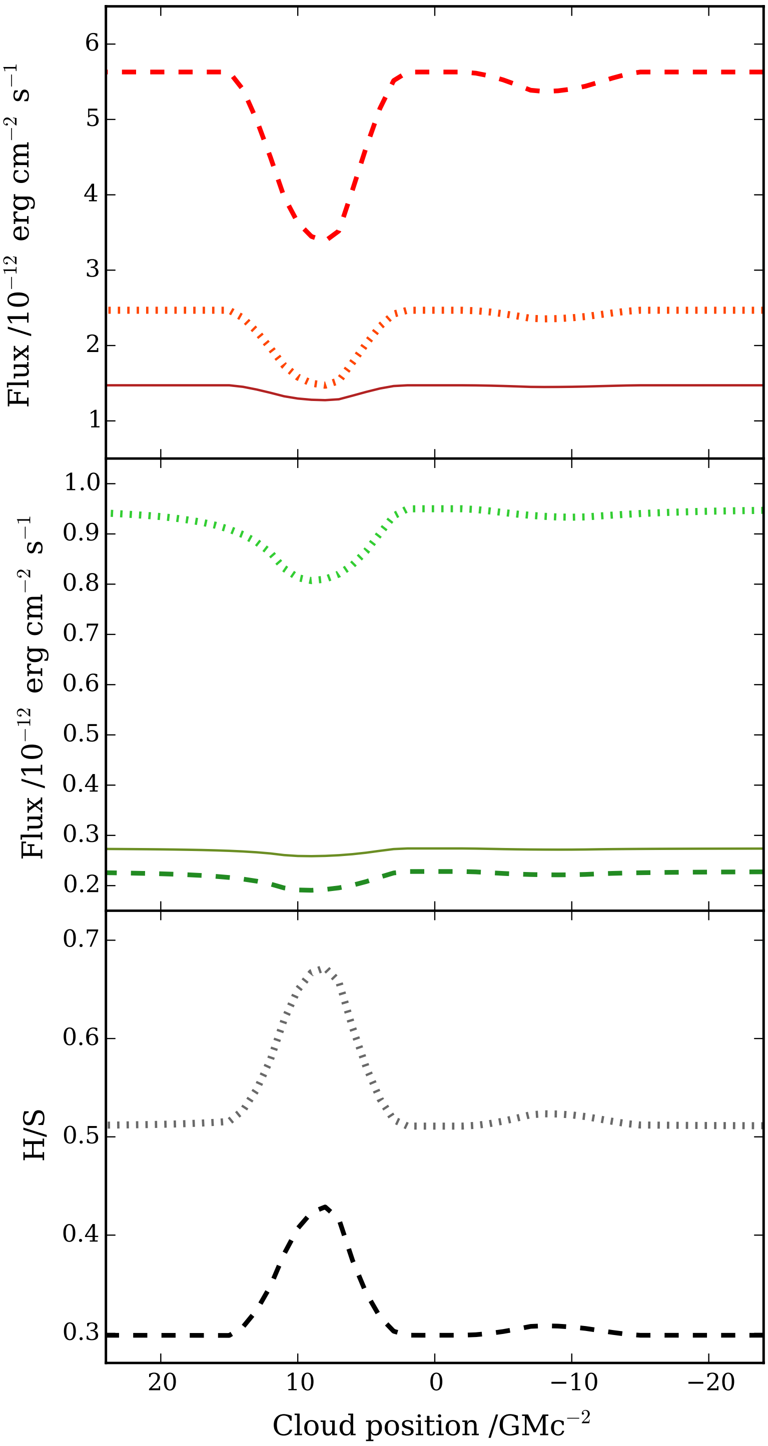

Figure 3.14: Lightcurves of the continuum (upper panel) and reprocessed (middle panel) spectral components during a neutral, $4\,r_\mathrm{g}$ Compton–thin cloud eclipse in a Schwarzshild black hole system. Dotted lines are for the soft X–ray band (0.3–0.7 keV), dashed lines are for the intermediate band (1–4 keV), and solid lines for the hard one (7–10 keV). Absorption depicts a double–peaked, asymmetric profile, with an unabsorbed plateau corresponding to a no radiation–emitting region.
Lower panel: H / S continuum–dominated lightcurves, showing the same features in a model–independent way. The hard band is 7–10 keV for both curves. We used the other two as soft bands: 0.3–0.7 keV (dotted grey lines) and 1–4 keV (dashed black lines), respectively.

order of magnitude greater than that of the reflected one. A characteristic double–peaked, asymmetric absorption profile is observed. The largest peak corresponds to absorption towards the approaching part of the disc, and the smallest to that towards its receding part, being the unabsorbed plateau in between due to the path followed by the cloud over the black hole shadow, from where no radiation emerges at all.

Absorption in the soft, intermediate, and hard bands of the continuum spectral component reaches 40.2, 39.8, and 13.4%, respectively, when the cloud is over the approaching side of the disc, at $\alpha = 8\, r_{\rm g}$ from the centre of the system. The secondary absorption peak occurs at $\alpha = -8\, r_{\rm g}$, with the cloud over its receding half. In this case, absorption is only 4.6% in the soft and intermediate bands, respectively, and 1.5% in the hard band. There is a plateau between the two peaks, where the flux is unabsorbed, corresponding to the cloud positions between 1 and $-1\, r_{\rm g}$, indicating an effective gap on the corona equivalent to $5\, r_{\rm g}$ in radius (given that the cloud itself has a radius of $4\, r_{\rm g}$).

In the reprocessed spectral component, absorption is much more smooth. The main absorption peak in the soft and intermediate bands get 14% and 15%, respectively, while in the hard band it is only 5%. Absorption in the minor peak reaches only 0.9, 1.9, and 0.5% in the soft, intermediate, and hard bands, respectively. It is worthy to mention that, while the continuum component is completely unabsorbed when the cloud is at a distance further than $\alpha = \pm 14\, r_{\rm g}$, the extense nature of the reprocessing region makes the reflected component to behave in a different way. When the cloud is located as far as at $\alpha = +20\,/\,-20\, r_{\rm g}$, absorption over the soft band reaches 1.65 / 0.52%, respectively; over the intermediate band it equals 2.00 / 0.51%; finally, on the hard one, it is 0.66 / 0.16%. However, the cloud positions for which this component is completely unabsorbed (i.e. the central plateau) span between $\alpha = -2$ and $+2\, r_{\rm g}$, pointing to a $6\, r_{\rm g}$ effective hole on the accretion disc.

The H / S ratio lightcurve of an eclipse characterized by the geometry and the parameters described above is shown in the lower panel of Fig. 3.14. It shows a plateau in the $(1, -1)\, r_{\rm g}$ region, and further away than $\pm 14\, r_{\rm g}$, as well as two peaks at $\pm 8\, r_{\rm g}$. This is clearly indicating that the continuum spectral component dominates over the reflection (which is not a surprise, since the flux of the first is one order of magnitude higher than that of the second in the whole energy range). Also, the principal peak measured over the plateau offset is 13 times higher than the secondary peak, which certainly is a measurable difference.

In conclusion, not only for this subsection, but for all Section 3.5, we propose the systematic analysis of unobscured AGN lightcurves in order to look for this kind of double–peaked asymmetric structures, and, if found, the application of our relativistic code for the eclipse characterization (see Chapter 6 for a thorough exposition on this issue). Again, for a complete catalog of H / S lightcurves, the interested reader is remitted to Appendix B.

3.6 Spectral–fitting to SWIFT J2127.4+5654 data

The singular shapes of the light curves described in Section 3.5, can explain the second rise observed in some other light curves detected in actual observations taken during BLR clouds eclipses. Risaliti et al. (2009b) describe variable partial covering in the time–resolved spectral analysis of the Seyfert galaxy NGC 1365, by using a model consisting of a constant continuum which is absorbed by a constant column density, plus a partial–covering component, with a different column density (constant as well) covered in a variable factor. The CF variations, shown in Fig. 3.15, are

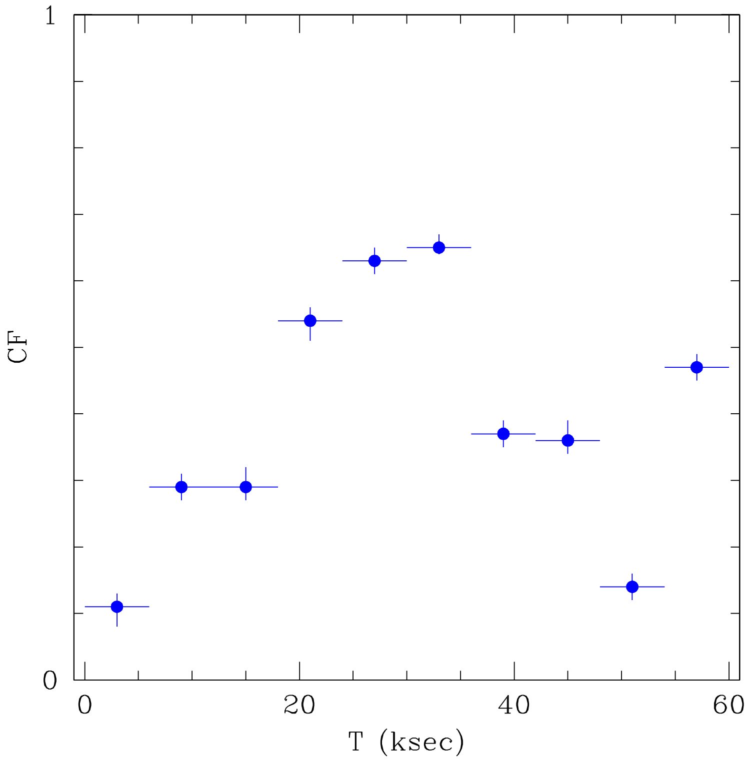

Figure 3.15: Covering fraction light curve of the partial covering component found in the Seyfert galaxy NGC 1365. Figure credit: Risaliti et al. (2009b). Notice the rise of the secondary peak at 55 – 60 ks.

highly significant and clearly show the signature of a complete transit of an eclipsing cloud. The same behaviour is shown by SWIFT J2127.4+5654 in Fig. 2.9. This inspires us to dig into the analysis of these relativistic effects by means of fits to real spectra. In the following paragraphs, we describe our study of GR effects in the eclipse detected in our *XMM–Newton* observation of SWIFT J2127.4+5654.

First we fix some parameters based in previous unabsorbed observations. The inclination angle of SWIFT J2127.4+5654 has been constrained by Miniutti et al. (2009) and by Patrick et al. (2011) to be $i = (46 \pm 4)^\circ$ and $i = \left(43^{+5}_{-10}\right)^\circ$ respectively. Therefore, we fix it to the central value of the common interval, $i = 45^\circ$. Also, we fix the SMBH spin to that computed by Marinucci et al. (2014) as $a = 0.58^{+0.11}_{-0.17}$, consistent with those given by Miniutti et al. (2009), Patrick et al. (2011), and Sanfrutos et al. (2013).

The photon index of the power law has been computed by several authors ($\Gamma = 2.06 \pm 0.03$, $\Gamma = 2.13^{+0.04}_{-0.03}$, $\Gamma = 2.08 \pm 0.01$ by Miniutti et al., 2009; Patrick et al., 2011; Marinucci et al., 2014, respectively). For simplicity, we stick to the value obtained by Sanfrutos et al. (2013), $\Gamma = 2.00 \pm 0.04$ (see also Chapter 2).

The emissivity index of the disc ranges in the literature from as low as $q = 2.6^{+1.0}_{-0.4}$ (as computed from 2007 *Swift* and *Suzaku* observations by Patrick et al., 2011, who explain that an increase in this parameter could be counterbalanced by larger absorption) to $q = 6.3^{+1.1}_{-1.0}$ as given by Marinucci et al. (2014) from 2012 *NuSTAR* and *XMM–Newton* data. Miniutti et al. (2009) get $q = 5.3^{+1.7}_{-1.4}$ from 2007 *Suzaku* observations. These two last values are consistent with what is explained in Chapter 2 and published by Sanfrutos et al. (2013) from 2010 *XMM–Newton* data, $q = 4.9 \pm 0.9$, so that we choose to fix this value.

Metal abundances are calculated as $A_{Fe} = 1.5 \pm 0.3$, $A_{Fe} = 0.3 \pm 0.2$ and $A_{Fe} = 0.71 \pm 0.05$ by Miniutti et al. (2009), Patrick et al. (2011), and Marinucci et al. (2014) respectively, so that we choose to stick to solar abundances. The ionization of the reflector is $\xi = 40^{+70}_{-35}$, $\xi < 13$ and $\xi < 8\,\mathrm{erg\,cm\,s^{-1}}$ for Miniutti et al. (2009), Patrick et al. (2011), and Marinucci et al. (2014) respectively, so that we cling to the value computed by Sanfrutos et al. (2013), $\xi = (10 \pm 6)\,\mathrm{erg\,cm\,s^{-1}}$. We adopt the high–energy cutoff $E_c = \left(108^{+11}_{-10}\right)\mathrm{keV}$, as given by Marinucci et al. (2014).

We fix too the column density of the neutral eclipsing cloud to the value derived in Chapter 2 (Sanfrutos et al., 2013), $N_\mathrm{H} = 2 \times 10^{22}\,\mathrm{cm^{-2}}$.

Finally, we assume that the cloud follows a Keplerian orbit co–rotating with the SMBH and the accretion disc, moving at velocity $v_c \leq 2100\,\mathrm{km\,s^{-1}}$, as shown in Chapter 2 and published by Sanfrutos et al. (2013). For a black hole mass of $M_{BH} = 1.5 \times 10^7\,M_\odot$, this is $v_c \leq 0.095\,r_\mathrm{g}\,\mathrm{ks^{-1}}$. The occultation event described in Chapter 2 lasts 126.4 ks, so that considering the upper limit in the velocity as the correct value, the cloud would travel a distance of $12\,r_\mathrm{g}$ within this lapse. As explained in Chapter 2, we divide the spectra in 24 equal sub–spectra (s1–s24), consequently each one of these sub–spectra covers $0.5\,r_\mathrm{g}$ in the cloud's orbit. We force the position $\alpha = 0\,r_\mathrm{g}$ to coincide with the lowest flux observations, i.e. between the spectra s16 and s17, so that our observation starts when the cloud is at $\alpha = 8\,r_\mathrm{g}$ and ends when it reaches $\alpha = -4\,r_\mathrm{g}$. The positions of the eclipsing cloud during each one of the 24 spectra are fix to the values shown in Table 3.2.

Then, the only parameters that are not frozen are the normalizations of the power law and the reflection component, and the radii of the obscuring cloud and the corona. These four parameters are free to vary. The normalization of the reflection component, as well as the cloud and source radii are constrained to be the same for all of the 24 spectra. The normalizations of the power law

Table 3.2: Position of the cloud for every spectrum of SWIFT J2127.4+5654 data

Spectrum	1	2	3	4	5	6	7	8
α (r_g)	7.75	7.25	6.75	6.25	5.75	5.25	4.75	4.25
Spectrum	9	10	11	12	13	14	15	16
α (r_g)	3.75	3.25	2.75	2.25	1.75	1.25	0.75	0.25
Spectrum	17	18	19	20	21	22	23	24
α (r_g)	-0.25	-0.75	-1.25	-1.75	-2.25	-2.75	-3.25	-3.75

Table 3.3: Fits of GR absorption model to SWIFT J2127.4+5654 data

Spectra	1, 6, 12	1, 6, 12, 17, 24	2, 5, 8, 10, 14	1–24
Fit	‘A1’	‘B1’	‘C1’	‘D1’
N_H	2^f	2^f	2^f	2^f
$r^{(\text{cloud})}$	2.5 ± 0.2	3.8 ± 0.3	3.1 ± 0.2	4.9 ± 0.2
$r^{(\text{source})}$	4.9 ± 0.2	6.0 ± 0.4	5.5 ± 0.2	7.8 ± 0.2
nors. PL	4.9 − 18.4	2.5 − 7.8	3.1 − 8.5	0.8 − 3.4
nor. REF	2.3 ± 0.3	1.3 ± 0.3	0.9 ± 0.3	1.4 ± 0.2
χ^2/dof	$678/586 \sim 1.16$	$1804/1298 \sim 1.39$	$1580/1393 \sim 1.13$	$10854/6643 \sim 1.63$
Fit	‘A2’	‘B2’	‘C2’	‘D2’
N_H	6.0 ± 1.0	14 ± 3	13 ± 3	17.5 ± 1.0
$r^{(\text{cloud})}$	2.8 ± 0.3	3.0 ± 1.0	3.1 ± 0.2	5.2 ± 0.1
$r^{(\text{source})}$	4.9 ± 0.2	5.0 ± 0.2	6.4 ± 0.4	9.0 ± 0.2
nors. PL	5.7 − 17.0	7.2 − 17.8	1.6 − 4.4	0.5 − 2.2
nor. REF	2.0 ± 0.6	3.4 ± 0.4	2.4 ± 0.5	6.8 ± 0.3
χ^2/dof	$591/585 \sim 1.01$	$1369/1297 \sim 1.06$	$1358/1392 \sim 0.98$	$8312/6642 \sim 1.25$

Column densities (N_H) are given in units of 10^{22} cm^{-2}. Radii (r) of the cloud and the source are given in r_g. Normalizations are expressed in units of $\times 10^{-4}$ photons keV^{-1} cm^{-2} s^{-1} at 1 keV. Notice that for the power law, a range of normalizations is given, within which the normalization computed for every individual spectrum is held. The superscript ‘^{f}’ means that the parameter is frozen. We provide fit plots for the 3 and 5 spectra cases in Fig. 3.17.

are allowed to vary independently for every spectrum.

We performed fits with four different subsets of the 24 spectra extracted from the *XMM–Newton* observation and used in Section 2.4.2: (i) one with only three representative spectra (fit ‘A1’: spectra 1, 6, and 12, filled red circles in Fig. 3.16), (ii) one adding two spectra to the first set (fit ‘B1’: spectra 1, 6, 12, 17 and 24, filled and empty red circles in Fig. 3.16), (iii) one with five different representative spectra (fit ‘C1’: spectra 2, 5, 8, 10, and 14, green circles in Fig. 3.16), and (iv) one more with all the 24 spectra (fit ‘D1’: spectra 1–24). The reason for doing this is that the fitting process is very time–consuming, so that a lot of computation time is saved considering fewer spectra first, and adding the rest later. The spectra are numbered from left to right in Figs. 2.9 and 3.16. Spectra 1–16 are assumed to be extracted when the cloud eclipses part of the approaching half of the disc, while spectra 17–24 are taken when the cloud is over the receding half of the disc, so that those spectra considered in fits ‘A1’ and ‘C1’ are extracted during the covering phase of the eclipse, i.e. when the cloud covers parts of the approaching half of the disc only. In contrast, fits ‘B1’ and ‘D1’ are performed by using spectra taken during all stages of the eclipse, i.e. during the covering and uncovering phases.

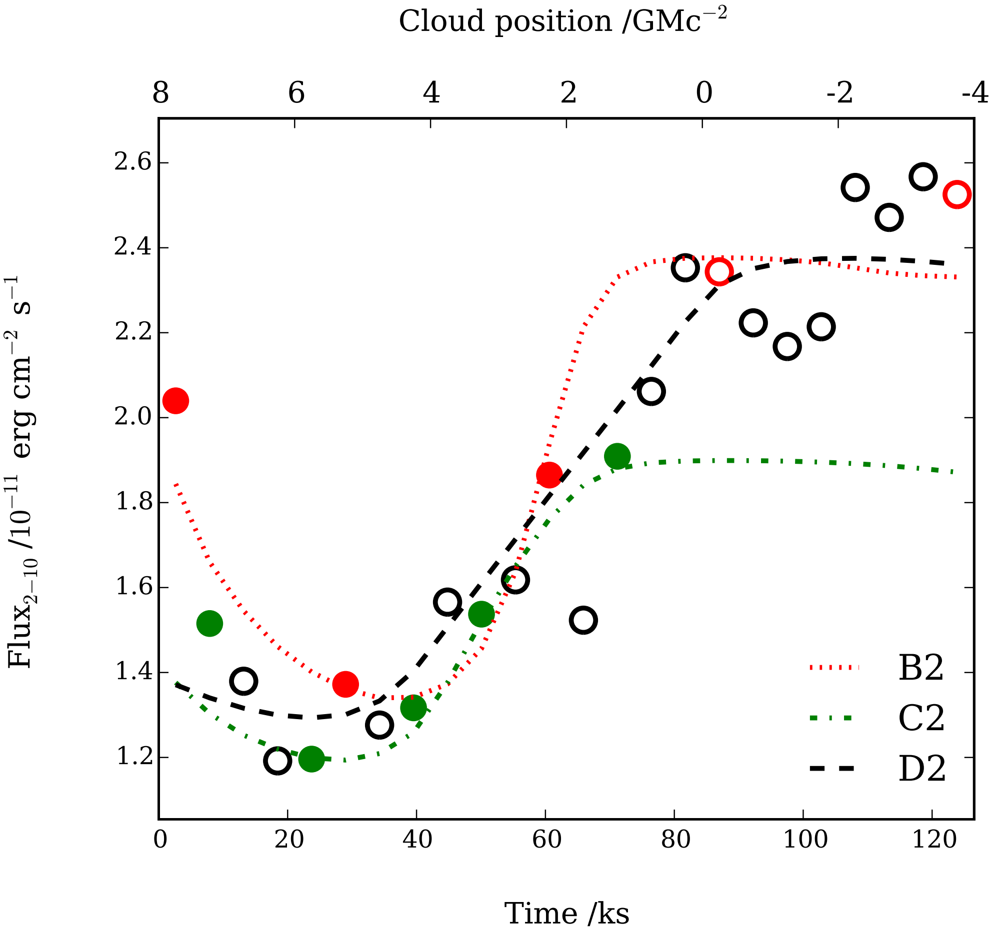

Figure 3.16: Evolution of the flux in the $2-10\,\mathrm{keV}$ band during the *XMM–Newton* observation of the eclipse in SWIFT J2127.4+5654. Filled red circles represent spectra 1, 6, and 12, as described in Table 3.3, with which fits 'A1' and 'A2' are performed. Empty red circles are for spectra 17 and 24. The five red circles mark the spectra with which fits 'B1' and 'B2' were performed. Green circles are for spectra 2, 5, 8, 10, and 14, and for fits 'C1' and 'C2'. All the 24 spectra were used in fits 'D1' and 'D2'. The dotted red line is the GR model predicted flux with spectral set 'B2' (five red points), the dot–dashed green line is for set 'C2' (five green points), and the dashed black line is for all the 24 spectra. We allow the cloud column density to vary in the three cases.

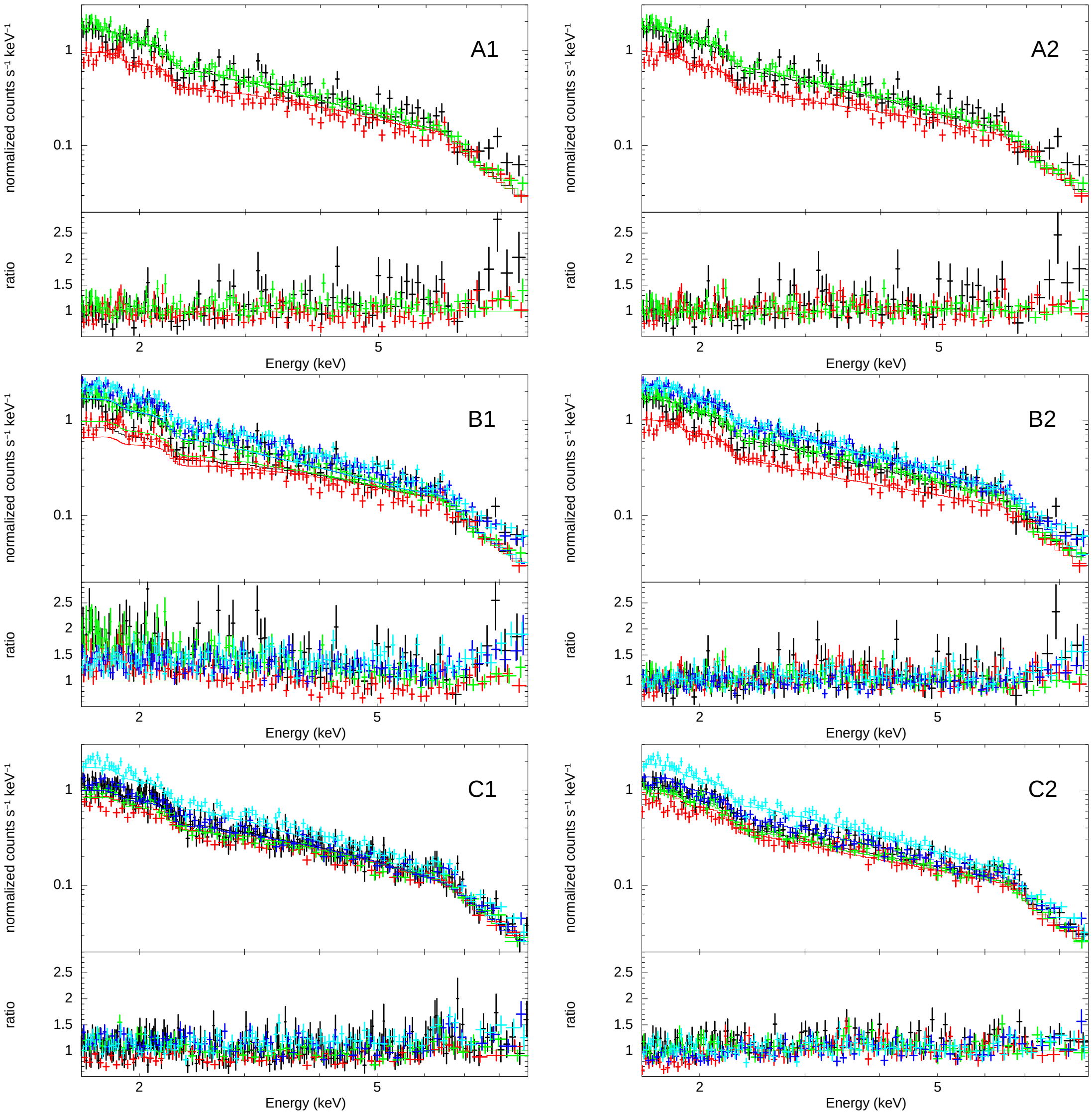

Figure 3.17: Best–fits of GR model to SWIFT J2127.4+5654 spectra. Left–hand panels: $N_{\rm H}$ is fixed to 2×10^{22} cm^{-2}. Right–hand panels: $N_{\rm H}$ is free to vary. The improvement of the fits when the column density of the cloud is freed becomes evident when comparing left–hand to right–hand panels. From top to bottom: fits to three (1, 6, 12), five (1, 6, 12, 17, 24), and other five (2, 5, 8, 10, 14) spectra. We do not show fits to 24 spectra for clarity reasons. Every panel is marked with the corresponding letter as coded in Table 3.3. The colours code is as follows. First and second rows: spectra 1, 6, and 12 are black, red, and green, respectively. Second row: spectra 17 and 24 are dark and light blue, respectively. Third row: spectra 2, 5, 8, 10, and 14 are black, red, green, dark blue and light blue, respectively.

The results of the four fits are shown in the upper block of Table 3.3. Fits ‘A1’ and ‘C1’ are good, with χ^2/dof between 1.1 and 1.2, but fits ‘B1’ and ‘D1’ are poorly constrained (χ^2/dof $\sim 1.4-1.6$). We further investigate any possible improvement by allowing the column density of the cloud to vary, and perform new fits with the same subsets: ‘A2’ (3 spectra), ‘B2’ and ‘C2’ (5 spectra), and ‘D2’ (24 spectra). All the fits get much better (χ^2/dof= 1.01, 1.06, 0.98, and 1.25, for subsets ‘A2’, ‘B2’, ‘C2’, and ‘D2’, respectively), as can be seen in the lower block of Table 3.3. The best–fit models and the data / model ratio of the GR model to three and five spectra of SWIFT J2127.4+5654 are shown in Fig. 3.17. Absorption is negligible in all spectra above $6-7$ keV, becoming important in the soft and intermediate X–rays. In the case of fit ‘A2’, flux in the $1-2$ keV band during spectrum 6 (red in panel ‘A2’ of Fig. 3.17) is $\sim 50\%$ lower than during spectrum 12 (green). In fit ‘B2’, the same flux during spectrum 6 is $\sim 60\%$ lower than during spectra 17 and 24 (blue in panel ‘B2’ of Fig. 3.17). In fit ‘C2’, flux during the most absorbed spectrum (no. 5, red in panel ‘C2’ of Fig. 3.17) is overestimated, so that we consider the second–most absorbed, spectrum 8 (green). The 1–2 flux is $\sim 40\%$ lower than during the less absorbed spectrum in the set (no. 14, light blue).

Fits ‘C’ and ‘A’ are the ones with better χ^2/dof. However, it is clear from Fig. 3.16 that ‘C2’ would not properly fit the spectral points taken during the occultation of the receding half of the disc. Therefore, we must discard this fit, as well as fits ‘C1’ and the two ‘A’ fits, for the same reason (although these fits are not shown for the sake of simplicity). A proper fit must then consider spectra from all the stages of the eclipse. Out of the remaining fits, the one that better constrains the system geometry is ‘B2’ (five spectra from all stages of the eclipse), with χ^2/dof= 1.06 (to be compared with χ^2/dof= 1.39, corresponding to the same fit but with a cloud column density fixed to 2×10^{22} cm^{-2}). According with the results of this fit, the source radius is $\sim 5\, r_{\rm g}$, the radius of the cloud is $\sim 3\, r_{\rm g}$, and its density $N_{\rm H} = 14 \pm 3 \times 10^{22}$ cm^{-2}. Also, fit ‘D2’ (considering all the 24 spectra) constrains well the parameters of the system, with χ^2/dof= 1.25 (to be compared with χ^2/dof= 1.63, corresponding to the same fit but with $N_{\rm H}$ fixed to 2×10^{22} cm^{-2}). The column density of the cloud is similar to that obtained from the fit to five points (‘B2’), namely $N_{\rm H} = (17.5\pm1.0)\times10^{22}$ cm^{-2}. The source and cloud radii are ~ 9 and $\sim 5\, r_{\rm g}$, respectively, i.e. both slightly larger than those obtained from the ‘B2’ fit. In any case, the ratio between the cloud and source sizes is approximately the same in both cases so far (as well as it is in the ‘B1’ and ‘D1’ fits): the cloud turns out to represent around $\sim 60\%$ of the source in size. In these two cases (‘B2’ and ‘D2’), the cloud is only a few times (less than one order of magnitude) thicker than when $N_{\rm H}$ was fixed (the ‘B1’ and ‘D1’ fits), with column densities ranging from ~ 1.1 up to $\sim 1.85\times10^{23}$ cm^{-2} (after taking errors into account), in stead of the originally fixed value of 2×10^{22} cm^{-2}. These results on the geometry of the system are complementary to those obtained when the GR eclipsing cloud code was not used (see Section 2.5), with cloud and source sizes $D_{\rm c} \leq 7\, r_{\rm g}$, and $D_{\rm s} \leq 10.5\, r_{\rm g}$, respectively.

3.7 Summary and conclusions of Chapter 3

Along this chapter we have derived some promising preliminary results. In Section 3.3 we have defined a model for the continuum X–ray emission plus the reflection component convolved with the relativistic kernel KYNCONV (Dovčiak et al., 2004), accounting for GR effects due to the proximity of the material in the inner accretion disc to the SMBH. We show in Section 3.5 that the occultation of these regions produces peculiar light curves depending on the size and nature of the eclipsing cloud, as well as on the sizes of the corona and the X–ray–reprocessing regions.

The study of such light curves allows us to discern how the flux–emission is distributed over the corona and the reprocessing regions within the accretion disc, and more specifically, permits us to use the hardness ratio lightcurves produced during an eclipse in a routine way in order to distinguish between compact and extended corona cases in a model–independent way. We can assert that the emission measured from our point of view is anisotropic: it is much larger from the parts of the disc that are running towards us in their orbital motion around the SMBH than from its receding parts. This is clearly an effect of Doppler boosting, so that its detection would be a strong indication that GR effects do indeed imprint the AGN X–ray spectra. However, any other interpretations for the detection of these kind of signatures should be addressed and discarded before asseverating that GR effects in the innermost regions of AGN can be characterised from the analysis of their X–ray spectra.

We may have already detected these disc emission anisotropies during some of these BLR clouds eclipses, since the peculiar shapes of the light curves are remarkably similar to those shown in Figs. 2.9, 3.15, and 2.3. This encourages us to deepen the study of these relativistic effects by fitting real spectra. In Section 3.6 we explored the detectability of GR effects in various subsets of the 24 X–ray spectra taken along the occultation event at SWIFT J2127.4+5654, described in Chapter 2. We find that our data are consistent with a system characterized by parameters found in previous studies ($i = 45°$, $a = 0.58$, $q = 4.9$), eclipsed by a Compton–thin, ionized cloud ($N_{\rm H} \sim 10^{23}\,{\rm cm}^{-2}$, $\xi \sim 10\,{\rm erg\,cm\,s}^{-1}$) moving at $2100\,{\rm km\,s}^{-1}$. The corona and the reprocessing region are consistent with being plane–parallel annuli, both with inner radius of $3.9\,r_{\rm g}$. The outer radius of the corona is between 5 and $9\,r_{\rm g}$. The radius of the obscuring cloud is between 3 and $5\,r_{\rm g}$. These results are consistent with those derived in Chapter 2.

4

The ionized outflowing clumpy torus in ESO 323–G77

This chapter is largely adapted from an article entitled "The ionized X–ray outflowing torus in ESO 323–G77: low–ionization clumps confined by homogeneous warm absorbers" ('paper II', Sanfrutos et al., 2016b, MNRAS, 457, 510), second part of the article "The properties of the clumpy torus and BLR in the polar–scattered Seyfert 1 galaxy ESO 323–G77 through X–ray absorption variability" ('paper I', Miniutti et al., 2014, MNRAS, 437, 1776), of which I was second author and contributed significantly. First I am introducing extensively the results obtained in 'paper I', and then I will deepen in the work done in 'paper II'.

In 'paper I' we reported results from 10 X–ray observations of the polar–scattered Seyfert 1.2 galaxy ESO 323–G77, obtained in seven epochs between 2006 and 2013 with *XMM–Newton*, *Swift*, *Chandra*, and *Suzaku* (see Table 4.1). Variations of the column density of a neutral absorber on the way to the intrinsic nuclear continuum account unambiguously for the spectral variability detected, wich ranges in time from months to years. The column density of this neutral absorber was found to span from few 10^{22} cm^{-2} to few 10^{23} cm^{-2} in all of the observations except one, found to be Compton–thick. The observation of the source in such a state revealed a column density of $N_{\rm H} = 1.5 \times 10^{24}$ cm^{-2}. The large variability observed supposed a valuable chance to study the X–ray absorbers in an active galaxy. Those were identified as the clumpy torus and the BLR of the standard model. For the individual clumps of the torus, we measured an average density of $n_{\rm c}^{\rm TOR} \leq 1.7 \times 10^{8}$ cm^{-3} and an average column density of $N_{\rm H}^{\rm TOR} \sim 4 \times 10^{22}$ cm^{-2}. For the clouds in the BLR, we estimated average densities of $n_{\rm c}^{\rm BLR} \sim 0.1 - 8 \times 10^{9}$ cm^{-3} and average column densities of $N_{\rm H}^{\rm BLR} \sim 10^{23} - 10^{24}$ cm^{-2}. We were able also to estimate the torus half–opening angle from the properties of the clumpy torus, which turned out to be $\sim 47°$.

In 'paper II' we reported on the long– and short–term X–ray spectral analysis of ESO 323–G77, with six observations from three epochs between 2006 and 2013 with *Chandra* (observations 5–8)

Table 4.1: Reference observation number, X–ray mission, detector, observation (starting) date, and net spectral exposure of all X–ray observations used in this work.

#	Mission	Detector	Date	Net exp. [ks]
1	XMM	EPIC pn	2006-02-07	~ 23
2	Swift	XRT PC	2006-06-28	~ 2
3			2006-08-17	~ 4
4			2006-09-14	~ 2
5	Chandra	MEG / HEG	2010-04-14	~ 46
6			2010-04-19	~ 60
7			2010-04-21	~ 118
8			2010-04-24	~ 67
9	Suzaku	XIS(0,3) / PIN	2011-07-20	~ 88
10	XMM	EPIC pn	2013-01-17	~ 89

and *XMM–Newton* (observations 1 and 10) . Four high–resolution *Chandra* observations give us a unique opportunity to study the properties of the absorbers in detail, as well as their short time–scale (days) variability. From the rich set of absorption features seen in the *Chandra* data, we identify two warm absorbers with column densities and ionizations that are consistent with being constant on both short and long time–scales, suggesting that those are the signature of a rather homogeneous and extended outflow. A third absorber, ionized to a lesser degree, is also present and it replaces the strictly neutral absorber that is ubiquitously inferred from the X–ray analysis of obscured Compton–thin sources. This colder absorber appears to vary in column density on long time–scales, suggesting a non–homogeneous absorber. Moreover, its ionization responds to the nuclear luminosity variations on time–scales as short as a few days, indicating that the absorber is in photoionization equilibrium with the nuclear source on these time–scales. All components are consistent with being cospatial and located between the inner and outer edges of the so–called dusty, clumpy torus. Assuming cospatiality, the three phases also share the same pressure, suggesting that the warm / hot phases confine the colder, most likely clumpy, medium. We discuss further the properties of the outflow in comparison with the lower resolution *XMM–Newton* data.

4.1 Introduction

AGN ordinarily show X–ray spectral variability on months to years time–scales, which is often related to absorption phenomena (e.g. Risaliti et al., 2002; Miniutti et al., 2014; Agís-González et al., 2014). In many cases, such long–term absorption variability can be associated with the transit of dusty clouds in our LOS, which reveals the presence of a clumpy, dusty torus at relatively large spatial scales, see e.g. Markowitz et al. (2014); Agís-González et al. (2014).

In the last few years, various examples of absorption variability within time–scales as short as hours or days have been reported, such as in NGC 4388, NGC 4151, NGC 1365, NGC 7582, and SWIFT J2127.4+5654, as reported in Elvis et al. (2004), Puccetti et al. (2007), Risaliti et al. (2009b), Bianchi et al. (2009), and Sanfrutos et al. (2013), respectively. As an example, the in–depth study of the short time–scale absorption variability in SWIFT J2127.4+5654 reveals unambiguously the transit of a single cloud in the LOS to a fairly compact X–ray source (few gravitational radii in size). Usually, the short time–scale absorption variability data are in good agreement with the existence of a set of dense, cold clouds with characteristic column densities of 10^{23} to $10^{24}\,\mathrm{cm}^{-2}$, physical densities of 10^9 to $10^{11}\,\mathrm{cm}^{-3}$ and velocities of the order of $10^3\,\mathrm{km\,s}^{-1}$ orbiting the X–ray source at radii of 10^3 to $10^4\,r_\mathrm{g}$, where $r_g = GM/c^2$ is the gravitational radius for a black hole of mass M. These properties suggest to identify the obscuring clouds with the same clouds that are responsible for the emission of broad optical / UV emission lines, i.e. with clouds in the BLR.

In the following we report results from four high–resolution *Chandra* observations of ESO 323–G77 taken between 2010 April 14 and 24. ESO 323–G77 is a bright (13.56 mag) polar–scattered Seyfert 1.2 galaxy (Véron-Cetty & Véron, 2006) at $z = 0.015$ (Dickens et al., 1986). It was first classified as an AGN by Fairall (1986). ESO 323–G77 is revealed to be a polar–scattered galaxy by the detection of high linear polarisation, ranging from ~ 2.2% at 8300 Å to ~ 7.5% at 3600 Å for the continuum (Schmid et al., 2003). Similar polarisation is found for the broad emission lines. The position angle of the polarisation is independent of wavelength, and perpendicular to the orientation of the [O III] ionization cone of the host galaxy. This suggests that the symmetry axis inclination of ESO 323–G77 is most likely of ~ 45° with respect to our LOS, intermediate between the characteristic inclination of Seyfert 1 and Seyfert 2 galaxies. Our viewing angle is therefore likely grazing the edge of the obscuring matter, namely the torus of the unified model (Antonucci, 1993). In order to perform a more complete analysis and to compare the absorbers' properties at different epochs, data from two high–quality *XMM–Newton* observations are also included from 2006 February 7 (Jiménez-Bailón et al., 2008) and 2013 January 17 (Miniutti et al., 2014).

4.2 Previous results

In 'paper I' we found X–ray absorption as a consequence of the action of the clumpy torus, the clouds in the BLR, and a warm / hot outflowing medium. As already mentioned, these results were based on the 10 X–ray observations shown in Table 4.1.

The X–ray spectra of all observations reported in Table 4.1 are shown in Fig. 4.1. In the upper panel we show the full variability range observed in ESO 323–G77 from the highest quality observations. The remarkable spectral variability observed is most likely associated with X–ray absorption variations. In the bottom panel of the same figure, we show the *Swift* observations revealing the fastest variability event of the overall monitoring: observation 2 (black) is significantly more absorbed than observation 3 (red), performed ~ 2 months after.

4.2.1 The structure of ESO 323–G77

On the one hand, the clumpy torus is accountable for X–ray absorption by a column density of $2 - 6 \times 10^{22}\,\mathrm{cm}^{-2}$. Variability in the X–ray absorption on timescales shorter than 3.6 years and longer than a few months confirms its clumpiness. We deduce the size of torus clumps to be $D_\mathrm{c}^\mathrm{TOR} \geq 3.5 \times 10^{14}\,\mathrm{cm}$, with a typical number density $n_\mathrm{c}^\mathrm{TOR} \leq 1.7 \times 10^8\,\mathrm{cm}^{-3}$. The torus half–opening angle is estimated by combining the averaged clumps column density ($\sim 4 \times 10^{22}\,\mathrm{cm}^{-2}$) with the ratio of the absorption cross section for dusty gas to that for electrons only (see the formalism of Liu & Zhang, 2011). Thus, we estimate a torus half–opening angle of ~ 47°, i.e. our LOS grazes the torus, intercepting its atmosphere.

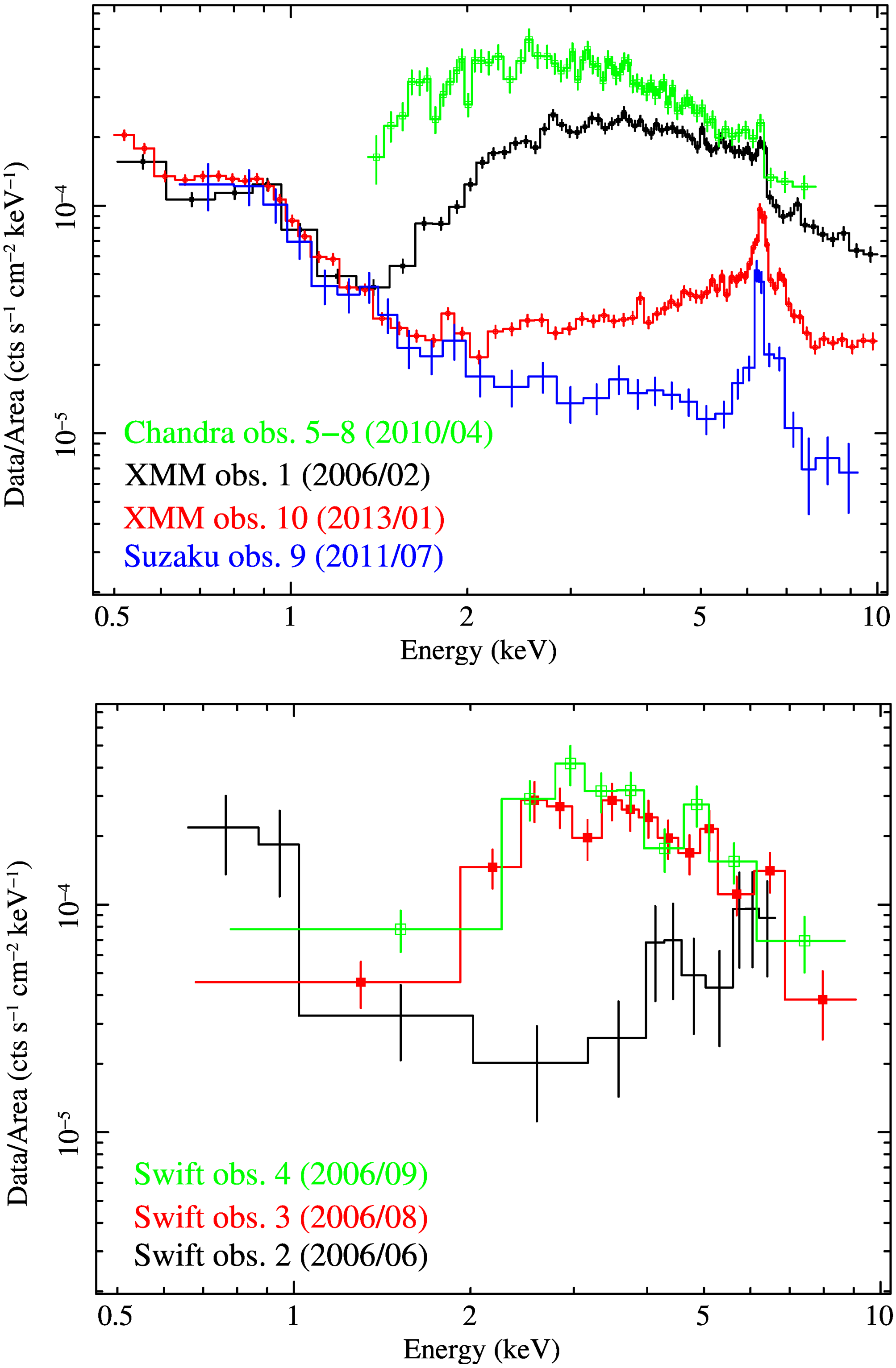

Figure 4.1: Up: range of X–ray absorption variability in ESO 323–G77 as observed with *XMM–Newton* (black for 2006, red for 2013), *Chandra* (green, only the High Energy Gratings (HEG) time–averaged data are shown for clarity), and *Suzaku* XIS (blue). Down: The *Swift* 2006 observations (black for June, red for August, green for September). Each spectrum has been rebinned for visual clarity and divided by the corresponding detector effective area to ease comparison.

On the other hand, X–ray absorption by column densities between 3×10^{23} and $3 \times 10^{24}\,\mathrm{cm}^{-2}$ is due to clouds in the BLR of the system. The X–ray variability allows us to estimate a typical BLR cloud size of $D_\mathrm{c}^\mathrm{BLR} = 0.9{-}50{\times}10^{14}$ cm, and number densities of $n_\mathrm{c}^\mathrm{BLR} = 0.1{-}8{\times}10^{9}\,\mathrm{cm}^{-3}$, in good agreement with the density required to produce the optical / UV broad emission lines. The number density is slightly lower than that deduced from occultation events in NGC 1365 and Mrk 766 (see Risaliti et al., 2009b, 2011a, respectively), which might mean that absorption in ESO 323–G77 takes place closer to the dust sublimation radius.

Finally, two highly–ionized, outflowing warm absorbers (first reported by Jiménez-Bailón et al., 2008) were confirmed. Their column densities are of the order of $\sim 10^{22} - 10^{23}\,\mathrm{cm}^{-2}$, and their outflow velocities are $1-4\times10^{3}\,\mathrm{km\,s}^{-1}$. One of the possible physical explanations for this outflow is that it is launched off the inner accretion disc as a wind. In the inner accretion disc regions, at typical radii of few hundreds r_g (see e.g. Risaliti & Elvis, 2010), radiation pressure is enough to boost gas up to escape velocities of $\sim 10^{4}\,\mathrm{km\,s}^{-1}$, i.e. one order of magnitude higher than what is observed. Therefore, the wind would have to move along a direction almost perpendicular to our LOS to be consistent with the velocity we estimate. This possibility is excluded, since our LOS has an inclination of $\sim 45°$ with respect to the system's axis (Schmid et al., 2003; Smith et al., 2004).

Assuming a given LOS–outflow misalignment of $0° - 25°$, and that the observed outflow velocity is actually the velocity component along our LOS, implies limits on the outflow launching radius of $R_\mathrm{wind} = 0.1 - 2.7 \times 10^{5}\,r_\mathrm{g} = 0.4 - 9.6 \times 10^{17}$ cm. This distance is of the order of (and slightly greater than) that of the BLR rather than that of the inner disc ($R_\mathrm{BLR} \sim 1 - 2 \times 10^{16}$ cm, Kaspi et al., 2005), therefore we pointed to the possibility that the ionized gas is the warm / hot medium existing in between the clouds in the BLR of the system, and pressure–confining them.

4.2.2 The Compton–thick nature of the absorber during the *Suzaku* observation

As can be seen in Fig. 4.1, the *Suzaku* observation is reflection–dominated. It presents a very prominent Fe Kα emission line, characterized by an equivalent width of ~ 800 eV. However, the X–ray Imaging Spectrometer (XIS) data (up to 10 keV) cannot discriminate between two different scenarios that can give rise to reflection–dominated spectra, namely (i) a Compton–thick state where the nuclear continuum is heavily absorbed only marginally contributing below 10 keV, or (ii) a switched–off state where the nuclear continuum is extremely dim, only leaving the reprocessed components below 10 keV.

The presence of the Hard X–ray Detector (HXD) on board *Suzaku* allows us to accurately measure the column density towards absorbed AGN. It is particularly useful the PIN detector, with good sensitivity up to tens of keV. However, the large FoV of the HXD ($34' \times 34'$) makes the PIN X–ray data to be contaminated by the nearby and relatively X–ray bright AGN ESO 323–G81, which is only $\sim 8.8'$ away from ESO 323–G77. The analysis of the spectra extracted of both ESO 323–G77 and ESO 323–G81 from the XIS 0 detector strongly suggests a nearly Compton–thick or Compton–thick state for the *Suzaku* observation of ESO 323–G77 (July 2011) with $N_\mathrm{H} \geq 9 \times 10^{23}\,\mathrm{cm}^{-2}$ at the 90% confidence level for any intrinsic flux of the source.

Summarizing, multi–epoch X–ray observations of ESO 323–G77 allowed us to study the properties of the broadband X–ray continuum and the X–ray absorption features. This way we were able to outline absorption by the clumps of the torus and the clouds in the BLR. A sketch of a possible geometry for the system of absorbers is shown in Fig. 4.2. The following sections are

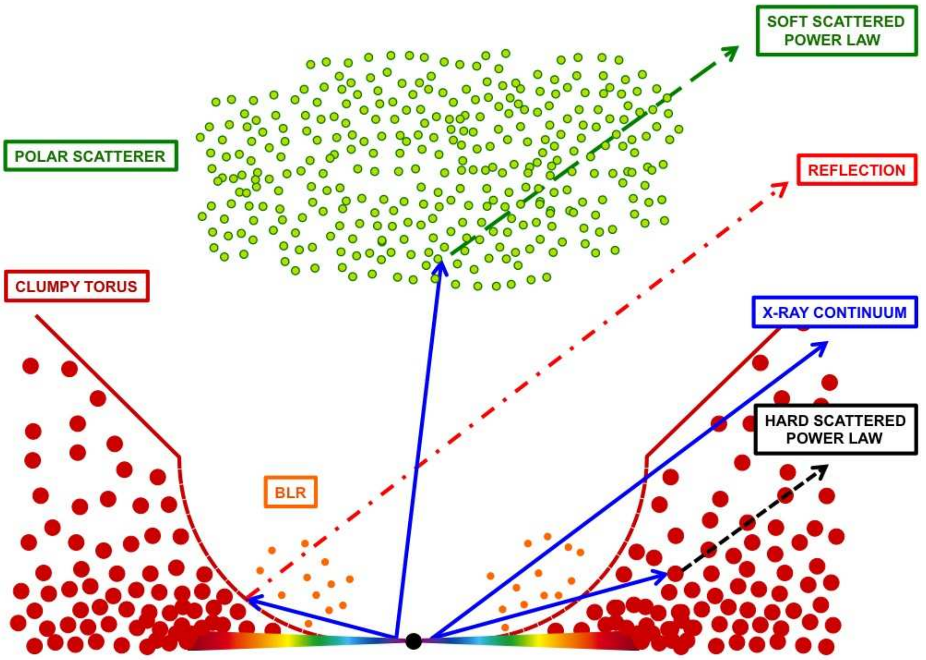

Figure 4.2: A sketch of a possible geometry for the system of absorbers, as suggested by the X–ray data. We assume an inclination angle of ~ 45°, and our LOS is on the right–hand–side of the figure. The intrinsic nuclear continuum is shown with solid blue lines and goes through one cloud of the clumpy torus. This situation is therefore appropriate for observations 1, 3, 4, and 5–8. The remaining observations correspond instead to one of the BLR clouds crossing our LOS. The continuum illuminates a polar scattering region which gives rise to the soft scattered power law component which is likely associated with part of the soft emission lines spectrum (long–dashed green line). For simplicity, we do not show star–forming regions that may be associated with the plasma emission model. The continuum also illuminates the far side of the clumpy torus which, at least at low latitudes, is likely optically–thick, producing the X–ray reflection spectrum (dot–dashed red line). Finally, the X–ray continuum intercepts clouds in the clumpy torus (and / or the BLR) out of our LOS. These clouds scatter part of the irradiating continuum into our LOS giving rise to a hard scattered power–law (short–dashed black line) that is absorbed by a different column density than the X–ray nuclear continuum, as it generally goes through a different system of clouds. Figure taken from Miniutti et al. (2014).

dedicated to the study of the warm absorbers in ESO 323–G77 through an extensive analysis of the high–resolution *Chandra* and *XMM–Newton* data.

4.3 X–ray Observations

XMM–Newton first observed ESO 323–G77 on 2006 February 7 for a total net exposure time of ~ 23 ks. Then, *Chandra* observed the source on four occasions in 2010 April with the HETGS: on the 14th (ID: 11848, for a total net exposure time of ~ 46 ks), on the 19th (ID: 12139, ~ 60 ks), on the 21st (ID: 11849, ~ 118 ks) and on the 24th (ID: 12204, ~ 67 ks). *XMM–Newton* observed the source again on 2013 January 17 for a total net exposure time of ~ 89 ks. Both *XMM–Newton* observations (IDs: 0300240501 and 0694170101 respectively) were performed in 'FULL WINDOW' mode with the optical 'THIN' filter applied. Standard data reduction was made with the SAS v12.0.1 software for *XMM–Newton* and with the CIAO v4.5 software for *Chandra*. Observation–dependent redistribution matrices and ancillary responses were generated as standard for every data set. Spectral analysis was performed using the XSPEC v12.8.1 software.

XMM–Newton EPIC source products were extracted from source–centred circular regions, and the corresponding background ones were estimated from source–free nearby areas. For the sake of simplicity, and after having checked the good agreement among the pn, MOS1 and MOS2 data, only EPIC-pn spectra in the 0.5–10 keV band are used in this study. Unfortunately, the RGS data do not offer enough spectral quality to be discussed in any of the available *XMM–Newton* observations, as discussed by Miniutti et al. (2014). As for *Chandra*, we use the MEG data in the 1.2–7 keV band, and the HEG ones in the 1.4–9 keV. Outside these energy bands, the high–resolution spectra are background dominated. We used these spectra in two forms: (i) separately when interested on the short time–scale variability of the absorbers, and (ii) merged into one single ~ 291 ks spectrum for each detector, representative of the broad–band X–ray continuum time–averaged over 10 days. The *XMM–Newton* spectra have been regrouped so that each bin contains 25 counts, while the *Chandra* spectra have been grouped to 4 channels per bin, and we use the χ^2 and C–statistic (Cash, 1979) for the *XMM–Newton* and *Chandra* spectral analysis respectively. Uncertainties correspond to the 90% confidence level for one interesting parameter, except if otherwise specified. Whenever fluxes were needed to be converted into luminosities, we have assumed a ΛCDM cosmology with $H_0 = 70\,\mathrm{km\,s^{-1}\,Mpc^{-1}}$, $\Omega_\Lambda = 0.73$, and $\Omega_M = 0.27$.

The X–ray spectra of the *XMM–Newton* and *Chandra* observations can be seen in Fig. 4.3. In order to facilitate comparison among them, all spectra have been divided by the effective area of each detector. Spectral variability on long time–scales is clearly present with absorption first decreasing between the first *XMM–Newton* observation (2006/02) and the *Chandra* one (2010/04) and then increasing significantly between the *Chandra* observation (2010/04) and the second *XMM–Newton* one (2013/01), as already studied in detail in our previous work on ESO 323–G77 (Miniutti et al., 2014).

4.4 The time–averaged 2010 *Chandra* spectrum

We start our analysis by considering the merged MEG and HEG data from *Chandra*, i.e. we consider the time–averaged, high–resolution *Chandra* data that are representative of the spectrum between 2010 April 14 and the 24.

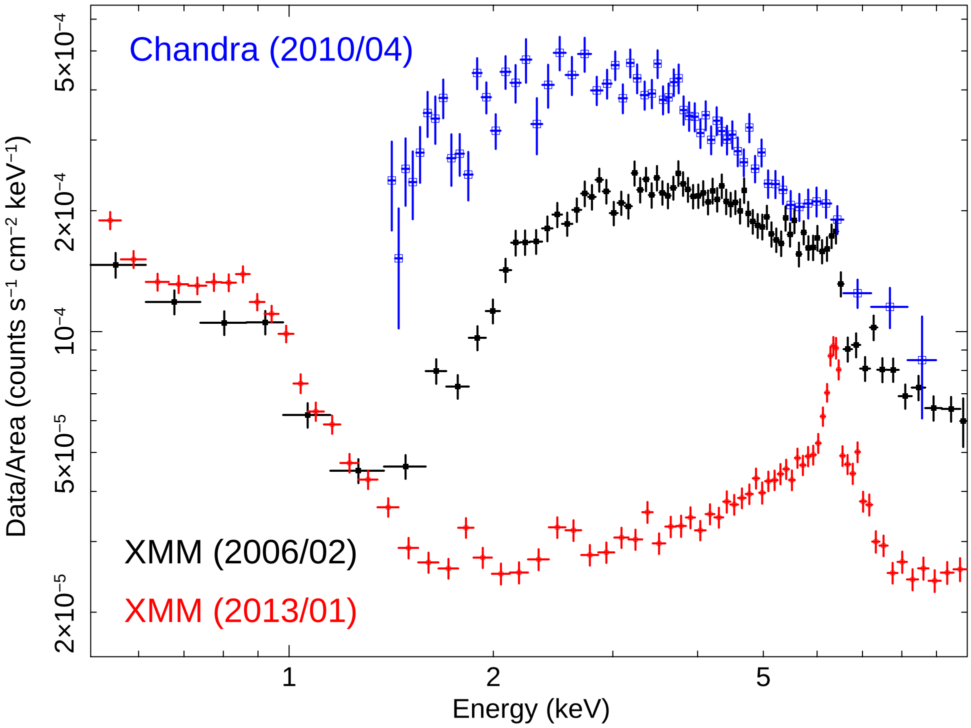

Figure 4.3: Long–term X–ray spectral variability of ESO 323–G77 as observed with *XMM–Newton* and *Chandra*. Only pn and HEG data, respectively, are shown for clarity. Data have been normalized to each detector effective area, and they have been rebinned for visual clarity.

Based on our previous analysis of the source (Miniutti et al., 2014), we consider a baseline model comprising Galactic absorption (Kalberla et al., 2005), a power law X–ray continuum, a reflection continuum (Nandra et al., 2007b) from neutral matter (with solar abundances and inclination fixed to an intermediate value of 45°), and a scattered soft X–ray power law typical of obscured AGN (Matt et al., 2013). The photon indices of the nuclear continuum and of the soft scattered component are forced to be the same, while their normalizations are free to vary independently. The reflection model intensity is set by the so–called reflection fraction R, with the geometrical meaning that $R = 1$ corresponds to the reflector covering half of the sky as seen by the irradiating source. The reflection model is convolved with a Gaussian kernel to account for any width of the associated emission lines (mainly Fe Kα). As for the absorbing systems we include, as a first approximation, a neutral absorber fully covering the nuclear X–ray continuum. A constant is introduced to account for calibration uncertainties between the two detectors.

The best–fitting baseline model produces a statistical result of $C = 2190$ for 1168 dof. The photon index is $\Gamma = 1.85 \pm 0.06$, and the X–ray continuum is absorbed by a column density of $N_{\rm H} = (3.3 \pm 0.2) \times 10^{22}\,{\rm cm}^{-2}$. The soft scattered power law has a normalization that is about 4 per cent that of the nuclear X–ray continuum. The reflection fraction of the reflection model is $R = 0.27 \pm 0.12$ and replacing the reflection model with a simple Gaussian emission line at ~ 6.4 keV gives a line energy of 6.39 ± 0.02 keV with EW of 50 ± 10 eV. The width of the line is in the range of $3 - 30$ eV and corresponds to a FWHM $\sim 330 - 3300\,{\rm km\,s}^{-1}$, consistent with an origin in the BLR or further out (e.g. the so–called torus). In our analysis we fix the width of the Gaussian kernel applied to the neutral reflection model to an intermediate value of 10 eV.

The best–fitting continuum model reveals the presence of a series of relatively strong absorption lines in the 1.2 − 2.7 keV range and around 7 keV. We then add a series of Gaussian absorption lines to our best–fitting model. Each line is in principle associated with three free parameters, namely rest frame energy, width, and intensity. After a few initial tests, we find that the width of most absorption lines cannot be well constrained by the data. In order to gain some insight on the typical line width, we select two of the strongest soft X–ray lines (at ~ 1.87 and ~ 2.02 keV at the galaxy redshift) and the two Fe absorption lines (at ~ 6.73 and ~ 6.99 keV), and we fit those lines with free Gaussian width. The two soft X–ray lines are both consistent with $\sigma = 10 \pm 3$ eV, while the two highly ionized Fe lines have $\sigma \leq 7$ eV. Hence, in the subsequent analysis, we fix the width of all Gaussian absorption lines to 10 eV, except that of the two highly ionized Fe lines which is instead fixed at 1 eV. Each Gaussian then only contributes with two free parameters (rest frame energy and intensity). The relatively large width of the soft X–ray lines is likely an indication of turbulence and / or of a contribution of different gas phases with different velocities to most lines.

We detect a total of 14 absorption lines, each producing an improvement of $\Delta C \geq 9.2$, i.e. each line is associated with a statistical significance larger than ~ 99 per cent for the two free parameters. The final statistical result is of $C = 1580$ for 1140 dof. In Table 4.2, we report the best–fitting parameters of the Gaussian absorption lines, as well as the corresponding identification and inferred outflow velocity. Errors on the lines parameters are computed using the STEPPAR command in XSPEC. The ΔC improvement for each individual line is computed by removing the line under inspection from the best–fitting model and by re–fitting the data reaching a new best–fit to be compared with the former.

As shown in Table 4.2, we can identify three main groups of absorption lines, likely associated with three different ionization states. The highest ionization phase (h) is associated with the Fe XXV and Fe XXVI absorption lines, with possible contributions to Si XIV and S XVI. An intermediate ionization state (l) is probed mainly by Si XIII, Si XIV and S XV with other possible contribution at Ne X, Mg XI, and Mg XII, as well as at S XVI. Finally, a series of Si absorption lines (Si VIII-X) is associated with a colder phase (c), which may also contribute, together with the intermediate ionization phase, at Ne X, Mg XI, and Mg XII.

According to our lines ID in Table 4.2, all phases have similar outflow velocities (of the order of 1000 − 2000 km s^{-1}), although excluding lines that may be associated with more than one single phase, the high ionization (h) and the cold phase (c) may be slightly slower than the intermediate zone (l).

4.4.1 A global absorption model

In order to reproduce the absorption features that are present in the data, we start our analysis by applying two ionized absorbers to the nuclear continuum, which is already absorbed by a neutral column of ~ 3×10^{22} cm^{-2}. We use the photoionization code PHASE, developed by Krongold et al. (2003). PHASE assumes a simple geometry that consists of a central source emitting an ionizing continuum with clouds of gas intercepting the LOS, in a plane parallel approximation. The ionization balance is calculated using CLOUDY (last described in Ferland et al., 2013). In this case, we use a simple power law SED with photon index $\Gamma = 2$ over the whole Lyman continuum. The SED is normalized to the historical 2–10 keV luminosity of ESO 323–G77 (Miniutti et al., 2014). This SED is shown in red in Fig. 4.4, and denoted by (u) for *unabsorbed*. We also include in the same figure another SED that will be defined and used later in this Section. The parameters of the code are (1) the ionization parameter defined as $U = Q\,(4\pi n R^2 c)^{-1}$ (Netzer, 2008), where Q is the photon rate integrated over the entire Lyman continuum, n is the gas number density and R

Table 4.2: Absorption lines detected with Gaussian models in the time–averaged *Chandra* spectra from the MEG and HEG detectors. The phase label (first column) refers to the phase of the gas that is likely responsible for the specific absorption line and it is coded as follows: h = high–ionization warm absorber (with typical temperature in the range of $10^6 - 10^7$ K), l = low–ionization warm absorber ($10^5 - 10^6$ K), c = cold absorber ($10^4 - 10^5$ K). The last column is the statistical improvement associated with the corresponding Gaussian model. We gather all the atomic transitions data from the AtomDB (Smith et al., 2001).

Phase	ID	Transition	$E_{\rm lab}$ (keV) / $\lambda_{\rm lab}$ (Å)	$E_{\rm restframe}$ (keV)	−EW (eV)	$v_{\rm outflow}$ (km s^{-1})	ΔC
l+c	Ne x	$1s \rightarrow 4p$	1.2770 / 9.708	1.283 ± 0.002	20 ± 4	1400 ± 450	40
l+c	Ne x	$1s \rightarrow 5p$	1.3077 / 9.481	1.314 ± 0.002	15 ± 4	1450 ± 450	18
l+c	Mg xi	$1s^2 \rightarrow 1s2p$	1.3522 / 9.169	1.359 ± 0.002	9 ± 5	1500 ± 450	11
l+c	Mg xii	$1s \rightarrow 2p$	1.4723 / 8.421	1.480 ± 0.002	15 ± 3	1550 ± 400	71
c	Si viii	$2p^3 \rightarrow 1s2s^22p^4$	1.7715 / 6.999	1.777 ± 0.002	13 ± 3	950 ± 300	28
c	Si ix	$2p^2 \rightarrow 1s2s^22p^3$	1.7909 / 6.923	1.797 ± 0.002	12 ± 2	1000 ± 350	27
c	Si x	$2p \rightarrow 1s2s^22p^2$	1.8084 / 6.856	1.816 ± 0.002	11 ± 3	1250 ± 350	24
l	Si xiii	$1s^2 \rightarrow 1s2p$	1.8650 / 6.648	1.875 ± 0.002	12 ± 2	1600 ± 300	63
l+h	Si xiv	$1s \rightarrow 2p$	2.0056 / 6.182	2.017 ± 0.002	18 ± 2	1700 ± 300	181
l	Si xiv	$1s \rightarrow 3p$	2.3765 / 5.217	2.388 ± 0.003	14 ± 3	1450 ± 350	25
l	S xv	$1s^2 \rightarrow 1s2p$	2.4605 / 5.039	2.473 ± 0.003	10 ± 3	1500 ± 400	17
l+h	S xvi	$1s \rightarrow 2p$	2.6218 / 4.729	2.632 ± 0.003	11 ± 3	1150 ± 350	28
h	Fe xxv	$1s^2 \rightarrow 1s2p$	6.7019 / 1.850	6.73 ± 0.01	49 ± 7	1250 ± 450	41
h	Fe xxvi	$1s \rightarrow 2p$	6.9650 / 1.780	6.99 ± 0.01	51 ± 9	1050 ± 450	36

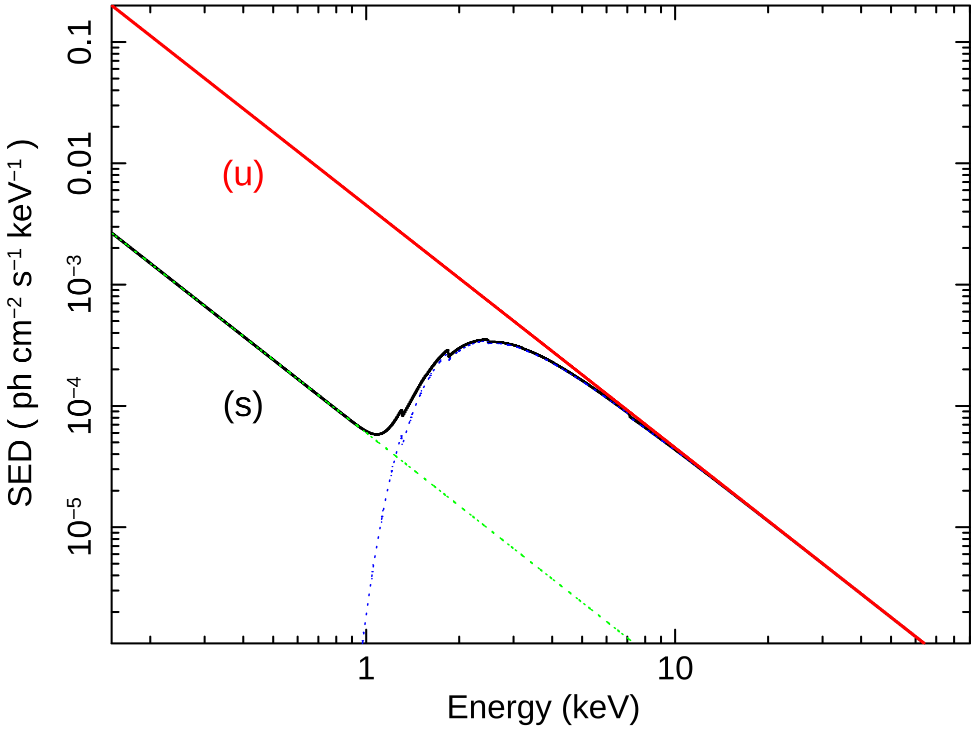

Figure 4.4: The unabsorbed (u) and soft–X–rays–absorbed (s) SEDs used in this work are shown as solid lines (upper and lower lines respectively) in a restricted X–ray regime. The overall SEDs can be obtained with a simple extrapolation between 1 Ry and infinity. In the (s) case the two main spectral components are also shown, namely the soft scattered power law and the absorbed nuclear continuum which dominate the spectrum below and above ~ 1 keV respectively.

the gas distance from the nuclear source of photons, (2) the equivalent hydrogen column density, (3) the outflow velocity, and (4) the internal microturbulent velocity. The electron temperature in the models presented here corresponds to the photoionization equilibrium of the gas.

The two ionized absorbers provide a large statistical improvement with respect to the baseline continuum model reaching $C = 1591$ for 1160 dof (to be compared with $C = 2190$ for 1168) and the best–fitting parameters are reported in Table 4.3 (Model 1). The data and best–fitting model are shown in the upper panels of Figs. 4.5–4.8. Although the model represents a significant statistical improvement, some of the absorption lines we detect with Gaussian models (see Table 4.2) are only poorly reproduced. This is particularly true for some Si lines between 1.7 and 1.8 keV (observed–frame) as seen in the upper panel of Fig. 4.6, for the S xv line around 2.4 keV (upper panel of Fig. 4.7), and for the Fe xxvi line that is only poorly accounted for (upper panel of Fig. 4.8). Some residuals are also left at the softest X–ray energies (see upper panel of Fig. 4.5), although they seem to have lower significance.

In our model, the series of Si lines around 1.8 keV are all due to the low–ionization l–phase ($\log U \sim -0.3$, see Model 1 in Table 4.3), while the strong Si xiv and S xvi lines are exclusively produced by the high–ionization h–phase together with the Fe lines ($\log U \sim 1.5$). Increasing the ionization of this hotter phase to better reproduce the Fe xxvi line decreases the strength of the Si xiv and S xvi ones, and worsen the fitting statistics because the l–phase is not hot enough to contribute there. This would be possible only increasing as well the ionization of the l–phase, but then the other Si lines would not be reproduced, as they are associated with lower ionization.

Table 4.3: Best–fitting parameters for the time–averaged MEG and HEG *Chandra* data. Column densities are expressed in cm^{-2}, the ionization parameter U is dimensionless by definition, while ξ is in units of $\mathrm{erg\,cm\,s^{-1}}$. The different columns are characterized by the different models for the absorbers. The symbol ‘n’ represents a strictly neutral absorber, ‘u’ and ‘s’ represent ionized absorbers modelled with the unabsorbed (u) or soft–absorbed (s) SED in PHASE, and ‘i’ an ionized absorber modelled with the XSTAR–based model ZXIPCF. The superscript ‘^{f}’ means that the parameter has been fixed, while the symbol ‘^{p}’ indicates that it reached the model upper / lower limit, respectively.

			Model 1	Model 2	Model 3	Model 4
			u×u×n	u×u×u	s×s×u	i×i×i
		Γ	1.85 ± 0.06	1.96 ± 0.05	1.95 ± 0.05	2.15 ± 0.07
Warm abs.	h–phase	$\log U$	1.5 ± 0.1	1.9 ± 0.2	0.0 ± 0.2	–
		$\log \xi$	–	–	–	4.1 ± 0.1
		$\log N_{\rm H}$	23.2 ± 0.1	23.4 ± 0.2	23.3 ± 0.2	23.7 ± 0.2
		$v_{\rm turb}$	$600 - 900^p$	$600 - 900^p$	$600 - 900^p$	200^f
		$v_{\rm outflow}$	1500 ± 200	1100 ± 200	1200 ± 200	800 ± 200
	l–phase	$\log U$	-0.3 ± 0.1	0.5 ± 0.1	-1.0 ± 0.1	–
		$\log \xi$	–	–	–	2.7 ± 0.2
		$\log N_{\rm H}$	22.50 ± 0.08	22.41 ± 0.09	22.49 ± 0.08	22.5 ± 0.1
		$v_{\rm turb}$	$500 - 900^p$	$600 - 900^p$	$600 - 900^p$	200^f
		$v_{\rm outflow}$	1400 ± 200	1750 ± 200	1700 ± 200	1850 ± 200
Cold abs.	c–phase	$\log U$	–	-0.45 ± 0.05	-0.56 ± 0.05	–
		$\log \xi$	–	–	–	1.6 ± 0.2
		$\log N_{\rm H}$	22.20 ± 0.06	22.70 ± 0.04	22.59 ± 0.05	22.9 ± 0.2
		$v_{\rm turb}$	–	600 ± 200	600 ± 200	200^f
		$v_{\rm outflow}$	–	1400 ± 300	1300 ± 300	1500 ± 300
		C / dof	1591 / 1160	1433 / 1157	1413 / 1157	1700 / 1160

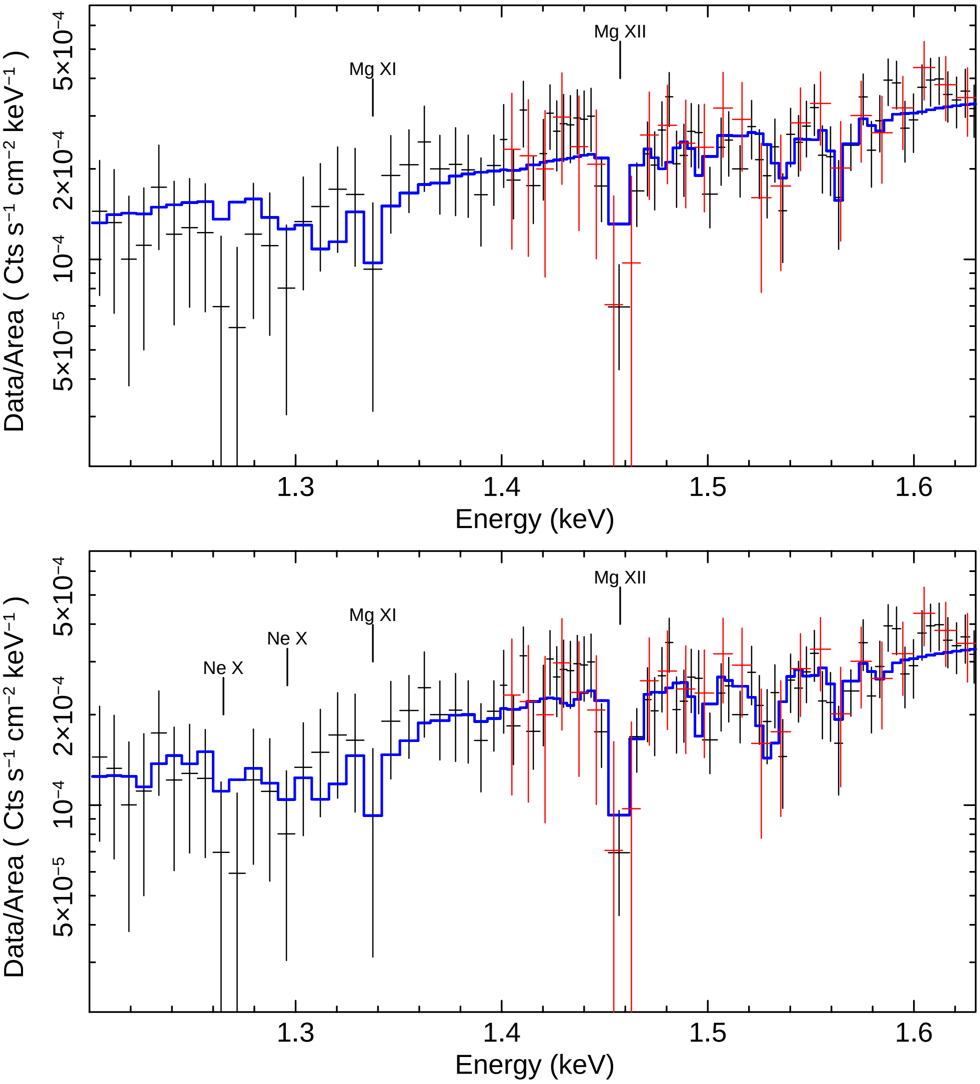

Figure 4.5: We show the area–corrected MEG (black) and HEG (red) data and best–fitting models in the 1.2–1.63 keV energy band. The upper panel refers to Model 1 in Table 4.3 (namely two ionized and one neutral absorbers), and the lower panel refers to Model 2 (three ionized absorbers). The best–fitting model (solid line) is only that convolved with the MEG response to ensure simplicity and visual clarity.

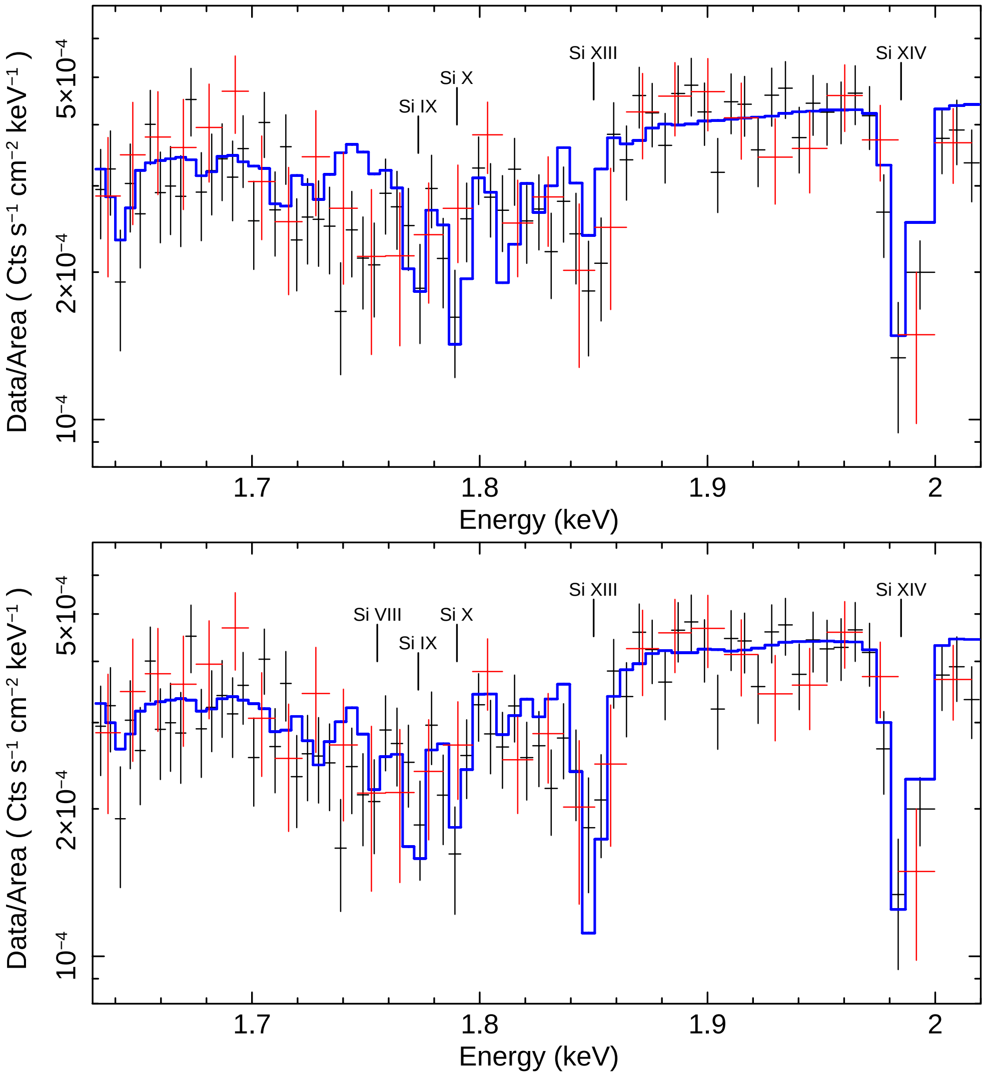

Figure 4.6: We show the area–corrected MEG (black) and HEG (red) data and best–fitting models in the 1.63–2.05 keV energy band. The upper panel refers to Model 1 in Table 4.3 (namely two ionized and one neutral absorbers), and the lower panel refers to Model 2 (three ionized absorbers). The best–fitting model (solid line) is only that convolved with the MEG response to ensure simplicity and visual clarity.

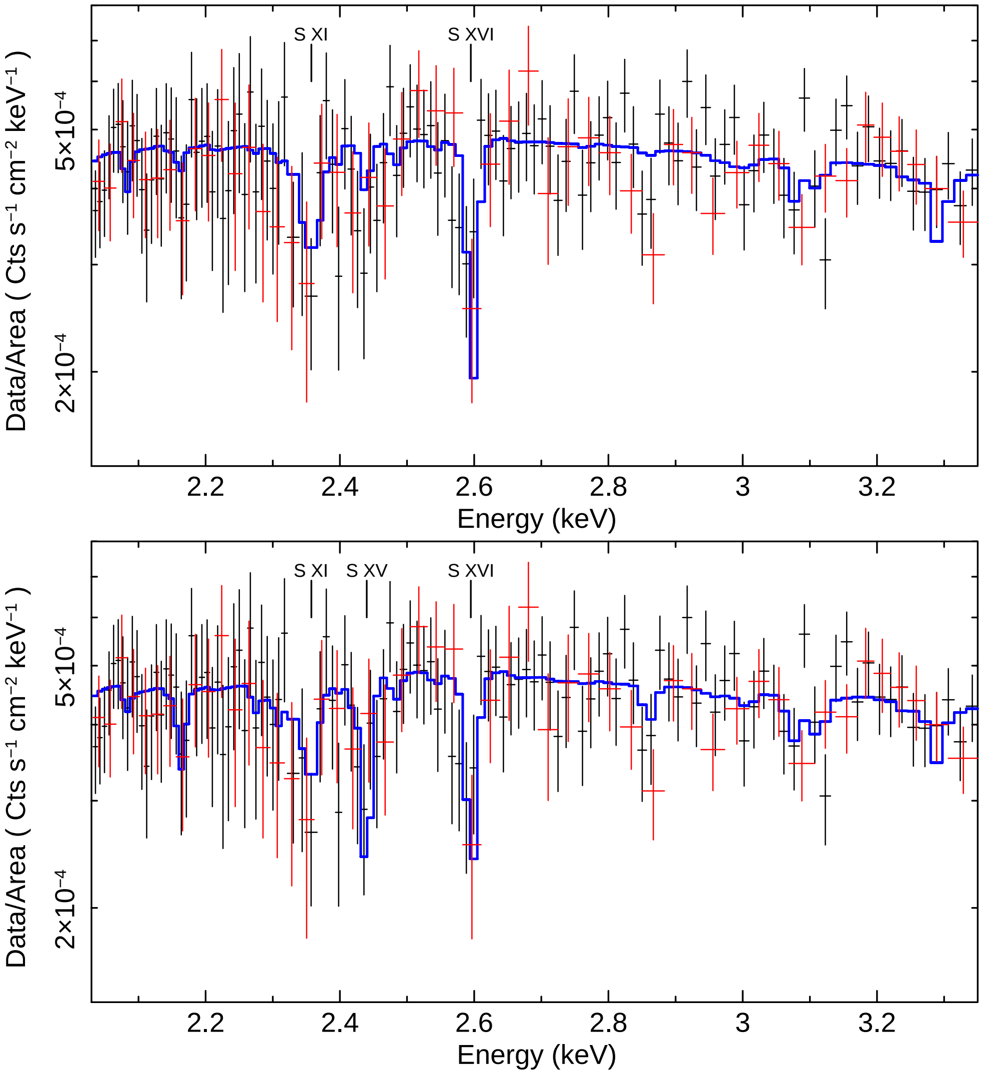

Figure 4.7: We show the area–corrected MEG (black) and HEG (red) data and best–fitting models in the 2.05–3.35 keV energy band. The upper panel refers to Model 1 in Table 4.3 (namely two ionized and one neutral absorbers), and the lower panel refers to Model 2 (three ionized absorbers). The best–fitting model (solid line) is only that convolved with the MEG response to ensure simplicity and visual clarity.

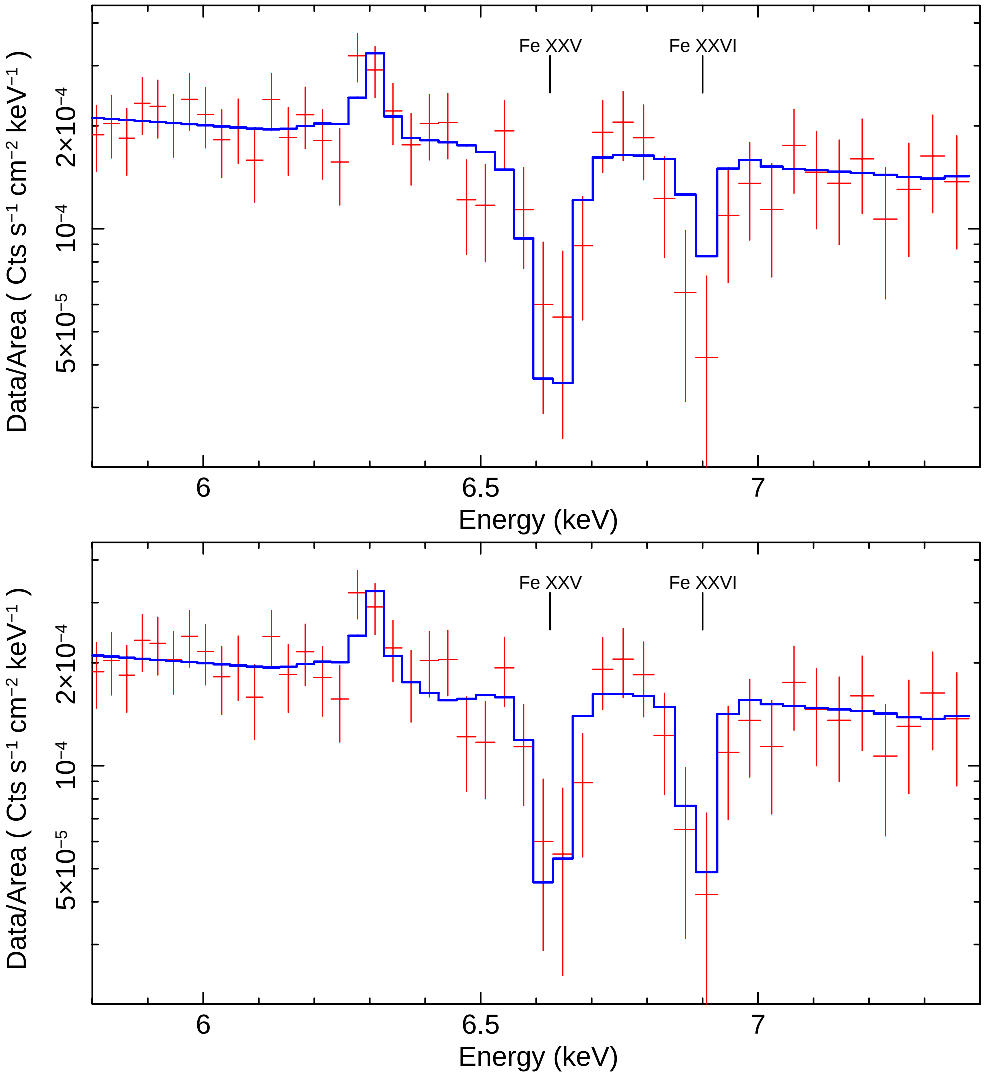

Figure 4.8: We show the area–corrected MEG (black) and HEG (red) data and best–fitting models in the 5.8–7.4 keV energy band. The left upper panel refers to Model 1 in Table 4.3 (namely two ionized and one neutral absorbers), and the lower panel refers to Model 2 (three ionized absorbers). Only HEG data and model are shown in the bottom panels to ensure simplicity and visual clarity.

The only sensible solution seems that of introducing a cold phase which may account for the Si lines around 1.8 keV allowing the ionization of the other two components to increase and to better reproduce the Si xiv, S xv, S xvi, and Fe xxvi lines. It would obviously be possible to simply introduce a third PHASE component. However, the ionization is likely to be low, so that we consider the possibility of replacing the cold absorber that characterizes our continuum model with a low–ionization absorber. Hence we replace the neutral absorber (so far modelled with the ZPHABS model in XSPEC) with a third PHASE component.

Replacing the neutral absorber with a third PHASE component produces a statistically significant improvement, and the best–fit reaches $C = 1433$ for 1157 dof (to be compared with $C = 1591$ for 1160 dof, obtained with two ionized and one strictly neutral absorber). The best–fitting parameters are reported in Table 4.3 (Model 2). The data and best–fitting model are shown in the lower panels of Figs. 4.5–4.8. The best–fitting models are shown in the two energy bands where the most relevant features are imprinted (a soft X–ray band up to ~ 2.7 keV is shown in the upper panel of Fig. 4.9, and the Fe K region in the upper panel of Fig. 4.10).

As expected, the ionization of the two absorbers of our previous model significantly increases. The h–phase is now characterized by $\log U \sim 1.9$, while the l–phase has $\log U \sim 0.5$. Now, the Si xiv and S xvi lines are well reproduced with contribution from both absorbers, while the high–ionization phase accounts very well for both the Fe xxv and Fe xxvi lines. The l–phase also accounts better for the S xv absorption feature around 2.4 keV. On the other hand, the new, colder absorber ($\log U \sim -0.45$) accounts for the Si complex around 1.8 keV (and also slightly improves the fit at the lowest energies, where Ne and Mg lines are detected, see Table 4.2). All the improvements of Model 2 with respect to Model 1 can be seen in the comparison between upper (Model 1) and lower (Model 2) panels of Figs. 4.5–4.8.

We measure a non–zero velocity for all phases. The outflow velocities are of $1100 \pm 200\,\mathrm{km\,s^{-1}}$ for the h–phase, of $\sim 1750 \pm 200\,\mathrm{km\,s^{-1}}$ for the l–phase, and of $1400 \pm 300\,\mathrm{km\,s^{-1}}$ for the coldest absorber (c–phase). The l–phase appears to be faster than the other two. This is consistent with the results reported in Table 4.2 where it was shown that lines associated with the h–phase only (the Fe lines) and those associated with the c–phase only (the Si viii to Si x lines) have velocities in the range of $900 - 1300\,\mathrm{km\,s^{-1}}$, while lines associated with the l–phase only (such as Si xiii and S xv) have marginally higher velocity ($1300 - 1800\,\mathrm{km\,s^{-1}}$). As for the turbulent velocities, the only one that can be constrained is that of the coldest component which is $v_{\mathrm{turb}}^{(c)} = 600 \pm 200\,\mathrm{km\,s^{-1}}$. Only lower limits are obtained for the other two phases with $600 \leq v_{\mathrm{turb}}^{(l,h)} \leq 900\,\mathrm{km\,s^{-1}}$ (note that the PHASE code only allows for $v_{\mathrm{turb}} \leq 900\,\mathrm{km\,s^{-1}}$).

As mentioned, we have so far used a common SED (a simple power law with photon index 2 over the whole Lyman continuum) for the three absorbers. This SED is represented with the symbol ‘u’ for *unabsorbed* in Table 4.3. However, as can be seen in the upper panel of Fig. 4.9, the cold component affects the spectral shape significantly in the soft X–rays. If the cold absorber is located closer to the nuclear source than the other phases, the h– and l–phase would see a different, absorbed SED. To explore the possible effects of such a scenario, we introduce a new SED, namely we consider the same nuclear power law with $\Gamma = 2$ as before, but absorbed by a column density of $3 \times 10^{22}\,\mathrm{cm^{-2}}$ of cold gas (representative of the effect of the c–phase). In the soft X–rays (and below), this new SED is therefore dominated by the soft, scattered power law which is always present. The luminosity of the soft power law is $L_{0.5-2} = 6.7 \times 10^{40}\,\mathrm{erg\,s^{-1}}$ while, as already mentioned, that of the nuclear continuum is the historical average for ESO 323–G77 ($L_{2-10} = 5.8 \times 10^{42}\,\mathrm{erg\,s^{-1}}$). Both luminosities are from Miniutti et al. (2014). This absorbed SED is represented with the symbol ‘s’ for *soft X–rays absorbed* in Table 4.3, and is shown in

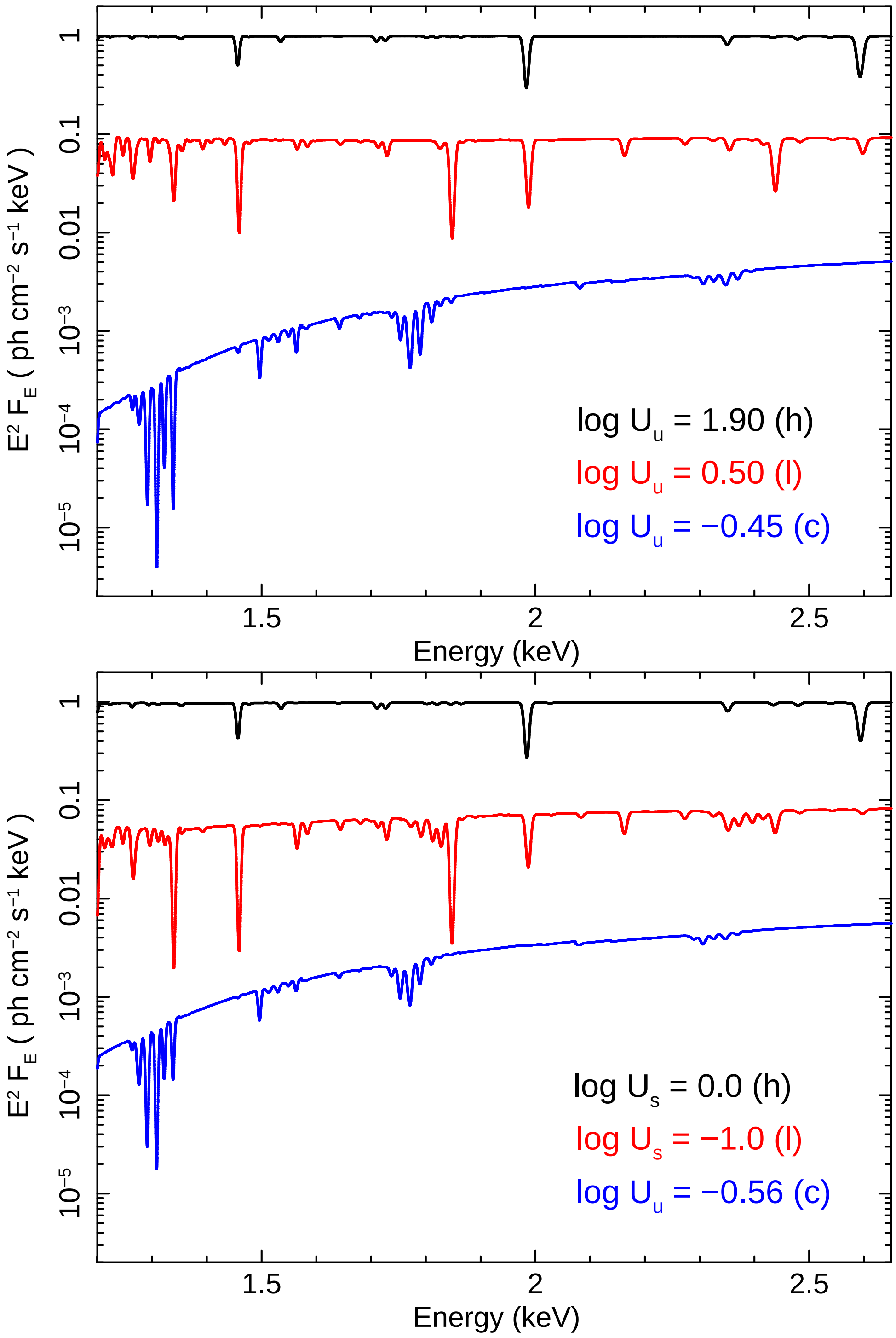

Figure 4.9: Best–fitting models for the three PHASE components in the soft X–ray band between 1.2 keV and 2.65 keV (where the strongest features are seen). The models are all applied to a power law with $\Gamma = 2$ and are rescaled in order to avoid confusion. The upper panel refers to Model 2 in Table 4.3, where all absorbers see the same, unabsorbed SED (u). The lower panel is for Model 3, where the h– and l–phases see a SED that is absorbed by a neutral column of 3×10^{22} cm^{-2} (s). As can be seen, the two models differ slightly in some of the line ratios, while the general structure is the same. In particular, the l–phase is always responsible for higher–ionization lines than the c–phase despite the nominally lower U obtained with Model 3 (lower panel).

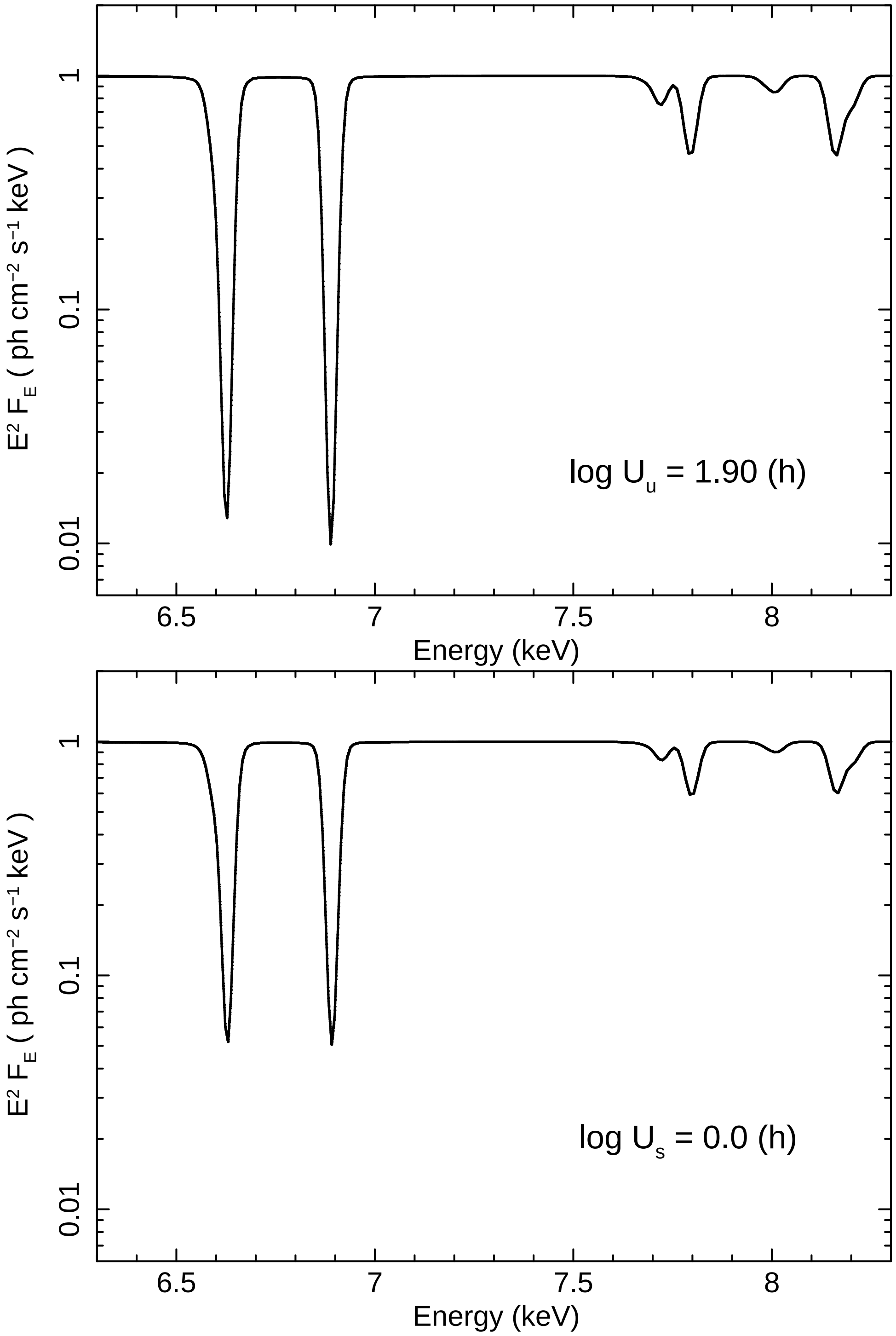

Figure 4.10: Here we show the Fe K region, where the only significant contribution is from the highly–ionized component. The models are all applied to a power law with $\Gamma = 2$ and are rescaled in order to avoid confusion. The upper panel refers to Model 2 in Table 4.3, where all absorbers see the same, unabsorbed SED (u). The lower panel is for Model 3, where the h– and l–phases see a SED that is absorbed by a neutral column of 3×10^{22} cm^{-2} (s). As can be seen, the two models differ slightly in some of the line ratios, while the general structure is the same. In particular, the h–phase is responsible for the same lines despite the nominally lower U obtained with Model 3 (lower panel).

black in Fig. 4.4 in order to ease comparison with the unabsorbed SED. The relation between the integrated photon rate Q for the unabsorbed SED (u) and the new, soft–X–ray–absorbed SED (s) is $Q_\mathrm{u} \simeq 50\, Q_\mathrm{s}$. The introduction of this new model enables us to explore the possibility that the c–phase is closer to the nuclear source than the other two (or at least cospatial with them), thus reducing the irradiating flux on the h– and l–phases. As the two warm / hot phases see the absorbed SED, while the c–phase still sees the unabsorbed one, the model is called s×s×u, as opposed to the case in which all phases see the same unabsorbed SED which is called u×u×u.

Repeating the analysis in the s×s×u configuration produces a relatively marginal improvement and gives $C = 1413$ for the same number of dof as in the u×u×u explored above (which gave $C = 1433$) and results are reported in Table 4.3 as Model 3. We believe that the ΔC between the two models is not sufficiently large to prefer one solution over the other on firm statistical grounds, but we take it as an indication that the c–phase is either more internal or at least cospatial with the other two, rather than more external.

Note that the ionization parameter of the two higher–ionization warm absorbers drops significantly with $\Delta \log U = \log U_u - \log U_s = 1.9 \pm 0.4$ for the h–phase and 1.5 ± 0.2 for the l–phase. This mostly reflects the change in ionizing photon rate Q due to the reduction of the SED at soft X–rays; indeed, both ΔU are consistent with the expected relation between the ionization parameters of the two different SEDs, namely $\Delta \log U = \Delta \log Q = \log(Q_u Q_s^{-1}) \simeq 1.7$. A marginal drop of the ionization of the c–phase is also seen despite an identical SED, but we must stress that fixing the ionization of the s×s×u model to be the same as in the u×u×u case, the fitting statistics is only marginally worse ($\Delta C = 5$), so that an acceptable solution with the same ionization for the cold phase does exist.

According to the ionization parameters of the three absorbers in the s×s×u (Model 3), one would assume that the l–phase (with $\log U \simeq -1.0$) is now colder than the c–phase ($\log U \simeq -0.6$). However, the two ionization parameters can not be directly compared, as they are associated with two different SEDs. In fact, the l–phase is still responsible for higher–ionization lines than the c–phase. This is shown in Fig. 4.9 and Fig. 4.10 where the upper and lower panels are associated with the u×u×u and s×s×u models respectively. Comparing upper and lower panels, it is clear that the best–fitting models for all three phases are only marginally different, despite the h– and l–phases have very different ionization parameters and that the l–phase is always responsible for higher ionization lines than the c–phase.

As a last step, in order to ease comparisons with other works / sources when using different photoionization models, we consider the XSTAR–based ZXIPCF model in XSPEC and repeat the analysis by using three ZXIPCF component instead of the three PHASE ones. The free parameters of the ZXIPCF model are the ionization parameter, defined as $\xi = L/(nr^2)$ where the luminosity is integrated between 1 and 1000 Ry, the column density, and the outflow velocity. As for the turbulent velocity, it is fixed to 200 km s^{-1} in the model. The intrinsic SED is a slightly steeper power law of $\Gamma = 2.2$ than for the PHASE model we used so far ($\Gamma = 2.0$).

The ZXIPCF–based model (Model 4 in Table 4.3) is a significantly worse description of the data than the equivalent u×u×u model based on the PHASE code (Model 2 in Table 4.3). This is mostly due to a worse description of the ionized Fe absorption lines that are only partially reproduced by the model. Moreover the softest X–ray energies (where Ne and Mg lines dominate) are not well reproduced, and residuals are also seen around 1.8 keV (mostly Si lines). The best–fitting ionization parameters are significantly higher than those of Model 2. This is expected because of the different definition of ionization parameters. In fact, assuming the same 2–10 keV luminosity for the two SEDs (one with $\Gamma = 2$, and the other with $\Gamma = 2.2$), the conversion between the

ZXIPCF ionization parameter and U is $\log\xi = 1.99 + \log U$. Indeed, the ionization parameters derived with the ZXIPCF–based Model 4 and those derived via the PHASE–based Model 2 are all consistent with that conversion within the errors (see Table 4.3). Besides the different treatment of atomic physics, one further possible reason for the worse description of the data with Model 4 with respect to Model 2 is that the ZXIPCF model assumes a relatively modest turbulent velocity of 200 kms , while the best–fitting parameters in Model 2 suggest a much higher $v_{\rm turb}$. Hence, we do not discuss any further the ZXIPCF model and we consider to have reached a satisfactory description of the *Chandra* time–averaged spectrum with Model 2 (or Model 3).

The resulting picture is the following: during the ~ 10 days corresponding to the time–averaged *Chandra* spectrum, the X–ray continuum in ESO 323–G77 is transmitted through three absorbers, ionized at different degrees. Although there is a slight difference in the statistical results from the two physical scenarios defined above (Model 2 and Model 3 in Table 4.3), we cannot claim a highly significant preference for one of the two scenarios. For simplicity, we adopt here the u×u×u Model 2. This choice allows us to compare directly the ionization parameters of the absorbers, as they all see the same SED. Moreover, as discussed above, there is no loss of generality because all parameters of Model 3 can be obtained from those of Model 2 simply rescaling the ionization parameters taking into account the different photon rate Q.

In this context, we characterize the warm absorbers (h– and l–phases) as two structures with ionization parameters of $\log U^{(\rm h)} \simeq 1.9$ and $\log U^{(\rm l)} \simeq 0.5$, and equivalent hydrogen column densities of the order of a few $\times 10^{23}$ and a few $\times 10^{22}\,\rm cm^{-2}$ respectively. The third absorber, previously thought to be neutral, turns out to be ionized, with $\log U^{(\rm c)} \simeq -0.45$ and a column density of few $\times 10^{22}\,\rm cm^{-2}$. As per the outflow velocities, there are no striking differences among the three ionization phases, and the most likely physical scenario appears to be one in which the warm absorbers and the coldest one are all part of an outflow characterized by velocities in the range of $\sim 1000 - 2000\,\rm km\,s^{-1}$, although the l–phase appears to be marginally faster than the other two phases.

4.5 Short time–scale absorbers variability

Having reached a fair description of the time–averaged *Chandra* data, we are now able to focus on the specific differences among the four *Chandra* observations performed during ten days in 2010 April. We start by applying the best–fitting model described above (Model 2 in Table 4.3) to the four *Chandra* observations. The continuum photon index is initially free to vary but, as no variability is seen after a few tests, it is forced to be the same in all observations. On the other hand, the continuum normalization is free to vary independently.

We initially force all absorbers parameters to be the same in all observations and we perform a joint fit to the four observations. This is done to obtain a benchmark result that will be used to assess the significance of any absorber variability once parameters will be let free to vary independently in each observation. We reach a statistical result of $C = 5351$ for 4673 dof. All parameters are consistent, within the errors, with those obtained from the time–averaged spectrum (Table 4.3) and they are given in the upper part of Table 4.4.

In order to explore any absorber variability, we then leave the ionization and column density of the three phases free to vary independently in the four observations, while keeping constant outflow and turbulent velocities for each phase (this assumption turns out to be justified by an a–posteriori

Table 4.4: Best–fitting results for the analysis of the four 2010 *Chandra* observations from April 14 to April 24 considered separately. The continuum photon index is initially free to vary but, after testing for its lack of variability, it is forced to be the same in all observations ($\Gamma = 1.97 \pm 0.06$). In the upper part of the table, we show the best–fitting results obtained if all the absorbers parameters are forced to be the same at all epochs (i.e. we reproduce the results obtained using the time–averaged spectrum, see Table 4.3 for comparison). The middle part of the table shows results obtained when the ionization and column density of the three absorbing phases are free to vary independently in each of the four observations while keeping, for each phase, common outflow and turbulent velocities. Finally, the lower part of the table shows results obtained by forcing all absorbers parameters to be the same at all epochs except the c–phase ionization, which is the only one that varies significantly. As it was the case for the time–averaged *Chandra* spectra, the turbulent velocity of the h– and l–phases is $\geq 600\,\mathrm{km\,s^{-1}}$ (with a model upper limit of $900\,\mathrm{km\,s^{-1}}$) while, in all fits, the c–phase is characterized by a turbulent velocity of $600 \pm 200\,\mathrm{km\,s^{-1}}$. Units are the same as in Table 4.3. The symbol '^{p}' means that the parameter reached the limit allowed by the model.

All phases forced to be constant at all epochs (C/dof = 5351/4673)									
	h–phase			l–phase			c–phase		
	$\log U$	$\log N_\mathrm{H}$	v_outflow	$\log U$	$\log N_\mathrm{H}$	v_outflow	$\log U$	$\log N_\mathrm{H}$	v_outflow
	2.1 ± 0.3	$23.7^{+0.3p}_{-0.3}$	1200 ± 200	0.5 ± 0.1	22.40 ± 0.09	1800 ± 300	-0.44 ± 0.05	22.70 ± 0.05	1450 ± 250
All phases allowed to vary in ionization and column density (C/dof = 5273/4655)									
	h–phase			l–phase			c–phase		
Obs. date	$\log U$	$\log N_\mathrm{H}$	v_outflow	$\log U$	$\log N_\mathrm{H}$	v_outflow	$\log U$	$\log N_\mathrm{H}$	v_outflow
April 14	2.0 ± 0.4	$23.7^{+0.3p}_{-0.3}$	1250 ± 250	0.5 ± 0.2	22.2 ± 0.2	1800 ± 350	-0.30 ± 0.08	22.7 ± 0.1	1500 ± 250
April 19	2.1 ± 0.4	$23.8^{+0.2p}_{-0.4}$	”	0.5 ± 0.2	22.3 ± 0.2	”	-0.60 ± 0.09	22.7 ± 0.1	”
April 21	2.1 ± 0.4	$23.8^{+0.2p}_{-0.4}$	”	0.5 ± 0.1	22.4 ± 0.2	”	-0.45 ± 0.08	22.7 ± 0.1	”
April 24	2.1 ± 0.4	$23.6^{+0.4p}_{-0.2}$	”	0.6 ± 0.1	22.5 ± 0.2	”	-0.34 ± 0.09	22.7 ± 0.1	”
All phases forced to be the same at all epochs, except the c–phase ionization (C/dof = 5289/4670)									
	h–phase			l–phase			c–phase		
Obs. date	$\log U$	$\log N_\mathrm{H}$	v_outflow	$\log U$	$\log N_\mathrm{H}$	v_outflow	$\log U$	$\log N_\mathrm{H}$	v_outflow
April 14	2.1 ± 0.3	$23.7^{+0.3p}_{-0.3}$	1200 ± 200	0.5 ± 0.1	22.40 ± 0.09	1800 ± 300	-0.31 ± 0.04	22.70 ± 0.05	1450 ± 250
April 19	”	”	”	”	”	”	-0.56 ± 0.07	”	”
April 21	”	”	”	”	”	”	-0.48 ± 0.06	”	”
April 24	”	”	”	”	”	”	-0.36 ± 0.04	”	”

check which shows no improvement if these parameters are allowed to vary). The new best–fitting result is $C = 5273$ for 4655 dof. The improvement is exclusively due to the variability of the c–phase ionization. All other parameters are consistent with remaining constant in the four observations, as shown in the middle part of Table 4.4.

We then perform a final fit where all parameters are forced to be the same in the four observations except the c–phase ionization (i.e. the only parameter that is significantly variable). This is done to derive the ΔC that is obtained when only the c–phase ionization is free to vary. We obtain $C = 5289$ for 4670 dof, i.e. an improvement by $\Delta C = 62$ for 3 dof with respect to the benchmark model (all absorbers forced to be constant). This demonstrates that the variability of the c–phase ionization is highly significant, and that a constant ionization can be safely excluded. The best–fitting parameters for this model are reported in the lower part of Table 4.4.

In order to gain some insights on the origin of the observed variability, we consider here the relationship between the absorber ionization and the 2–10 keV nuclear luminosity. Under the assumption of no intrinsic variation of the SED shape between the four *Chandra* observations (as it is the case, since the photon index is consistent with being constant) and of the gas density and location, the X–ray luminosity is proportional to the photon rate Q that enters the definition of ionization parameter $U = Q(4\pi cnR^2)^{-1}$, i.e. doubling the luminosity implies that Q and therefore U is twice as large (as the SED is a simple power law, the luminosity can be considered in any arbitrary band). Hence, we do expect a linear relationship between ionization U and luminosity if the absorbing gas phase is in photoionization equilibrium with the ionizing continuum. We consider the $U - L_{2-10}$ relationship instead of the $U - Q$ one, because we prefer to use two direct observables.

As can be seen in Table 4.4, the ionization of the h– and l–phases is consistent with being constant during the 10 days probed by the *Chandra* observations. However, the relatively large errors imply that the two parameters could also be linearly related to L_{2-10} at the same significance level, so that no information can be obtained for the two warm / hot phases. Hence, we focus here on the c–phase only, which is the only one showing significant ionization variability. Fig. 4.11 shows the c–phase ionization as a function of the 2–10 keV X–ray luminosity (in log − log space). The shaded area is the range of $\log U$ obtained when all absorbers parameters (including the c–phase ionization) are forced to be the same at all epochs (see upper part of Table 4.4), while data points are those reported in the lower part of the same table. The solid line represents the best–fitting relation of the form $\log U = a \log L_{2-10} + b$, where a is fixed to unity to show that a linear relationship between U and L_{2-10} is indeed consistent with the data. The tilted dashed lines represent the associated uncertainty (at the 99 per cent confidence level). Letting a free to vary confirms the linear relation although with relatively large error ($a = 1.1 \pm 0.4$) and excludes, as expected, the case of constant U ($a = 0$).

We then conclude that the observed variability is driven by the linear response of the c–phase ionization to variations of the intrinsic luminosity (or photon rate Q). This strongly suggests that the c–phase is dense enough to be in photoionization equilibrium with the irradiating nuclear source on time–scales as short as a few days. As mentioned, the h– and l–phase are consistent with both constant ionization and with a linear relationship between U and X–ray luminosity, so that no information is gained in those cases. Repeating the analysis with the s×s×u configuration (i.e. assuming Model 3 of Table 4.3 as baseline instead of Model 2) gives very similar results, and only the c–phase ionization is significantly variable (and satisfies again a linear relationship between U and L_{2-10}).

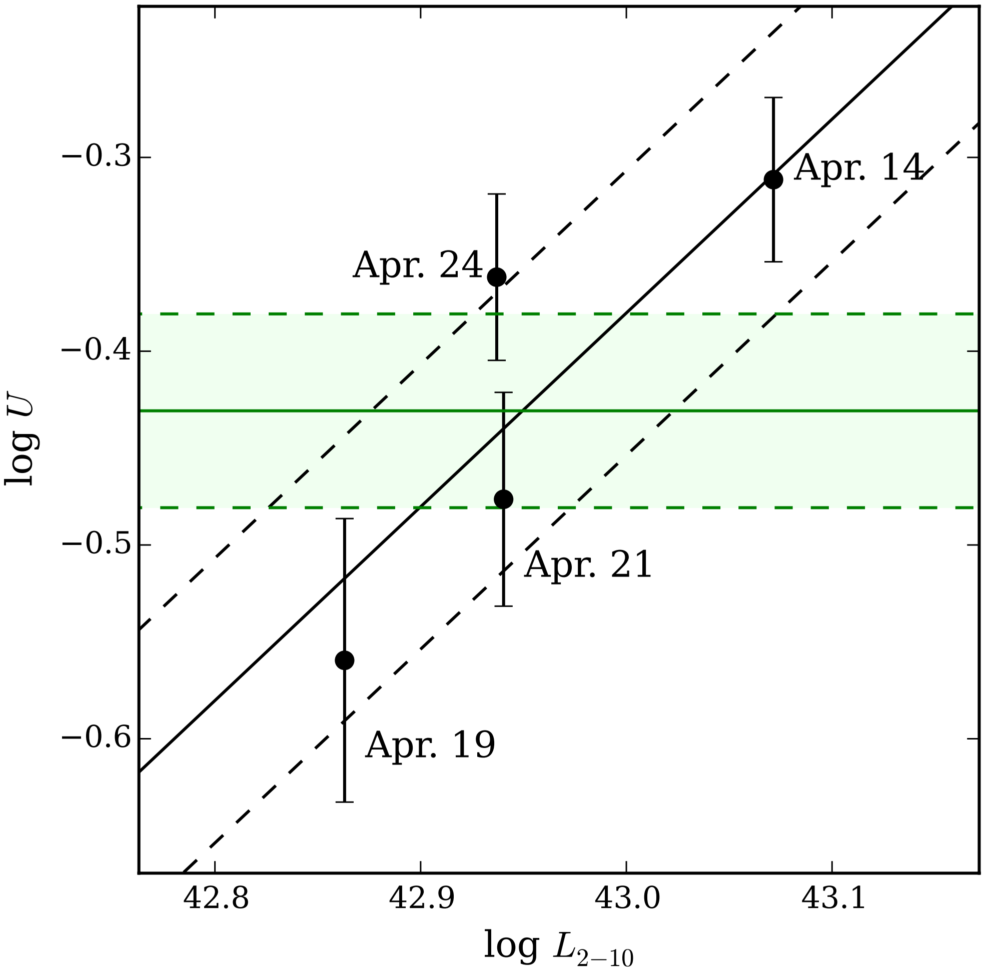

Figure 4.11: The ionization of the c–phase component is shown as a function of the 2 – 10 keV X–ray luminosity in log – log space. The shaded area between horizontal dashed lines is the best–fitting interval obtained when U is forced to be the same at all epochs (see upper part of Table 4.4). The data correspond to the case where all absorbers parameters, except the c–phase ionization, are kept constant between the four *Chandra* observations (lower part of Table 4.4). The tilted solid line is the best–fitting linear relation between U and L_{2-10}, i.e. $\log U = a \; \log L_{2-10} + b$ with a fixed to unity, and the tilted dashed lines represent the statistical fitting error given here at the 99 per cent confidence level. This shows that the data are consistent with a linear relation between U and L_{2-10}, as expected if the gas is in photoionization equilibrium with the irradiating continuum. Letting a free to vary confirms the linear relation although with relatively large error ($a = 1.1 \pm 0.4$). Note that some changes in gas properties (or intrinsic SED) may be present between April 21 and 24, which would explain the slightly different ionization of the c–phase despite an almost identical luminosity.

Table 4.5: Best–fitting common parameters for the simultaneous broad–band analysis of the 2006 and 2013 *XMM–Newton* observations. Luminosities are in units of $10^{42}\,\mathrm{erg\,s^{-1}}$, temperatures and energies are given in keV, the column density is in units of $10^{22}\,\mathrm{cm^{-2}}$ and the line intensity is given in units of 10^{-6} photons $\mathrm{s^{-1}\,cm^{-2}}$. For parameters that are different between the two observations (nuclear continuum photon index and luminosity as well as its column density), see text.

Common constant components in the 2006 / 2013 *XMM–Newton* observations				
Soft scatt.	APEC (1)		APEC (2)	
$L_{0.5-2}$	kT (keV)	$L_{0.5-2}$	kT (keV)	$L_{0.5-2}$
$(6.7 \pm 0.3) \times 10^{-2}$	0.80 ± 0.04	$(2.8 \pm 0.2) \times 10^{-2}$	0.09 ± 0.03	$(9 \pm 1) \times 10^{-3}$
Cold refl.	Hard scatt.		Ionized Fe line	
L_{2-10}	$L^{\mathrm{scatt}} / L^{\mathrm{nucl}}$	N_{H}	E_{rest}	Intensity
0.31 ± 0.02	0.14 ± 0.03	7.5 ± 0.8	6.50 ± 0.04	5.3 ± 1.7

4.6 The 2006 and 2013 *XMM–Newton* observations

The best–fit models reached in the previous Sections characterize the ionization states, equivalent column densities and outflow velocities of three absorbers (all ionized at different degrees, and all with similar outflow velocities), based on the rich set of absorption lines detected in 2010 with *Chandra*. Here, we refine our results as far as possible adding data from *XMM–Newton* observations of 2006 and 2013 (pn), that have been previously studied by Jiménez-Bailón et al. (2008) and Miniutti et al. (2014) respectively.

The resolution of the *Chandra* HETGS is much greater than that of *XMM–Newton* EPIC-pn instrument, so that the pn spectra do not show the profusion of lines that the HEG / MEG spectra do. However, in order to try to assess the variability of the absorbers detected with *Chandra*, we consider here the *XMM–Newton* pn spectra from the 2006 and 2013 observations.

The relatively simple baseline continuum model used so far is not an adequate description of the *XMM–Newton* data. This is for two main reasons: (i) the *XMM–Newton* data extend down to 0.5 keV (as opposed to the *Chandra* data that do not have sufficient signal–to–noise ratio below 1.2 keV) and reveal structure in the soft X–rays, and (ii) the *XMM–Newton* observations (especially the 2013 one) are more heavily absorbed than the *Chandra* one (see e.g. Fig. 4.3) and an additional hard X–ray component is visible in the heavily absorbed 2013 *XMM–Newton* spectrum.

As discussed extensively by Miniutti et al. (2014), the soft X–ray structure is well reproduced by adding two thermal plasma components (the APEC model in XSPEC) to the soft power law which represents the scattered re–emission of the nuclear continuum by some extended gas. On the other hand, the 2013 *XMM–Newton* spectrum requires an additional power law in the hard X–ray band, absorbed by a column density that is different from that affecting the nuclear emission. This component was interpreted by Miniutti et al. (2014) as scattered emission in a clumpy absorber. The idea is that, if the main absorber is clumpy instead of homogeneous, the observed spectrum should comprise not only a transmitted component (i.e. the nuclear continuum absorbed by the particular clump that happens to be in our LOS) but also a scattered component due to clumps out of the LOS that intercept the nuclear emission re–directing part of it into the LOS. As this scattered component reaches us after passing through the clumpy absorber itself, it is absorbed by the spatially–averaged column density of the clumps rather than by that of the particular one that is in the LOS at the given epoch. This explains why the scattered component is absorbed by a different column density than the nuclear continuum, although the scattered fraction (i.e. basically the ratio between the scattered and nuclear luminosity) and the column density towards the scattered component should be the same at all epochs (as they represent spatially–averaged values). Miniutti et al. (2014) have derived a scattered fraction of 15 ± 3 per cent and a (neutral) column density of $(7.6 \pm 0.8) \times 10^{22}\,\mathrm{cm}^{-2}$ towards the scattered component. Note that the scattered component makes a non–negligible contribution to the hard X–ray spectrum only when the nuclear continuum is sufficiently absorbed (i.e. for column densities significantly higher than $7 \times 10^{22}\,\mathrm{cm}^{-2}$), which only occurs during the 2013 *XMM–Newton* observation.

We then consider a new baseline continuum model comprising all the above components. The global baseline model and its main components are shown in Fig. 4.12. These are a power law plus optically–thin emission from collisionally–ionized plasma accounting for the soft X–ray band (below ~ 2 keV), and three more components giving account of the hard X–ray band: a heavily absorbed power law as the intrinsic nuclear continuum, an unabsorbed X–ray reflection component from optically–thick matter, and an additional power law contributing in the 2–4 keV band and absorbed by a lower column density than the intrinsic nuclear continuum. The last component, introduced to model the residuals in the 2–4 keV band during the more absorbed *XMM–Newton* observation 10, is not typical of the AGN X–ray spectra. We explain this component as the result of a number of different clumps absorbing part of the nuclear continuum and scattering other part back into our LOS. Within this scenario, the power law peaking at 2–4 keV is a proxy encrypting the true geometry of the clumpy absorber / scatterer. Miniutti et al. (2014) found that the scattered contribution represents a constant fraction of the nuclear continuum (14 ± 3%).

Once explained the new model, we first perform a joint fit to the two *XMM–Newton* observations and we force all parameters that are not expected to vary between the two epochs to be the same, namely (i) the temperature and normalization of the two APEC components, (ii) the photon index and normalization of the soft scattered power law, (iii) the column density towards the hard scattered power law as well as the hard scattered fraction, and (iv) the flux of the neutral reflection component (carrying the Fe Kα emission line). The best–fitting model produces $\chi^2 = 1649$ for 1445 dof. Close inspection of the Fe Kα region reveals the presence of some emission structure bluewards of the line, especially in the more heavily absorbed 2013 *XMM–Newton* observation. We add a Gaussian emission line forcing it to have the same properties in the two observations and we reach $\chi^2 = 1612$ for 1443 dof for an additional Gaussian emission line at 6.50 ± 0.04 keV (in the galaxy rest frame). When the line intensity is allowed to vary between the two observations, no improvement is obtained, and the line EW is ~ 35 eV in 2006 and ~ 85 eV in 2013, reflecting the lower X–ray continuum in 2013. If no energy shift is assumed, the line most likely arises from ionized Fe emission.

All parameters that are kept in common between the two observations are reported in Table 4.5. As for the variable parameters, they are the nuclear continuum photon index and normalization, and the (neutral) column density towards it. As already shown by Miniutti et al. (2014), the 2006 *XMM–Newton* observation is absorbed by a column of $\sim 5.6 \times 10^{22}\,\mathrm{cm}^{-2}$, while the column density during the 2013 observation is one order of magnitude higher. The two photon indices are consistent with each other within the errors ($\Gamma = 1.95 \pm 0.07$ in 2006 and 2.0 ± 0.1 in 2013).

Having derived a baseline continuum model for the two observations, we now search for signatures of absorption features. All common parameters are fixed to their best–fitting values obtained from the joint fit of the two observations (see Table 4.5) and we consider the two observations separately. The baseline model (with common parameters fixed at their best–fitting values) results in $\chi^2 = 829$ for 705 dof for the 2006 observation and $\chi^2 = 783$ for 749 dof for the 2013 one. We first add a series of Gaussian absorption lines with width fixed at 1 eV and redshift fixed at the galaxy one,

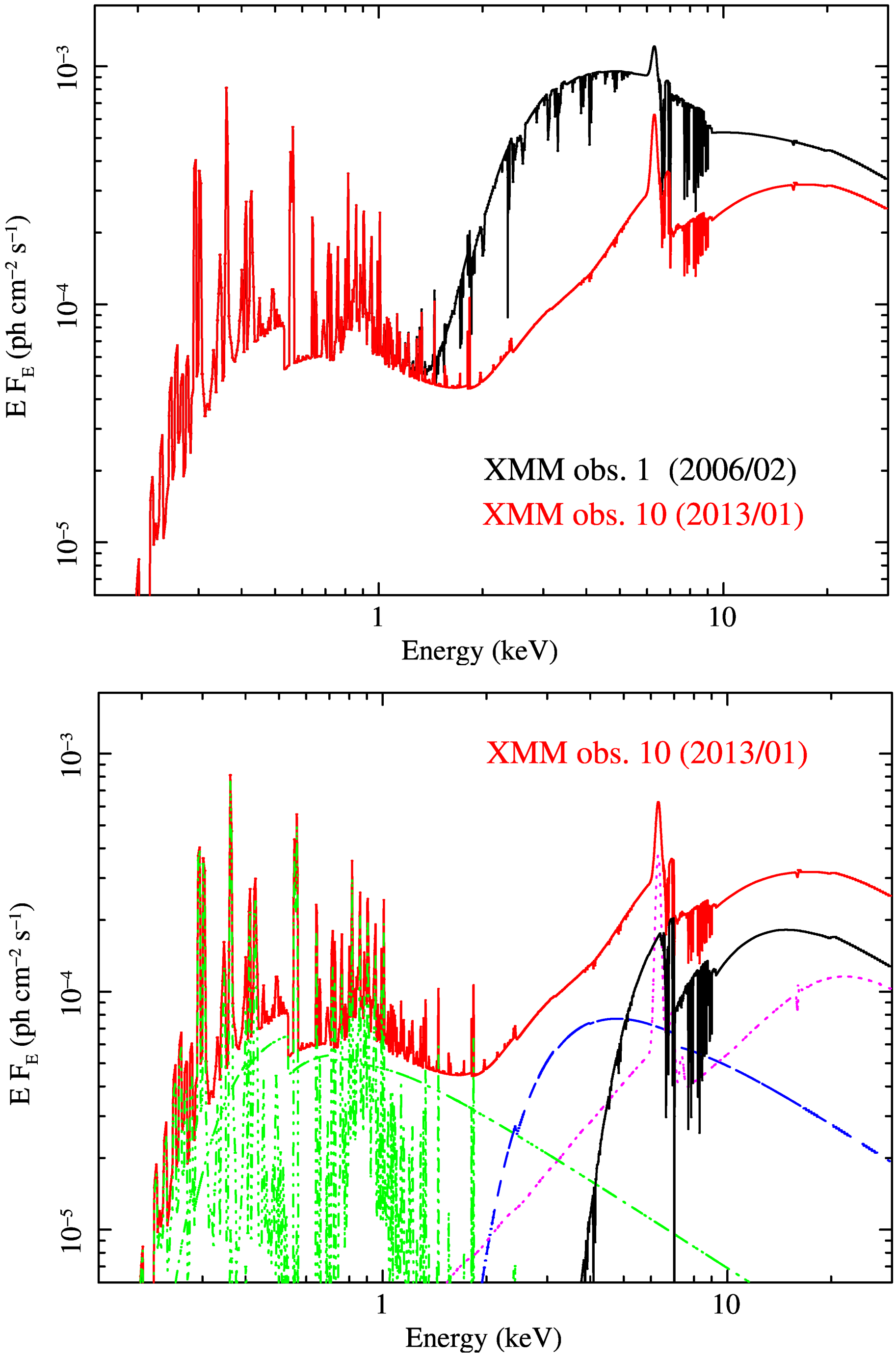

Figure 4.12: The best–fitting models for *XMM–Newton* observations 1 and 10 are shown in the upper panel and are extrapolated to higher energies than the data (i.e. to energies ≥ 10 keV) for clarity. In the lower panel, we re–plot the total best–fitting model for the more absorbed *XMM–Newton* observation 10, but include also all spectral components. The soft X–ray band below ∼ 2 keV is described by extended (constant) emission comprising a power law contribution and optically–thin emission from collisionally–ionized plasma (dot–dashed green lines). The hard X–ray band comprises contributions from (i) a heavily absorbed power law representing the intrinsic nuclear continuum (solid black line); (ii) an unabsorbed X–ray reflection component from optically–thick matter (dotted magenta line); and (iii) an additional power law contributing mainly in the 2–4 keV band and absorbed by a lower column density than the intrinsic nuclear continuum (dashed blue line). Figure credit: Miniutti et al. (2014).

and we report the lines improving the fit by more than $\Delta\chi^2 = 9.2$ in Table 4.6 together with their possible identification for the 2006 and 2013 observations.

4.6.1 The 2006 *XMM–Newton* observation

The two more significant lines are detected at 6.75 ± 0.03 and at 7.06 ± 0.04 keV. If identified with Fe xxv and Fe xxvi respectively, the observed lines are associated with high outflow velocities and, considering the large errors, with a possible common outflow velocity of $3100 \pm 400\,\mathrm{km\,s^{-1}}$. This outflow velocity is significantly higher than that derived from the *Chandra* data from the same two absorption lines (which have a common outflow velocity of $1150 \pm 350\,\mathrm{km\,s^{-1}}$). The absorption line at ~ 2.64 keV (see Table 4.6) is not highly significant, and can be probably associated with S xvi, although the very large error on the line energy does not allow to place a secure label on this feature. If the line is indeed associated with S xvi, the outflow velocity is consistent with that of the two ionized Fe lines (although with large error), possibly indicating a common origin in a highly ionized wind. The other two, less significant absorption lines in the 2006 observation have no clear identification (see Table 4.6).

The detection of Fe xxv and Fe xxvi absorption lines means that a hot phase with similar ionization as that detected in 2010 with *Chandra* is present in the 2006 observation as well, so we replace all Gaussian absorption lines with a PHASE model. The PHASE model produces a significant improvement, and we reach $\chi^2 = 712$ for 701 dof (to be compared with $\chi^2 = 829$ for 705 dof of the baseline continuum model). The absorber has $\log U = 2.0 \pm 0.3$, a column density of $\log N_{\mathrm{H}} \geq 23.4$, and an outflow velocity of $2700 \pm 1100\,\mathrm{km\,s^{-1}}$, consistent within the relatively large error with the common outflow velocity of $3100 \pm 400\,\mathrm{km\,s^{-1}}$ derived from the energy shift of the Fe xxv and Fe xxvi absorption lines.

As can be seen in Table 4.6, we do not find any absorption line that may be related to the l– or c–phases detected in the high–resolution *Chandra* data. However, it is interesting to see if gas with similar properties as seen in the 2010 *Chandra* observation is consistent with the 2006 *XMM–Newton* data as well. We first add an l–phase, fixing all of its parameters to those detected with *Chandra* (see Table 4.3, Model 2). The statistical result ($\chi^2 = 710$ for 701 dof) cannot be distinguished from the one with no l–phase ($\chi^2 = 712$ for the same number of dof). Letting all the parameters of the l–phase free to vary does not produce any improvement. We conclude that gas with the same properties as the l–phase detected with *Chandra* in 2010 is neither required nor excluded by the *XMM–Newton* data. Its non–detection is likely due to (i) the worse energy resolution of the pn data, and (ii) the higher column density of the coldest phase which lowers significantly the signal–to–noise ratio in the relevant spectral region (starting to be dominated by extended emission and scattered light rather than by the X–ray nuclear continuum).

As for the strictly neutral absorber (with column density of $\sim 5.6 \times 10^{22}\,\mathrm{cm^{-2}}$), we replace it with an ionized PHASE model. As no absorption lines associated with that component are detected, we fix its outflow velocity to that detected with *Chandra*, namely $1400\,\mathrm{km\,s^{-1}}$ (see Model 2 in Table 4.3). The replacement, however, does not produce any improvement, and the resulting ionization parameter is only an upper limit of $\log U \lesssim -0.3$. Hence, a non–zero ionization of the coldest phase is neither required nor excluded by the *XMM–Newton* data. The column density of this coldest phase presents some degree of degeneracy with the (basically unconstrained) ionization parameter and can take any value between $\log N_{\mathrm{H}} \simeq 22.7$ and $\log N_{\mathrm{H}} \simeq 23.3$ (the lower column density being associated with the lowest possible ionization, $\log U = -3$).

Table 4.6: Absorption lines detected with Gaussian models in the *XMM–Newton* EPIC-pn spectra. Every line contributes with two free parameters (rest frame energy and intensity). Only lines producing a statistical improvement of $\Delta\chi^2 \geq 9.2$ are reported.

2006 *XMM–Newton* observation

Phase	ID	Transition	$E_{\rm lab}$ (keV) / $\lambda_{\rm lab}$ (Å)	$E_{\rm restframe}$ (keV)	−EW (eV)	$v_{\rm outflow}$ (km s^{-1})	$\Delta\chi^2$
h	S XVI	$1s \rightarrow 2p$	2.6218 / 4.729	2.64 ± 0.03	20 ± 10	2050 ± 3350	10
h	Fe XXV	$1s^2 \rightarrow 1s2p$	6.7019 / 1.850	6.75 ± 0.03	80 ± 20	2150 ± 1300	44
h	Fe XXVI	$1s \rightarrow 2p$	6.9650 / 1.780	7.06 ± 0.04	90 ± 20	4050 ± 1350	37
–	–	–	–	7.7 ± 0.1	60 ± 30	–	11
–	–	–	–	8.4 ± 0.1	60 ± 30	–	11

2013 *XMM–Newton* observation

Phase	ID	Transition	$E_{\rm lab}$ (keV) / $\lambda_{\rm lab}$ (Å)	$E_{\rm restframe}$ (keV)	−EW (eV)	$v_{\rm outflow}$ (km s^{-1})	$\Delta\chi^2$
–	–	–	–	2.15 ± 0.03	40 ± 15	–	18

However, as shown in the previous Section, the c–phase ionization responds to the continuum variations on short time–scales during the 2010 *Chandra* 10–days–long monitoring, and this response can be used to break the degeneracy between ionization and column density in the 2006 data. This is because, assuming a perfectly homogeneous c–phase even on long time–scales (i.e. no clumpiness for the c–phase) the 2006 ionization can be predicted from the 2010 one by considering the different intrinsic continuum luminosity at the two epochs. For a fixed SED shape (and the photon indices in 2006 and 2010 are consistent with each other), the 2–10 keV X–ray intrinsic luminosity is proportional to the photon rate Q and hence to the ionization state U. As the c–phase ionization during the 2010 *Chandra* observation is $\log U = -0.45$ (see Model 2 in Table 4.3) and since the intrinsic 2–10 keV luminosity in 2006 is a factor of ~ 1.3 lower than in 2010, the 2006 c–phase must have ionization $\log U = -0.56$ if the c–phase is homogeneous (as opposed to clumpy) on long time–scales.

This removes the degeneracy between column density and ionization during the 2006 *XMM–Newton* observation, and allows us to check whether the absorber is indeed homogeneous as opposed to clumpy, by comparing the 2006 and 2010 column densities directly. This comparison is shown in Fig. 4.13 in terms of the statistical improvement as a function of column density for the 2010 (left) and 2006 (right) observations. Although the difference is small in absolute terms, the two column densities are inconsistent with each other at more than 5σ, indicating the non–homogeneous nature of the c–phase absorber on long time–scales. A clumpy absorber is also strongly suggested by the presence of a hard scattered component during the much more heavily absorbed 2013 *XMM–Newton* observation as discussed in detail by Miniutti et al. (2014).

We do not replace the neutral absorber towards the hard scattered component with an ionized one because this component has an almost negligible contribution in the 2006 *XMM–Newton* observation and it is only strictly required by the 2013 *XMM–Newton* data (Miniutti et al., 2014).

The best–fitting parameters for our final model, comprising the highly ionized h–phases and the two neutral absorbers towards the continuum and the hard scattered component are reported in Table 4.7. Fig. 4.14 (top) shows the high–energy spectrum from the 2006 observation together with our best–fitting model, dominated by the Fe emission lines at 6.4 and ~ 6.5 keV, and by the h–phase component.

4.6.2 The 2013 *XMM–Newton* observation

The only significant absorption line detected in the 2013 *XMM–Newton* spectrum is at ~ 2.15 keV (see Table 4.6). Its identification is difficult, and we also note that the feature occurs close to where a significant drop in quantum efficiency is seen for the pn detector, so that we cannot exclude that it has an instrumental origin. Hints for high–energy absorption lines bluewards of the Fe Kα emission line are seen, but none reaches the required $\Delta\chi^2 = 9.2$ when Gaussian models are considered.

With no absorption lines, applying detailed photoionization codes to the 2013 data will likely result in overmodelling. However, the nuclear and scattered continua are still absorbed by strictly neutral matter, while from the *Chandra* observations, we have indications that even the coldest component is in fact ionized. Note also that, based on the long–term variability properties of the coldest absorber, Miniutti et al. (2014) have interpreted the 2013 data with absorption from a cloud of the BLR as opposed to the 2006 *XMM–Newton* and 2010 *Chandra* observations where the c–phase was associated with a clumpy absorber at the torus scale.

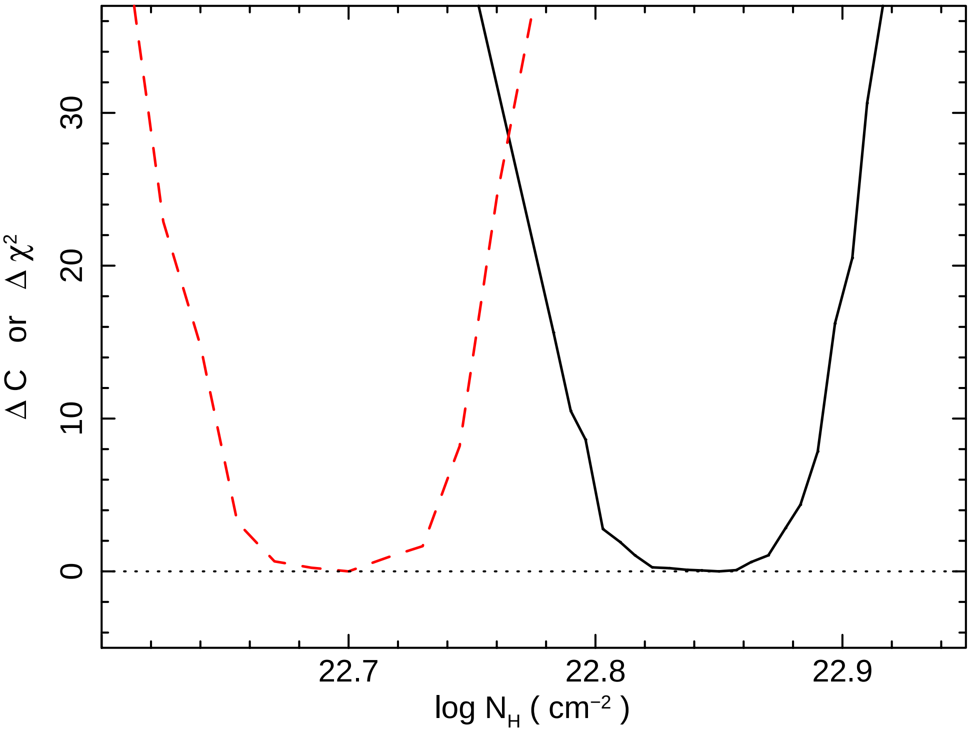

Figure 4.13: The statistical improvement as a function of the c–phase column density for the 2010 *Chandra* (left) and the 2006 *XMM–Newton* (right) observations as obtained with the STEPPAR command in XSPEC. We use the ΔC and $\Delta\chi^2$ values for the *Chandra* and the *XMM–Newton* data respectively. All parameters are free to vary during the minimization except the ionization of the c–phase during the 2006 *XMM–Newton* observation. This ionization is fixed to that expected under the assumption of a homogeneous rather than clumpy absorber ($\log U = -0.56$, see text for details). The column densities of the c–phase at the two epochs are similar but inconsistent with each other at more than 5σ, strongly suggesting the inhomogeneous nature of the c–phase.

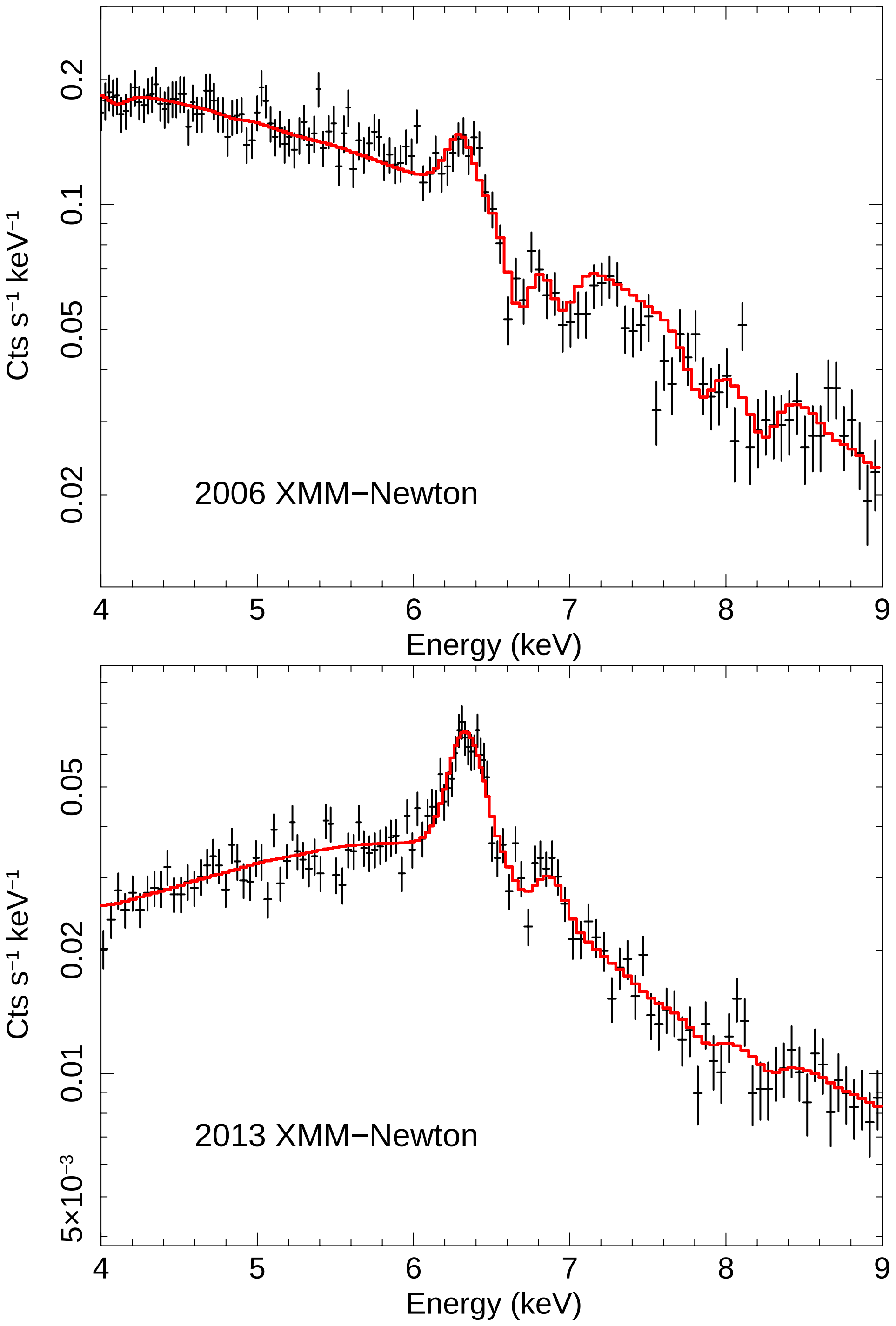

Figure 4.14: The high–energy part of the *XMM–Newton* EPIC–pn spectra from the 2006 (top) and 2013 (bottom) observations is shown together with the best–fitting model. The high–energy absorption features are well reproduced by the h–phase, although the significance of this component is relatively low in the 2013 data. The improvement of the statistical result with the addition of the h–phase is $\Delta\chi^2$ = 117 for 4 dof in the 2006 data and only $\Delta\chi^2$ = 14 in the 2013 data. Data have been slightly rebinned for visual clarity.

Table 4.7: Best–fitting parameters for the *XMM–Newton* observations. For the 2006 observation, the two c–phases are here modelled with a strictly neutral absorber at rest, as no improvement is obtained by replacing them with a PHASE model (see text for details on the parameters obtained when an ionized model is used instead). The superscript '^{f}' means that the parameter is fixed, the symbol '^{p}' indicates that the error on one parameter reached the limit of the model. Units as in Table 4.3.

			2006	2013
		Γ	1.95 ± 0.07	2.0 ± 0.1
		$L^{\rm nucl}_{2-10}$	7.5	5.8
Warm abs.	h–phase	$\log U$	2.0 ± 0.3	2.0 ± 0.3
		$\log N_{\rm H}$	$23.7^{+0.3p}_{-0.3}$	$23.6^{+0.4p}_{-0.4}$
		$v_{\rm turb}$	100 – 900	100 – 900
		$v_{\rm outflow}$	2700 ± 1100	4100 ± 1700
Cold abs.	c–phase	$\log U$	–	0.2 ± 0.2
		$\log N_{\rm H}$	22.7 ± 0.2	23.8 ± 0.1
		$v_{\rm turb}$	–	100 – 900
		$v_{\rm outflow}$	0^f	1400^f
Scatt. abs.	c–phase	$\log U$	–	$\lesssim -0.3$
		$\log N_{\rm H}$	22.9^f	22.9 ± 0.2
		$v_{\rm turb}$	–	100 – 900
		$v_{\rm outflow}$	0^f	1400^f
		χ^2 / dof	712/701	754/739

We test this scenario in the following way: we first replace the neutral absorber towards the nuclear continuum with a PHASE model. The lack of absorption features means that we are unlikely to be sensitive to outflow velocities, and we choose to fix it to the 2010 c–phase outflow velocity (1400 km s^{-1}). The model produces $\chi^2 = 772$ for 747 dof, slightly better than the baseline ($\chi^2 = 783$ for 749 dof). We obtain $\log U^{\rm nucl} \sim 0.2$ with $\log N_{\rm H}^{\rm nucl} \sim 23.8$ for the c–phase towards the nuclear continuum. Hence, the main absorber in 2013 is significantly more highly ionized than that in 2006 and 2010 (as well as being associated with a much higher column density). As for the hard scattered component absorber, replacing it with a PHASE model outflowing at 1400 km s^{-1} does provide a very marginal improvement ($\chi^2 = 768$ for 743 dof), but its ionization is only an upper limit of $\log U^{\rm scatt} \lesssim -0.3$. Letting the outflow velocities of the two absorbers free to vary does not provide any improvement, and the large errors are consistent with zero velocity (as well as with velocities of a few thousands km s^{-1} in both outflow and inflow), showing that we are not sensitive to this parameter, as expected.

As some hints for high–energy absorption lines are seen in the data, we add a highly ionized PHASE component to assess whether the h–phase can be detected in the 2013 *XMM–Newton* data. In this case, we leave the outflow velocity free to vary, as it may be possible to constrain it if a set of low EW absorption features is present in the data (although none is individually significant). We reach a best–fit of $\chi^2 = 754$ for 739 dof, marginally better than that with no h–phase component ($\chi^2 = 768$ for 743 dof). The h–phase has $\log U \sim 2.0$, $\log N_{\rm H} \sim 23.6$, and an outflow velocity of 4100 ± 1700 km s^{-1}. As it was the case for the 2006 *XMM–Newton* observation adding an l–phase with the same properties as that detected in 2010 with *Chandra* neither improve nor worsen the best–fit. Hence such a component is not required by the data, but its presence cannot be excluded either. Our final best–fitting parameters are reported in Table 4.7 and the high–energy spectrum from the 2013 observation is shown in the bottom panel of Fig. 4.14, where the (low significance) h–phase imprints some weak absorption features.

Summarizing, the 2006 observation shows a clear h–phase with ionization and column density of the order of those detected with the high–resolution *Chandra* data (note, however, that its outflow velocity is significantly higher). Although the 2006 data do not allow us to distinguish between a strictly neutral and an ionized c–phase, we have shown that the 2006 c–phase column density is most likely different from the 2010 one, strongly suggesting that the c–phase is not homogeneous on long time–scales, but rather most likely clumpy.

In 2013, the nuclear continuum is absorbed by a much higher column (close to $10^{24}\,\mathrm{cm}^{-2}$) of higher ionization gas ($\log U \sim 0.2$), and a low significance h–phase is detected with similar properties to that observed in 2006. The heavily absorbed 2013 X–ray spectrum reveals the presence of a hard scattered component. The scattered fraction is ~ 14 per cent, and the scattered emission is transmitted through a gas phase with $\log U \lesssim -0.3$ and $\log N_{\mathrm{H}} \sim 22.9$. A phase with intermediate ionization is not required by the 2006 and 2013 *XMM–Newton* data, but an l–phase with the same properties as that detected with *Chandra* in 2010 is consistent with both data sets.

4.7 Discussion

The temperature and ionization state of the three absorbers we have detected with *Chandra* are similar to those of warm absorbers typically detected in Seyfert 1 galaxies. Column densities are however on the high side for standard warm absorbers, see e.g. Torresi et al. (2010) or Gupta et al. (2013). Moreover, the column density of the coldest absorbing system is of the same order, or even higher, than that of the higher ionization components while, in general, higher ionizations are associated with larger columns (e.g. Zhang et al., 2015). These differences can be interpreted naturally within a scenario in which ESO 323–G77 represents a source intermediate between Seyfert 1 and Seyfert 2 galaxies. In fact, considering the polar–scattered nature of the source, and its likely intermediate inclination of $\sim 45^\circ$ (Schmid et al., 2003), ESO 323–G77 appears to lie precisely in that intermediate–inclination region of the parameter space. In this framework, the cold absorber we detect would be the same warm absorber as seen in other sources, with its special properties due to the orientation at which we are seeing this source: grazing the edge of the clumpy torus. Objects observed at higher inclination angles (with respect to the symmetry axis) than ESO 323–G77 correspond to highly X–ray obscured Seyfert 2 galaxies; sources viewed at slightly lower inclination angles are typical Seyfert 1 galaxies with standard warm absorbers; objects at even lower inclination angles result into a Seyfert 1 optical classification and are likely to be characterized by the absence of warm absorbers (i.e. polar Seyfert 1 galaxies offering a naked view of the innermost X–ray emitting region).

The three absorbers we detect in the high–resolution *Chandra* data have similar outflow velocities, suggesting a common origin. Only the coldest one responds with ionization changes to intrinsic luminosity variations on short time–scales (days). The coldest absorber is most likely clumpy, as suggested by the comparison between the column densities derived in 2010 and in 2006, and by the need for an extra hard scattered component in the heavily absorbed 2013 observation, as discussed already by Miniutti et al. (2014). On the other hand, the highest–ionization phase is consistent with the same ionization and column density on both short and long time–scales, although its outflow velocity appears to be variable on long time–scales. As for the intermediate zone (the l–phase), it is only detected in the high–resolution, relatively unobscured *Chandra* observation. However, a phase with similar properties is allowed (not required) to be present in the *XMM–Newton* data as well. This suggests that the warm absorbers are distributed in a more homogeneous way than the coldest one. Such properties (similar outflow velocities, clumpiness of the denser, colder absorber, and relatively homogeneous distribution of the warmer phases) suggest to consider a solution in which all absorbers are part of the same outflow, with the warmer phases providing the pressure confinement that is necessary to support relatively long–lived, dense, colder clouds [although originally considered for the BLR case, see e.g. Krolik et al. (1981) for the multi–phase confinement model, and Emmering et al. (1992) and Elvis (2000) for the idea of an outflowing multi–phase structure of the BLR].

Such a scenario cannot be directly confirmed by the data, but we can at least test whether the three absorbers detected in the 2010 *Chandra* observation are consistent with being in pressure equilibrium. In order to derive the properties of the three gas phases, we need to estimate the product nR^2 which, by definition, only depend on the ratio between photon rate and ionization (Q/U). This means that deriving the gas properties from the u×u×u configuration (Model 2 in Table 4.3) or from the s×s×u one (Model 3) gives the same result (we have shown in Section 4.4.1 that, for the h– and l–phases, the drop in U obtained with Model 3 is simply proportional to the drop in Q due to the different, absorbed SED). For simplicity, as well as for consistency with the previous Sections, we continue to use the u×u×u configuration (Model 2) as best–fitting model from which we derive estimates on the gas properties. As mentioned, consistent results are obtained using Model 3 instead.

4.7.1 The ‘cold’ absorber in 2010

We proceed with orders–of–magnitude estimates of the properties of the absorbing gas. According to our best–fitting model (Model 2 in Table 4.3), the photon rate integrated from 1 Ry to infinity is $Q \simeq 1.8 \times 10^{53}$ photons s^{-1} during the 10 days probed by the *Chandra* time–averaged spectrum.

From the fact that the cold absorber is in photoionization equilibrium with the impinging continuum within 5 days, as shown in Fig. 4.11, and using the formula and procedures of Nicastro et al. (1999) with the recombination time–scales and fractions for Si viii–x for the best–fitting ionization parameter $\log U^{(c)} = -0.45$, one can estimate a lower limit on the cold absorber number density of $n^{(c)} \gtrsim 5 \times 10^4\,\mathrm{cm^{-3}}$ (using other ions produces a difference of a few per cent only). Using the definition of U, one has that $R^{(c)} \lesssim 5 \times 10^{18}\,\mathrm{cm} \simeq 1.6\,\mathrm{pc}$. A lower limit on the location of the c–phase can be obtained by considering that the observed outflow velocity (~ 1400 kms) cannot be lower than the escape velocity at the minimum launching radius. Knowing that the black hole mass is $M_{\mathrm{BH}} \simeq 2.5 \times 10^7\,M_\odot$ (Wang & Zhang, 2007), we derive $R^{(c)} \gtrsim 3 \times 10^{17}\,\mathrm{cm} \simeq 0.1\,\mathrm{pc}$. Note that the dust sublimation radius in ESO 323–G77 is located at ~ 0.14 pc (Miniutti et al., 2014), so that the c–phase is consistent with being located somewhere between the inner and outer edges of the so–called torus (Krolik & Kriss, 2001). This conclusion agrees well with that reached by e.g. Blustin et al. (2005) who, based on the analysis of high energy–resolution data on a sample of 23 AGN, have shown that warm absorbers most likely originate as outflows from the dusty torus.

Using again the definition of ionization parameter, the lower limit on $R^{(c)}$ translates into an upper limit on the number density, namely $n^{(c)} \lesssim 10^7\,\mathrm{cm^{-3}}$. Finally, using derived values of $n^{(c)}$, the observed column density $\log N_{\mathrm{H}}^{(c)} \simeq 22.7$, and assuming a spherical absorbing cloud, the diameter of the cloud $D^{(c)}$ is in the range of $[5 \times 10^{15} - 10^{18}]$ cm. Having constrained the absorber density and knowing its equilibrium temperature (which is ~ $5{\times}10^4$ K according to our best–fitting PHASE model), the pressure of this component can be estimated as $P = k_{\mathrm{B}} n T$ (where k_{B} is the Boltzmann constant), so that $P^{(c)} = [3 \times 10^{-7} - 7 \times 10^{-5}]\,\mathrm{dyne\,cm^{-2}}$.

Finally, let us compute the kinetic power of the cold absorber in order to check if it could contribute to the AGN feedback, and therefore to the evolution of the galaxy. Tombesi et al. (2013) derive that, once the outflow reaches a constant terminal velocity, its kinetic power is determined by Eq. 4.1:

$$\dot{E}_K = \frac{1}{2}\dot{M}_{\rm outflow} v_{\rm outflow}^2, \tag{4.1}$$

where $\dot{M}_{\rm outflow}$ is the mass outflow rate, which can be calculated from the expression derived by Krongold et al. (2007) for a biconical geometry (Eq. 4.2):

$$\dot{M}_{\rm outflow} = \mu \pi m_p N_{\rm H} v_{\rm outflow} R f(\delta, \phi), \tag{4.2}$$

where m_p is the proton mass, the value of μ is calculated as $1/1.23$ by Krongold et al. (2007) and as $1/1.4$ by Tombesi et al. (2013), considering solar abundances, and $f(\delta, \phi)$ is a factor depending on the disc and wind orientation. This factor is of the order of unity for angles between the disc and the LOS $\delta > 20°$ (for the case of ESO 323–G77, $\delta \sim 45°$), and between the disc and the wind $\phi > 45°$ (disc winds are usually considered roughly vertical, $\phi \sim 90°$). Hence, we approximate the mass outflow rate as $\dot{M}_{\rm outflow} = \pi m_p N_{\rm H} v_{\rm outflow} R$. For an outflow velocity of $\sim 1500\,{\rm km\,s^{-1}}$, an intermediate distance of $R \sim 10^{18}$ cm, and a column density of $\log N_{\rm H} = 22.7$, we get a mass outflow rate of $\dot{M}_{\rm outflow} \sim 2 \times 10^{-9} M_\odot$. This implies a kinetic power of $\dot{E}_K \sim 4 \times 10^{41}\,{\rm erg\,s^{-1}}$, i.e. 0.3% of the bolometric luminosity of ESO 323–G77, not enough to significantly contribute to AGN feedback.

4.7.2 The two warm absorbers in 2010

In order to check if the warm / hot absorbers can pressure–confine the clumpy coldest phase, we assume here cospatiality of the three phases, as suggested by the similar outflow velocities. Hence, for all absorbers, we assume $R = [0.3 - 5] \times 10^{18}$ cm. Using $Q \simeq 1.8 \times 10^{53}$ photons s^{-1} and the best–fitting ionization parameters of the h– and l–phases ($\log U^{\rm (h)} \simeq 1.9$ and $\log U^{\rm (l)} \simeq 0.5$), one can constrain the number densities of the two warm absorbers to be $n^{\rm (h)} = [2 \times 10^2 - 7 \times 10^4]\,{\rm cm^{-3}}$ and $n^{\rm (l)} = [6 \times 10^3 - 2 \times 10^6]\,{\rm cm^{-3}}$, respectively. According to our best–fitting model, the temperature of the two warm absorbers is 5.8×10^6 K for the h–phase and 5.5×10^5 K for the l–phase, so that their pressure is $P^{\rm (h)} = [10^{-7} - 6 \times 10^{-5}]\,{\rm dyne\,cm^{-2}}$ and $P^{\rm (l)} = [4 \times 10^{-7} - 10^{-4}]\,{\rm dyne\,cm^{-2}}$ respectively. The pressure of the warm absorbers is in both cases consistent with that derived for the c–phase. The common pressure interval for the three phases to be in pressure equilibrium is $P^{\rm (c,h,l)} = [4 \times 10^{-7} - 6 \times 10^{-5}]\,{\rm dyne\,cm^{-2}}$.

We then conclude that the wind we detect in the data from the 2010 *Chandra* observations is consistent with being associated with the atmosphere of the clumpy torus, and with being arranged in three phases in pressure equilibrium with each other, with the coldest clumps being confined by the more homogeneous and hotter phases. Note that we cannot claim that both the h– and l–phases contribute to the confinement, but only that they are both consistent with this role which may be well dominated by one of the two phases.

Now we compute the mass outflow rate and the kinetic power of the warm absorbers in 2010 as we did in Section 4.7.1. With the assumption of cospatiality ($R \sim 10^{18}$ cm, $v_{\rm outflow} \sim 1500\,{\rm km\,s^{-1}}$), from Eq. 4.2 we get that the mass outflow rates for the intermediate and high ionization absorbers are $\sim 10^{-9}$ and $\sim 2 \times 10^{-8} M_{\odot}$, respectively, therefore being their kinetic power $\sim 2 \times 10^{41}$ and $\sim 4 \times 10^{42}$ erg s^{-1}, i.e. 0.1% and 2% of the bolometric luminosity of ESO 323–G77, respectively. Hence, the mechanical power of the highly ionized warm absorber detected in 2010 turns out to be significant enough to contribute to AGN feedback (at least ~ 0.5% of the bolometric luminosity, Tombesi et al., 2013). In this aspect, this means an important indication for the interplay of the AGN wind with the host galaxy on large scales.

4.7.3 The absorbers in 2006 and 2013

The ionization of the c–phase is only poorly constrained during the 2006 *XMM–Newton* observation. However, its column density is clearly higher than that during the 2010 *Chandra* observation, demonstrating the clumpiness of this component. The truly different case is represented by the 2013 *XMM–Newton* observation, where a much higher column density and ionization for the c–phase are obtained. As mentioned, Miniutti et al. (2014) have interpreted the c–phase in 2013 as due to a clump (cloud) of the BLR, as opposed to the 2010 (and probably 2006) observations where we just show that the c–phase is most likely associated with the clumpy torus.

We first assume that the 2013 c–phase has the same origin as in 2006 and 2010, namely that it is confined within the inner and outer edges of the torus. According to our best–fitting model, the photon rate in the 2013 *XMM–Newton* observation is $Q \simeq 10^{53}$ photons s^{-1} and the best–fitting ionization of the cold phase is $\log U \simeq 0.2$. Hence, if the 2013 absorber was cospatial with the c–phase detected in 2010 with *Chandra*, its density should be ~ 8 times lower than in 2010 ($(Q/U)^{(2013)} \simeq (Q/U)^{(2010)}/8$). Given the much higher column density observed in 2013 ($N_{\rm H}^{(2013)} \simeq 12.6\, N_{\rm H}^{(2010)}$), the 2013 absorbing cloud should be larger in size by a factor of ~ 100 with respect to the 2010 absorber. Since the 2010 absorber has an estimated diameter larger than 5×10^{15} cm, the 2013 cloud would have a diameter of at least 5×10^{17} cm. Even assuming the highest possible orbital velocity for the range of radii associated with the torus (~ 1100 km s^{-1}), a cloud of that size would cover a negligibly small X–ray emitting region for about 140 years.

The X–ray history of ESO 323–G77 excludes that this is the case, as variability associated with column density of the order of that observed during the 2013 observation do occur on time–scales as short as 1 month, as demonstrated by Miniutti et al. (2014) using *Swift* data. In order to produce such short time–scale variability, any absorber must be smaller and denser by orders of magnitude, which places the 2013 absorber much closer in, in a region of the parameter space that is roughly consistent with the dust–free BLR (note, however, that the 2013 absorber is not necessarily associated with a cloud that produces the optical broad lines, as its ionization parameter is likely too high to produce the correct line ratios). Moreover, if the 2013 absorber were associated with the dusty torus, UV variability between 2006 and 2013 would have been expected, due to the dramatic increase in column density. However, as reported by Miniutti et al. (2014), no decrease in UV fluxes was detected in 2013 despite the increase in the X–ray column density by about one order of magnitude, which strongly suggests that the 2013 c–phase is dust–free and thus part of the BLR rather than of the dusty torus. We then conclude that while the 2006 cold absorber is most likely part of the same clumpy absorbing structure as in 2010 (at spatial scales consistent with the dusty, clumpy torus), the 2013 absorber is more consistent with being associated with a denser and dust–free clump of the BLR, in line with the ones detected, for example, in NGC 1365 (Risaliti et al., 2009a), SWIFT J2127.4+5654 (Sanfrutos et al., 2013) or Mrk 335 (Longinotti et al., 2013).

On the other hand, the h–phase has similar ionization and column density in all observations, but its outflow velocity appears to be higher in the 2006 and 2013 *XMM–Newton* observations than in the 2010 *Chandra* one. This may indicate that this highly ionized phase is also somewhat clumpy, or that it is more efficiently accelerated when the X–ray continuum is suppressed by c–phase absorption (the *Chandra* observation being the less absorbed).

4.8 Summary and conclusions of Chapter 4

We present results from six observations of the polar–scattered Seyfert 1.2 galaxy ESO 323–G77. Four observations were taken by the HETGS on board *Chandra* within 10 days in 2010 April. Two more observations were taken with *XMM–Newton* and are considered here for comparison. The first one, obtained in 2006, is slightly more absorbed than the *Chandra* one. The second (2013) is much more heavily absorbed (see e.g. Fig. 4.3).

The high–resolution *Chandra* data are characterized by a rich set of absorption lines that can be associated with three outflowing absorbing gas phases with different ionizations. A highly ionized phase (h–phase) is responsible for the Fe xxv and Fe xxvi absorption lines and it also contributes to the observed Si xiv and S xvi features. An intermediate–ionization zone (l–phase) is mostly revealed by Si xiii-xiv and S xv-xvi, and contributes as well at low energies where absorption due to Ne x and Mg xi-xii is seen. A third, low–ionization phase (c–phase) is also detected and accounts for the Si viii-x lines while contributing, together with the l–phase, at Ne x and Mg xi-xii as well. The latter phase replaces the strictly neutral absorber that is ubiquitously observed in Compton–thin AGN at X–ray energies. Here we show that this absorber is in fact both ionized and outflowing. The three phases are outflowing with velocities of the order of $1000 - 2000\,\mathrm{km\,s^{-1}}$, and there is evidence for the l–phase to be slightly faster than the other two. The c–phase ionization responds to luminosity variation on time–scales as short as a few days, demonstrating that the gas is dense enough to be in photoionization equilibrium with the continuum on short time–scales. Its clumpiness is suggested by the variation of its column density between the 2006 and the 2010 observations (as well as by the presence of a hard scattered component which contributes significantly to the X–ray spectrum in heavily absorbed data sets; see Miniutti et al., 2014). On the other hand the warm / hot phases are consistent with having the same ionization and column density on both short and long time–scales, suggesting that they are distributed in a more homogeneous way.

We show that the data are consistent with three cospatial phases with similar outflow velocities and confined between the inner (~ 0.1 pc) and outer (~ 1.6 pc) edges of the so–called clumpy, dusty torus. Moreover, under this assumption, the three phases share the same pressure. This calls for a rather natural scenario in which relatively cold, dense clouds are pressure confined by the more homogeneous warm / hot phases. Such torus–scale outflow may well represent the outer part of an outflow launched further in, which may give rise to the full system of BLR and obscuring torus in AGN replacing, with a wind solution, the classical structure of standard unification schemes (Emmering et al., 1992; Elvis, 2000; Elitzur & Shlosman, 2006).

The 2013 *XMM–Newton* observation is much more heavily obscured by a gas phase with one order of magnitude higher column density and ionization than in 2010. We show that this absorber is unlikely to be cospatial with the 2006 and 2010 c–phase at torus–like spatial scales, and that it must be associated with a smaller, denser structure. This places the 2013 c–phase within the dust–free BLR, although the ionization is likely too high to give rise to the observed optical broad lines.

In our analysis we detect both the BLR and the outflowing torus components, which implies that all structures are within observational reach in ESO 323–G77, possibly thanks to an ionizing favourable viewing angle of ~ 45°, intermediate between classical Seyfert 1 and Seyfert 2 galaxies.

5

Summary and concluding remarks

In Chapter 2 we confirm the detection of a relativistically broadened Fe Kα line in a ~ 130 ks observation of the NLS1 galaxy SWIFT J2127.4+5654 with *XMM–Newton*. From these data we measure:

i) an intermediate black hole spin of $a \sim 0.5$, and

ii) a relatively high observer inclination of $i \sim 44°$.

Also, significant flux and spectral variability is present throughout the observation. We perform a time–resolved spectral analysis in order to determine the origin of the observed spectral variability. Our results are consistent with being affected by additional neutral absorption only partially–covering the X–ray source during the first 90 ks. Assuming the spectral variability to be driven by changes of the absorber CF, we show that the CF evolution is consistent with one single cloud crossing our LOS during the first 90 ks of the exposure. The following constraints on the absorbing cloud are found:

i) column density of $N_{\rm H} = \left(2.0^{+0.2}_{-0.3}\right) \times 10^{22}\,{\rm cm}^{-2}$,

ii) number density of $n_{\rm c} \geq 1.5 \times 10^{9}\,{\rm cm}^{-3}$,

iii) diameter of $D_{\rm c} \leq 1.5 \times 10^{13}\,{\rm cm}$,

iv) distance of $R_{\rm c} \geq 4.3 \times 10^{16}\,{\rm cm}$,

v) Keplerian velocity of $v_{\rm c} \leq 2100\,{\rm km\,s}^{-1}$.

All these properties are consistent with those of a BLR cloud partially covering a compact X–ray source during the *XMM–Newton* observation. The identification of the absorber with a BLR cloud is also supported by the observed optical broad line FWHM $\sim 2000\,{\rm km\,s}^{-1}$ (Malizia et al., 2008). By assuming a flattened BLR geometry and an inclination of $i = 44°$, the FWHM implies a Keplerian velocity of $1.4 \times 10^3\,\mathrm{km\,s^{-1}}$, consistent with the cloud velocity upper limit. We also constrain the size of the X–ray emitting region by using the partial eclipse. The CF evolution implies an upper limit on the X–ray source size of $D_\mathrm{s} \leq 2.3 \times 10^{13}\,\mathrm{cm} = 10.5\,r_g/M_\mathrm{best}$ where M_best is the black hole mass in units of $1.5 \times 10^7\,M_\odot$. Such a compact X–ray emitting region is consistent both with previous results based on similar occultation events in the X–rays and with microlensing results. It is also consistent with the steep emissivity profile measured for the reflection component.

All these results point to a partial eclipse by a BLR cloud of the X–ray continuum source in SWIFT J2127.4+5654, in line with the mounting observational evidence that part of the observed X–ray absorption in AGN is due to a clumpy absorber whose properties and location can be identified with either the BLR or with a clumpy torus (when absorption variability occurs on long time–scales) which probably are just different parts of the same obscuring region. Notice too that the inclination we measure enhances the probability of X–ray eclipses. Our analysis strongly suggests that the X–ray continuum is produced in a compact region only a few r_g in size, which is consistent with the detection of a reflection component off the inner accretion disc.

In Chapter 3 we investigated the GR effects due to the proximity of the innermost regions of the accretion disc to the central SMBH, by means of a relativistic model capable to discern the parameters involved in an occultation event. The eclipsing of those regions produces peculiar light curves that allow us to compute the flux distribution from the corona and the disc apparent to the observer. By the effect of Doppler boosting, anisotropies arise, whose detection would definitely prove AGN X–ray spectra carry the signature of GR effects.

Features similar to those described in the paragraph above have already been detected (see Figs. 2.9 and 3.15, corresponding to SWIFT J2127.4+5654 and NGC 1365, respectively). This encourages us to deepen the study of these relativistic effects by fitting real spectra of SWIFT J2127.4+5654. We conclude that our data are consistent with a system characterized by parameters found in previous studies ($i = 45°$, $a = 0.58$, $q = 4.9$), eclipsed by a Compton–thin, ionized cloud ($N_\mathrm{H} \sim 10^{23}\,\mathrm{cm^{-2}}$, $\xi \sim 10\,\mathrm{erg\,cm\,s^{-1}}$) moving at $2100\,\mathrm{km\,s^{-1}}$. The corona and the reprocessing region are plane–parallel annuli, both with inner radius of $3.9\,r_\mathrm{g}$. The outer radius of the corona is between 5 and $9\,r_\mathrm{g}$, and the radius of the obscuring cloud is between 3 and $5\,r_\mathrm{g}$. These results are consistent with those derived in Chapter 2.

In Chapter 4 we present a thorough analysis from six observations of the polar–scattered Seyfert 1.2 galaxy ESO 323–G77. We detect both the BLR and the outflowing torus components, which implies that all structures are within observational reach in ESO 323–G77, possibly thanks to an ionizing favourable viewing angle of $\sim 45°$, intermediate between classical Seyfert 1 and Seyfert 2 galaxies.

The four high–resolution *Chandra* observations present a rich set of absorption lines as the signature of three outflowing absorbing gas phases with different ionizations: two highly ionized phases (warm / hot) and a low–ionization one (cold), which replaces the neutral absorber commonly observed in unobscured AGN at the X–rays. We demonstrate that the three phases are outflowing at

$\sim 1000-2000\,\mathrm{km\,s^{-1}}$. The low–ionization phase responds to intrinsic luminosity variations of the source on days time–scales, which demonstrates that the gas is dense enough to be in photoionization equilibrium with the continuum on short time–scales. We also find the cold absorber to be clumpy, as suggested by the variation of its column density between the 2006 and the 2010 observations as well as by the presence of a hard scattered component which contributes significantly to the X–ray spectrum in heavily absorbed data sets. On the other hand the warm / hot phases are consistent with having the same ionization and column density on both short and long time–scales, suggesting homogeneity.

The 2013 *XMM–Newton* observation is much more heavily obscured than in 2010. We show that the absorber in this observation is unlikely to be cospatial with the 2006 and 2010 cold phase at torus–like spatial scales, and that it must be associated with a smaller, denser structure within the dust–free BLR.

We show that the 2010 data are consistent with three cospatial phases outflowing at similar velocities and confined between the inner and outer edges of the clumpy, dusty torus. Moreover, the three phases share the same pressure, so that we claim for a natural scenario in which relatively cold, dense clouds are pressure confined by the more homogeneous warm / hot phases. Such torus–scale outflow may well represent the outer part of an outflow launched further in, which may give rise to the full system of BLR and obscuring torus in AGN, replacing, with a wind solution, the classical structure of standard, unification schemes.

6

Future work

Exhaustive search and analysis of X–ray eclipses

By the moment, occultation events have been studied only from *XMM–Newton* data from observations of SWIFT J2127.4+5654, as addressed in Chapters 2 and 3. In a forthcoming work, we will fit *XMM–Newton* archival data of other sources of interest appart from SWIFT J2127.4+5654, such as NGC 1365, MCG 6–30–15, or 1H 0707–495, among many others. We will also simulate spectra from other instruments. In this context, we will study the effect of eclipses produced by thicker clouds in harder bands by means of *NuSTAR*. We will also perform simulations of spectroscopic data from the future X–ray observatory *Athena*, considering more complex models giving account of a forest of resolved absorption lines, by combining the PHASE code by Krongold et al. (2003) with the KYN code by Dovčiak et al. (2004), in order to take advantage of the outstanding spectral resolution that will fulfill *Athena*. Among the technical issues to take into account, it will be important to refine the determination of any possible degeneracies among the parameters, as well as to study variations in the soft excess band, where the sensitivity of our instruments gets its highest.

Multiwavelength study of AGN outflows

Since X–ray photons are produced in the closest environments of SMBHs, the X–ray energy band is a key piece of the electromagnetic spectrum for our understanding of the black hole physics and the accretion processes. However, the optical and UV wavelengths are crucial to understand the gas surrounding the AGN and the nuclear winds. Also, radio frequencies are fundamental in the study of the relativistic jets. The most powerful tool to carry out a thorough analysis of the AGN as a whole is, therefore, made by the combination of multiwavelength data.

The great importance of winds is due to their ubiquity among AGN. High–resolution X–ray spectra are required to study these nuclear winds, since the absorption lines produced by these photoionized winds is imprinted in the X–ray band. Refining of the AGN models, and understanding their nature and their relation with their environment is one of the main goals of modern Astrophysics. The systematic study of nuclear winds in interesting objects, others than ESO 323–G77 (comprehensively analysed in Chapter 4) from a multiwavelength approach, will allow us to estimate the location, velocity, structure and physical properties of high–velocity outflows, and to better understand these systems and their relation with the jets and the AGN feedback.

A

XSPEC models used within this work

In this appendix we collect all models used along this thesis work in the XSPEC environment, listed in alphabetical order. A brief description of each one of them is included, followed by the definition of the parameters involved. References are provided when needed.

APEC

Astrophysical Plasma Emission Code. It is an emission spectrum from collisionally–ionized diffuse gas calculated using the AtomDB code (Smith et al., 2001).

Parameter 1: plasma temperature in keV.

Parameter 2: Metal abundances, including C, N, O, Ne, Mg, Al, Si, S, Ar, Ca, Fe, and Ni. He is fixed at cosmic value.

Parameter 3: z, redshift.

Parameter 4: normalization computed as $\frac{10^{-14}}{4\pi[D_{\rm A}(1+z)]^2}\int n_{\rm e}n_{\rm H}dV$, where $D_{\rm A}$ is the angular diameter distance to the source in cm, and $n_{\rm e}$ and $n_{\rm H}$ are the electron and H densities in $\rm cm^{-3}$.

cutoffpl

Power law with high energy exponential cutoff. It is modelled by $M(E) = KE^{-\alpha}e^{-E/\beta}$.

Parameter 1: α, the power law photon index.

Parameter 2: β, the e–folding energy of exponential cutoff in units of keV.

Parameter 3: K, a constant in units of photons $\rm keV^{-1}\,cm^{-2}\,s^{-1}$ at 1 keV.

kerrconv

Convolution model. It convolves the current spectrum with the accretion disc line shape, keeping the black hole spin as free parameter (Brenneman & Reynolds, 2006).

Parameter 1: q^{in}, emissivity index for the inner disc.

Parameter 2: q^{out}, emissivity index for the outer disc.

Parameter 3: $r_{\rm br}$, break radius separating the inner and outer portions of the disc, in units of gravitational radii.

Parameter 4: a, dimensionless black hole spin.

Parameter 5: i, disc inclination angle with respect to our LOS, in degrees.

Parameter 6: R^{in}, inner radius of the disc in units of the radius of marginal stability.

Parameter 7: R^{out}, outer radius of the disc in units of the radius of marginal stability.

KYNCONV

KYN is a set of the KY XSPEC models (named after Karas and Yaqoob) with the following features:

(i) Non–axisymmetry: only part of the disc may be emitting, as defined by parameters dr and dϕ.

(ii) Obscuration by a circular cloud.

(iii) The computations are parallelized with threads.

(iv) The pre–calculated tables contain impact parameters (α and β coordinates), thus in principle non–Keplerian (but still geometrically thin) discs are possible, However, the definitions of the disc velocity would have to be changed inside the code.

KYNCONV is a relativistic convolution model with broken power–law emissivity, which produces accretion discs spectra in the strong gravity regime. It adds all relativistic effects due to strong gravity and fast motions close to the black hole, and allows to obscure part of the emission with a circular cloud whose size and position can be fitted (Dovčiak et al., 2004).

Parameter 1: a, the black hole spin.

Parameter 2: θ_o, the observer's inclination (0 = pole–on, 90 = edge–on).

Parameter 3: `rin`, inner disc edge.

Parameter 4: `ms`, definition of inner edge (0: `rin = par03`; 1: the same, but if `par03<rms` then `rin=rms`; 2: `rin=par03×rms`, `rout = par05×rms`).

Parameter 5: `rout`, outer disc edge

Parameter 6: ϕ, lower azimuth of the disc segment (-180° – 180°).

Parameter 7: dϕ, width of the disc segment (0° – 360°).

Parameter 8: $q^{\rm out}$, emissivity index above the break radius (-20 – 20).

Parameter 9: $q^{\rm in}$, emissivity index below the break radius (-20 – 20).

Parameter 10: `rb`, (0 – 160).

Parameter 11: `jump`, how the slope of the power law changes (0 – 10^6).

Parameter 12: `limb`, isotropy in the emission of the intrinsic flux (-10 – 10; with 0 = isotropic).

Parameter 13: α, "impact parameter" giving the cloud's coordinates in the X–axis in units of gravitational radii (-100 – 100). If $\alpha > 0$ the cloud is on the left of the black hole, if $\alpha < 0$ the cloud is on the right.

Parameter 14: β, "impact parameter" giving the cloud's coordinates in the Y–axis in units of gravitational radii (-100 – 100). If $\beta > 0$ the cloud is above the black hole, if $\beta < 0$ the cloud is below.

Parameter 15: r, cloud's radius in units of gravitational radii (0 – 100).

Parameter 16: z, redshift.

Parameter 17: `ntable`, defines which fits file with tables to use (no. 80 in this work).

Parameter 18: `nrad`, number of radial grid points.

Parameter 19: `division`, type of step in radial integration (0 for equidistant, 1 for exponential).

Parameter 20: `nphi`, number of azimuthal grid points (1 – 20000).

Parameter 21: `ne loc`, number of points in energies that are used (3 – 5000, for this work `ne loc` = 100).

Parameter 22: `smooth`, takes 3 consecutive points and averages them in order to smooth the resulting spectrum (0: no, 1: yes).

Parameter 23: `Stokes`, polarization output of the computation (0: photon number density flux, Stokes parameter is I/E; 1: Stokes parameter is Q/E; 2: Stokes parameter is U/E; 3: Stokes parameter is V/E; 4: degree of polarization; 5: linear polarization angle $\chi = 1/2 \arctan U/Q$; 6: circular polarization angle $\psi = 1/2 \arcsin V/\sqrt{Q^2 + U^2 + V^2}$).

Parameter 24: `nthreads`, number of computation threads (4, in the case of this work).

Parameter 25: `normtype`, sets normalization as follows:

(i) 0: normalization is set by total flux.

(ii) -2: normalization is set by flux at its maximum.

(iii) > 0: normalization is set by flux at an energy defined by the entered value in keV.

(iv) -1: the output is not renormalized.

pexmon

Neutral Compton reflection model with self–consistent Fe and Ni lines.

Parameter 1: Γ, power–law photon index.

Parameter 2: E_c, cutoff energy in units of keV (with no cutoff if $E_\mathrm{c} = 0$).

Parameter 3: scaling factor for reflection (< 0 for no direct component, 1 for isotropic source above the disc).

Parameter 4: z, redshift.

Parameter 5: abundance of elements heavier than He (relative to Solar).

Parameter 6: iron abundance (relative to Solar).

Parameter 7: inclination angle (in degrees).

Parameter 8: normalization in units of photons $\mathrm{keV^{-1}\,cm^{-2}\,s^{-1}}$ at 1 keV. It is the photon flux at 1 keV of the cutoff power law only (without reflection) in the Earth frame.

phabs

Photoelectric absorption modelled by $M(E) = e^{-N_\mathrm{H}\sigma(E)}$, where $\sigma(E)$ is the photoelectric cross–section not including Thomson scattering. The only free parameter in the model is the equivalent hydrogen column density in units of 10^{22} atoms $\mathrm{cm^{-2}}$.

PHASE

Photoionization code which assumes a geometry consisting of a central source emitting an ionizing continuum with clouds of gas intercepting the LOS, in a plane parallel approximation (Krongold et al., 2003).

Parameter 1: $\log U$, logarithm of the ionization parameter, defined as $U = Q\,(4\pi n R^2 c)^{-1}$ (Netzer, 2008), where Q is the photon rate integrated over the entire Lyman continuum, n is the gas number density and R the gas distance from the nuclear source of photons.

Parameter 2: $\log n_{\mathrm{H}}$, equivalent H column density.

Parameter 3: v, internal microturbulent velocity of the gas.

Parameter 4: z, redshift, from which the outflow velocity of the gas is computed.

Parameter 5: a switch parameter (0 or 1). If it is set to 0, the code goes through a loop to read the data. The code must be run this way the first time that it is used in a given XSPEC session. If it is set to 1, it makes the code to run faster, and it also generates two output files with information of the gas: one with equivalent widths of the absorption lines associated with the ions, and the other one with their column densities.

powerlaw

Simple power law photon spectrum. It is modelled by $M(E) = KE^{-\alpha}$.

Parameter 1: α, the dimensionless power law photon index.

Parameter 2: K, a constant in units of photons $\mathrm{keV^{-1}\,cm^{-2}\,s^{-1}}$ at 1 keV.

reflext

Reflection by a constant density illuminated atmosphere (Ross & Fabian, 2005). The reflected spectrum is calculated for an optically–thick atmosphere, like the surface of an accretion disk, of constant density illuminated by radiation with a power–law spectrum. The illumination has a high–energy exponential cutoff with e–folding energy fixed at 300 keV and a sharp lower energy cutoff at 0.1 keV. The reflected spectrum is calculated over the range 1 eV to 1 MeV.

Parameter 1: Fe abundance relative to solar value (0.1 – 10.0). Abundances of other elements are fixed at solar values (Morrison & McCammon, 1983).

Parameter 2: Γ, photon index for illuminating power–law spectrum (1.0 – 3.0).

Parameter 3: ξ, ionization parameter ($30 - 10^4\ \mathrm{erg\,cm\,s^{-1}}$).

Parameter 4: z, redshift.

Parameter 5: normalization of reflected spectrum.

xillver

A table model for modeling the component of emission that is reflected from an illuminated accretion disc (García et al., 2013). It is intended for use when the thermal disc flux is faint compared to the incident power–law flux. The models are expected to provide an accurate description of the Fe K emission line.

Parameter 1: Γ, photon index of the illuminating power–law spectrum (1.0 – 3.4).

Parameter 2: ξ, ionization given by $\xi = 4\pi F/n$, where F is the flux of the illuminating radiation and $n = 10^{15}\,\mathrm{cm}^{-3}$ is the gas density ($0 < \log\xi < 4.7$).

Parameter 3: Fe abundance with respect to the solar value (0.5 – 10).

Parameter 4: E_c, exponential high–energy cutoff for the power–law (20 keV – 1 MeV).

Parameter 5: Inclination angle of our LOS with respect to the disc's normal ($5^\circ - 85^\circ$).

zgauss

Redshifted variant of a gaussian line profile. It is modelled by $M(E) = K\frac{1+z}{\sigma\sqrt{2\pi}}e^{\frac{-(E(1+z)-E_L)^2}{2\sigma^2}}$.

Parameter 1: E_L, line energy in keV.

Parameter 2: σ, line width in keV.

Parameter 3: z, redshift.

Parameter 4: K, a constant in units of photons $\mathrm{keV}^{-1}\,\mathrm{cm}^{-2}\,\mathrm{s}^{-1}$ in the line.

zpcfabs

Redshifted variant of a partial covering fraction absorption modelled by $M(E) = 1 - C_f\left(1 - e^{-N_\mathrm{H}\sigma(E[1+z])}\right)$.

Parameter 1: N_H, equivalent hydrogen column density in units of 10^{22} atoms cm^{-2}.

Parameter 2: C_f, dimensionless covering fraction, between 0 and 1.

Parameter 3: z, redshift.

zxipcf

Partial covering absorption by partially ionized material. This model uses a grid of XSTAR photionized absorption models for the absorption, then assumes that this only covers some fraction C_f of the source, while the remaining $(1 - C_f)$ of the spectrum is seen directly (Reeves et al., 2008).

Parameter 1: N_H, column density in units of $10^{22}\,\mathrm{cm}^{-2}$.

Parameter 2: $\log\xi$, logarithm of the ionization, where $\xi = L/nr^2$.

Parameter 3: C_f, covering fraction.

Parameter 4: z, redshift.

B

X–ray lightcurves of BLR clouds eclipses

In the following pages we show several light curves produced during X–ray eclipses by clouds of different sizes and densities. The left column of every figure corresponds to a column density of $N_{\mathrm{H}} = 10^{23}\,\mathrm{cm}^{-2}$, the middle column to $N_{\mathrm{H}} = 10^{24}\,\mathrm{cm}^{-2}$, and the right column to $N_{\mathrm{H}} = 5 \times 10^{24}\,\mathrm{cm}^{-2}$. The rows, from top to bottom, correspond to clouds of radius 2, 4, 6, 8, and $10\,r_{\mathrm{g}}$. In the even pages, flux light curves are shown for every physical configuration of the system; the corresponding H / S ratio light curves are shown in the odd pages.

The physical configurations described in the following are: extended corona and reprocessing regions, compact corona and extended reprocessing regions, and compact corona and reprocessing regions. For the first situation, Schwarzshild and maximally rotating Kerr black holes are considered. For the other two, only the maximally rotating Kerr black hole case is explored.

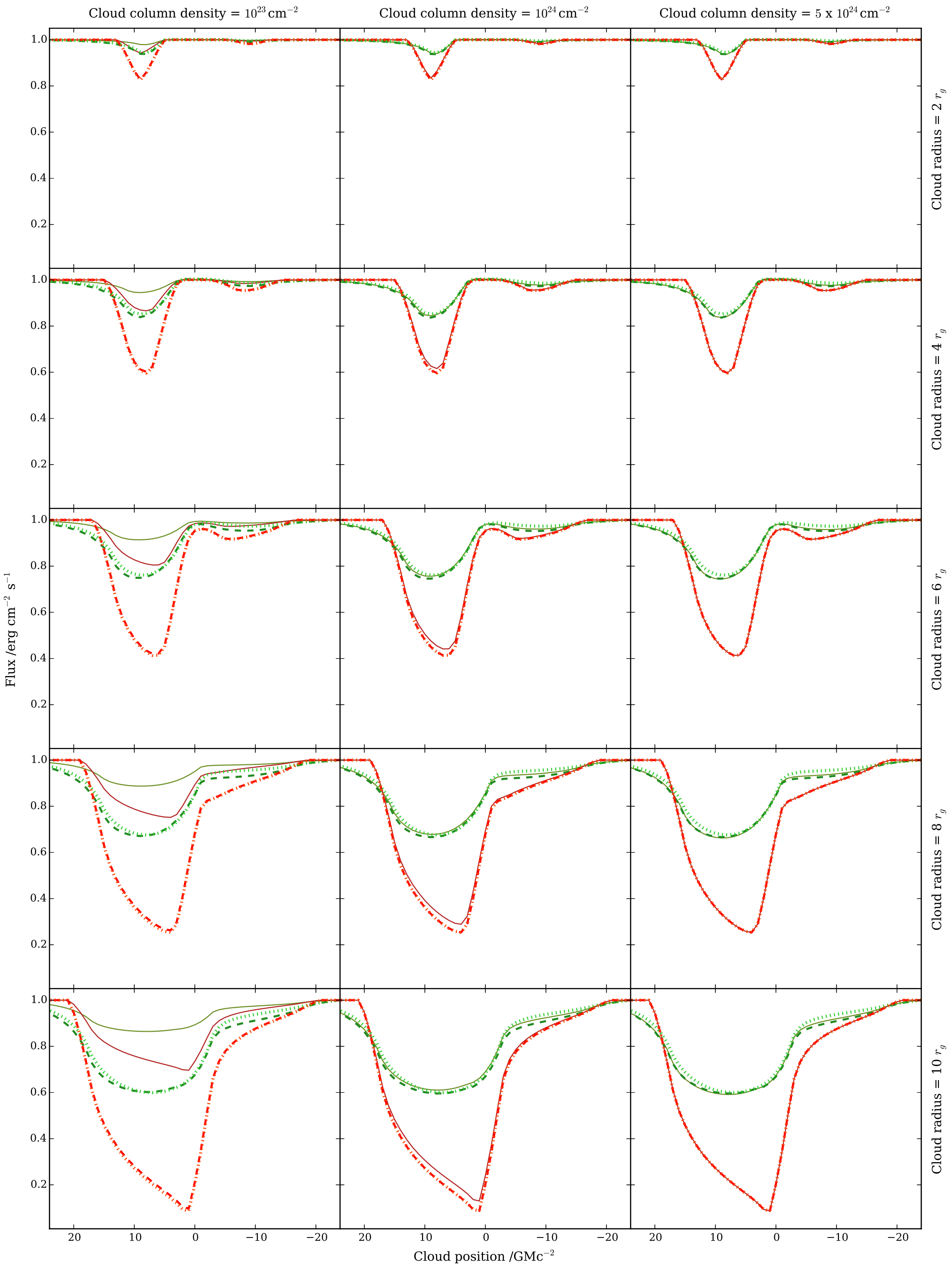

Figure B.1: Lightcurves during various eclipses. Schwarzshild black hole, extended corona ($r = 10\,r_g$), relatively low emissivity index ($q = 3$), i.e. reflection from extended regions in the disc. The cloud ionization is $\xi = 10^{-3}\,\mathrm{erg\,cm\,s^{-1}}$. Reddish curves: continuum component; greenish curves: reprocessed emission. Solid lines: $7 - 10\,\mathrm{keV}$; dashed lines: $1 - 4\,\mathrm{keV}$; dotted lines: $0.3 - 0.7\,\mathrm{keV}$. From top to bottom panels: cloud radius = 2, 4, 6, 8, and $10\,r_g$, respectively. From left to right panels: cloud column density = 10^{23}, 10^{24}, and $5 \times 10^{24}\,\mathrm{cm}^{-2}$, respectively.

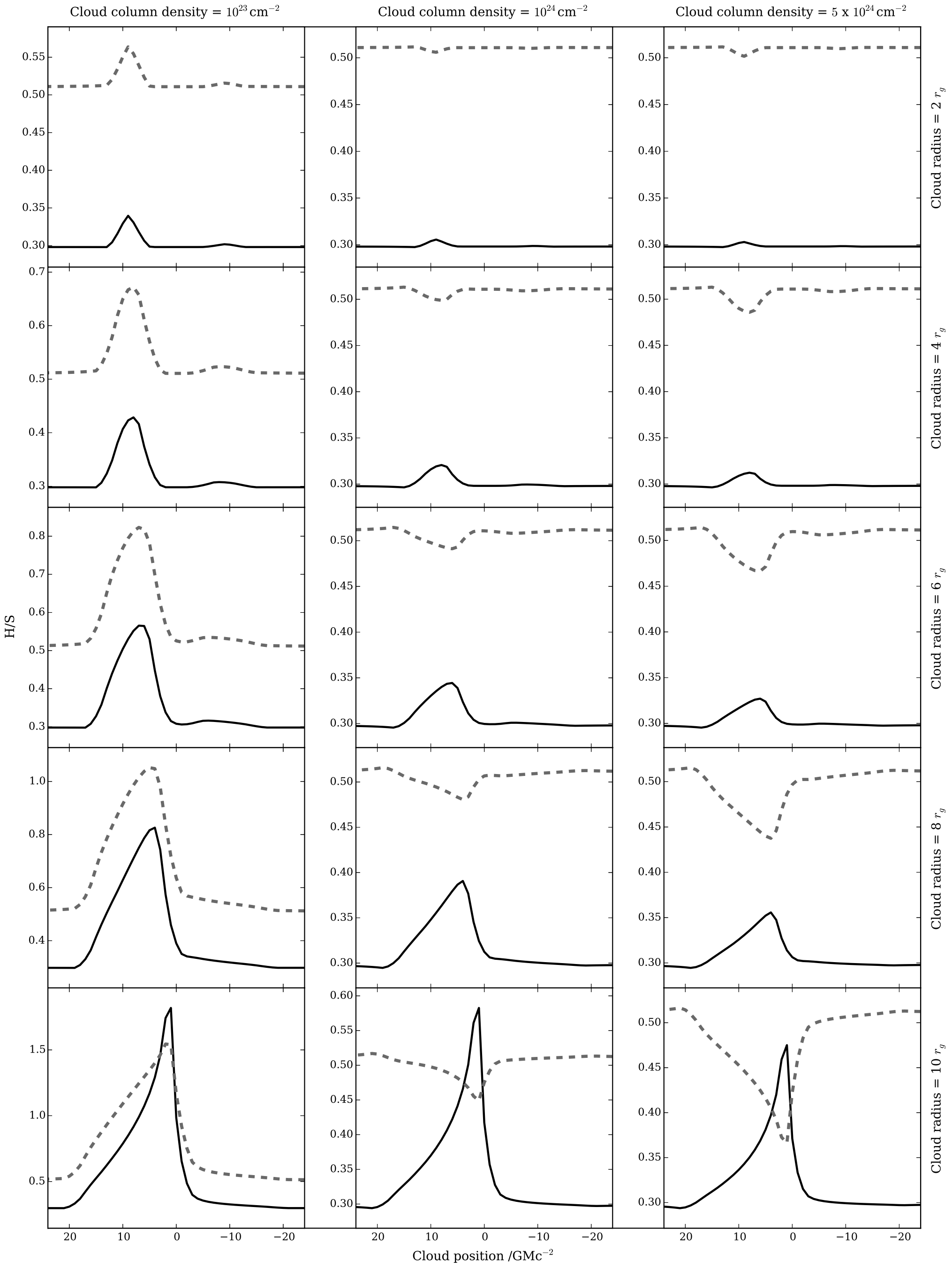

Figure B.2: H / S ratio lightcurves during various eclipses. Schwarzshild black hole, extended corona ($r = 10\,r_\mathrm{g}$), relatively low emissivity index ($q = 3$), i.e. reflection from extended regions in the disc. The cloud ionization is $\xi = 10^{-3}\,\mathrm{erg\,cm\,s^{-1}}$. The hard band is $7 - 10\,\mathrm{keV}$. The soft bands are $0.3 - 0.7\,\mathrm{keV}$ and $1 - 4\,\mathrm{keV}$ for the dashed grey and the solid black curves, respectively. From top to bottom panels: cloud radius = 2, 4, 6, 8, and $10\,r_\mathrm{g}$, respectively. From left to right panels: cloud column density = 10^{23}, 10^{24}, and $5 \times 10^{24}\,\mathrm{cm}^{-2}$, respectively.

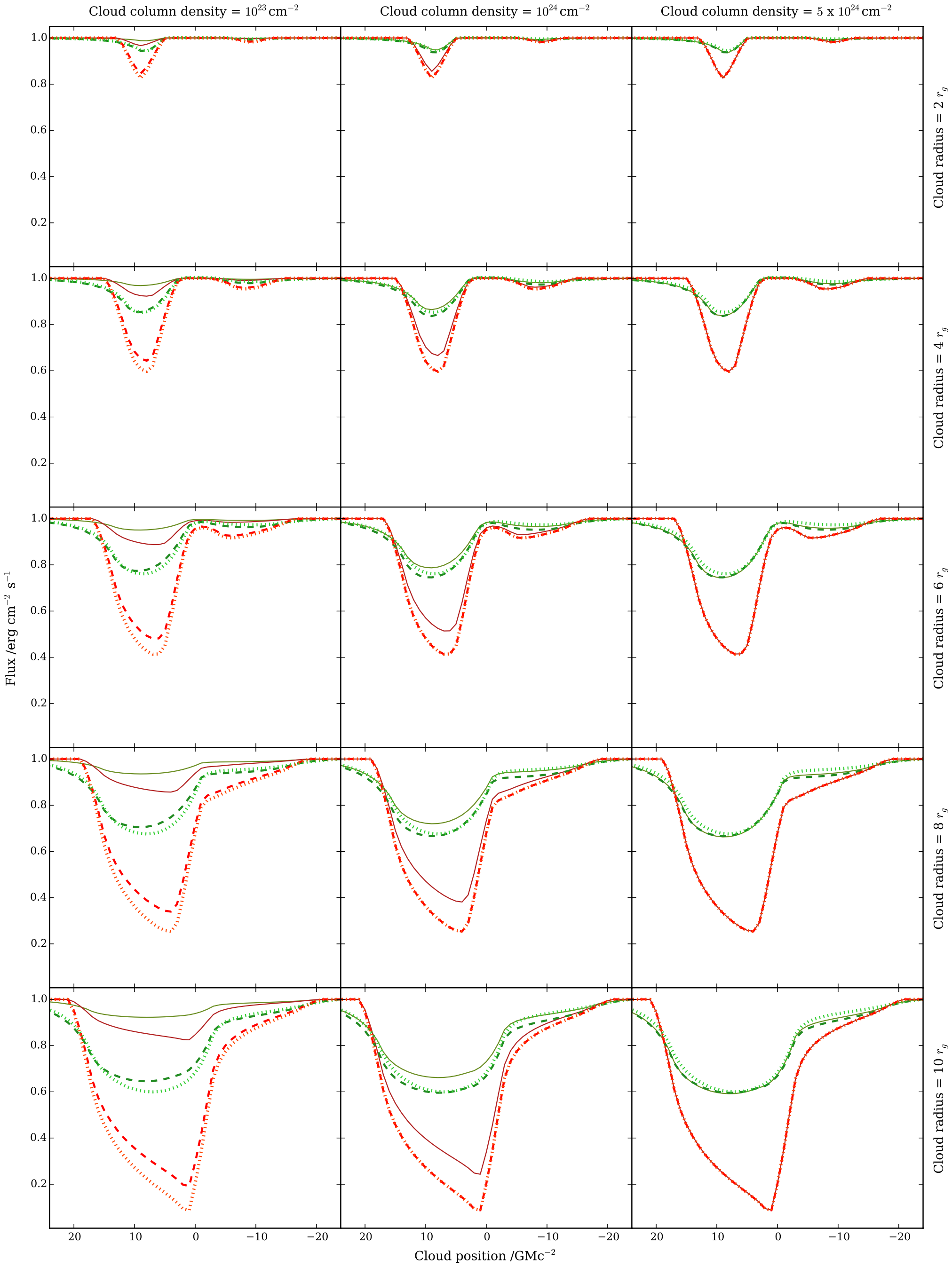

Figure B.3: Lightcurves during various eclipses. Schwarzschild black hole, extended corona ($r = 10\,r_g$), relatively low emissivity index ($q = 3$), i.e. reflection from extended regions in the disc. The cloud ionization is $\xi = 10\,\mathrm{erg\,cm\,s^{-1}}$. Reddish curves: continuum component; greenish curves: reprocessed emission. Solid lines: $7-10$ keV; dashed lines: $1-4$ keV; dotted lines: $0.3-0.7$ keV. From top to bottom panels: cloud radius = 2, 4, 6, 8, and 10 r_g, respectively. From left to right panels: cloud column density = 10^{23}, 10^{24}, and $5 \times 10^{24}\,\mathrm{cm}^{-2}$, respectively.

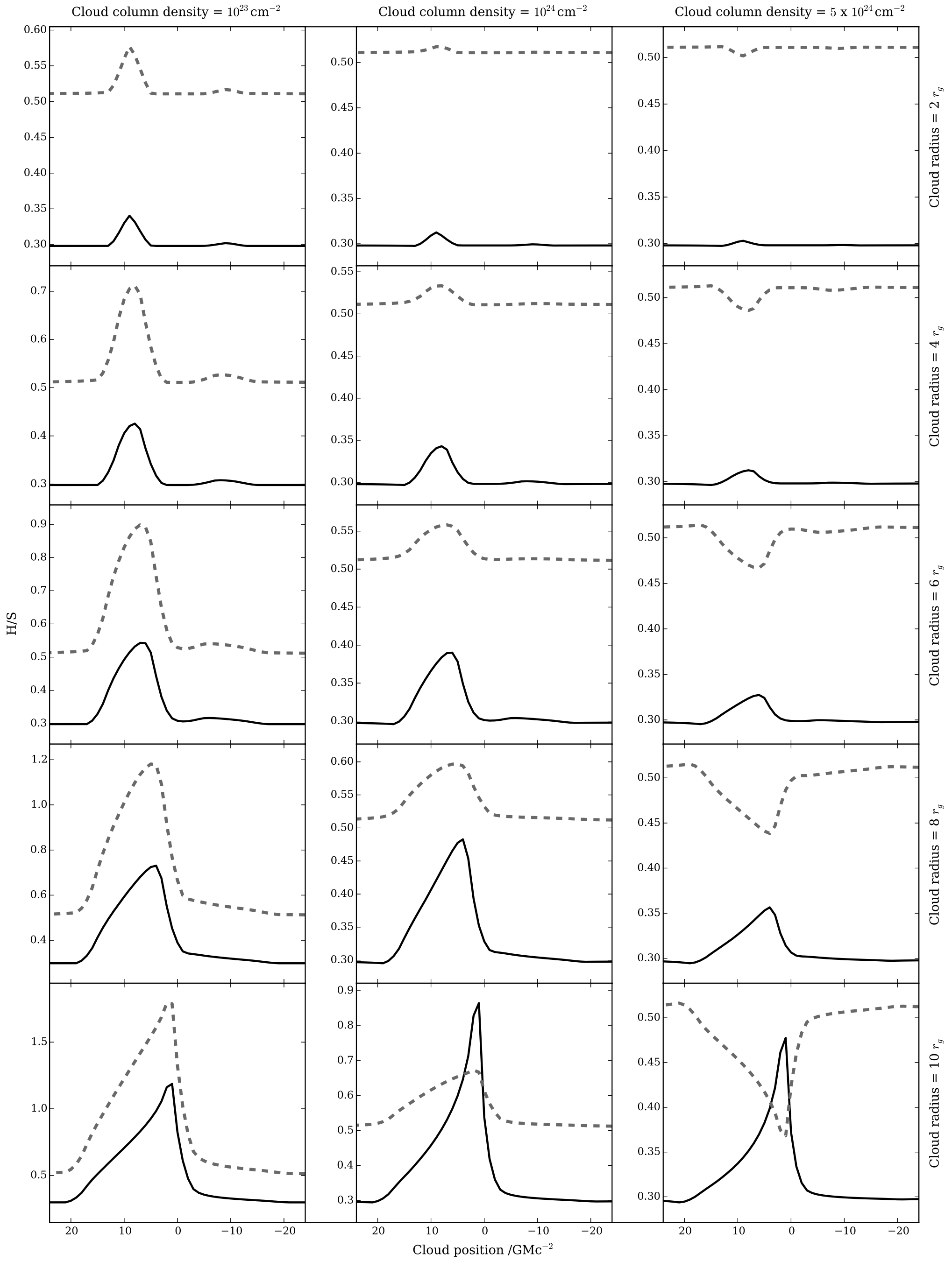

Figure B.4: H / S ratio lightcurves during various eclipses. Schwarzschild black hole, extended corona ($r = 10\,r_\mathrm{g}$), relatively low emissivity index ($q = 3$), i.e. reflection from extended regions in the disc. The cloud ionization is $\xi = 10\,\mathrm{erg\,cm\,s^{-1}}$. The hard band is $7 - 10$ keV. The soft bands are $0.3 - 0.7$ keV and $1 - 4$ keV for the dashed grey and the solid black curves, respectively. From top to bottom panels: cloud radius = 2, 4, 6, 8, and $10\,r_\mathrm{g}$, respectively. From left to right panels: cloud column density = 10^{23}, 10^{24}, and $5 \times 10^{24}\,\mathrm{cm}^{-2}$, respectively.

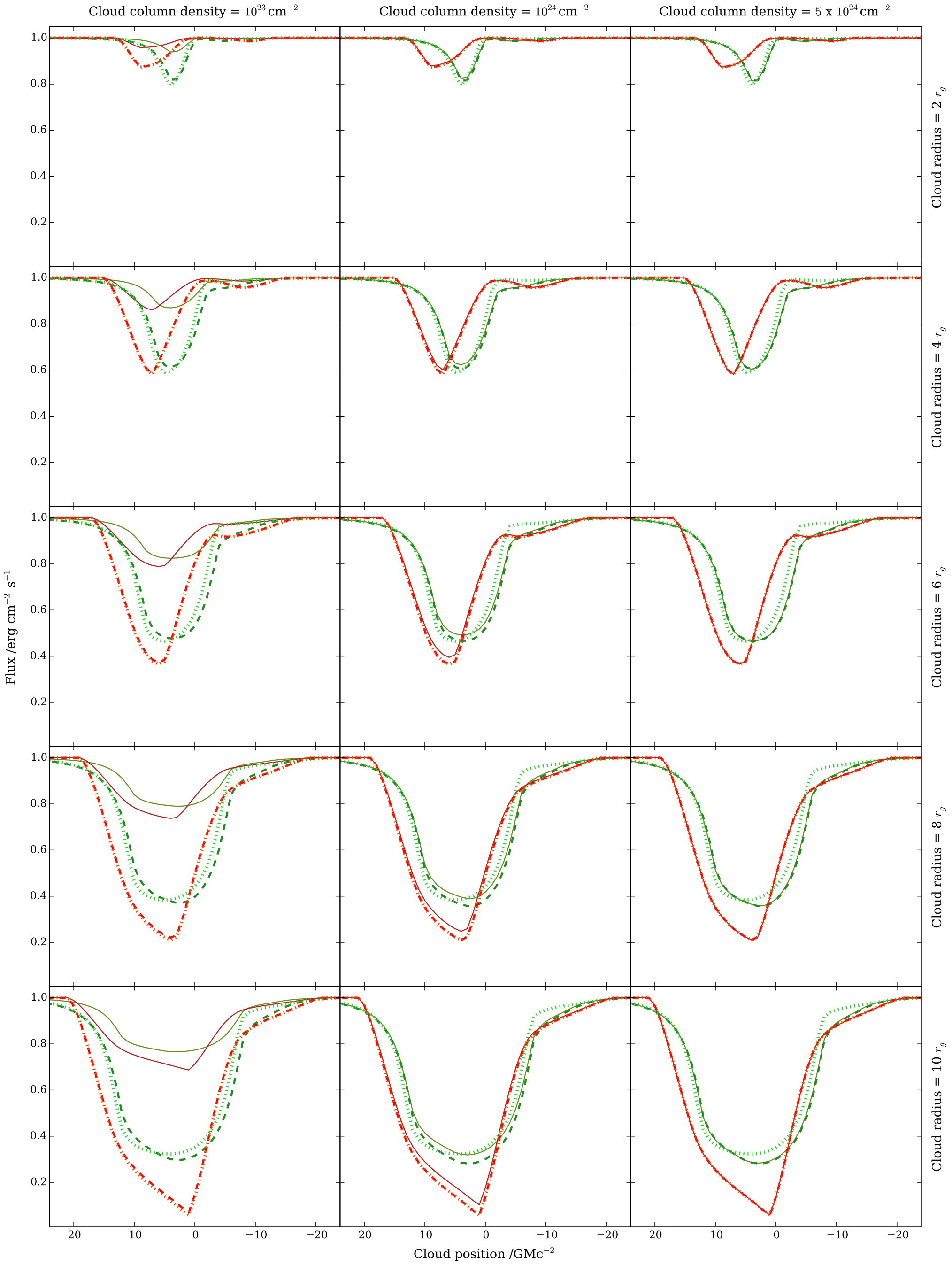

Figure B.5: Lightcurves during various eclipses. Maximally Kerr black hole, extended corona ($r = 10\,r_g$), relatively low emissivity index ($q = 3$), i.e. reflection from extended regions in the disc. The cloud ionization is $\xi = 10^{-3}$ erg cm s^{-1}. Reddish curves: continuum component; greenish curves: reprocessed emission. Solid lines: 7 − 10 keV; dashed lines: 1 − 4 keV; dotted lines: 0.3 − 0.7 keV. From top to bottom panels: cloud radius = 2, 4, 6, 8, and 10 r_g, respectively. From left to right panels: cloud column density = 10^{23}, 10^{24}, and 5×10^{24} cm^{-2}, respectively.

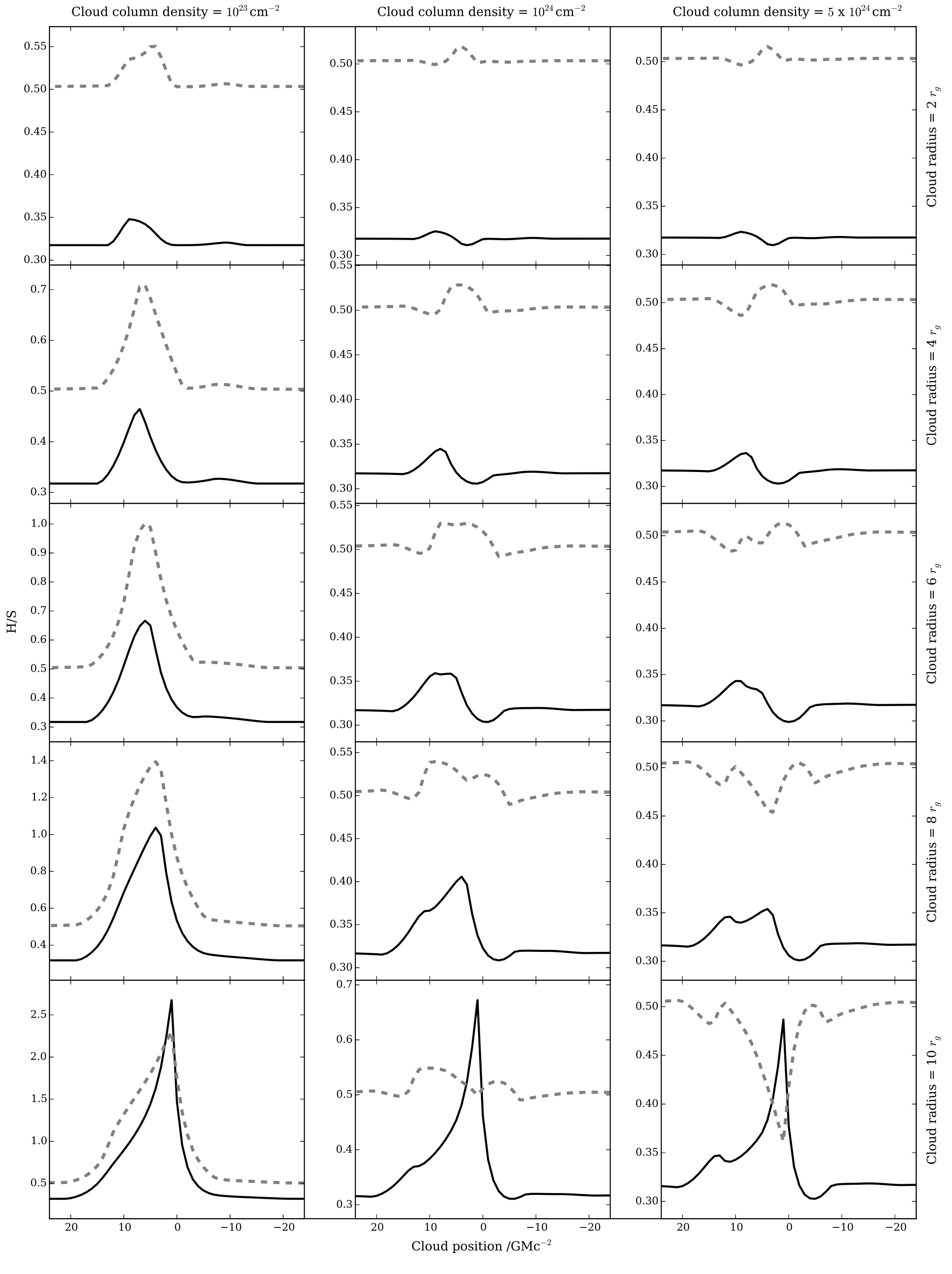

Figure B.6: H / S ratio lightcurves during various eclipses. Maximally Kerr black hole, extended corona ($r = 10\,r_\mathrm{g}$), relatively low emissivity index ($q = 3$), i.e. reflection from extended regions in the disc. The cloud ionization is $\xi = 10^{-3}\,\mathrm{erg\,cm\,s^{-1}}$. The hard band is $7 - 10$ keV. The soft bands are $0.3 - 0.7$ keV and $1 - 4$ keV for the dashed grey and the solid black curves, respectively. From top to bottom panels: cloud radius = 2, 4, 6, 8, and $10\,r_\mathrm{g}$, respectively. From left to right panels: cloud column density = 10^{23}, 10^{24}, and 5×10^{24} cm^{-2}, respectively.

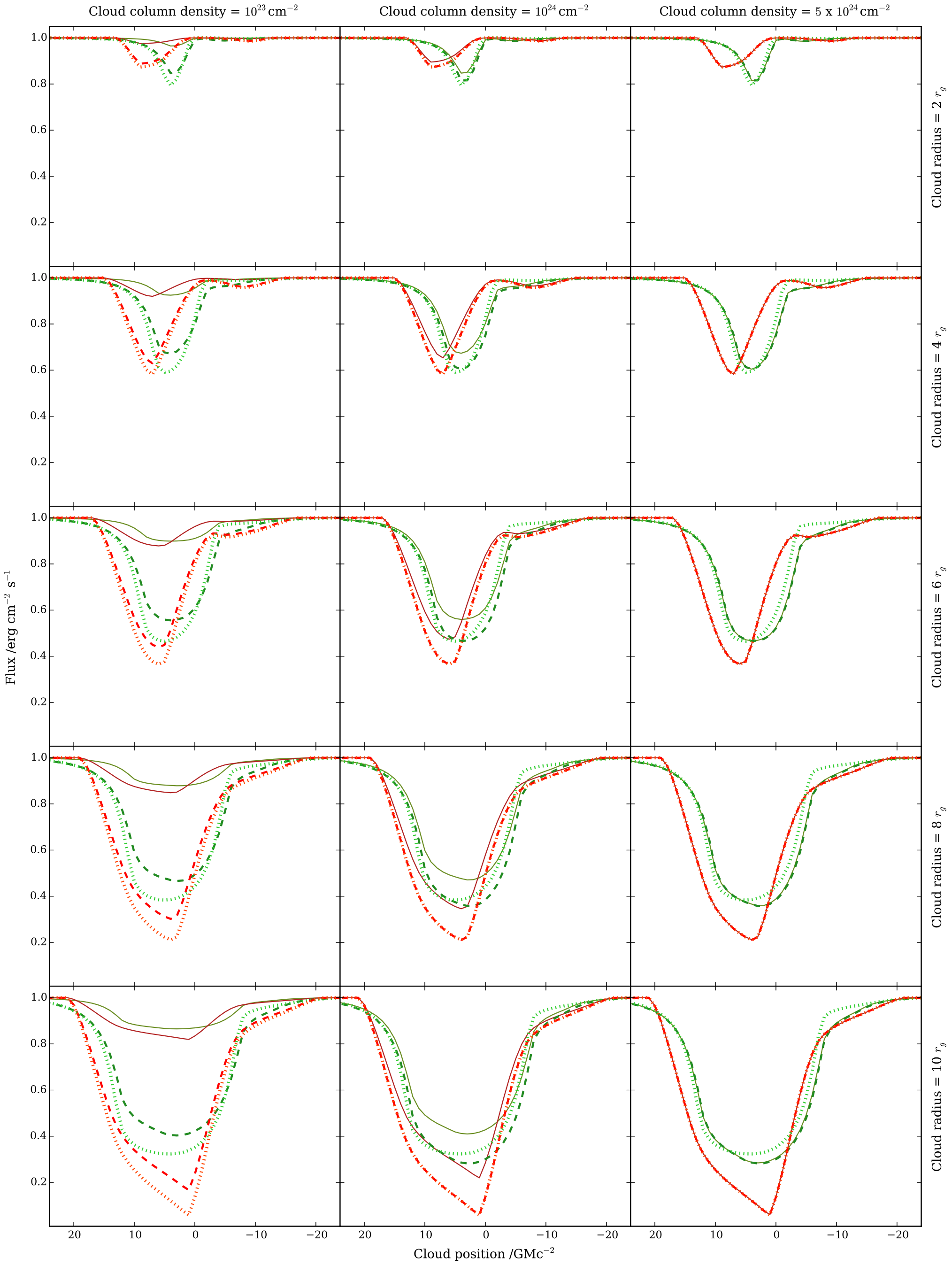

Figure B.7: Lightcurves during various eclipses. Maximally Kerr black hole, extended corona ($r = 10\,r_g$), relatively low emissivity index ($q = 3$), i.e. reflection from extended regions in the disc. The cloud ionization is $\xi = 10\,\mathrm{erg\,cm\,s^{-1}}$. Reddish curves: continuum component; greenish curves: reprocessed emission. Solid lines: 7 − 10 keV; dashed lines: 1 − 4 keV; dotted lines: 0.3 − 0.7 keV. From top to bottom panels: cloud radius = 2, 4, 6, 8, and $10\,r_g$, respectively. From left to right panels: cloud column density = 10^{23}, 10^{24}, and 5×10^{24} cm^{-2}, respectively.

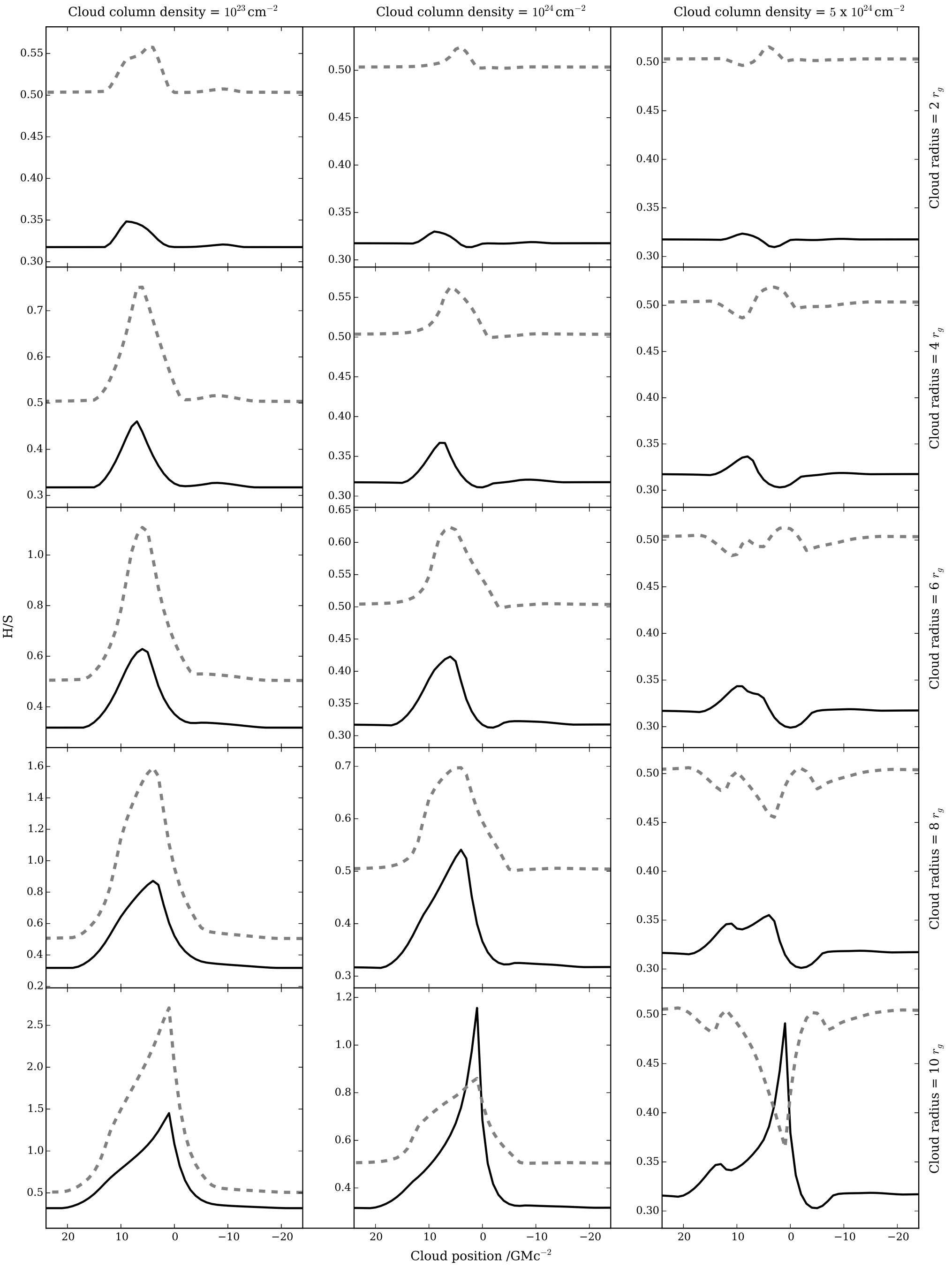

Figure B.8: H / S ratio lightcurves during various eclipses. Maximally Kerr black hole, extended corona ($r = 10\,r_g$), relatively low emissivity index ($q = 3$), i.e. reflection from extended regions in the disc. The cloud ionization is $\xi = 10\,\mathrm{erg\,cm\,s^{-1}}$. The hard band is 7 − 10 keV. The soft bands are 0.3 − 0.7 keV and 1 − 4 keV for the dashed grey and the solid black curves, respectively. From top to bottom panels: cloud radius = 2, 4, 6, 8, and $10\,r_g$, respectively. From left to right panels: cloud column density = 10^{23}, 10^{24}, and 5×10^{24} cm^{-2}, respectively.

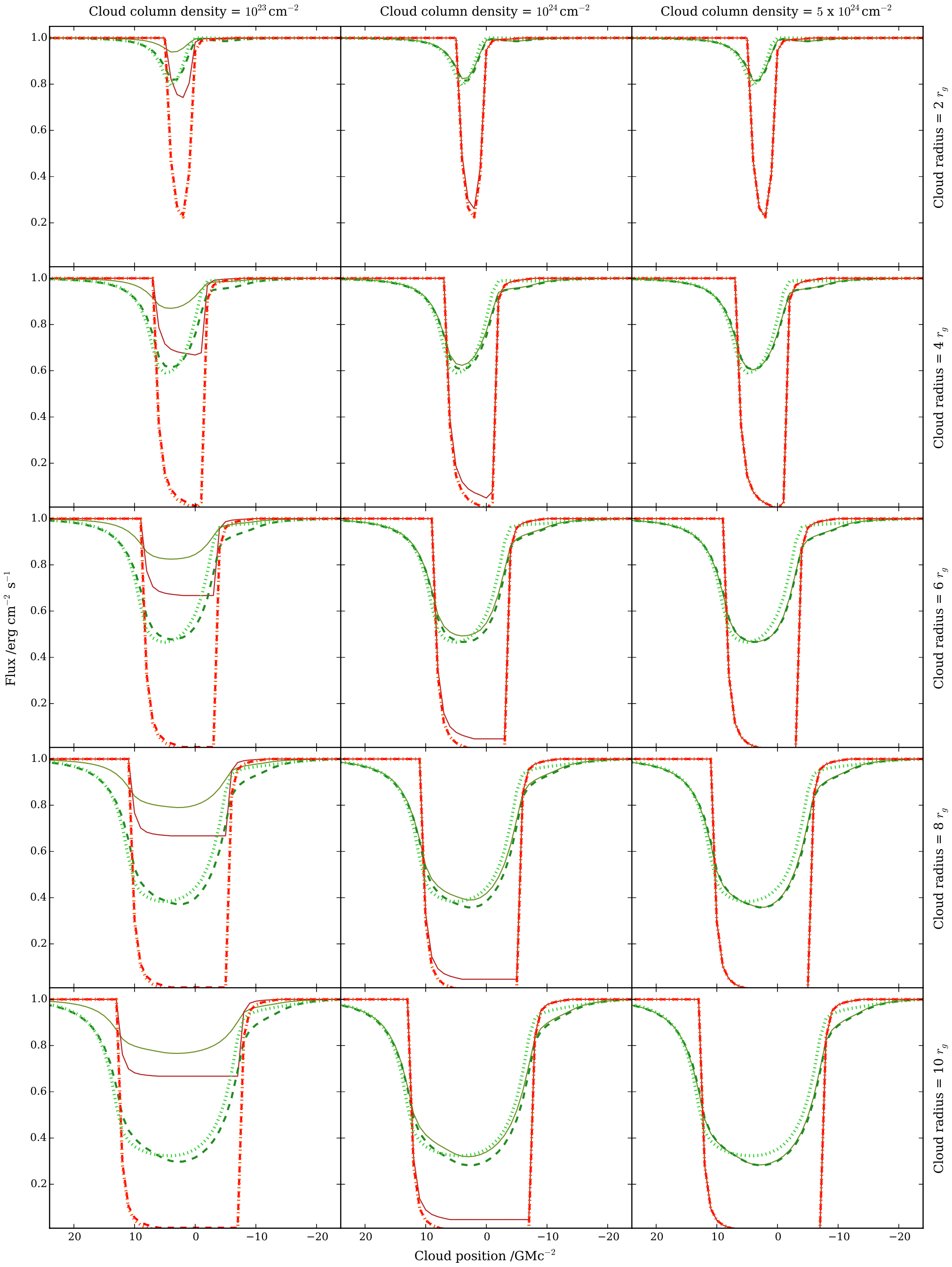

Figure B.9: Lightcurves during various eclipses. Maximally Kerr black hole, compact corona ($r = 2\,r_g$), relatively low emissivity index ($q = 3$), i.e. reflection from extended regions in the disc. The cloud ionization is $\xi = 10^{-3}$ erg cm s^{-1}. Reddish curves: continuum component; greenish curves: reprocessed emission. Solid lines: 7 − 10 keV; dashed lines: 1 − 4 keV; dotted lines: 0.3 − 0.7 keV. From top to bottom panels: cloud radius = 2, 4, 6, 8, and 10 r_g, respectively. From left to right panels: cloud column density = 10^{23}, 10^{24}, and 5×10^{24} cm^{-2}, respectively.

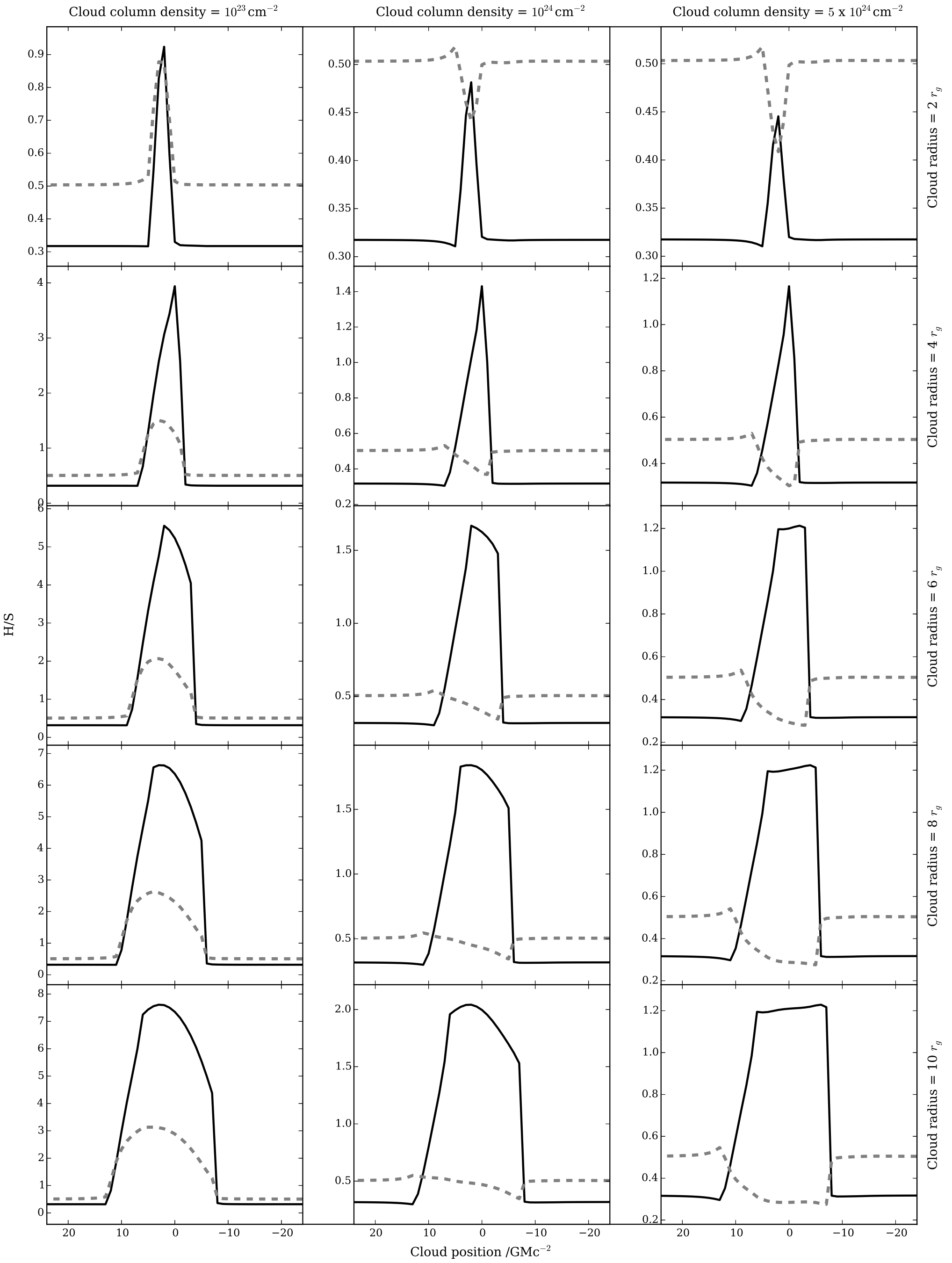

Figure B.10: H / S ratio lightcurves during various eclipses. Maximally Kerr black hole, compact corona ($r = 2\,r_{\rm g}$), relatively low emissivity index ($q = 3$), i.e. reflection from extended regions in the disc. The cloud ionization is $\xi = 10^{-3}\,{\rm erg\,cm\,s^{-1}}$. The hard band is $7 - 10$ keV. The soft bands are $0.3 - 0.7$ keV and $1 - 4$ keV for the dashed grey and the solid black curves, respectively. From top to bottom panels: cloud radius = 2, 4, 6, 8, and $10\,r_{\rm g}$, respectively. From left to right panels: cloud column density = 10^{23}, 10^{24}, and 5×10^{24} cm^{-2}, respectively.

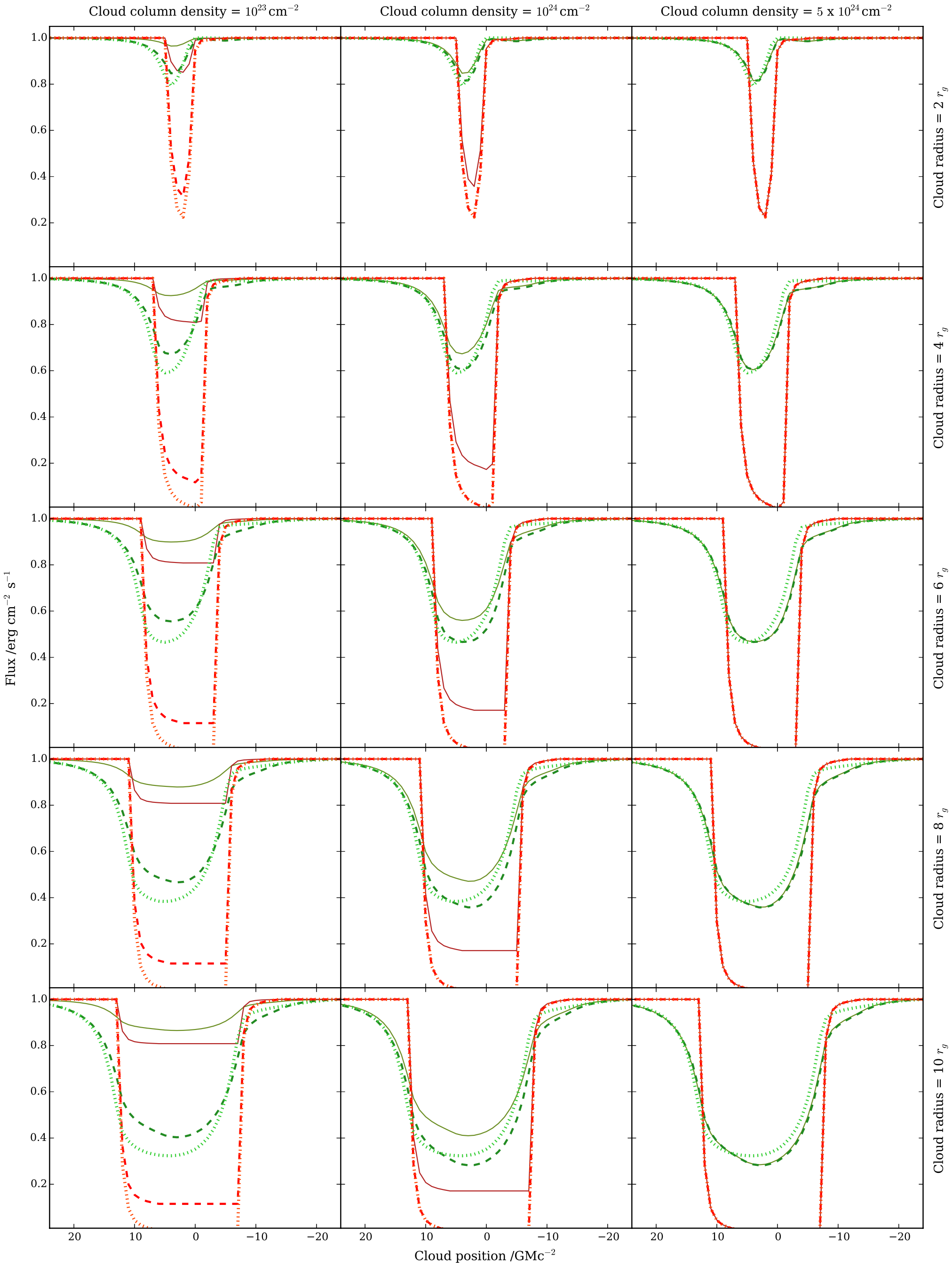

Figure B.11: Lightcurves during various eclipses. Maximally Kerr black hole, compact corona ($r = 2\,r_g$), relatively low emissivity index ($q = 3$), i.e. reflection from extended regions in the disc. The cloud ionization is $\xi = 10\,\mathrm{erg\,cm\,s^{-1}}$. Reddish curves: continuum component; greenish curves: reprocessed emission. Solid lines: 7 − 10 keV; dashed lines: 1 − 4 keV; dotted lines: 0.3 − 0.7 keV. From top to bottom panels: cloud radius = 2, 4, 6, 8, and 10 r_g, respectively. From left to right panels: cloud column density = 10^{23}, 10^{24}, and $5 \times 10^{24}\,\mathrm{cm^{-2}}$, respectively.

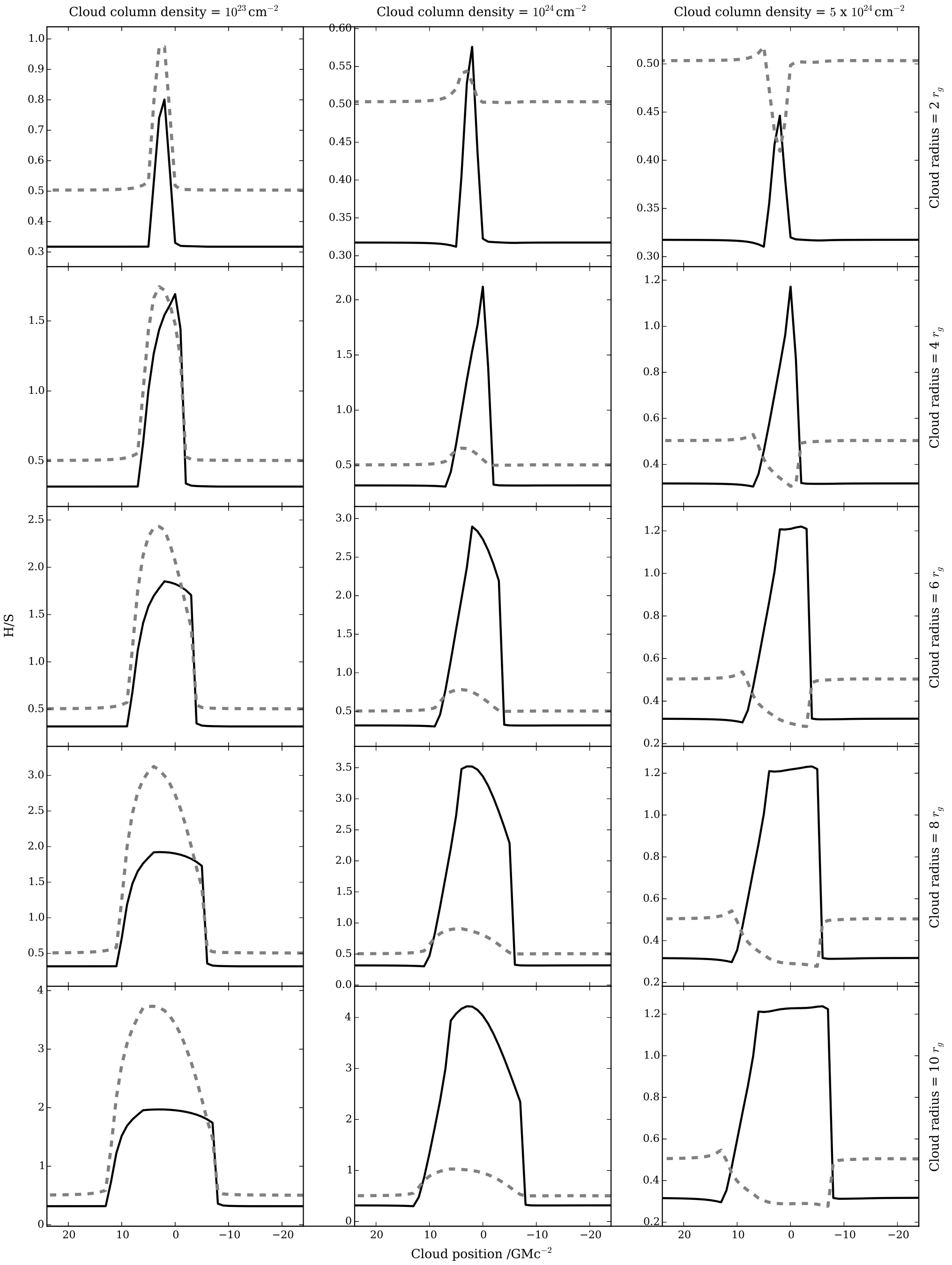

Figure B.12: H / S ratio lightcurves during various eclipses. Maximally Kerr black hole, compact corona ($r = 2\,r_\mathrm{g}$), relatively low emissivity index ($q = 3$), i.e. reflection from extended regions in the disc. The cloud ionization is $\xi = 10\,\mathrm{erg\,cm\,s^{-1}}$. The hard band is $7 - 10$ keV. The soft bands are $0.3 - 0.7$ keV and $1 - 4$ keV for the dashed grey and the solid black curves, respectively. From top to bottom panels: cloud radius = 2, 4, 6, 8, and $10\,r_\mathrm{g}$, respectively. From left to right panels: cloud column density = 10^{23}, 10^{24}, and $5 \times 10^{24}\,\mathrm{cm^{-2}}$, respectively.

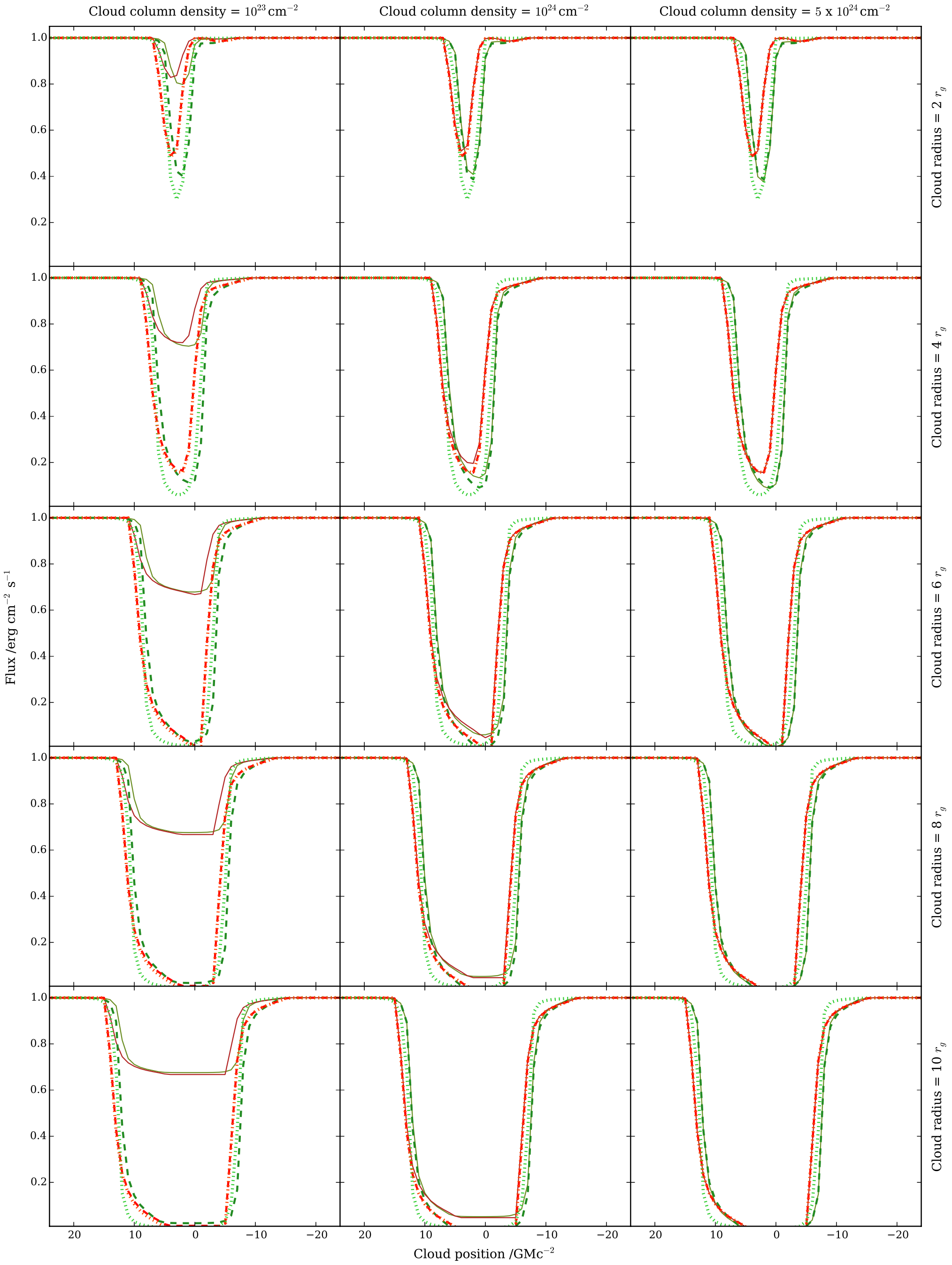

Figure B.13: Lightcurves during various eclipses. Maximally Kerr black hole, compact corona ($r = 4\,r_g$), steep emissivity index ($q = 7$), i.e. reflection from compact regions in the disc. The cloud ionization is $\xi = 10^{-3}$ erg cm s^{-1}. Reddish curves: continuum component; greenish curves: reprocessed emission. Solid lines: $7 - 10$ keV; dashed lines: $1 - 4$ keV; dotted lines: $0.3 - 0.7$ keV. From top to bottom panels: cloud radius = 2, 4, 6, 8, and 10 r_g, respectively. From left to right panels: cloud column density = 10^{23}, 10^{24}, and 5×10^{24} cm^{-2}, respectively.

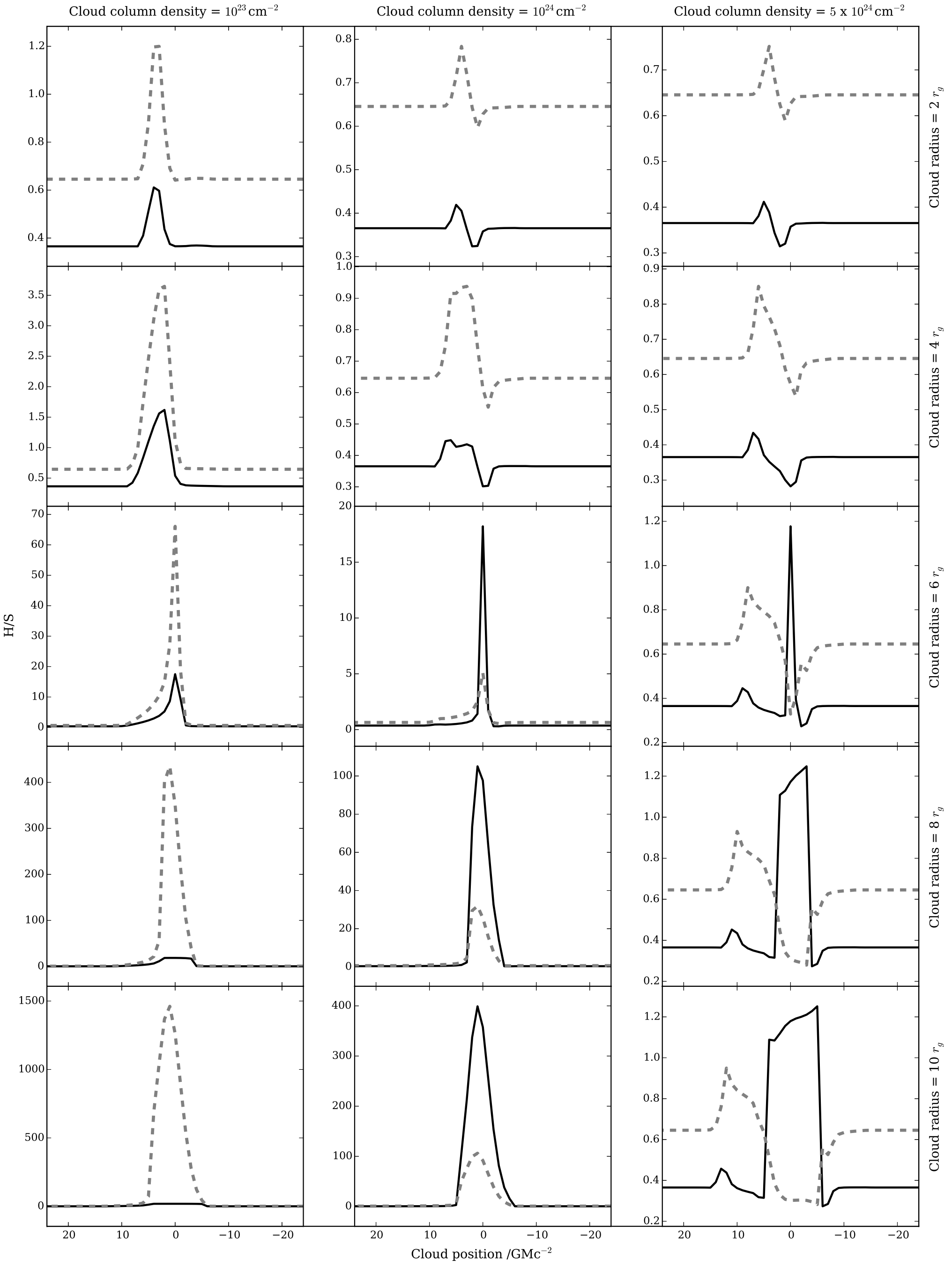

Figure B.14: H / S ratio lightcurves during various eclipses. Maximally Kerr black hole, compact corona ($r = 4\,r_\mathrm{g}$), steep emissivity index ($q = 4$), i.e. reflection from compact regions in the disc. The cloud ionization is $\xi = 10^{-3}\,\mathrm{erg\,cm\,s^{-1}}$. The hard band is 7 − 10 keV. The soft bands are 0.3 − 0.7 keV and 1 − 4 keV for the dashed grey and the solid black curves, respectively. From top to bottom panels: cloud radius = 2, 4, 6, 8, and 10 r_g, respectively. From left to right panels: cloud column density = 10^{23}, 10^{24}, and $5 \times 10^{24}\,\mathrm{cm}^{-2}$, respectively.

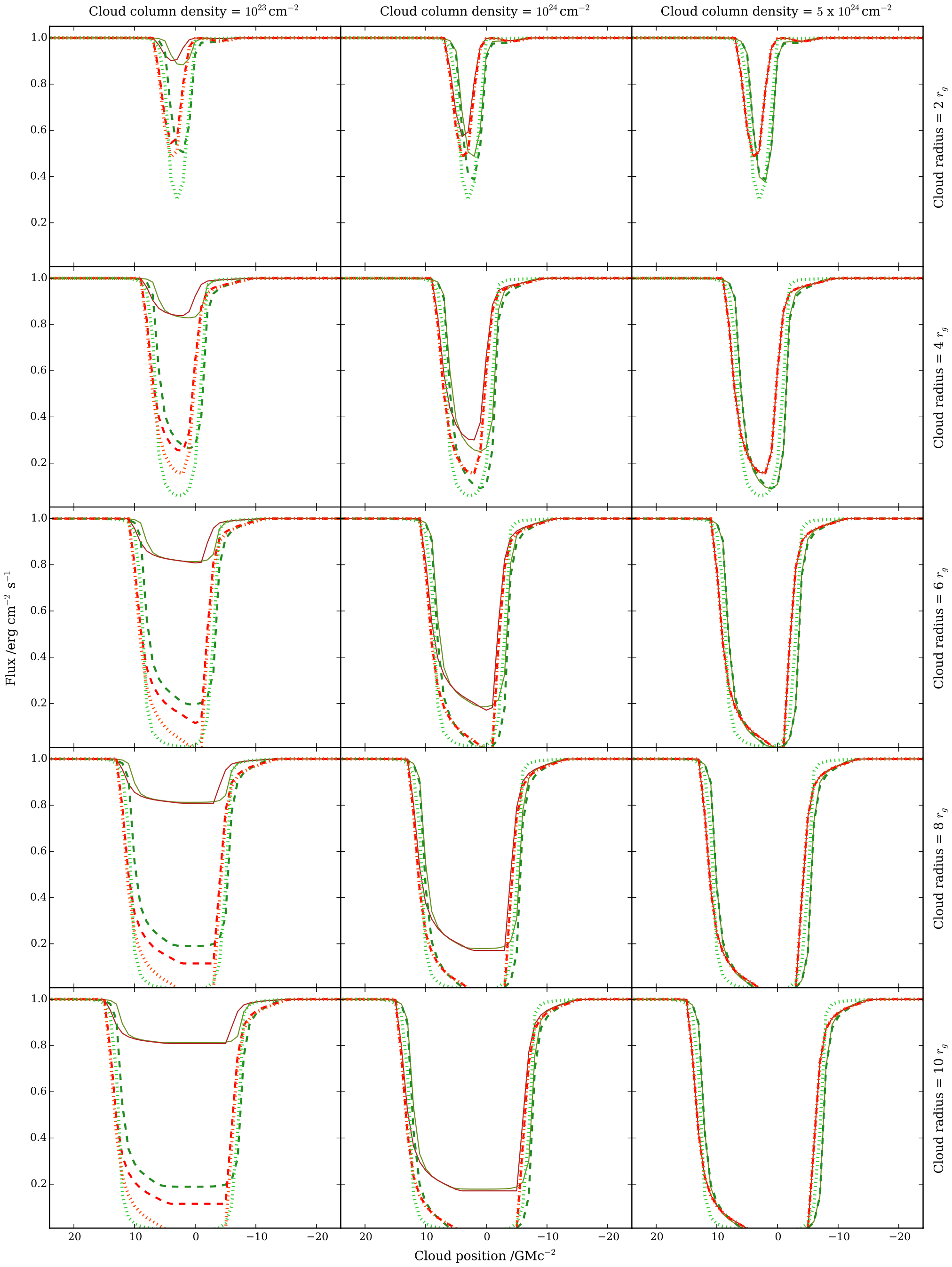

Figure B.15: Maximally Kerr black hole, compact corona ($r = 4\, r_g$), steep emissivity index ($q = 7$), i.e. reflection from compact regions in the disc. The cloud ionization is $\xi = 10\,\mathrm{erg\,cm\,s^{-1}}$. Reddish curves: continuum component; greenish curves: reprocessed emission. Solid lines: $7 - 10\,\mathrm{keV}$; dashed lines: $1 - 4\,\mathrm{keV}$; dotted lines: $0.3 - 0.7\,\mathrm{keV}$. From top to bottom panels: cloud radius = 2, 4, 6, 8, and $10\, r_g$, respectively. From left to right panels: cloud column density = 10^{23}, 10^{24}, and $5 \times 10^{24}\,\mathrm{cm}^{-2}$, respectively.

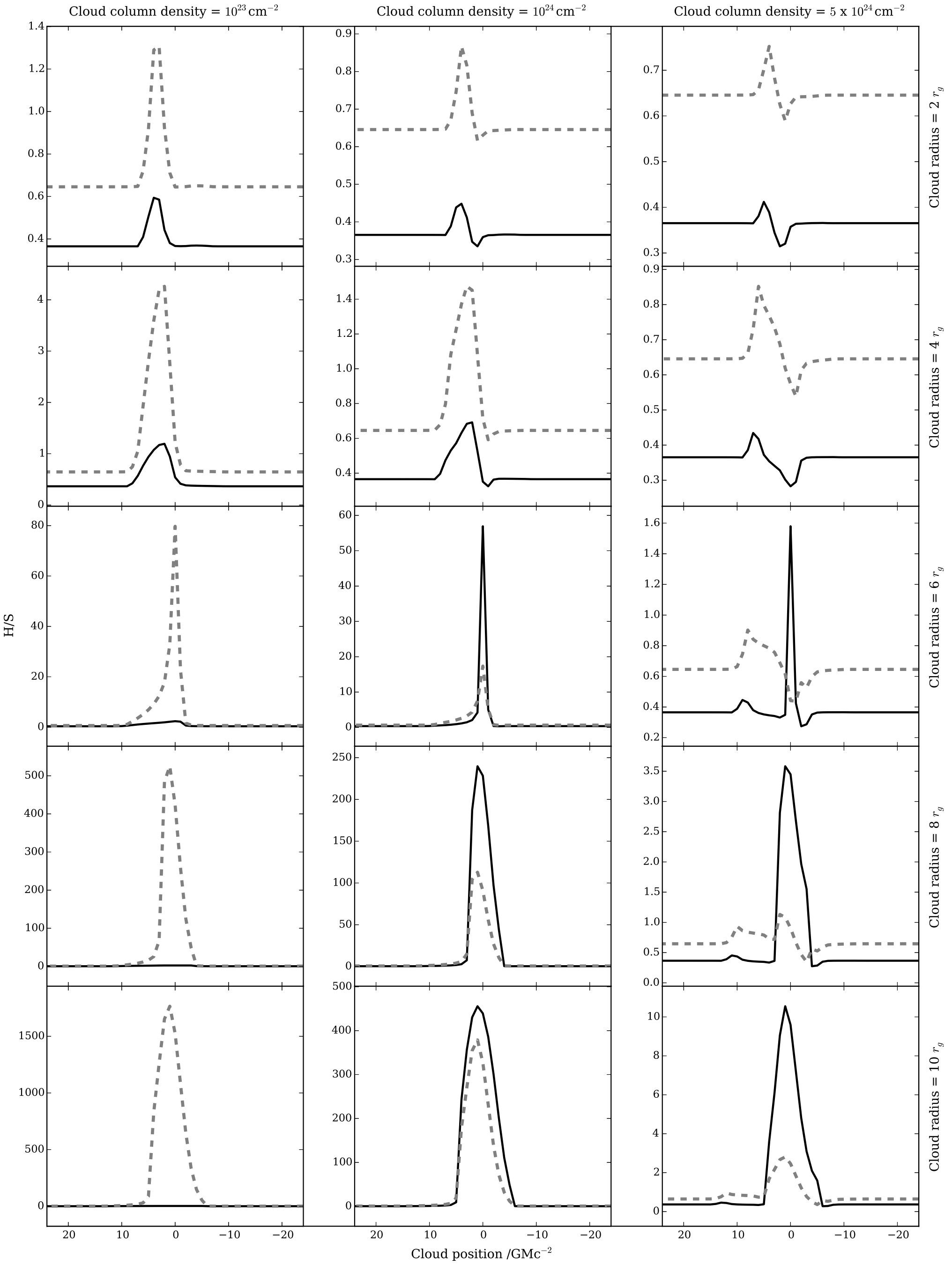

Figure B.16: H / S ratio lightcurves during various eclipses. Maximally Kerr black hole, compact corona ($r = 4\,r_g$), steep emissivity index ($q = 7$), i.e. reflection from compact regions in the disc. The cloud ionization is $\xi = 10\,\mathrm{erg\,cm\,s^{-1}}$. The hard band is 7 – 10 keV. The soft bands are 0.3 – 0.7 keV and 1 – 4 keV for the dashed grey and the solid black curves, respectively. From top to bottom panels: cloud radius = 2, 4, 6, 8, and 10 r_g, respectively. From left to right panels: cloud column density = 10^{23}, 10^{24}, and 5×10^{24} cm^{-2}, respectively.

Bibliography

Abramowicz M. A., Piran T., 1980, ApJ Letters, 241, L7

Abramowicz M. A., Czerny B., Lasota J. P., Szuszkiewicz E., 1988, ApJ, 332, 646

Abramowicz M. A., Chen X., Kato S., Lasota J. P., Regev O., 1995, ApJ Letters, 438,

Agís-González B., Miniutti G., Kara E., Fabian A. C., Sanfrutos M., Risaliti G., Bianchi S., Strotjohann N. L., Saxton R. D., Parker M. L., 2014, MNRAS, 443, 2862

Alonso-Herrero A., Rieke M. J., Rieke G. H., Shields J. C., 2000, ApJ, 530, 688

Antonucci R., 1993, ARA&A, 31, 473

Antonucci R. R. J., Miller J. S., 1985, ApJ, 297, 621

Araya Salvo C., Mathur S., Ghosh H., Fiore F., Ferrarese L., 2012, ApJ, 757, 179

Arnaud K. A., 1996, in Astronomical Data Analysis Software and Systems V. p. 17

Augusto P., Gonzalez-Serrano J. I., Gizani N. A. B., Perez-Fournon I., Edge A. C., 2001, A&AT, 20, 275

Balbus S. A., Hawley J. F., 2003, in Falgarone E., Passot T., eds, Lecture Notes in Physics, Berlin Springer Verlag Vol. 614, Turbulence and Magnetic Fields in Astrophysics. pp 329–348 (`arXiv:astro-ph/0203353`)

Baldwin J. A., Ferland G. J., Korista K. T., Hamann F., Dietrich M., 2003, ApJ, 582, 590

Balick B., Brown R. L., 1974, ApJ, 194, 265

Barthel P. D., 1989, ApJ, 336, 606

Barvainis R., 1987, ApJ, 320, 537

Begelman M. C., 1986, Annals of the New York Academy of Sciences, 470, 51

Begelman M. C., Blandford R. D., Rees M. J., 1984, Reviews of Modern Physics, 56, 255

Bentz M. C., et al., 2007, ApJ, 662, 205

Bentz M. C., et al., 2009, ApJ, 705, 199

Bianchi S., Piconcelli E., Chiaberge M., Bailón E. J., Matt G., Fiore F., 2009, ApJ, 695, 781

Blandford R. D., McKee C. F., 1982, ApJ, 255, 419

Blandford R. D., Payne D. G., 1982, MNRAS, 199, 883

Blandford R. D., Znajek R. L., 1977, MNRAS, 179, 433

Blustin A. J., Page M. J., Fuerst S. V., Branduardi-Raymont G., Ashton C. E., 2005, A&A, 431, 111

Boller T., Brandt W. N., Fink H., 1996, A&A, 305, 53

Boller T., Brandt W. N., Fabian A. C., Fink H. H., 1997, MNRAS, 289, 393

Boyle B. J., Shanks T., Croom S. M., Smith R. J., Miller L., Loaring N., Heymans C., 2000, MNRAS, 317, 1014

Brandt W. N., Pounds K. A., Fink H., Fabian A. C., 1996, in Zimmermann H. U., Trümper J., Yorke H., eds, Roentgenstrahlung from the Universe. pp 429–430

Brenneman L. W., Reynolds C. S., 2006, ApJ, 652, 1028

Brenneman L. W., Reynolds C. S., 2009, ApJ, 702, 1367

Brenneman L. W., et al., 2011, ApJ, 736, 103

Cash W., 1979, ApJ, 228, 939

Cooke B. A., et al., 1978, MNRAS, 182, 489

Dai X., Kochanek C. S., Chartas G., Kozłowski S., Morgan C. W., Garmire G., Agol E., 2010, ApJ, 709, 278

Davis S. W., Laor A., 2011, ApJ, 728, 98

De Robertis M. M., Osterbrock D. E., 1985, in Bulletin of the American Astronomical Society. p. 587

De Rosa A., Panessa F., Bassani L., Bazzano A., Bird A., Landi R., Malizia A., Molina M., Ubertini P., 2012, MNRAS, 420, 2087

Den Herder J. W., et al., 2001, A&A, 365, L7

Dewey D., 2003, Chandra News, 10, 11

Dickens R. J., Currie M. J., Lucey J. R., 1986, MNRAS, 220, 679

Dietrich M., Hamann F., Shields J. C., Constantin A., Vestergaard M., Chaffee F., Foltz C. B., Junkkarinen V. T., 2002, ApJ, 581, 912

Done C., Pounds K. A., Nandra K., Fabian A. C., 1995, MNRAS, 275, 417

Dopita M. A., Sutherland R. S., 1995, ApJ, 455, 468

Dovčiak M., Karas V., Yaqoob T., 2004, ApJS, 153, 205

Dovčiak M., et al., 2013, preprint, (`arXiv:1306.2331`)

Drake J., 2002, Chandra News, 9, 14

Dressler A., Richstone D. O., 1988, ApJ, 324, 701

Dullemond C. P., van Bemmel I. M., 2005, A&A, 436, 47

Eckart A., Genzel R., 1996, Nature, 383, 415

Eckart A., Genzel R., Ott T., Schödel R., 2002, MNRAS, 331, 917

Efstathiou A., Rowan-Robinson M., 1995, MNRAS, 273, 649

Eisenhauer F., et al., 2005, ApJ, 628, 246

Elitzur M., 2012, ApJ Letters, 747, L33

Elitzur M., Shlosman I., 2006, ApJ Letters, 648, L101

Elvis M., 2000, ApJ, 545, 63

Elvis M., Risaliti G., Nicastro F., Miller J. M., Fiore F., Puccetti S., 2004, ApJ Letters, 615, L25

Emmering R. T., Blandford R. D., Shlosman I., 1992, ApJ, 385, 460

Fabian A. C., 1999, Proceedings of the National Academy of Science, 96, 4749

Fabian A. C., Miniutti G., 2005, ArXiv Astrophysics e-prints,

Fabian A. C., Rees M. J., Stella L., White N. E., 1989, MNRAS, 238, 729

Fabian A. C., Iwasawa K., Reynolds C. S., Young A. J., 2000, PASP, 112, 1145

Fabian A. C., Celotti A., Blundell K. M., Kassim N. E., Perley R. A., 2002, MNRAS, 331, 369

Fabian A. C., Miniutti G., Gallo L., Boller T., Tanaka Y., Vaughan S., Ross R. R., 2004, MNRAS, 353, 1071

Fabian A. C., Miniutti G., Iwasawa K., Ross R. R., 2005, MNRAS, 361, 795

Fabian A. C., Lohfink A., Kara E., Parker M. L., Vasudevan R., Reynolds C. S., 2015, MNRAS, 451, 4375

Fairall A. P., 1986, MNRAS, 218, 453

Falcke H., Sherwood W., Patnaik A. R., 1996, ApJ, 471, 106

Fanaroff B. L., Riley J. M., 1974, MNRAS, 167, 31

Fanidakis N., Baugh C. M., Benson A. J., Bower R. G., Cole S., Done C., Frenk C. S., 2011, MNRAS, 410, 53

Fath E. A., 1909, PhD thesis, University of California, Berkeley.

Feltre A., Hatziminaoglou E., Fritz J., Franceschini A., 2012, MNRAS, 426, 120

Ferland G. J., Peterson B. M., Horne K., Welsh W. F., Nahar S. N., 1992, ApJ, 387, 95

Ferland G. J., Porter R. L., van Hoof P. A. M., Williams R. J. R., Abel N. P., Lykins M. L., Shaw G., Henney W. J., Stancil P. C., 2013, Rev. Mex. Astron. Astrofis., 49, 137

Ferrarese L., Ford H., 2005, Space Sci. Rev., 116, 523

Ferrarese L., Merritt D., 2000, ApJ Letters, 539, L9

Filho M. E., Fraternali F., Markoff S., Nagar N. M., Barthel P. D., Ho L. C., Yuan F., 2004, A&A, 418, 429

Forman W., Jones C., Cominsky L., Julien P., Murray S., Peters G., Tananbaum H., Giacconi R., 1978, ApJS, 38, 357

Forster K., Halpern J. P., 1996, ApJ, 468, 565

Fossati G., Maraschi L., Celotti A., Comastri A., Ghisellini G., 1998, MNRAS, 299, 433

Fritz J., Franceschini A., Hatziminaoglou E., 2006, MNRAS, 366, 767

García J., Dauser T., Reynolds C. S., Kallman T. R., McClintock J. E., Wilms J., Eikmann W., 2013, ApJ, 768, 146

Garmire G. P., Bautz M. W., Ford P. G., Nousek J. A., Ricker Jr. . G. R., 2003, in Truemper J. E., Tananbaum H. D., eds, SPIE Vol. 4851, X-Ray and Gamma-Ray Telescopes and Instruments for Astronomy.. pp 28–44, doi:10.1117/12.461599

Gavazzi G., Zaccardo A., Sanvito G., Boselli A., Bonfanti C., 2004, A&A, 417, 499

Gebhardt K., et al., 2000, ApJ Letters, 539, L13

Genzel R., Eckart A., Ott T., Eisenhauer F., 1997, MNRAS, 291, 219

Ghez A. M., Klein B. L., Morris M., Becklin E. E., 1998, ApJ, 509, 678

Ghez A. M., Morris M., Becklin E. E., Tanner A., Kremenek T., 2000, Nature, 407, 349

Ghisellini G., Celotti A., Fossati G., Maraschi L., Comastri A., 1998, MNRAS, 301, 451

Giacconi R., Kellogg E., Gorenstein P., Gursky H., Tananbaum H., 1971, ApJ Letters, 165, L27

González-Martín O., Masegosa J., Márquez I., Guainazzi M., Jiménez-Bailón E., 2009, A&A, 506, 1107

Granato G. L., Danese L., Franceschini A., 1997, ApJ, 486, 147

Grandi P., Tagliaferri G., Giommi P., Barr P., Palumbo G. G. C., 1992, ApJS, 82, 93

Grupe D., 1996, PhD thesis, Univ. Göttingen

Grupe D., Beuermann K., Thomas H. C., Mannheim K., Fink H. H., 1998, A&A, 330, 25

Gu M., Cao X., Jiang D. R., 2001, MNRAS, 327, 1111

Gültekin K., et al., 2009, ApJ, 698, 198

Gupta A., Mathur S., Krongold Y., Nicastro F., 2013, ApJ, 768, 141

Haardt F., Maraschi L., 1991, ApJ Letters, 380, L51

Halpern J. P., 2006, The Astronomer's Telegram, 847, 1

Heckman T. M., 1980, A&A, 87, 152

Heisler C. A., Lumsden S. L., Bailey J. A., 1997, Nature, 385, 700

Hewett P. C., Foltz C. B., Chaffee F. H., 1995, AJ, 109, 1498

Ho L. C., Filippenko A. V., Sargent W. L. W., Peng C. Y., 1997, ApJS, 112, 391

Hönig S. F., Kishimoto M., Gandhi P., Smette A., Asmus D., Duschl W., Polletta M., Weigelt G., 2010, A&A, 515, A23

Hönig S. F., Kishimoto M., Tristram K. R. W., Prieto M. A., Gandhi P., Asmus D., Antonucci R., Burtscher L., Duschl W. J., Weigelt G., 2013, ApJ, 771, 87

Hubble E. P., 1926, ApJ, 64

Hunt L. K., Zhekov S., Salvati M., Mannucci F., Stanga R. M., 1994, A&A, 292, 67

Iwasawa K., Koyama K., Awaki H., Kunieda H., Makishima K., Tsuru T., Ohashi T., Nakai N., 1993, ApJ, 409, 155

Iwasawa K., et al., 1996, MNRAS, 282, 1038

Iwasawa K., Miniutti G., Fabian A. C., 2004, MNRAS, 355, 1073

Jansen F., et al., 2001, A&A, 365, L1

Jiménez-Bailón E., Krongold Y., Bianchi S., Matt G., Santos-Lleó M., Piconcelli E., Schartel N., 2008, MNRAS, 391, 1359

Kalberla P. M. W., Burton W. B., Hartmann D., Arnal E. M., Bajaja E., Morras R., Pöppel W. G. L., 2005, A&A, 440, 775

Kaspi S., Smith P. S., Netzer H., Maoz D., Jannuzi B. T., Giveon U., 2000, ApJ, 533, 631

Kaspi S., Maoz D., Netzer H., Peterson B. M., Vestergaard M., Jannuzi B. T., 2005, ApJ, 629, 61

Kellermann K. I., Sramek R., Schmidt M., Shaffer D. B., Green R., 1989, AJ, 98, 1195

Kellermann K. I., Lister M. L., Homan D. C., Vermeulen R. C., Cohen M. H., Ros E., Kadler M., Zensus J. A., Kovalev Y. Y., 2004, ApJ, 609, 539

Kennicutt Jr. R. C., 1992, ApJS, 79, 255

Kewley L. J., Groves B., Kauffmann G., Heckman T., 2006, MNRAS, 372, 961

Khachikian E. Y., Weedman D. W., 1974, ApJ, 192, 581

Kormendy J., Ho L. C., 2013, ARA&A, 51, 511

Kormendy J., Richstone D., 1995, ARA&A, 33, 581

Koski A. T., 1978, ApJ, 223, 56

Krolik J. H., 1999, Active galactic nuclei: from the central black hole to the galactic environment

Krolik J. H., Kriss G. A., 2001, ApJ, 561, 684

Krolik J. H., McKee C. F., Tarter C. B., 1981, ApJ, 249, 422

Krongold Y., Nicastro F., Brickhouse N. S., Elvis M., Liedahl D. A., Mathur S., 2003, ApJ, 597, 832

Krongold Y., Nicastro F., Elvis M., Brickhouse N., Binette L., Mathur S., Jiménez-Bailón E., 2007, ApJ, 659, 1022

Lawrence A., Elvis M., 2010, ApJ, 714, 561

Lehto H. J., Czerny B., McHardy I. M., 1993, MNRAS, 261, 125

Lira P., Johnson R. A., Lawrence A., Cid Fernandes R., 2007, MNRAS, 382, 1552

Lira P., Videla L., Wu Y., Alonso-Herrero A., Alexander D. M., Ward M., 2013, ApJ, 764, 159

Liu Y., Zhang S. N., 2011, ApJ Letters, 728, L44

Longinotti A. L., Krongold Y., Kriss G. A., Ely J., Gallo L., Grupe D., Komossa S., Mathur S., Pradhan A., 2013, ApJ, 766, 104

Lovelace R. V. E., Wang J. C. L., Sulkanen M. E., 1987, ApJ, 315, 504

Lynden-Bell D., 1969, Nature, 223, 690

Maiolino R., Rieke G. H., 1995, ApJ, 454, 95

Maiolino R., Risaliti G., Salvati M., Pietrini P., Torricelli-Ciamponi G., Elvis M., Fabbiano G., Braito V., Reeves J., 2010, A&A, 517, A47

Malizia A., Bassani L., Bird A. J., Landi R., Masetti N., de Rosa A., Panessa F., Molina M., Dean A. J., Perri M., Tueller J., 2008, MNRAS, 389, 1360

Mannheim K., Schulte M., Rachen J., 1995, A&A, 303, L41

Marinucci A., Risaliti G., Wang J., Bianchi S., Elvis M., Matt G., Nardini E., Braito V., 2013, MNRAS, 429, 2581

Marinucci A., et al., 2014, MNRAS, 440, 2347

Markowitz A. G., Krumpe M., Nikutta R., 2014, MNRAS, 439, 1403

Marshall N., Warwick R. S., Pounds K. A., 1981, MNRAS, 194, 987

Matt G., Bianchi S., Marinucci A., Guainazzi M., Iwasawa K., Jimenez Bailon E., 2013, A&A, 556, A91

Matthews T. A., Sandage A. R., 1963, ApJ, 138, 30

McHardy I., Czerny B., 1987, Nature, 325, 696

McKernan B., Yaqoob T., 1998, ApJ Letters, 501, L29

McLeod K. K., Rieke G. H., 1995, ApJ, 441, 96

Miley G., 1980, ARA&A, 18, 165

Miller J. S., Goodrich R. W., 1990, ApJ, 355, 456

Miller P., Rawlings S., Saunders R., 1993, MNRAS, 263, 425

Miniutti G., Fabian A. C., 2004, MNRAS, 349, 1435

Miniutti G., Fabian A. C., Goyder R., Lasenby A. N., 2003, MNRAS, 344, L22

Miniutti G., Panessa F., de Rosa A., Fabian A. C., Malizia A., Molina M., Miller J. M., Vaughan S., 2009, MNRAS, 398, 255

Miniutti G., Brandt W. N., Schneider D. P., Fabian A. C., Gallo L. C., Boller T., 2012, MNRAS, 425, 1718

Miniutti G., Sanfrutos M., Beuchert T., Agís-González B., Longinotti A. L., Piconcelli E., Krongold Y., Guainazzi M., Bianchi S., Matt G., Jiménez-Bailón E., 2014, MNRAS, 437, 1776

Minkowski R., 1958, PASP, 70, 143

Miyoshi M., Moran J., Herrnstein J., Greenhill L., Nakai N., Diamond P., Inoue M., 1995, Nature, 373, 127

Monier R., Halpern J. P., 1987, ApJ Letters, 315, L17

Morrison R., McCammon D., 1983, ApJ, 270, 119

Mosquera A. M., Kochanek C. S., Chen B., Dai X., Blackburne J. A., Chartas G., 2013, ApJ, 769, 53

Mulchaey J. S., Mushotzky R. F., Weaver K. A., 1992, ApJ Letters, 390, L69

Mushotzky R. F., Done C., Pounds K. A., 1993, ARA&A, 31, 717

Nandra K., O'Neill P. M., George I. M., Reeves J. N., 2007a, MNRAS, 382, 194

Nandra K., O'Neill P. M., George I. M., Reeves J. N., 2007b, MNRAS, 382, 194

Nandra K., Barret D., Barcons X., Fabian A., den Herder J. W., Piro L., Watson M., Adami C., Aird J., Afonso J. M., e. a., 2013, preprint, (`arXiv:1306.2307`)

Narayan R., Yi I., 1995, ApJ, 452, 710

Nenkova M., Sirocky M. M., Ivezić v. Z., Elitzur M., 2008a, ApJ, 685, 147

Nenkova M., Sirocky M. M., Nikutta R., Ivezić v. Z., Elitzur M., 2008b, ApJ, 685, 160

Netzer H., 2008, New Astron. Rev., 52, 257

Netzer H., 2015, preprint, (`arXiv:1505.00811`)

Neugebauer G., Soifer B. T., Matthews K., Elias J. H., 1989, AJ, 97, 957

Nicastro F., Fiore F., Matt G., 1999, ApJ, 517, 108

Novikov I. D., Thorne K. S., 1973, in Dewitt C., Dewitt B. S., eds, Black Holes (Les Astres Occlus). pp 343–450

Oke J. B., 1963, Nature, 197, 1040

Osterbrock D. E., 1977, ApJ, 215, 733

Osterbrock D. E., 1981, ApJ, 249, 462

Osterbrock D. E., 1989, Astrophysics of gaseous nebulae and active galactic nuclei

Osterbrock D. E., Pogge R. W., 1985, ApJ, 297, 166

Osterbrock D. E., Shaw R. A., 1988, ApJ, 327, 89

Padovani P., Giommi P., 1996, MNRAS, 279, 526

Paggi A., Wang J., Fabbiano G., Elvis M., Karovska M., 2012, ApJ, 756, 39

Patrick A. R., Reeves J. N., Porquet D., Markowitz A. G., Lobban A. P., Terashima Y., 2011, MNRAS, 411, 2353

Perola G. C., Matt G., Cappi M., Fiore F., Guainazzi M., Maraschi L., Petrucci P. O., Piro L., 2002, A&A, 389, 802

Peterson B. M., 1993, PASP, 105, 247

Peterson B. M., 1997, An Introduction to Active Galactic Nuclei: Cambridge, New York Cambridge University Press, 1997 Physical description xvi, 238 p. ISBN 0521473489

Peterson B. M., 2006, in Alloin D., ed., Lecture Notes in Physics, Berlin Springer Verlag Vol. 693, Physics of Active Galactic Nuclei at all Scales. p. 77, doi:10.1007/3-540-34621-X_3

Peterson B. M., Wandel A., 1999, ApJ Letters, 521, L95

Peterson B. M., Denney K. D., De Rosa G., Grier C. J., Pogge R. W., Bentz M. C., Kochanek C. S., Vestergaard M., Kilerci-Eser E., Dalla Bontà E., Ciroi S., 2013, ApJ, 779, 109

Pier E. A., Krolik J. H., 1992, ApJ, 401, 99

Piro L., Balucinska-Church M., Fink H., Fiore F., Matsuoka M., Perola G. C., Soffitta P., 1997, A&A, 319, 74

Ponti G., Miniutti G., Cappi M., Maraschi L., Fabian A. C., Iwasawa K., 2006, MNRAS, 368, 903

Pounds K. A., McHardy I. M., 1988, in Tanaka Y., ed., Physics of Neutron Stars and Black Holes. pp 285–299

Pounds K. A., Done C., Osborne J. P., 1995, MNRAS, 277, L5

Pringle J. E., 1981, ARA&A, 19, 137

Puccetti S., Fiore F., Risaliti G., Capalbi M., Elvis M., Nicastro F., 2007, MNRAS, 377, 607

Recondo-Gonzalez M. C., Wamsteker W., Clavel J., Rodriguez-Pascual P. M., Vio R., Ting-Gui W., Santos-Lleo M., Makino F., 1997, A&AS, 121

Rees M. J., 1984, ARA&A, 22, 471

Reeves J., Done C., Pounds K., Terashima Y., Hayashida K., Anabuki N., Uchino M., Turner M., 2008, MNRAS, 385, 108

Reid M. J., Readhead A. C. S., Vermeulen R. C., Treuhaft R. N., 1999, ApJ, 524, 816

Reynolds C. S., Fabian A. C., 1995, MNRAS, 273, 1167

Reynolds C. S., Fabian A. C., 2008, ApJ, 675, 1048

Reynolds C. S., Nowak M. A., 2003, PhR, 377, 389

Reynolds C. S., Brenneman L. W., Lohfink A. M., Trippe M. L., Miller J. M., Reis R. C., Nowak M. A., Fabian A. C., 2012, in Petre R., Mitsuda K., Angelini L., eds, American Institute of Physics Conference Series Vol. 1427, American Institute of Physics Conference Series. pp 157–164 (`arXiv:1112.0036`), doi:10.1063/1.3696170

Risaliti G., Elvis M., 2010, A&A, 516, A89

Risaliti G., Elvis M., Nicastro F., 2002, ApJ, 571, 234

Risaliti G., Bianchi S., Matt G., Baldi A., Elvis M., Fabbiano G., Zezas A., 2005, ApJ Letters, 630, L129

Risaliti G., Elvis M., Fabbiano G., Baldi A., Zezas A., Salvati M., 2007, ApJ Letters, 659, L111

Risaliti G., et al., 2009a, MNRAS, 393, L1

Risaliti G., et al., 2009b, ApJ, 696, 160

Risaliti G., Nardini E., Salvati M., Elvis M., Fabbiano G., Maiolino R., Pietrini P., Torricelli-Ciamponi G., 2011a, MNRAS, 410, 1027

Risaliti G., Nardini E., Elvis M., Brenneman L., Salvati M., 2011b, MNRAS, 417, 178

Rodríguez-Ardila A., Mazzalay X., 2006, MNRAS, 367, L57

Ross R. R., Fabian A. C., 2005, MNRAS, 358, 211

Rozanska A., Malzac J., Belmont R., Czerny B., Petrucci P. O., 2015, preprint, (`arXiv:1504.03160`)

Sako M., Kinkhabwala A., Kahn S. M., Behar E., Paerels F., Gu M. F., Brinkman A. C., Kaastra J. S., Liedahl D. A., 2002, in Boller T., Komossa S., Kahn S., Kunieda H., Gallo L., eds, X-ray Spectroscopy of AGN with Chandra and XMM-Newton. p. 191 (`arXiv:astro-ph/0207404`)

Salpeter E. E., 1964, ApJ, 140, 796

Sambruna R. M., Maraschi L., Urry C. M., 1996, ApJ, 463, 444

Sanfrutos M., Miniutti G., Agís-González B., Fabian A. C., Miller J. M., Panessa F., Zoghbi A., 2013, MNRAS, 436, 1588

Sanfrutos M., Miniutti G., Dovčiak M., Agís-González B., 2016a, Astron. Nachr., 337, 546

Sanfrutos M., Miniutti G., Krongold Y., Agís-González B., Longinotti A. L., 2016b, MNRAS, 457, 510

Sargent W. L. W., Young P. J., Lynds C. R., Boksenberg A., Shortridge K., Hartwick F. D. A., 1978, ApJ, 221, 731

Saripalli L., 2012, ApJ, 144, 85

Schmid H. M., Appenzeller I., Burch U., 2003, A&A, 404, 505

Schmidt M., 1963, Nature, 197, 1040

Schmidt M., 1968, ApJ, 151, 393

Schmitt H. R., Donley J. L., Antonucci R. R. J., Hutchings J. B., Kinney A. L., Pringle J. E., 2003, ApJ, 597, 768

Seyfert C. K., 1943, ApJ, 97, 28

Shakura N. I., Sunyaev R. A., 1973, A&A, 24, 337

Shankar F., Weinberg D. H., Miralda-Escudé J., 2009, ApJ, 690, 20

Shen Z. Q., Lo K. Y., Liang M. C., Ho P. T. P., Zhao J. H., 2005, Nature, 438, 62

Slipher V. M., 1915, Popular Astronomy, 23, 21

Smith H. J., Hoffleit D., 1963, AJ, 68, 292

Smith R. K., Brickhouse N. S., Liedahl D. A., Raymond J. C., 2001, ApJ, 556, L91

Smith J. E., Robinson A., Alexander D. M., Young S., Axon D. J., Corbett E. A., 2004, MNRAS, 350, 140

Stalevski M., Fritz J., Baes M., Nakos T., Popović L. Č., 2012, MNRAS, 420, 2756

Stasińska G., 1984, A&A, 135, 341

Stern B. E., Poutanen J., Svensson R., Sikora M., Begelman M. C., 1995, ApJ Letters, 449, L13

Stirpe G. M., 1990, A&A, 85, 1049

Strüder L., et al., 2001, A&A, 365, L18

Sulentic J. W., Marziani P., Dultzin-Hacyan D., 2000, ARA&A, 38, 521

Szuszkiewicz E., Malkan M. A., Abramowicz M. A., 1996, ApJ, 458, 474

Tadhunter C., 2008, New Astron. Rev., 52, 227

Tanaka Y., et al., 1995, Nature, 375, 659

Tatum M. M., Turner T. J., Sim S. A., Miller L., Reeves J. N., Patrick A. R., Long K. S., 2012, ApJ, 752, 94

Tombesi F., Cappi M., Reeves J. N., Nemmen R. S., Braito V., Gaspari M., Reynolds C. S., 2013, Monthly Notices of the Royal Astronomical Society, Volume 430, Issue 2, p.1102-1117, 430, 1102

Torresi E., Grandi P., Longinotti A. L., Guainazzi M., Palumbo G. G. C., Tombesi F., Nucita A., 2010, MNRAS, 401, L10

Tran H. D., Miller J. S., Kay L. E., 1992, ApJ, 397, 452

Tueller J., Barthelmy S., Burrows D., Falcone A., Gehrels N., Grupe D., Kennea J., Markwardt C. B., Mushotzky R. F., Skinner G. K., 2005, The Astronomer's Telegram, 669, 1

Turner T. J., George I. M., Nandra K., Turcan D., 1999, ApJ, 524, 667

Turner M. J. L., et al., 2001, A&A, 365, L27

Turner T. J., Miller L., Reeves J. N., Kraemer S. B., 2007, A&A, 475, 121

Ulrich M. H., Maraschi L., Urry C. M., 1997, ARA&A, 35, 445

Urry M., 2003, in Collin S., Combes F., Shlosman I., eds, Astronomical Society of the Pacific Conference Series Vol. 290, Active Galactic Nuclei: From Central Engine to Host Galaxy. p. 3 (`arXiv:astro-ph/0301309`)

Urry C. M., Padovani P., 1995, PASP, 107, 803

Urry C. M., Padovani P., Stickel M., 1991, ApJ, 382, 501

Vaughan S., Fabian A. C., 2004, MNRAS, 348, 1415

Véron-Cetty M. P., Véron P., 2006, A&A, 455, 773

Walter R., Fink H. H., 1993, A&A, 274, 105

Wandel A., Mushotzky R. F., 1986, ApJ Letters, 306, L61

Wandel A., Peterson B. M., Malkan M. A., 1999, ApJ, 526, 579

Wang J. M., Zhang E. P., 2007, ApJ, 660, 1072

Wang J. M., Szuszkiewicz E., Lu F. J., Zhou Y. Y., 1999, ApJ, 522, 839

Wang J., Fabbiano G., Elvis M., Risaliti G., Karovska M., Zezas A., Mundell C. G., Dumas G., Schinnerer E., 2011, ApJ, 742, 23

Ward M. J., Wilson A. S., Penston M. V., Elvis M., Maccacaro T., Tritton K. P., 1978, ApJ, 223, 788

Warwick R. S., Pounds K. A., Turner T. J., 1988, MNRAS, 231, 1145

White N. E., Fabian A. C., Mushotzky R. F., 1984, A&A, 133, L9

White R. L., Helfand D. J., Becker R. H., Glikman E., de Vries W., 2007, ApJ, 654, 99

Wiita P. J., 2001, ArXiv Astrophysics e-prints,

Wilkins D. R., Gallo L. C., 2015a, MNRAS, 448, 703

Wilkins D. R., Gallo L. C., 2015b, MNRAS, 449, 129

Wills B. J., Shang Z., Yuan J. M., 2000, New Astron. Rev., 44, 511

Wilson A. S., Tsvetanov Z. I., 1994, AJ, 107, 1227

Woo J. H., Urry C. M., 2002, ApJ Letters, 581,

Worrall D. M., 2009, A&A Rev., 17, 1

Xie G., Dai B., Liang E., Ma L., Jiang Z., 2001, PASJ, 53, 469

Young P. J., Westphal J. A., Kristian J., Wilson C. P., Landauer F. P., 1978, ApJ, 221, 721

Zamanov R., Marziani P., Sulentic J. W., Calvani M., Dultzin-Hacyan D., Bachev R., 2002, ApJ Letters, 576, L9

Zhang S. N., Ji L., Kallman T. R., Yao Y. S., Froning C. S., Gu Q. S., Kriss G. A., 2015, MNRAS, 447, 2671

Zhou Y. Y., Yu K. N., Young E. C. M., Wang J. M., Ma E., 1997, ApJ Letters, 475, L9